Enhanced Analysis of Load Transfer Mechanism and Deformation Estimation for Ground Improvement Using Concrete Injected Columns

A thesis in fulfilment of the requirement for the award of the degree

Doctor of Philosophy

from

University of Technology Sydney (UTS)

by

BALAKA GHOSH, BEng, MEng (UTS)

School of Civil and Environmental Engineering,

Faculty of Engineering and Information Technology

2018

CERTIFICATE OF ORIGINAL AUTHORSHIP

I confirm that the work done in this thesis has been an original work which has not previously been submitted for an evaluation unless as acknowledged within the text.

I also affirm that I have authored the thesis. All assistance for my research and preparation of this thesis has been acknowledged. Moreover, I also affirm that all literature and sources of information used in this research are indicated.

This research is supported by the Australian Government Research Training Program.

Balaka Ghosh

July 2019

ABSTRACT

This thesis presents analytical solutions to predict the response of the load transfer platform (LTP) on columns stabilised soft soil subjected to any shape of pressure loadings. The effect of the bending and shear deformations of LTP and the nonlinear stress strain behaviour of soft soil are incorporated into the analytical model. The cracked reinforced Timoshenko beam is proposed and implemented to model LTP to consider the shear and flexural deformations. Soft soil is idealised by spring-dashpot system to include the time-dependent non-linear behaviour. The columns and geosynthetics are modelled with linear Winkler springs in the applied range of stresses and rough elastic membrane, respectively. Influence of negligible tensile strength compared to the compressive strength of granular materials in LTP is also considered. Furthermore, a parametric study has been conducted to investigate how the parameters such as the column spacings, the thickness of LTP, the tensile stiffness of geosynthetics, and the degree of consolidation of the soft soil affect the response of LTP on improved soft soil. Moreover, the results from the proposed cracked Timoshenko beam theory (capturing the combined shear and bending stiffness of LTP) have been compared with results from the Euler-Bernoulli model (capturing deflection due to bending only) and the Pasternak model (capturing deformation due to shear only).

This research also provides rigorous solutions to estimate the settlement of the soft soils under embankment load when double layer of geosynthetics reinforcements have been used in the load transfer platform. The response function of the system in plane strain condition has been attained by developing governing differential equations for the proposed mechanical model and its solutions. To develop analytical equations, the basic

differential equations of a Timoshenko beam subjected to a distributed transverse load and a foundation interface pressure, generated from the Kerr foundation model is applied. Furthermore, the suitability of the Kerr foundation model for engineering calculations of LTP are evaluated. In addition, the results from the proposed model simulating the soft soil as the Kerr foundation model are compared to the corresponding solutions when the soft soil is idealised by Winkler and Pasternak foundations. Additionally, to assess the overall behaviour of the multilayer geosynthetic reinforced granular layer as well as that of the single layer geosynthetic reinforced granular layer parametric studies are also carried out. The developed analytical model can be applied by practicing engineers to predict the deflection of the LTP and mobilised tension in the geosynthetic reinforcement.

In addition, this research presents the results of a numerical investigation into the performance of geosynthetic-reinforced column-supported embankment in soft ground. A three-dimensional finite-element model was employed to compare the results with a case study on a number of governing factors such as the downward and lateral movement of soft soil, the stress transferred to column, and the developed excess pore water pressure. The soft soil is represented by the Modified Cam-Clay model (MCC) while the linear elastic and perfectly plastic model adopting the failure criterion of Mohr-Coulomb is applied for medium dense to dense gravel, cobble soil, the granular platform and the embankment. By adopting Hoek-Brown model (HB) to simulate concrete injected columns, non-linear stress-strain relationship is considered in this study. It should be noted that the geometry and other physical properties of the soils and columns considered in this study have been adopted from Gerringong upgrade project, a ground improvement mission taken place in New South Wales, Australia.

To my father, Ramendra Sundar Ghosh, my mother, Bandana Ghosh, and my beloved husband Soumya Das, who shared love and strength with me throughout this marvellous journey.

ACKNOWLEDGEMENT

A casual discussion with my supervisor during my Masters' days gave me the opportunity of a lifetime to pursue doctoral studies at University of Technology Sydney (UTS). Not only I have developed a flavour and passion for my subject, this journey has also offered me profound experience in my academic career. Such achievements have been possible only because of the support and guidance from my supervisors, assistance from my geotechnical research fellows, encouragement from work colleagues and lastly sacrifices made by my family.

Firstly, I would like to appreciate my principal supervisor A/Prof Behzad Fatahi and my co-supervisor A/Prof Hadi Khabbaz for their structured and exhaustive guidance not only limited to the specific field of study but beyond. PhD is a challenge and having such wonderful mentors who constantly support me, equipped me well to deal with that challenge. My PhD thesis could not have been achieved without their constructive feedback and worthy recommendations.

Secondly, I am thankful to Prof Jian-Hua Yin for providing valuable insights and my geotechnical research fellows who have been directly or indirectly involved in my doctoral study. More specifically, I am indebted to my co-researcher Harry Nguyen for his assistance with investigation of field report.

Furthermore, I would sincerely acknowledge the Faculty of Engineering and Information Technology at UTS and the Centre of Built Infrastructure Research (CBIR) for providing me the platform to pursue my PhD. I appreciate Ms Van Le and Ms Phyllis Agius for their flexibility and kind assistance. I would also like to acknowledge the support received from Dr. Richard Kelly, Mr. Mohammad Qazafi, and Mr. Zico Lai from SMEC; Mr.

Graham Yip, Dr. A. H. M. Kamruzzaman, Mr. Daniel Horan, and Mr. Adrian Rouse from Roads and Maritime Services (RMS); Mr. Michael Marix-Evans from Fulton Hogan; and Philippe Vincent (Menard Oceania). Valuable advices from Mr. Roger Santos (Formerly at Fulton Hogan) and Jeff Hsi (formerly at SMEC) are not gone unnoticed.

In addition, I would like to recognise the kind words of encouragement, support and assistance from my work colleagues particularly Anthony Garnaut, James McIntosh and Chris Smyth.

To succeed in a monumental challenge of this sort required a very strong family support. I would like to acknowledge my family for all the sacrifices that they have made to support me through this journey. In particular, my parents who travelled to Australia multiple times to provide support at home, my in-laws for their constant encouragement from overseas. Last but not least, I would like to thank my beloved husband, Soumya Das, who is constantly an epitome of support and strength to me.

LIST OF PUBLICATIONS

❖ Published Journal Articles

Ghosh B., Fatahi B., Khabbaz H., and Yin J.H. (2017), 'Analytical study for double-layer geosynthetic reinforced load transfer platform on column improved soft soil', Geotextiles and Geomembranes, **45** (5): 508–536.

Ghosh B., Fatahi B., and Khabbaz H., (2017). 'Analytical solution to analyse LTP on column improved soft soil considering soil nonlinearity', International Journal of Geomechanics. **17** (3): 1–24.

❖ Published Conference Papers

Ghosh B., Fatahi B., Khabbaz H., and Kamruzzaman A. H. M., (2016). 'Analysis of CMC-Supported Embankments Considering Soil Arching', Proceedings of the Geo-China 2016 International Conference, Shandong, China. ASCE Geotechnical Special Publication (**GSP 265**): 286–293.

Ghosh B., Fatahi B., and Khabbaz H., (2016). 'Mechanical Model to Analyse Multilayer Geosynthetic Reinforced Granular Layer in Column Supported Embankments', Procedia Engineering: Proceedings of The 3rd International Conference on Transportation Geotechnics, **143**: 387–394.

Ghosh B., Fatahi B., Khabbaz H., and Hsi G., (2015). 'Reinforced Timoshenko Beam Theory to Simulate Load Transfer Mechanism in CMC Supported Embankments', Proceedings of 12th Australia New Zealand Conference on Geomechanics, Wellington, New Zealand, 1099–1106.

Ghosh B., Fatahi B., Khabbaz H., and Kamruzzaman A. H. M., (2015). 'Assessing Load Transfer Mechanism in CMC-Supported Embankments Adopting Timoshenko Beam Theory', Proceedings of XVI European Conference on Soil Mechanics and Geotechnical Engineering: Geotechnical Engineering for Infrastructure and development, Edinburgh, 577–582.

TABLE OF CONTENTS

LIST OF FIGURES

LIST OF TABLES

LIST OF ABBREVIATIONS

EB: Euler-Bernoulli beam;

BH: Borehole;

CD: Construction day;

CIC Concrete Injected Column;

CL: Centreline;

CPT Cone penetration test;

CS: Cross section;

DMM: Deep Soil Mixing Method;

EB: Euler-Bernoulli beam;

GR: Geosynthetic reinforcement

GRCS: Geosynthetic reinforced column-supported;

HB: Hoek-Brown;

I: Inclinometer;

LTP: Load transfer platform;

MC: Mohr-Coulomb;

MCC Modified Cam Clay;

NA: Neutral axis;

OCR: Over consolidation ratio;

PC: Pressure cell;

PSL: Pasternak shear layer;

PVD: Pre-fabricated drain;

SP: Settlement plate;

SRR: Stress reduction ratio;

TB: Timoshenko beam

VP: Vibrating wire piezometer;

NOMENCLATURE

The following notations are used in this research:

a: diameter of the pile (m);

a_r: area replacement ratio (non-dimensional);

A_c: plan area of the column (m^2);

A_p: plan area or cross section area of the column or pile (m^2);

A_h: cross section area of the granular layer in hogging region after cracking (m^2);

A_s: cross section area of the granular layer in sagging region after cracking (m^2);

A_r: cross section area of the geosynthetics (m^2);

A_w: plan area of CIC wall in plane strain (m^2);

C: shear stiffness of the beam (kN/m);

C_h : shear stiffness of the load transfer platform in hogging region (kN/m);

C_s: shear stiffness of the load transfer platform in sagging region (kN/m);

d: diameter of the column (m);

D: bending stiffness of Timoshenko beam (kN.m);

D_h: equivalent bending stiffness of the load transfer platform in hogging region (kN.m);

D_s: equivalent bending stiffness of the load transfer platform in sagging region (kN.m);

e_0: initial void ratio;

E: efficacy or Young's modulus;

E': effective stiffness (kN/m^2);

E_c: Young's modulus of the concrete injected column material (kN/m^2);

E_g: Young's modulus of the granular material in load transfer platform (kN/m^2);

E_r: elastic stiffness of the geosynthetic reinforcement (kN/m^2);

f_{ck}: 28-days compressive strength of concrete (MPa);

G: shear modulus of the soft soil (kPa);

h: thickness of the load transfer platform before cracking (m);

h_h: distance of the neutral axis from the compression surface of the load transfer platform for hogging moment (m);

h_h: distance of the neutral axis from the compression surface of the load transfer platform for sagging moment (m);

H: depth of the soft soil (m);

H: height of the embankment (m);

H_c: length of the columns (m);

H_s: depth of the soft soil (m);

I_h: second moment of inertia of the granular fill about neutral axis for hogging (m^3);

I_s: second moment of inertia of the granular fill about neutral axis for sagging (m^3);

J: stiffness of the geosynthetic reinforcement (kN/m);

K_0: lateral earth pressure coefficient;

K_p: passive earth pressure (kPa);

M: bending moment of the beam (kN.m);

n: modular ratio (non-dimensional) or stress concentration ratio;

k_c: modulus of subgrade reaction for the column ($kN/m^2/m$);

k_{0s}: initial modulus of subgrade reaction for the soft soil foundation ($kN/m^2/m$);

k_{1s}: stiffened modulus of subgrade reaction for the soft soil foundation ($kN/m^2/m$);

k_s: modulus of subgrade reaction for the soft foundation soil ($kN/m^2/m$);

k_{sc}: shear correction coefficient of the Timoshenko beam (non-dimensional);

k_l: modulus of subgrade reaction for the soft soil foundation attached to the bottom of shear layer ($kN/m^2/m$);

k_{sc}: shear correction coefficient of the Timoshenko beam (non-dimensional);

k_u: modulus of subgrade reaction for the soft soil foundation attached to LTP ($kN/m^2/m$);

K_c: equivalent modulus of the subgrade reaction for column (kN/m);

$(K_c)_{eq}$: equivalent modulus of the subgrade reaction for column (kN/m);

p: transverse pressure on the beam from super structure (kPa);

P_r: distributed load acting on geosynthetics between adjacent piles (kPa);

q: normal stress at the interface of the beam and the soft soil (kPa);

q_0: surcharge (kPa);

Q: shear force (kN);

s: centre to centre spacing between the two adjacent columns or piles (m);

s': clear spacing between the two adjacent columns or piles (m);

S_r: tensile stiffness of the geosynthetics (kN/m);

S_r^b: tensile stiffness of the bottom geosynthetic reinforcement (kN/m);

S_r^t: tensile stiffness of the top geosynthetic reinforcement (kN/m);

T: tension mobilised in the geosynthetic layer (kN/m);

U: degree of consolidation of the soft soil (%);

V: shear force in the beam (kN/m);

w: transverse deflection (m);

$\hat{w}$: deflection of the load transfer platform beyond which k_{0s} becomes k_{1s} (m);

y_h: distance between the neutral axis and the centroid axis of the load transfer platform in hogging region (m);

y_s: distance between neutral and centroid axes of the load transfer platform in sagging region (m);

y_r distance of the geosynthetic from the centroid axis of load transfer platform (m);

y_r^b: distance of the bottom geosynthetic layer from the centroid axis of load transfer platform (m);

y_r^t : distance of the top geosynthetic layer from the centroid axis of load transfer platform (m);

ε: strain in geosynthetics;

σ_c: stress transferred to pile (kPa);

σ_s: stress transferred to soil (kPa);

γ: unit weight (kN/m^3);

ρ: soil arching ratio;

υ: Poisson's ratio;

υ_g: Poisson's ratio of the granular material (non-dimensional);

υ_r: Poisson's ratio of the geosynthetics (non-dimensional);

υ_r^t : Poisson's ratio of the top geosynthetic reinforcement (non-dimensional);

υ_r^b: Poisson's ratio of the bottom geosynthetic reinforcement (non-dimensional);

λ: slope of the normal consolidation line;

κ: slope of the elastic swelling line;

θ: rotation angle of the cross section of the beam (radian);

ϕ: frictional angle (degree);

ϕ' effective friction angle;

ψ: rotation angle of Timoshenko beam (radian);

ψ': effective dilatancy angle;

CHAPTER 1

1. INTRODUCTION

1.1. General

Due to the increase in population and urbanisation, finding suitable lands for construction of infrastructure, housing and social facilities have become challenging for geotechnical engineers. Problematic soils such as soft clays, expansive soils, loose sands, collapsible and erodible soils have been identified and studied for many decades. Soft soils generally have low bearing capacity, resulting in large settlement when experiencing the load of structures. Slope instability, lateral movement, cracking, and collapse are common phenomena when structures are built on problematic soils. Most of problematic soils have low shear strength and experience instability, which can damage constructions, built on the soil. Preventing these damages not only is a great challenge for geotechnical engineers, but also requires high maintenance. In some instance, the repair costs for construction on problematic soils can be in the order of billions of dollars. Soil improvement techniques have become commercial and considered as of the popular solutions proposed by geotechnical engineering to improve the soil properties, and further to extend the suitable lands for construction. There are several soil improvement techniques, which can be applied either individually or in combination as shown in Figure 1.1. The selection of a right technique or a combination of techniques depends on a several factors, including the soil properties, the significance of structure, site conditions, and the time and monetary constraints of the development. Due to the rapid progress of

technology, soil improvement methods and equipment have improved the efficiency and allow construction on marginal ground such as seaside areas or muddy lands. Indeed, soil improvement techniques vary from simple to complex, and economical to expensive.

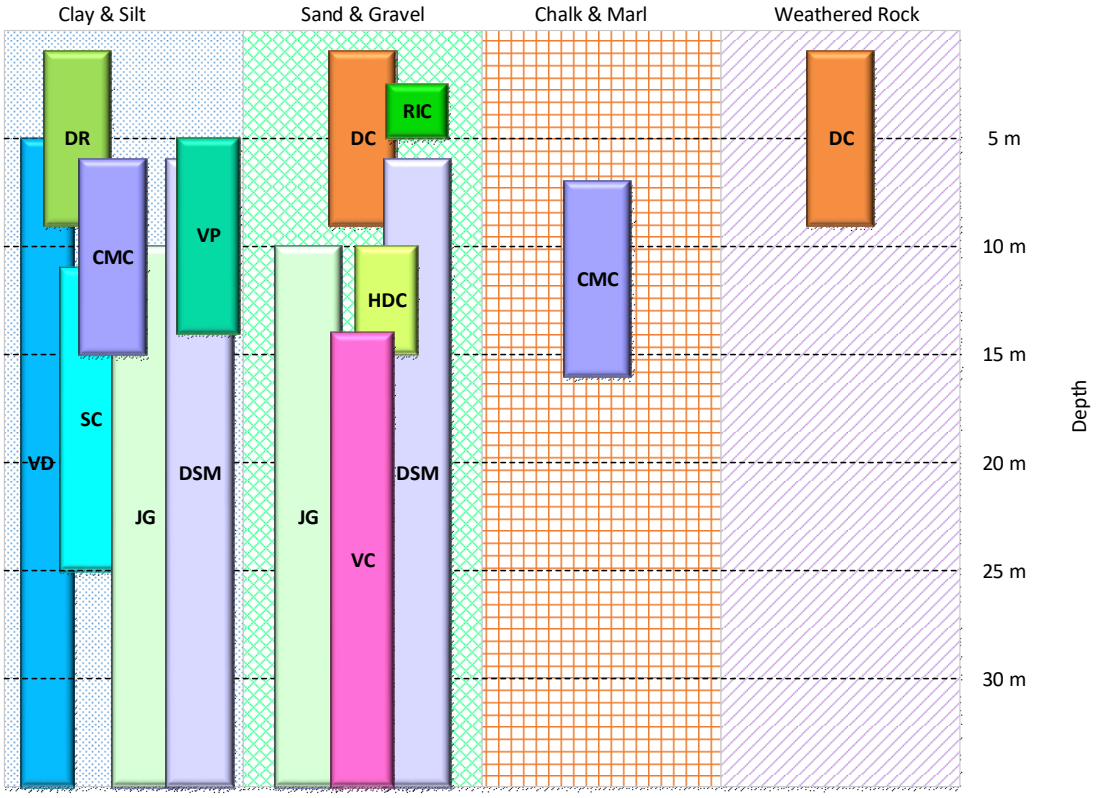

DR: Dynamic compaction; DC: Dynamic replacement; DSM: Deep soil mixing; HDC: Heavy dynamic compaction; CMC: Controlled modulus column; JG: Jet grouting; RIC: Rapid impact compaction; SC: Stone column; VC: Vibro-compaction; VD: Vertical drain; VP: Vacuum preloading

Figure 1.1. Range of ground improvement techniques.

The concrete injected column (CIC) is one of the ground improvement techniques to meet the higher demand for the transport infrastructure, particularly near waterways comprising weak soil layers. This ground improvement technique improves the soil characteristics of a compressible soil layer and reduces its compressibility by use of rigid soil reinforcement columns. Unlike soil improvement using piles, which is considered to support the entire load of the structure on the piles, CICs increase the stiffness of the soil mass to globally reduce both total and differential settlements by distributing the load of

the structure between soil and CICs as displayed in Figure 1.2. Introducing geosynthetic reinforcement (GR) within the granular fill materials above the columns, which is known as the load transfer platform (LTP) results in a more efficient transfer of load to the columns in the form of an arching mechanism in column-supported embankments. The interaction between the reinforced granular layer, the columns, and the soft soil below the granular layer change their actual behaviour considerably.

Several three-dimensional models of a bridge approach embankment reinforced by a layer of geosynthetics and supported by deep mixed (DM) columns or piles adopting coupled mechanical and hydraulic are proposed in the literature using PLAXIS 3D or FLAC^{3D}. Effect of construction sequence on the development and dissipation of excess pore water pressure are presented and discussed. Several researchers have conducted numerical analysis of an axisymmetric model of geosynthetic-reinforced and pile-supported embankments and suggested that inclusion of geosynthetic in earth platforms can reduce the total and differential settlements above the pile heads, and at the ground surfaces, promote efficient load transfer from the soil to the piles and reduce the possibility of soil yielding above the pile heads. Most of the numerical studies related to soil arching are conducted on pile-supported embankments. Very limited studies have been carried out on CIC-supported embankments resting over soft soil.

Apart from the consistent growth in numerical models to investigate the behaviour of the load transfer platform over column stabilised soft clays, analytical studies have recently become more accessible due to the vast improvements in computational capabilities. This has enabled practising geotechnical engineers to analytically predict the deformation of LTP and assess the load transfer mechanism. It should be noted that despite their limitations in assessing complex geometries and soil plasticity, analytical approaches can

be widely applicable for problems with homogeneous and nonhomogeneous differential equations under complex boundary and initial conditions.

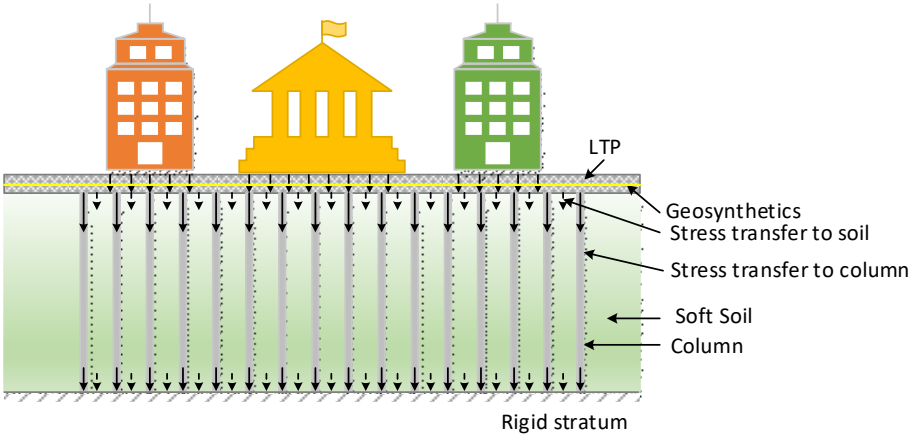

Figure 1.2. Load transfer mechanism of concrete injected columns-supported structures.

Therefore, this research is a further effort in this direction to present a mechanical model that can be applied for the analysis of settlement response of the geosynthetic-reinforced CIC-supported embankment system. In addition, a full-scale three-dimensional numerical model of the CIC-supported embankments with the finite element method using PLAXIS 3D software is developed. Following sections in this chapter describes the statement of problem and the concept of mechanistic behaviour of soil, the research objectives and scopes, and an outline of the thesis.

1.2. Statement of Problem

For CIC-supported embankments, according to the serviceability limit state design, it is necessary to ensure the deformation of the embankment does not lead to the disruption of serviceability criteria in the embankments. Therefore, estimation of the settlement of underlying saturated soft soil at any stage of consolidation is the most important task for engineers. In recent years, many researchers have studied the load-settlement response of

reinforced granular layer to develop simple mechanical models of the LTP that simulate real situations. A mechanical model can be described in terms of mechanical elements such as beams (Pasternak beams, Euler-Bernoulli beams or Timoshenko beams), Winkler springs, Terzaghi's spring-dashpot system, and elastic membranes. These elements can easily be understood on the basis of fundamental concepts of mechanics which are shown in Figure 1.3.

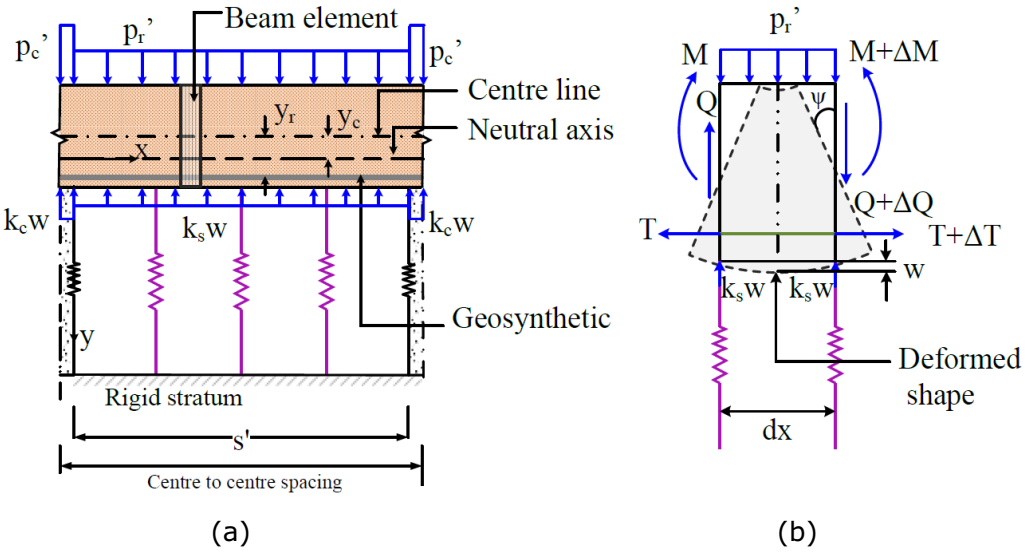

Figure 1.3. Fundamental concepts of mechanics for LTP beam: (a) stresses on LTP of a CIC-supported embankment and (b) details of internal and external forces acting on the finite LTP beam element.

A modified Pasternak model, a new foundation model to represent the geosynthetic reinforced soil, where Pasternak shear layer (1954) is combined with Winkler's springs (1867). However, neither Winkler nor Pasternak model considers both bending and shearing. Euler-Bernoulli beam on elastic foundation model has been attempted to solve the SSI problem considering the bending only. However, very little attention is paid to Timoshenko beam model (1921) on elastic foundation considering bending and shearing

to represent the engineered granular layer. Most of the models reported in the literature are also developed for single-layer reinforced systems without considering columns (Yin, 2000a; Yin, 2000b; Maheshwari and Viladkar, 2009). Therefore, currently no closed form solution of the load-settlement response of the reinforced granular layer-soil-column system is available in the literature, which considers both the bending and the shear deformation of the multilayer geosynthetic-reinforced granular layer. In addition, it has been observed that very limited studies have been conducted on embankments resting over column-improved soft soil considering mechanistic behaviour of column-supported embankment incorporating the arching effect. Furthermore, the existing mechanical and analytical research studies in the literature adopt linear elastic load-displacement response of soil in soil-structure interactions problems. Hence, a simplified linear load-displacement relationship for soil may not result in realistic and accurate predictions. Indeed, the nonlinear load-displacement response of soil should be considered in the problem of soil-structure interaction (SSI) to achieve more accurate and realistic predictions. However, it is understood that no closed-form solution is currently available considering Timoshenko beam on nonlinear elastic foundation.

Over the past few decades, several numerical studies have been conducted on geosynthetic reinforced column-supported embankments. However, it is revealed from the literature review that none of the existing finite element or finite different models can consider the non-linear stress strain relationship of columns along with pre-fabricated drains with a varying over consolidation ratio of soil in a full-scale three-dimensional condition.

Whether immediately or post-construction, damage and cracks in structures are a challenging issue for organisations that design and construct foundations on improved

soft soil. Allowable maximum post-construction settlement is less than a certain value (e.g. 100 – 200 mm) over the structure's life-time and limit the differential settlement to a certain change in grade (e.g. 0.5% and 0.3% for flexible and rigid pavements, respectively). Thus, precise predictions of the mechanical properties of CIC improved soft soil including stress-strain relationship, strength and compressibility parameters, is important for design. Many geotechnical organisations adopt various methods to reduce settlement of structures. However, some expected post-construction and differential settlements are still observed. This clearly indicates that uncertainties in the existing design methods are excessive and unacceptable. This is not significant if observed settlement is within expectation. However, variability and uncertainties regarding lateral and differential deformations can result problems. Under-predicting lateral deformations can cause unsatisfactory performance of the project, whereas conservative design to account for uncertainties can result in un-economic design. This research will aim to predict the horizontal and vertical deformations of CIC improved ground precisely, with clear significance for design and construction organisations, the transport industry, and the community as users of infrastructure, and governments and private sector road operators as the source of funding for infrastructure. Moreover, the safety of structures resting on the poor ground will be substantially increased.

1.3. Objectives and Scope of Research

Key aim of this research is to develop analytical models to predict the deformation of the load transfer platform and the tension mobilised in the geosynthetic reinforcement under three categories while soft soil is idealised by: (1) linear Winkler foundation, (2) non-linear Winkler foundation, and (3) Kerr foundation. Flexural and shear behaviour of the geosynthetic reinforced granular layer are considered in the proposed models. In addition,

effects of negligible tensile strength of the granular materials in the load transfer platform is addressed and incorporated in the proposed solutions. Graphical presentations mainly highlight effects of the column spacings, thickness of the load transfer platform, the degree of consolidation of the soft soil, stiffness of the geosynthetic reinforcement and the soft soil in settlement of the load transfer platform, mobilised tension in the geosynthetic reinforcements, and the flexural and shear behaviour of load transfer platform. This study also demonstrates the validation of each model by comparing the results to the corresponding solutions when the soft soil is idealised by several other existing simple foundation models. During this research, it is felt that the analytical solution in plane strain and 3D conditions are considered only in average sense. Therefore, 3D finite element method using PLAXIS is adopted to investigate the behaviour of a column-supported embankment in which the data are taken from a real case study.

The specific objectives of analytical study in this research are as follow:

- Providing an analytical model for predicting the behaviour of the load transfer platform on column improved soft soil in plane strain condition;
- Estimating the deformation of the load transfer platform and mobilised tension in the geosynthetic reinforcement;
- Investigating the effects of several parameters such as column spacings, LTP thickness, and stiffness of the geosynthetic reinforcement;
- Evaluating the efficiency of the proposed analytical models; and
- Employing a three-dimensional model to back analyse the field results of a case study
- Investigating stress distribution between columns and soils

- Estimating bending moment and shear force developed in the column
- Examining and comparing the excess pore water pressure with field monitored data
- Comparing the deflection of soft soil and columns

For the analytical procedure, the principles of solid mechanics are used. To develop analytical equations, the basic differential equations of a Timoshenko beam subjected to a distributed transverse load and a foundation interface pressure, generated from the foundation model are employed. Fourier series is utilised to consider the distribution of vertical loading on LTP. The homogeneous solution of the governing sixth order nonhomogeneous differential equation was found from the roots of the characteristic polynomial equation. Then adopting the method of Undetermined Coefficients, the particular solution is obtained. For the numerical procedure, this research is further work of three-dimensional finite element analysis where varied OCR of soft soil in non-horizontal foundation soil profiles, taking into account the non-linear stress-strain behaviour of columns. Hoek-Brown model (HB) is adopted to simulate the behaviour of columns. Using the Modified Cam Clay (MCC) to idealise the soft soil in finite element analysis, the changes in the pore water pressure during the consolidation are also considered. Additionally, the three-dimensional model has been employed to back analyse the field results of a case study, where the complexity of modelling the interface between the concrete injected columns (CIC) and pre-fabricated vertical drains (PVD) improve soil areas is examined.

In summary, this study comprises the following parts:

- Developing analytical solutions to predict the settlement of the LTP on linear soft soil in plane strain condition, while capturing both shear and flexural behaviour of the load transfer platform;
- Developing analytical solutions for the geosynthetic reinforced granular layer in plane strain condition while non-linear behaviour of the soft soil has been incorporated;
- Developing an analytical solution to predict the behaviour of the load transfer platform in plane strain condition while shear and flexural deformation of the soft soil foundation are addressed; and
- Verifying the proposed models for with existing analytical solutions previously published in the literature.

In addition, it is necessary to address some limitations of the research. They can be summarised as follows:

- Columns rest on a rigid stratum;
- Possible pull-out resistance force of geosynthetics from the surrounding granular material is omitted;
- Soil cementation and soil creep are neglected;
- Effect of column failure is ignored;
- Interaction between columns and surrounding soil is not taken into account.

1.4. Organisation of Thesis

Seven chapters are presented in this thesis, including:

- Chapter 1 promptly presents a general view as well as an importance of mechanistic behaviour of soil in analysing column improved soft soil. In addition, the scope and objectives are clearly highlighted in this chapter.
- Chapter 2 delivers a comprehensive literature review of arching theory on column-supported embankments, and analysis of beam on elastic foundation in soil-structure interaction (SSI) problems. Moreover, existing analytical and numerical models of column stabilised soft soil are critically reviewed in this chapter.
- Chapter 3 presents the detailed development of analytical model to predict the time dependent settlement of the load transfer platform (LTP) to any shape of pressure loading while capturing both shear and bending deformation of the soil in the load transfer platform. Non-linear behaviour of the soft soil is introduced to the analytical derivation. Changes in the maximum deformation of LTP and the maximum tension in geosynthetics are discussed and graphically demonstrated. Besides, to check for the validity of the proposed analytical solution, a verification exercise against other existing analytical solutions is presented.
- Chapter 4 introduces an accurate analytical model to predict behaviour of LTP on column reinforced soft soil by idealising the physical modelling of the LTP on the soil media as "membrane reinforced Timoshenko beam" on Kerr foundation. Then, an analytical solution for the governing differential equation is proposed. The suitability of the Kerr foundation model for engineering calculations of LTP are evaluated while LTP is subjected to symmetric loading. Deflection and rotation of the LTP, moments and shears in the LTP, shear forces in the soft soil, and tension in the geosynthetics are examined against several existing analytical solutions. In addition, results of parametric studies by investigating effects of

column spacings, LTP thickness, stiffness of geosynthetics and soft soil on the behaviour of LTP, are reported in this chapter.

- Chapter 5 introduces an analytical model to predict behaviour of LTP on column reinforced soft soil for different distributions of loadings induced by arching in the embankment by idealising the physical modelling of the LTP on the soil media as "membrane reinforced Timoshenko beam" on Winkler foundation. The effects of column stiffness and consolidation of the saturated soil are also incorporated in the model. Then, an analytical solution for the governing differential equation is suggested. Deflection and rotation of the LTP, moment and shear in the LTP, and tension in the geosynthetics are investigated under different pressure distribution due to different existing arching theories. This chapter also includes a mechanical model to predict the behaviour of a multilayer geosynthetic reinforced granular fill soft soil system improved with concrete injected columns underneath the embankment. Simultaneously, deformation of geosynthetics implanted granular layer due to bending and shear is considered in this chapter. Tension established in the geosynthetics, rotation and settlements of the improved soft ground are predicted using the proposed model.
- Chapter 6 presents a full-scale three-dimensional numerical modelling of geosynthetic reinforced column and pre-fabricated vertical drain supported embankment. The analysis is carried out in PLAXIS 3D which is based on finite element analysis. Vertical and horizontal settlement of soft soil, and excess pore water pressure generated in the soft soil, stress transferred to column are compared with the real case field monitored results. Moreover, stress distribution on geosynthetics, columns, and soils have been discussed. Behaviour of columns are also investigated in terms of lateral deflection, bending moment, and shear force.

- Finally, Chapter 7 briefly delivers the summary of the thesis and then presents the conclusions and recommendations for forthcoming studies. This chapter is followed by references and appendices.

CHAPTER 2

2. LITERATURE REVIEW

2.1 General

Geosynthetic reinforced column-supported (GRCS) embankments are increasingly being used for large storage tanks in ports, major highway embankments and retaining walls on soft ground near waterways, runway extensions on filled ground, and numerous commercial and residential multi-storey buildings. Controlled Modulus Columns (CMC) enables an efficient transfer of applied loads down to a competent layer (typically stiff to very stiff clay/silt or medium dense to dense sand). This ground improvement technique is based on a load sharing concept between the rigid inclusions and the natural soil which results in a settlement reduction and a bearing capacity increase of natural soil. In case of Pile foundations, it is only the piles that carry load from the superstructure without utilising the existing natural soil. Stone columns are also an essential ground improvement technique with additional advantage of proving a drainage path. Concrete injected columns (CICs) are a sustainable and cost-effective ground improvement technology that transmit load from the foundation to a lower bearing stratum through a composite CIC/soil matrix. The load transfer mechanism among all of the components in GRCS, including the embankment fill, load transfer platform, the CICs and the foundation soils, are complicated. Model tests, theoretical analysis and numerical analysis were conducted to investigate the load transfer mechanism in embankments on soft soil supported by piles, deep soil mixing columns and stone columns. Several design methods have been proposed to meet the demand from practice. However, little attention has been paid to embankments built

on CICs improved soft soil. The purpose of this chapter is to summarize the existing analysis and design approaches for two important and related design issues for GRCSs: (1) determining the stress distribution between columns and soils, and (2) identifying the effect of load distribution on the geosynthetic reinforcement in the load transfer platform at the base of embankment.

2.2 Ground Improvement Using Concrete Injected Columns (CICs)

Ground improvement technology using concrete injected column (CICs) has been widely adopted in many areas in Europe, where traditional ground improvement techniques, such as stone columns and piles, have been excluded because of presence of very soft and/or organic soils. CIC allows heavily structures to be constructed on ground bearing foundations, including roads, embankments, silos and tanks. During the operation of CIC, an auger is screwed in to soil to a designed depth. This method increases the strength of weak soil and or enhances the bearing capacity by densifying surrounding soils. When the auger is extracted a concrete column is developed by pressure grouting to improve the surrounding soils. Hence, CIC results in a composite ground improvement solution by enhancing stiffness characteristics, allowing CICs and the surrounding soils to share the applied load. Figure 2.1a and b show the comparison of load transfer mechanism between CIC-improved soft soil and pile embedded soft soil.

Han and Gabr (2002) indicated that the mechanism of load transfer in pile-supported embankments is a combination of the soil arching effect in the embankment fill, the reinforcement effect of geosynthetic if provided, and the load transfer between piles and soils as a result of their stiffness difference. Hewlett and Randolph (1988) and Low *et al.* (1994) investigated soil arching in the piled embankments using model tests and the developed theoretical solutions for estimating the degree of the load transfer between piles and soil. The

mechanism of load transfer is much more complicated than just the soil arching. A number of numerical analyses were conducted to investigate the load transfer mechanism, e.g. Han and Gabr (2002), Zhuang (2009). Deb (2010) has proposed a mathematical model explaining the behaviour of column-supported geosynthetic-reinforced embankments.

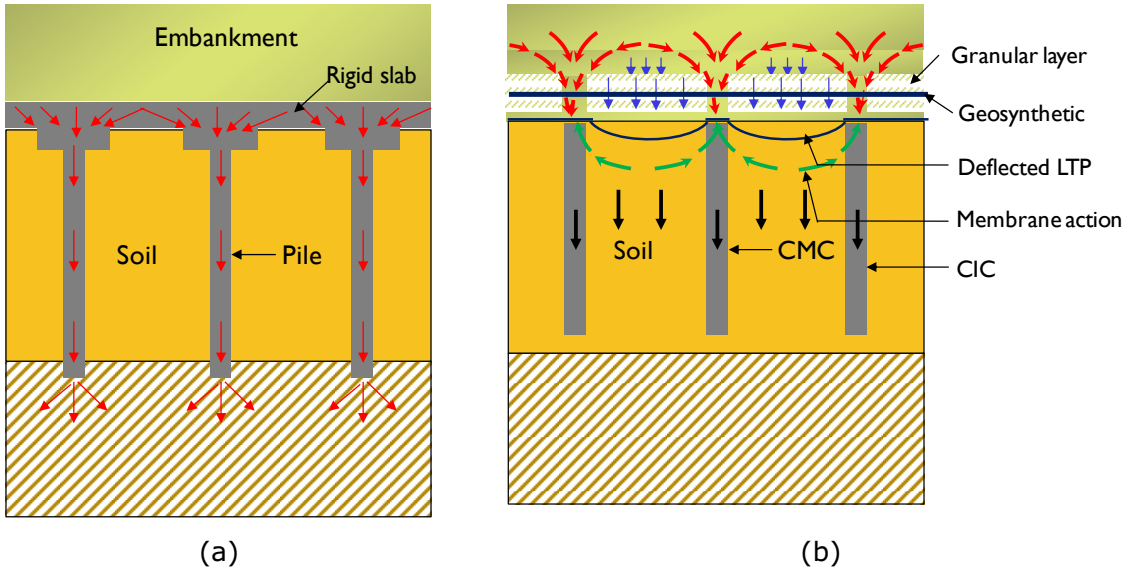

Figure 2.1. Principle of load transfer mechanism in: (a) Pile and (b) CIC.

Concrete injected column (CIC) supported embankments, which contain foundation soil, CICs, geosynthetic if needed, and embankment fill, have been increasingly used for embankments over soft soils. When compared with other ground improvement methods for soft soils, the CICs supported embankments have the advantages of rapid construction, small vertical and lateral deformations, minimum spoil generation and global stability. Conceptually, the soil–CIC mass behaves as a composite mass of greater stiffness than the initial untreated ground, reducing settlements induced by the weight of the structure and traffic loads to within allowable ranges.

2.3 Theory of Soil Arching in Column-Supported Embankments

Arching is defined by McNulty (1965) as "the ability of a material to transfer loads from one location to another in response to a relative displacement between the locations. A system of shear stresses is the mechanism by which the loads are transferred." Figure 2.2a illustrates this concept. Considering the soil on a rigid base, there is no tendency for differential movement and hence, no soil arching occurs. The stress acting at a point "a" in Figure 2.2b is the overburden stress of γH, where γ is the unit weight of the soil above the rigid base and H is the height of the soil prism. When one of the local supports at the point "a" is removed, the point "a" is in tension, and a roof tension arch is formed. The true arch collapses as the soil is not in equilibrium. The soil settles in an inverted arch, the adjacent soil develops the required shear strength and the soil reach equilibrium state. The transfer of pressure from the yielding portion to the stationary portion is called arching.

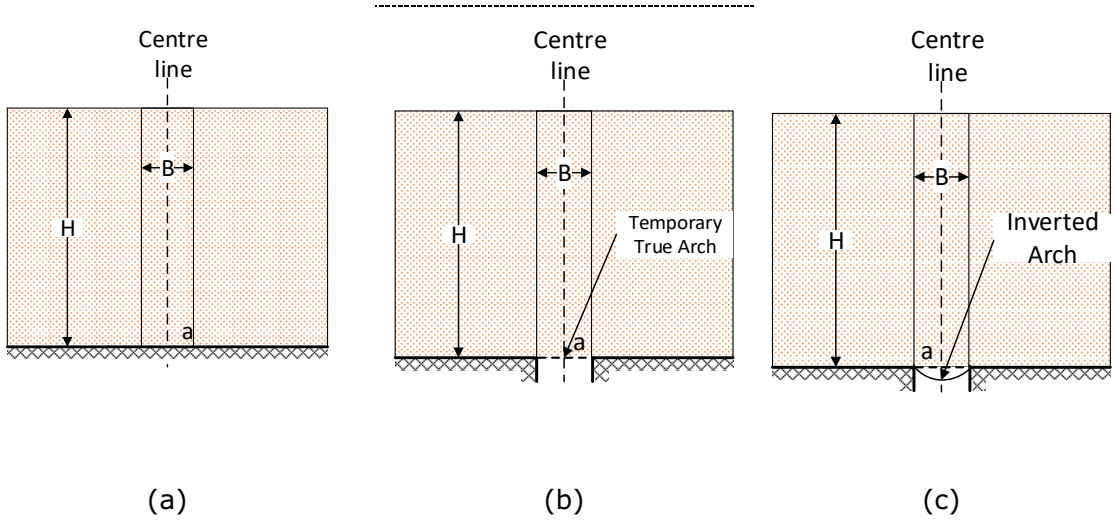

Figure 2.2. Different stages of soil arching to demonstrate: (a) the soil mass overlying a potential void; (b) the formation of a true arch (Void under soil mass); and (c) soil mass collapses to form an inverted arch (modified after McKelvey, 1994).

Several methods have been proposed to model the soil arching behaviour in the literature. Terzaghi (1936) considered the shear strength along the soil prism, which is mobilized to a

certain height, at which the plane of equal settlement exists. Giroud *et al.* (1990) applied model used by McNulty (1965) to deal with soil layer-geosynthetic systems overlying voids. Hewlett and Randolph (1988) considered limit equilibrium in a domed region for the sand between the two piles. Most of the load above the crown was transferred onto the support through the crown. Schmertmann (1991) proposed that all the load within the triangular beneath the geosynthetic i.e. cavity below the geosynthetic layer was existed as shown in Figure 2.2c, and all the pressure was to be carried by the geosynthetic. In all the cases discussed above, it was assumed that there was no subsoil support.

2.4 Load Transfer system in Geosynthetic Reinforced Column-Supported Embankments

The layer of geosynthetics in between granular working platform and the embankment fill form a stiffened load transfer platform (LTP) that supports load transfer mechanism. The weight of the fill (W_1 and W_2 in Figure 2.3) tends to move downward due to the presence of soft soil below the geosynthetic layer. This downward motion is resisted by the shear resistance (τ in Figure 2.3) provided by the fill on the pile caps. The shear resistance reduces the pressure acting on the geosynthetic, but increases the load acting on the caps. In the case, where the geosynthetic reinforced platform is perfectly rigid, there is no differential settlement developed. However, there is still load distribution occurring between columns and soil because of the difference in stiffness of column and soil.

To assess the degree of arching in soil of a piled embankment construction, some definitions have been used by different researchers. The following terms and their definitions are often referred in the next sections.

Stress Concentration Ratio (n):

The degree of the load transfer was quantified by Han and Gabr (2002) using an index-stress concentration ratio, which is named as the ratio of stress on the pile caps (σ_c) and the stress on subsoil (unreinforced embankment, σ_s) and/or reinforcement (reinforced embankment, p_b) which are shown in Figure 2.3.

$$n = \begin{cases} \frac{\sigma_c}{\sigma_s}, & \text{for unreinforced embankment} \\ \frac{\sigma_c}{p_b}, & \text{for reinforced embankment} \end{cases} \quad (2\text{-}1)$$

Figure 2.3. illustrates all the variables used in Eq. (2-1).

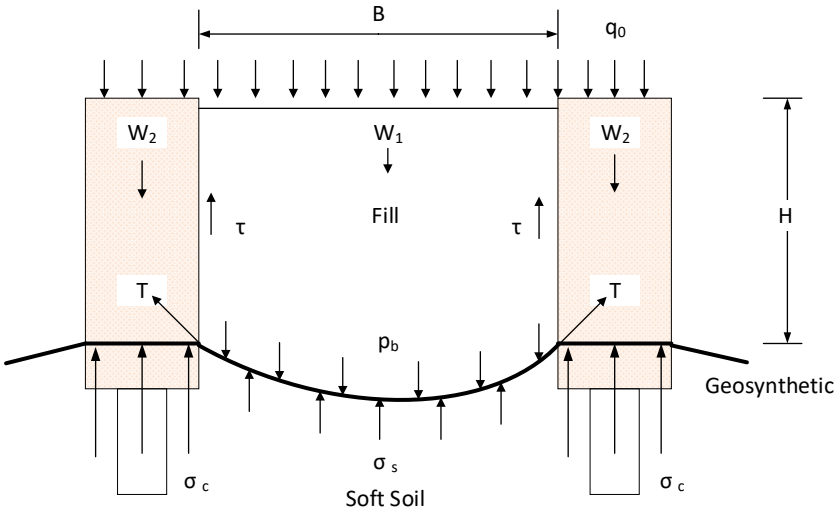

Figure 2.3. Load transfer mechanism (modified after Han and Gabr, 2002).

Efficacy (E):

The proportion of embankment weight carried by the piles in a pile supported embankment is defined as "efficacy" (Hewlett and Randolph, 1988). Efficacy is therefore, expressed as a percentage by weight of the embankment fill carried by the piles or pile cap beams (Low *et al.*, 1994).

$$E = \frac{P}{(\gamma H + q_0)s_x s_y} \quad (2\text{-}2)$$

where s_x and s_y are the pile centreline spacing in X-direction and Y-direction, respectively. P is the total force carried by the pile caps, γ is the unit weight of the embankment, H is the height of embankment, and q_0 is the surcharge acting on top of the embankment.

Soil Arching Ratio (ρ) or Stress Reduction Ratio (SRR):

McNulty (1965) proposed that soil arching ratio is the ratio of the applied vertical pressure acting on trap door in McNulty's study (geosynthetic in this research) to the value of $(\gamma H + q_0)$.

$$\rho \text{ or } SRR = \frac{p_b}{\gamma H + q_o} \quad (2\text{-}3)$$

where p_b is the vertical stress acting on top of granular layer (unreinforced embankment) or on top of geosynthetic (reinforced embankment), γ is the unit weight of the embankment, H is the height of embankment, and q_0 is the surcharge acting on top of the embankment.

2.5 Design of Geosynthetic Reinforcement

The load from embankment that is acting on the soft soil due to soil arching will be transferred to the columns by membrane action of geosynthetics. The tension developed in geosynthetics is evaluated using cable or membrane theory. However, the formulations are different depending on the method of determining the load on the geosynthetic. Numerous methods exist in the literature to determine the tension produced in the geosynthetic reinforcement. These methods are well recognized and can be adopted by any design guidelines or standards if the vertical stress transferred to the geosynthetic layer is known.

2.5.1 Parabolic Method

The parabolic method assumes that the shape of the deformed reinforcement when described in a two-dimensional space is parabolic and then calculates the tension in the reinforcement. BS8006-1 (2010) and Low *et al.* (1994) adopted parabolic method to determine the tension in geosynthetic. The general equation to obtain the tension is as follows.

$$T = \frac{P_r(s^2-a^2)}{4a}\sqrt{1+\frac{1}{6\varepsilon}} \tag{2-4}$$

where T is the tension developed in reinforcement, P_r is the distributed load acting on geosynthetics between adjacent piles, s is the centre to centre spacing of adjacent piles, a is the diameter of the pile, and ε is the strain in geosynthetics.

2.5.2 Tensioned Membrane Method

The tensioned membrane method was introduced by Collin (2004). According to this approach, tension in the geosynthetic can be obtained by the following equation.

$$T = \frac{P_r(s-a)\Omega}{\sqrt{2}} \tag{2-5}$$

where T is the tension developed in reinforcement, P_r is the distributed load acting on geosynthetics between adjacent piles, s is the centre to centre spacing of adjacent piles, a is the diameter of the pile, Ω is a dimensionless parameter shown in Table 2.1 or from Eq. (2-6), and ε is the strain in geosynthetic.

$$1+\varepsilon = 2\,\Omega \sin^{-1}\left(\frac{1}{2\,\Omega}\right) \tag{2-6}$$

Design strain of 5% is used in this approach. However, to eliminate the strain term and obtain the tension, stress strain compatibility $\varepsilon = (T/J)$ can be used, where J is the stiffness of the geosynthetic reinforcement.

Table 2.1. Values of Ω (Collin, 2004)

Ω	Design reinforcement strain (%)
2.07	1
1.47	2
1.23	3
1.08	4
0.97	5

In order to compare the various methods, a stress reduction ratio denoted as SRR is defined. The ratio of the average vertical stress acting on the reinforcement to the overburden pressure due to the embankment fill is known as stress reduction ratio.

$$\text{SRR} = \frac{2W_T(s-a)}{\gamma H(s^2-a^2)} = \frac{1-\text{Efficacy}}{1-\text{Area ratio}} \tag{2-7}$$

where SRR is the stress concentration ratio, W_T is the distributed load acting on geosynthetics between adjacent piles, s is the centre to centre spacing of adjacent piles, a is the diameter of the pile, γ is the unit weight of the embankment fill materials, and H is the height of the embankment.

2.6 Numerical and Experimental Studies of Column-Supported Embankments

Geosynthetic reinforced column-supported embankments are commonly used ground improvement technique to mitigate the risks of structural instability, bearing capacity failure, excessive horizontal movements, and large differential settlements when embankments are built on soft soils. The columns can be structural piles with reinforcing bars, deep soil mixing

columns, or Concrete Injected Columns without any reinforcement. Concrete injected columns are installed by a specially designed auger, attached to the Kelly bar of a powerful piling rig (see Figure 2.4). The auger used to install CICs rotates and penetrates into the ground at the control speed. Indeed, the soil is destructured by the auger head and then laterally displaced into the surrounding soils thanks to the upper large displacement body. As the auger head approaches the desired depth, the concrete or grout is pumped through the hollow stem of the auger during the withdrawal of the auger tool.

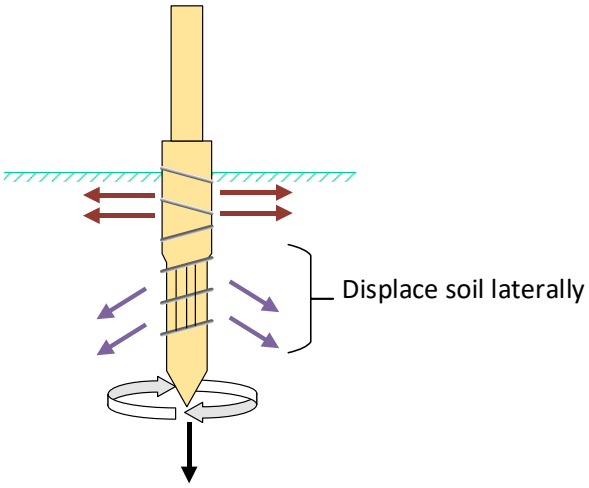

Figure 2.4. Augur of a rigid inclusion, concrete injected column.

The design of the geosynthetic reinforced column-supported embankments is a complex problem. It involves many properties of the embankment fill, geosynthetics, columns, and underlying soil layers. In order to investigate the load transfer procedure in the entire soil-column-embankment system, analytical and numerical techniques have been considered in the literature. However, to evaluate more complex time dependent behaviour of the system, numerical modelling is often required. Nowadays, numerical modelling analysis have become more popular to simulate the short and long-term performance of column-supported embankments due to improvements in computer capabilities as well the development of more realistic material models. Several numerical methods are available to simulate geosynthetic reinforced column-supported embankments such as finite element method, finite difference

method, boundary element, mesh free, and discrete element methods. However, majority of the existing literature adopted finite element and finite difference methods (Russell and Pierpoint, 1997; Liu *et al.*, 2007; Zheng *et al.*, 2009; Huang and Han, 2010; Bhasi and Rajagopal, 2015b; Liu and Rowe, 2015; Yoo, 2015) . On the other hand, Han et al. (2011) and Jenck et al. (2009) adopted the discrete element method for numerical analysis of embankments. The combination of finite element and finite difference methods has also been used by Le Hello and Villard (2009).

Due to its simplicity compared to three-dimensional modelling, most of the existing research studies adopted two-dimensional modelling. However, in many occasions predictions from three-dimensional modelling proved to be more accurate and realistic in comparison to simplified two-dimensional modelling. A series of parametric studies to evaluate the behaviour of a column-supported embankment were performed by Tandel et al. (2013) using three-dimensional modelling. The linear elastic – perfectly plastic Mohr-Coulomb constitutive model was adopted to simulate the columns, and embankments, while soft soil was idealised by perfectly elastic material model. Tandel et al. (2013) suggested two critical factors that influence the behaviour of the embankment: (a) the ratio of column spacing to the diameter; and (b) a non-dimensional parameter related to geosynthetic stiffness, column diameter and soil modulus. Jenck et al. (2009) proposed a finite difference three-dimensional numerical modelling procedure for an embankment on soft soil improved by piles using FLAC^{3D}. Soft soil and embankment were simulated by Modified Cam Clay and Mohr-Coulomb models, respectively, while linear elastic behaviour was assumed for piles. A numerical study to assess the effects of geosynthetic reinforcement viscosity on behaviour of embankments supported by deep-mixing-method (DMM) columns was conducted by Liu and Rowe (2015). Sub-soil and geosynthetic were modelled by elliptical cap and viscoelastic constitutive models, respectively. In that study, the behaviour of embankment and DMM columns were idealised by linear elastic

– perfectly plastic Mohr-Coulomb model. One of the conclusions was that relatively stiffer and less viscous reinforcement reduced the post-consolidation horizontal toe movement of the soil.

The load transfer mechanism in pile-supported embankment was also numerically investigated by Han and Gabr (2002). The contribution of the foundation soil to withstand the load from the embankment was incorporated by Han and Gabr (2002). An axisymmetric unit cell using the finite difference method implemented in a commercial software package named FLAC was used to analyse a single pile within the pile-supported embankment. Mohr-Coulomb failure criteria was assumed for soft soil. The influence of the stiffness of geosynthetics and modulus of pile on load transfer were examined which were neglected by design method proposed by Hewlett and Randolph (1988) and BS8006-1 (2010). It is proven that the maximum tension developed in the geosynthetic increases with the increase of embankment height, stiffness of geosynthetic and elastic modulus of material of the pile. However, the failure mechanisms and the differential and the lateral deformation of the embankment are not explained in their study.

The literature review reveals that small-scale physical model tests, full scale field tests, finite element and finite difference studies along with analytical studies have been conducted to examine the behaviour of the column-supported embankments. For the very first time, the effect of geosynthetic reinforcement was taken into account quantitatively by Jones *et al.* (1990). A field investigation was carried by Gartung *et al.* (1996) on a railway embankment which is supported by rectangular arrangements of piles. Embankment was reinforced with three layers of geosynthetic reinforcement. Various field measurements from instrumentations such as strains in the geosynthetics, settlements at the base of the embankments, settlements and the tilt of the pile caps were reported. Soil settled the maximum around 50 mm while the only 10 mm settlement of pile caps reported.

2.7 Empirical and Analytical Model of Column-Supported Embankments

Empirical or analytical design models for the design of column supported embankments include two calculation steps. The first step calculates the arching behaviour in the fill. The second calculation step describes the load-deflection behaviour of the geosynthetic reinforcement. In the first step load above the arch directly is transferred to column due to arching. The residual load is applied to the geosynthetic reinforcement strip between two adjacent columns as the vertical load. Through the membrane action of geosynthetic, part of vertical load is transferred to the column and rest of the vertical is transferred to subsoil. Then tension in the GR is determined due to part of the vertical load as well as due to lateral spreading of embankment. In second step the strain in geosynthetic is calculated. This research concentrates on geosynthetic reinforcement when it is being used combined with column supports. However, there have been many case studies in the literature which show that only geosynthetics at the base of embankment without pile support can also prevent the lateral movements, reduce the settlements and thus increase the stability of the embankments (Fowler and Edris Jr, 1987; Rowe and Soderman, 1987; Hird, 1992; Rowe and Li, 1999; Chai *et al.*, 2002). The two most widely adopted design methods, discussed in the following section, are: Hewlett and Randolph (1988) theory and the method introduced by Low *et al.* (1994).

2.7.1 Method of Hewlett and Randolph (1988)

Hewlett and Randolph (1988) derived theoretical solutions based on observations from experimental tests of arching in a granular soil. The 'arches of sand' transmit the majority of the embankment load onto the pile caps, with the subsoil carrying load predominantly from the 'infill' material below the arches. The arches were assumed to be semi-circular (in 2D, spanning between two adjacent piles) and hemispherical domes (in 3D, spanning between two diagonal piles) and of uniform thickness, with no overlap as shown in Figure 2.5b. The process

also assumed that the pressure acting the subsoil is uniform. Hewlett and Randolph (1988) proved that, for a 2-dimensional case, the critical point of the arch is always at the crown or the pile cap. However, it is necessary to consider the value of σ_s resulting from failure of the arch either at the crown as shown in Figure 2.6a or pile caps which is shown in Figure 2.6b – the largest value will be critical. For low fill embankment heights, failure was considered to occur at the crown of the arch. The greater value of the result from Eqs. (2-8) and (2-9) determines stress acting on the surface of the subsoil.

According to Hewlett and Randolph (1988), at crown, stress acting on subsoil is as follows:

$$\sigma_s = \frac{\gamma(s-a)}{\sqrt{2}} + \left[\gamma\left(1-\frac{a}{s}\right)^{2(K_p-1)}\right] \times \left[H - \frac{s}{\sqrt{2}}\left(\frac{K_p-2}{(2K_p-3)}\right)\right] + \frac{\gamma(s-a)}{\sqrt{2}(2K_p-3)} \quad (2\text{-}8)$$

At top of pile cap, stress acting on subsoil is as follows:

$$\sigma_s = \frac{\gamma H}{\left(\frac{2K_p}{K_p+1}\right)\times\left[\left(1-\frac{a}{s}\right)^{1-K_p} - \left(1-\frac{a}{s}\right)\times\left(1-\frac{a}{s}K_p\right)\right] + \left(1-\frac{a^2}{s^2}\right)} \quad (2\text{-}9)$$

where K_p is the passive earth pressure. Figure 2.5b illustrates all the definitions used in Eqs. (2-8) and (2-9). This method does fulfil the vertical equilibrium criterion when determining the stress on the geosynthetic layer and the equation is as below:

$$a^2\sigma_c + (s^2 - a^2)\sigma_s = s^2\gamma H \quad (2\text{-}10)$$

where σ_c is the stress transferred to pile, s is the diagonal distance of piles, a is the diameter of the pile, γ and H are the unit weight and height of the embankment, respectively.

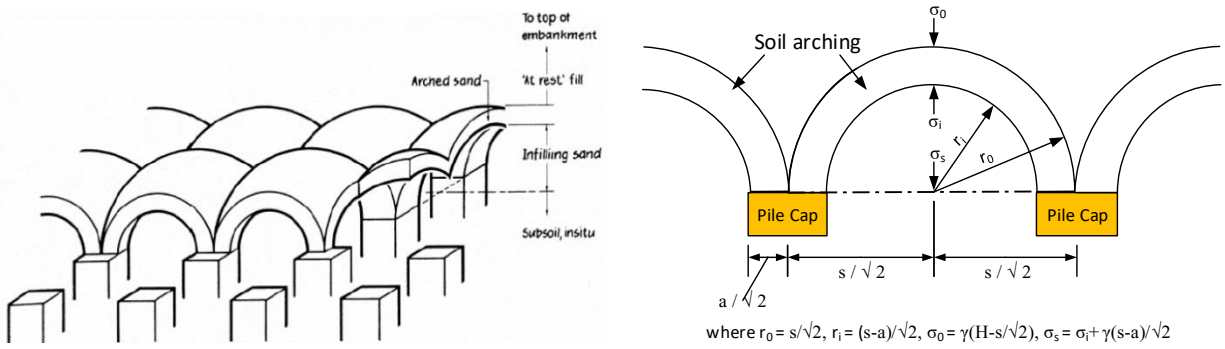

(a) (b)

Figure 2.5. Hewlett and Randolph's (1988) proposed: (a) hemispherical domes model in three dimension and (b) semicircular model in two dimensions (modified after Hewlett and Randolph's,1988).

According to the study carried out by Hewlett and Randolph (1988), efficacy (E) and stress concentration ratio (n) can be obtained by the following equations.

$$E = \frac{a^2\sigma_c}{s^2\gamma H} = 1 - \frac{\sigma_s(s^2-a^2)}{s^2\gamma H} = 1 - \frac{SRR(s^2-a^2)}{s^2} \quad (2\text{-}11)$$

and

$$n = \frac{\sigma_c}{\sigma_s} = \frac{s^2\gamma H-(s^2-a^2)\sigma_s}{a^2\sigma_s} \quad (2\text{-}12)$$

Line load acting on geosynthetic reinforcement (GR) is:

$$W_T = \frac{s(\gamma H+q)}{s^2-a^2}(1 - E_{min})s^2 \quad (2\text{-}13)$$

where E_{min} is the minimum of efficacy at crown and efficacy on cap beam, q is the stress transferred to pile, s is the distance of piles, a is the diameter of the pile, γ and H are the unit weight and height of the embankment, respectively.

Tension in geosynthetic layer can be determined using the following equation where design strain of 5% is assumed as per BS8006-1 (2010).

$$T_{RP} = \frac{SRR \times \gamma H(s^2 - a^2)}{4a}\sqrt{\left(1 + \frac{1}{6\varepsilon}\right)} \tag{2-14}$$

The stress reduction factor is evaluated using limiting plastic equilibrium. The stress reduction ratio at the crown and at top of pile cap is given by (Hewlett and Randolph, 1988):

$$SRR = \begin{cases} \left(1 - \frac{a}{s}\right)^{2(K_p - 1)}\left(1 - \frac{s}{H\sqrt{2}} \cdot \frac{2(K_p - 1)}{(2K_p - 3)}\right) + \frac{(s-a)}{H\sqrt{2}} \cdot \frac{2(K_p - 1)}{(2K_p - 3)} & \text{at crown} \\ \dfrac{1}{\left(\frac{2K_p}{K_p + 1}\right)\left(\left(1 - \frac{a}{s}\right)^{(1 - K_p)} - \left(1 - \frac{a}{s}\right)\left(1 + \frac{a}{s}K_p\right)\right) + \left(1 - \frac{a^2}{s^2}\right)} & \text{at pile cap} \end{cases} \tag{2-15}$$

The higher of the two stress reduction ratios is used for the calculations. Hence, it considers the worst-case scenario.

2.7.2 Method of Low et al. (1994)

Model tests and theoretical analysis were carried out by Low *et al.* (1994) to investigate the arching in embankments on soft ground supported by piles with cap beams and geotextiles. This method uses soil arching concept suggested by Hewlett and Randolph (1988). Low *et al.* (1994) introduced the body force or surcharge in the plane strain differential equation of the vertical equilibrium along with a new parameter to take in to account the possible non-uniform vertical stress on the soft soil underneath the geosynthetic layer. Low *et al.* (1994) has also introduced geosynthetic in Hewlett and Randolph's model. Instead of pile caps, Low *et al.* (1994) used cap beams in their models. But the results of this study can be used to analyse GRCS embankment problems. Low *et al.* (1994) developed equations and charts which can be beneficial to evaluate the effect on the load transfer to the soft ground when geosynthetic reinforcements are used. But the application of this model is limited to linearly elastic soft

ground only. Equilibrium analyses at the two positions (at crown and at top of cap beam) lead to two equations for the stress acting on the surface of the subsoil.

Low *et al.* (1994) concluded from their parametric study that the element of an arch at crown as shown in Figure 2.6a is more critical than the element at pile cap as displayed in Figure 2.6b. In their parametric study they used K_p within a range of 3 to 7.5, H/s between 0.5 and 10, δ between 0.05 and 0.3 and α between 0.8 and 1.0.

Theoretical analysis without Geotextiles:

A semi cylindrical sand arch in two dimension with a thickness equal to half the width of the cap beam as displayed in Figure 2.7a has been analysed by Low *et al.* (1994). From the equation of radial equilibrium of an element at crown, Low *et al.* (1994) developed equation for σ_s assuming limit state analysis. In Eq. (2-16), σ_i is the vertical stress beneath inner boundary of crown, σ_r is the radial stress in sand arch, σ_s is the vertical stress on top of soft ground (or geotextile, if used) midway between cap beams, σ_θ is the tangential stress in sand arch. For limit analysis, the tangential stress $\sigma_s = K_p\sigma_r$. where $K_p = (1 + \sin\varphi)/(1 - \sin\varphi)$, φ is an angle of shearing resistance.

$$\sigma_s = \sigma_i + \frac{\gamma(s-b)}{2} = \frac{\gamma(K_p-1)(s-b)}{2(K_p-2)} + \left(1 - \frac{b}{s}\right)^{K_p-1}\left[\gamma H - \frac{s\gamma}{2} - \frac{s\gamma}{2(K_p-2)}\right] \quad (2\text{-}16)$$

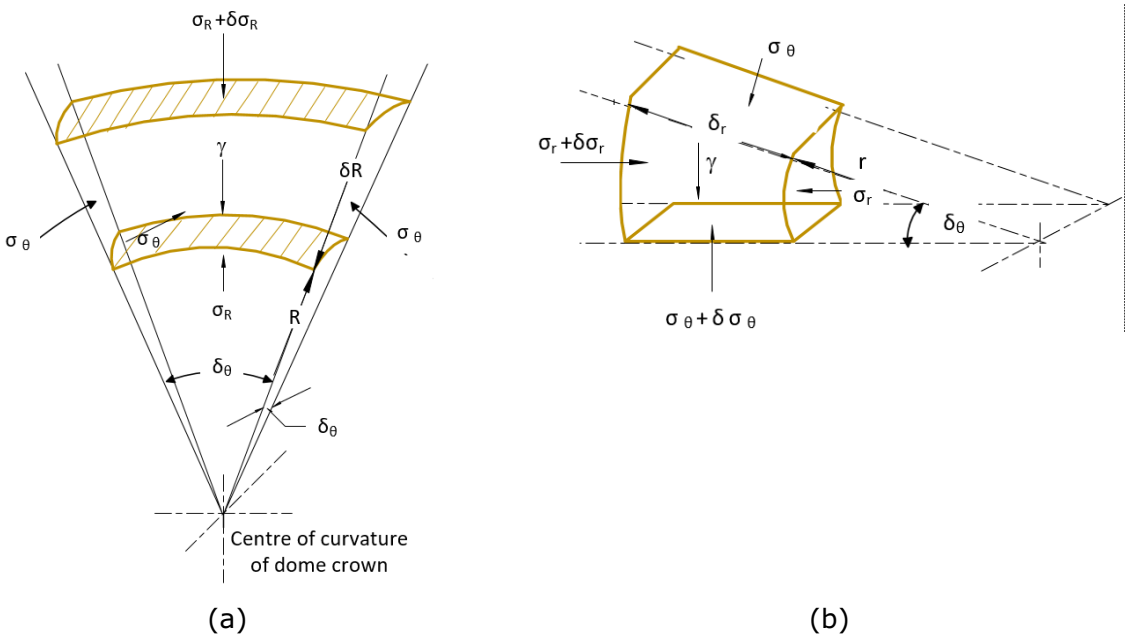

Figure 2.6. Equilibrium analysis of an element: (a) at crown and (b) at just above pile cap (modified after Hewlett and Randolph, 1988).

To consider the possible non-uniform vertical stress on the soft ground, Low *et al.* (1994) introduced a coefficient α so that ($\alpha\sigma_s$) is an equivalent uniform stress (σ_s') acting on the soft ground as shown in Figure 2.7b. This method satisfies the vertical equilibrium when calculating the stress on the geosynthetic layer and the equilibrium equation is:

$$b^2\sigma_c + (s^2 - b^2)\alpha\sigma_s = s^2\gamma H \qquad (2\text{-}17)$$

where σ_c is the stress transferred to pile, s is the spacing, H is the height of embankment, b is the width of pile cap, and γ is the unit weight of embankment.

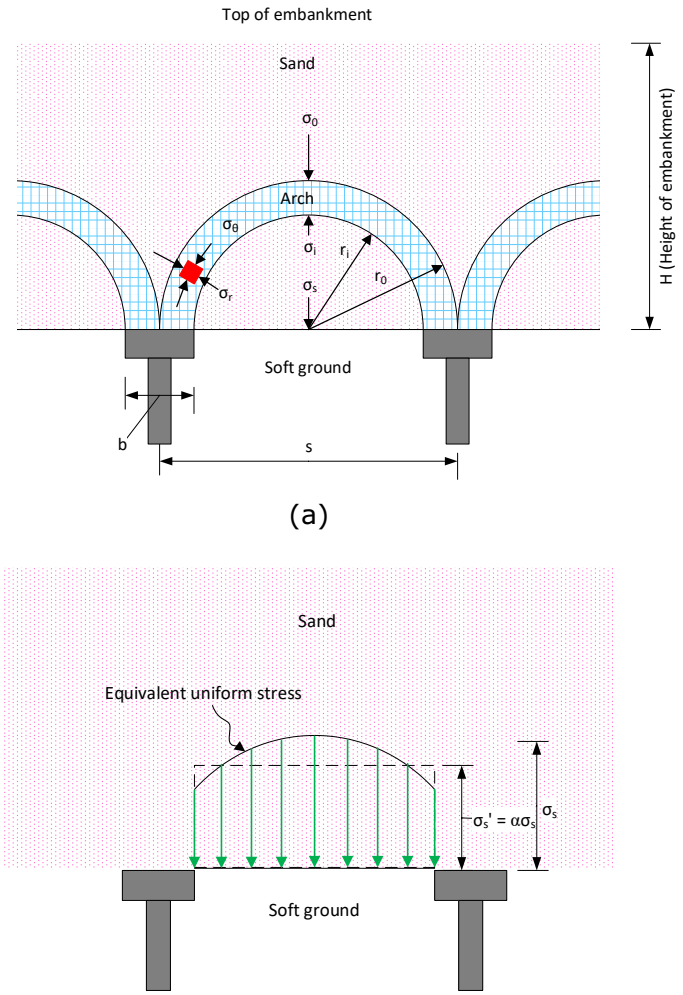

Figure 2.7. Analytical model to illustrate: (a) semi-cylindrical sand arch and (b) distribution of load on soft-soil (modified after Low et al., 1994).

By converting from plane-strain to 3D, efficiency (E) and stress concentration ratio (n) can be written as:

$$E = 1 - \frac{(s^2 - b^2)\alpha\sigma_s}{s^2\gamma H} \text{ and } n = \frac{s^2\gamma H - \alpha(s^2 - b^2)\sigma_s}{b^2\alpha\sigma_s} \quad (2\text{-}18)$$

Above equations of efficacy and stress reduction ratio are only valid for $H/s \geq 0.5$.

Theoretical analysis with Geotextiles:

The deformed shape of geotextile is idealized as a circular arc of radius R with a subtended angle 2θ and a maximum displacement t (to be determined) midway between the cap beams as demonstrated in Figure 2.8. The equation of equilibrium of vertical forces is:

$$b^2\sigma_c + (s^2 - b^2)p_0 = s^2\gamma H \tag{2-19}$$

Efficacy and stress concentration ratio are therefore,

$$E = 1 - \frac{(s^2-b^2)p_0}{s^2\gamma H} \qquad \text{and} \qquad n = \frac{s^2\gamma H-(s^2-b^2)p_0}{b^2 p_0} \tag{2-20}$$

From the equilibrium of vertical forces, stress acting on geotextile as displayed in Figure 2.9a is:

$$p_o = \left(\sigma_s - \frac{tM}{D}\right) = \frac{2K_G(\theta-\sin\theta)}{s'} \tag{2-21}$$

From the geometry of the shape of deformation of geotextiles θ is:

$$\theta = \sin^{-1}\left[\frac{4\frac{t}{s'}}{1+4\left(\frac{t}{s'}\right)^2}\right] \quad \text{and} \quad \varepsilon_G = \frac{\theta-\sin\theta}{\sin\theta} \tag{2-22}$$

where σ_s is the acting on top of the geotextile as illustrated in Figure 2.9b, M is the modulus of a linearly elastic soft ground, D is the original thickness of soft ground, p_o is the uniform loading on geotextile as illustrated in Figure 2.9c, K_G is the tensile stiffness of geotextile, and ε_G is the axial strain in the geotextile.

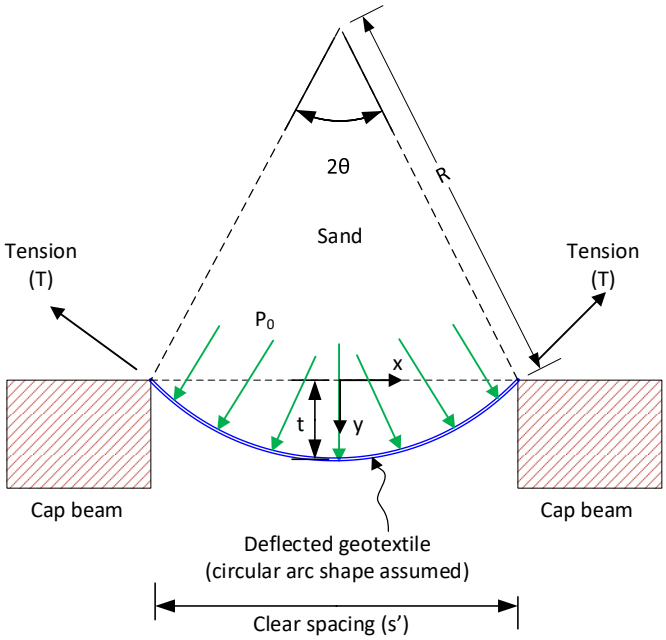

Figure 2.8. Geotextile overlying cap beams and soft ground (modified after Low et al., 1994).

Low *et al.* (1994) used trial "t" values until a reaction force was obtained that satisfied the vertical force equilibrium (which is $s'p_o = 2K_G(\theta - \sin\theta)$), and if the maximum reinforcement displacement is known, it can be used directly to calculate θ. Low *et al.* (1994) idealized the deformed shape of geotextile as a circular arc of radius R with a subtended angle 2θ and a maximum displacement t (to be determined) midway between the cap beams (Figure 2.9a). The geotextile is assumed fixed at the edges of the caps. By geometry (Figure 2.9b):

$$\frac{t}{s'} = \frac{1-\cos\theta}{2\sin\theta} \text{ and } R = \frac{s-b}{2\sin\theta} \tag{2-23}$$

After satisfying vertical equilibrium of forces with assumed "t", tension in geosynthetic can be calculated using following equation:

$$T = p_o R = \left(\sigma_s - \frac{tM}{D}\right) R = \frac{2K_G R(\theta-\sin\theta)}{s-b} \tag{2-24}$$

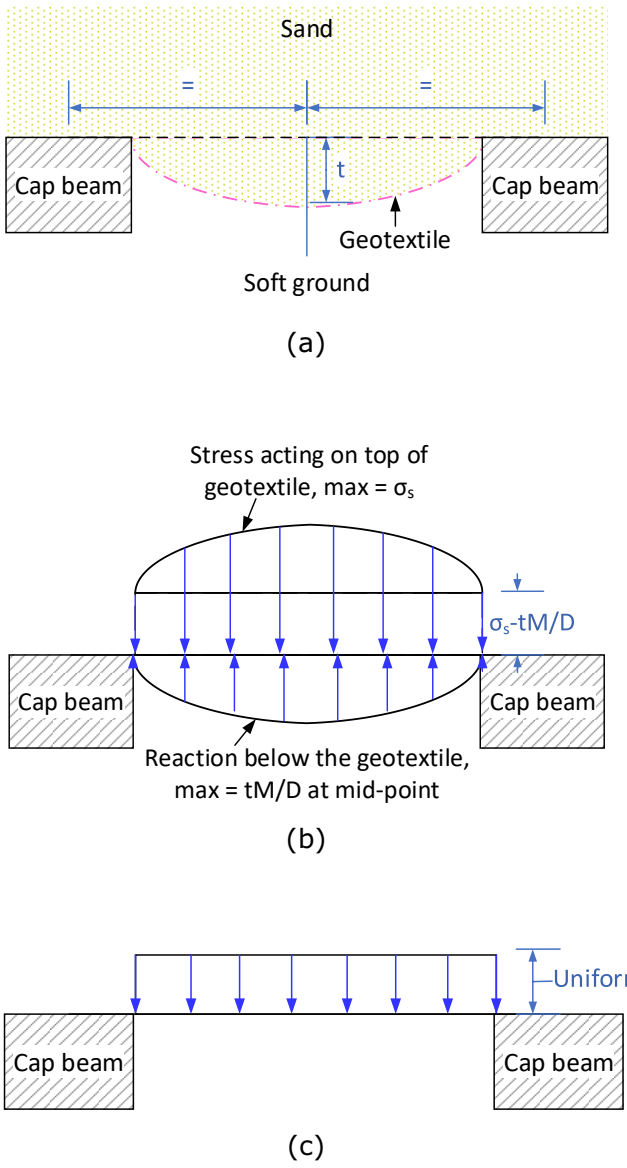

Figure 2.9. Low et al. (1994) proposed model to display: (a) assumed shape of geotextile deformation; (b) stresses acting on geotextile; and (c) idealized pressure distribution on geotextile (modified after Low et al., 1994).

Low *et al.* (1994) used trial t values until a reaction force was obtained that satisfies the vertical force equilibrium, and if the maximum reinforcement displacement is known, it can be used directly to calculate θ.

Low *et al.* (1994) reported the stress reduction ratios (SRR) as:

$$SRR = \begin{cases} \frac{\alpha\sigma_s}{\gamma H} & \text{without geotextile} \\ \frac{p_0}{\gamma H} & \text{with geotextile} \end{cases} \quad (2\text{-}25)$$

Due to ignoring interface shear transfer between geosynthetic and soil, higher load may transfer to pile according to Low *et al.* (1994).

2.8 Design Guidelines

There are several design guidelines are presented for the design of geosynthetic reinforced column-supported embankments. In this section, methods proposed in BS8006-1 (2010) and EBGEO (2010) guidelines are discussed.

2.8.1 British Standard: BS8006 (2010)

BS8006-1 (2010) is the British Standard process used for design of embankments with reinforced soil foundations on poor ground. In 1995, the first version of the British Code was published. This design process is based on simplified analyses that has been developed by Jones *et al.* (1990), which is based on formula proposed by Marston and Anderson (1913) for positive projecting conduits. However, in this section, the details of the original equations suggested by Jones *et al.* (1990) will be discussed. Some modification in BS8006-1 (2010) is proposed by van Eekelen *et al.* (2011).

The vertical stress acting on the pile caps in three dimensions can be calculated as:

$$p_c' = \sigma_v' \left(\frac{c_c a}{H}\right)^2 \quad (2\text{-}26)$$

where a is the width of square pile caps, p_c' is the vertical stress on pile caps, σ_v' is the factored average vertical stress at the base of the embankment = $f_{fs}\gamma H + f_q w_s$, w_s is the uniformly distributed surcharge loading, f_{fs} and f_q are the partial load factor, H is the height of the the

embankment fill, C_c is arching coefficient. BS8006-1 (2010) assumes square arrangement of square piles. If the pile is circular with diameter "d" equivalent width of the pile has to be calculated using $a_{equ} = 0.886d$.

BS8006-1 (2010) gives empirical equations for arching coefficient as follows:

$$C_c = \begin{cases} 1.95\frac{H}{a} - 0.18\,, & \text{for end} - \text{bearing piles(unyielding)} \\ 1.5\frac{H}{a} - 0.07, & \text{for friction and other piles} \end{cases} \tag{2-27}$$

There are two different conditions of arching are considered in the code depending on the critical height of the embankment which is $H_c = 1.4(s - a)$ as shown in Figure 2.10. If $0.7(s - a) \leq H \leq 1.4(s - a)$, the partial arching occurs as per BS8006-1 (2010). While the full arching condition occurs when the height of embankment, $H > 1.4\,(s - a)$. As per BS8006-1 (2010) the distributed load, W_T, as shown in Figure 2.11, supported by the reinforcement between adjacent pile caps, may be obtained from:

$$W_T = \begin{cases} \frac{1.4sf_{fs}\gamma(s-a)}{s^2-a^2}\left(s^2 - a^2\left(\frac{p_c'}{\sigma_v'}\right)\right) & \text{for full arching} \\ \frac{s(f_{fs}\gamma H + f_q w_s)}{s^2-a^2}\left(s^2 - a^2\left(\frac{p_c'}{\sigma_v'}\right)\right) & \text{for partial arching} \end{cases} \tag{2-28}$$

Thus, the vertical stress acting on geosynthetic reinforcement for both cases can be obtained from the following equation:

$$p_r = \frac{2W_T}{s+a} \tag{2-29}$$

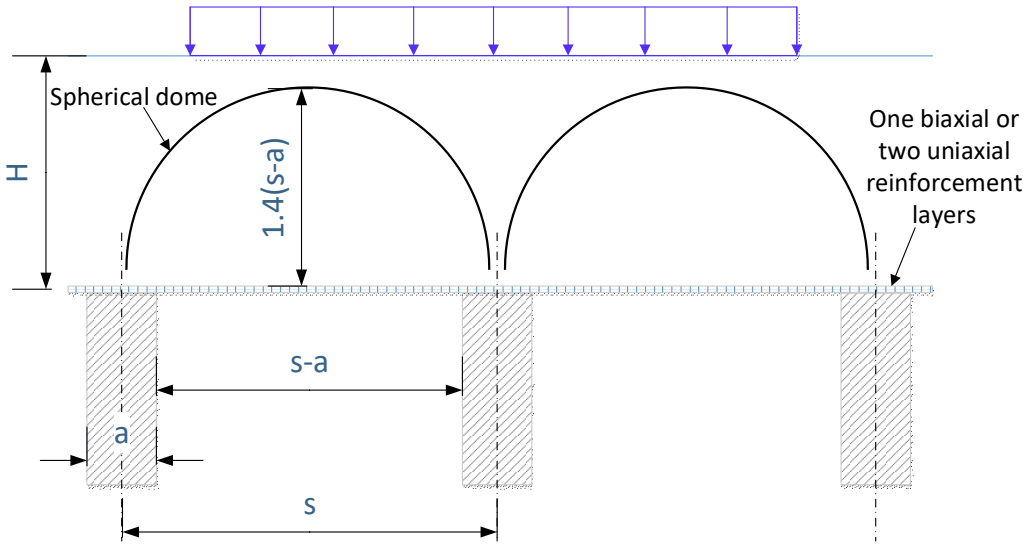

Figure 2.10. Arching dome according to British Standard (modified after Alexiew, 2004).

The British Standard BS8006-1 (2010) suggests following formula to calculate tension in geosynthetics.

$$T_{RP} = \frac{W_T(s-a)}{2a}\sqrt{\left(1+\frac{1}{6\varepsilon}\right)} = \frac{P_r(s^2-a^2)}{4a}\sqrt{\left(1+\frac{1}{6\varepsilon}\right)} \tag{2-30}$$

where T_{RP} is the tensile load in the reinforcement due to vertical load from the embankment only as displayed in Figure 2.11, ε is the maximum allowable strain in the reinforcement. 5% strain in the geosynthetic reinforcement is generally assumed in BS8006-1 (2010).

Based on the above equations, the stress reduction ratios are given by:

$$SRR = \begin{cases} \frac{2s}{(s+a)(s^2-a^2)}\left[s^2 - a^2\left(\frac{p_c'}{\sigma_v'}\right)\right] & \text{for full arching} \\ \frac{2.8s}{(s+a)^2 H}\left[s^2 - a^2\left(\frac{p_c'}{\sigma_v'}\right)\right] & \text{for partial arching} \end{cases} \tag{2-31}$$

Pile efficacy can be determined by following equations:

$$E = \begin{cases} 1 - \frac{2}{s(s+a)}\left[s^2 - a^2\left(\frac{p_c'}{\sigma_v'}\right)\right] & \text{for full arching} \\ 1 - \frac{2.8 f_{fs}\gamma(s-a)}{s(s+a).\sigma_v'}\left[s^2 - a^2\left(\frac{p_c'}{\sigma_v'}\right)\right] & \text{for partial arching} \end{cases} \quad (2\text{-}32)$$

However, the above equations generated stress reduction ratios greater than one for some embankment problems, which is impractical. Since BS8006-1 (2010) does not satisfy the vertical equilibrium when calculating the line load on the geosynthetic layer, it results this unrealistic outcome.

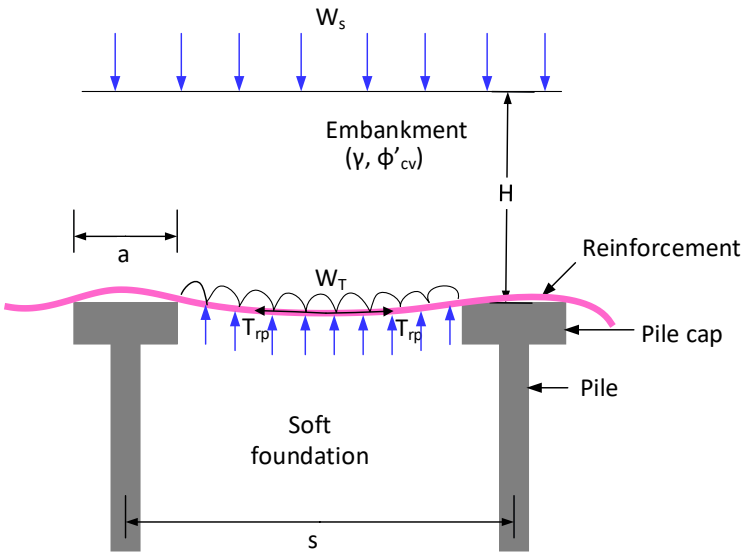

Figure 2.11. Variables used in determination of T_{RP} (modified after BS8006-1, 2010).

Several existing design methods (Terzaghi, 1943; Guido, 1987; Hewlett and Randolph, 1988) for pile-supported embankments were compared and discussed by Russell and Pierpoint (1997). From the comparison of the two case studies, BS8006-1 (2010) was seemed to be inconsistent. BS8006-1 (2010) does not satisfy the equilibrium of vertical forces when calculating the line load on the geosynthetic reinforcement. That leads to unrealistic results for some embankment problems. Some alterations of BS8006-1 (2010) were proposed by van Eekelen *et al.* (2011), in order to eliminate the shortcomings when calculating the line load on

the geosynthetic layer. The new equations proposed satisfy the vertical equilibrium for partial arching condition, but not for full arching condition. However, they give more realistic values.

The pile efficacy considering the modified equations proposed by van Eekelen *et al.* (2011) are:

$$E = \begin{cases} 1 - \frac{1}{s^2}\left[s^2 - a^2\left(\frac{p_c'}{\sigma_v'}\right)\right] & \text{for full arching} \\ 1 - \frac{1.4(s-a)}{s^2 H}\left[s^2 - a^2\left(\frac{p_c'}{\sigma_v'}\right)\right] & \text{for partial arching} \end{cases} \quad (2\text{-}33)$$

The stress reduction ratio is obtained from the recommended equations, which are given below.

$$SRR = \begin{cases} \frac{1}{(s^2-a^2)}\left[s^2 - a^2\left(\frac{p_c'}{\sigma_v'}\right)\right] & \text{for full arching} \\ \frac{1.4}{(s+a)H}\left[s^2 - a^2\left(\frac{p_c'}{\sigma_v'}\right)\right] & \text{for partial arching} \end{cases} \quad (2\text{-}34)$$

where s and a are the spacing and diameter of pile, respectively, p_c' and σ_v' are the stresses transferred to pile and surrounding soil, respectively.

Tension in geosynthetic reinforcement due to lateral sliding of fill was not a point of interest of any of the above methods (e.g. Hewlett and Randolph, 1988; Low *et al.*, 1994) as the purpose of those studies were not to evaluate the total tension developed in geosynthetic reinforcement, but to assess the arching effect in load distribution mechanism in the embankments. However, geosynthetics are stressed by lateral thrust by fill material.

According to BS8006-1 (2010) the reinforcement tensile load T_{ds} that resists the outward thrust of the fill material can be calculated as:

$$T_{ds} = 0.5K_a\left(f_{fs}\gamma H + 2f_q w_s\right)H \quad (2\text{-}35)$$

where T_{ds} is the tensile load in the reinforcement per metre run needed to resist the lateral thrust of the embankment fill, K_a is the active earth pressure coefficient ($Ka = \tan^2\left(45° - \frac{\varphi_{cv}}{2}\right)$), H is the height of the embankment (displayed in Figure 2.12), γ is the unit weight of the embankment fill, w_s is the surcharge intensity on top of the embankment, f_{fs} is the partial load factor for soil unit weight (Table 22 in BS8006-1 (2010)), f_q is the partial load factor for external applied loads (Table 22 in BS8006-1 (2010)), and φ_{cv} is the friction angle of fill materials.

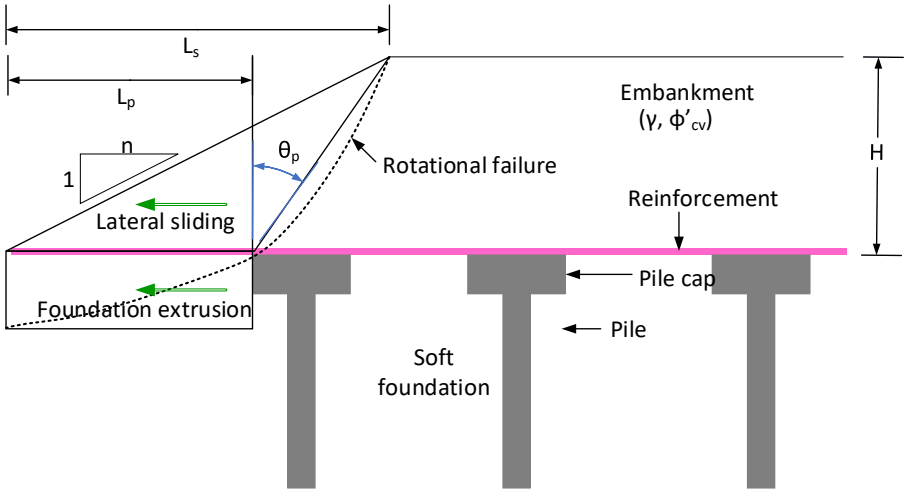

Figure 2.12. Outer limit of pile caps (modified after BS8006-1, 2010).

To protect the embankment from this horizontal sliding, the minimum reinforcement bond length L_e (as shown in Figure 2.13) is required which can be calculated as:

$$L_e \geq \frac{T_{ds} f_s f_n}{\gamma h \frac{a' \tan \varphi'_{cv}}{f_{ms}}} \qquad (2\text{-}36)$$

where f_s is the partial factor for reinforcement sliding resistance (Table 22 in BS8006, 2010), f_n is the partial factor governing the economic ramifications of failure (Table 9 in BS8006, 2010), h is the average height of embankment fill above the reinforcement length L_e, a′ is the interaction coefficient relating the soil/reinforcement bond angle to $\tan\varphi'_{cv}$, φ'_{cv} is the large

strain angle of friction of the embankment fill under effective stress conditions, f_{ms} is the partial material factor applied to $\tan\varphi'_{cv}$ (Table 22 in BS8006-1 (2010)).

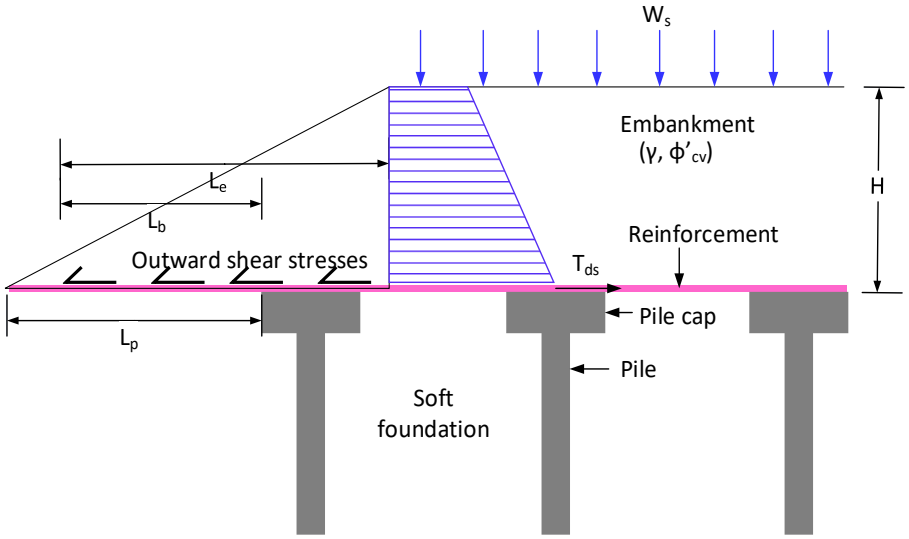

Figure 2.13. Lateral sliding at fill and reinforcement interface (modified after BS8006-1, 2010).

2.8.2 German Standard: EBGEO (2010)

Kempfert *et al.* (1997) adopted the idea of the Hewlett and Randolph (1988) approach, with a modification for low-height embankments using the multi shell arching theory. The German standard EBGEO, 2010 considers arches spanning between diagonal columns or pile caps based on research carried out by Kempfert *et al.* (1999), Zaeske (2001), Zaeske (2002), and Kempfert *et al.* (2004). This method first evaluates stress distribution in the embankment without considering geosynthetic reinforcement, which results in the vertical stress on top of columns and on the top of subsoil p_r. In the next step, it assumed existence of geosynthetic and apply stress p_r to geosynthetic as external load to calculate tension developed in geosynthetic reinforcement.

The vertical stress on the geosynthetic reinforcement layer (p_r) is given by the following equation:

$$p_r = \lambda_1^{\chi}\left(\gamma + \frac{q}{h}\right)\left[h\left(\lambda_1 + h_g^2\lambda_2\right)^{-\chi} + h_g\left(\left(\lambda_1 + \frac{h_g^2\lambda_2}{4}\right)^{-\chi} - \left(\lambda_1 + h_g^2\lambda_2\right)^{-\chi}\right)\right] \quad (2\text{-}37)$$

where

$$\lambda_1 = \frac{1}{8}(s_d - d)^2, \lambda_2 = \frac{{s_d}^2 + 2ds_d - d^2}{2{s_d}^2}, \chi = \frac{d(K_p - 1)}{\lambda_2 s_d} \quad (2\text{-}38)$$

and

$$h_g = \begin{cases} \frac{s_d}{2}, & \text{for } h \geq \frac{s_d}{2} \\ h, & \text{for } h < \frac{s_d}{2} \end{cases} \quad (2\text{-}39)$$

where d is the pile (or pile cap) diameter, K_p is the passive earth pressure coefficient, h_g is the arch height, q is the surcharge, h is the height of embankment, γ is the unit weight of embankment fill, and s_d is the diagonal pile spacing.

Unlike Hewlett and Randolph (1988) method, the upper and lower surfaces in the arch are not concentric as shown in Figure 2.14(a) according to this guidelines. This design guideline adopts the multi-shell arching theory based on the research conducted by Zaeske (2001) as displayed in Figure 2.14(b).

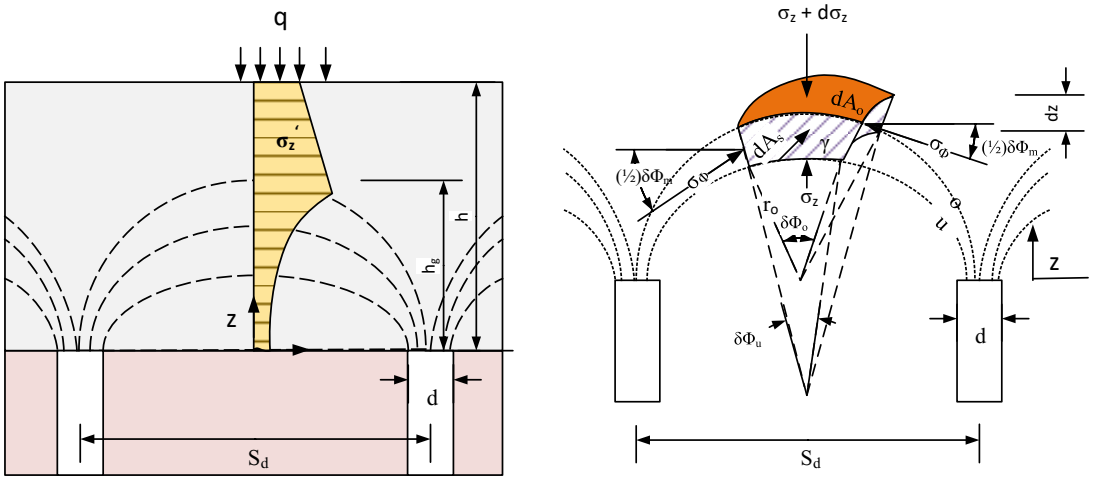

Figure 2.14. Multi arching model (modified after Zaeske, 2001 and 2002).

This process does satisfy the vertical equilibrium of forces when determining the stress on the geosynthetic layer and the equilibrium equation is as following:

$$A_p\sigma_c + (s_x s_y - A_p)p_r = s_x s_y(\gamma h + q) \tag{2-40}$$

where σ_c is the stress transferred to pile and A_p is the area of a circular pile.

The maximum strain can be found using the suggested graph which is shown in Figure 2.15 after calculating the vertical stress acting on the geosynthetic layer. Then the tension developed in the geosynthetic can be found using the considering the equation of stress strain compatibility.

$$T = J\varepsilon \tag{2-41}$$

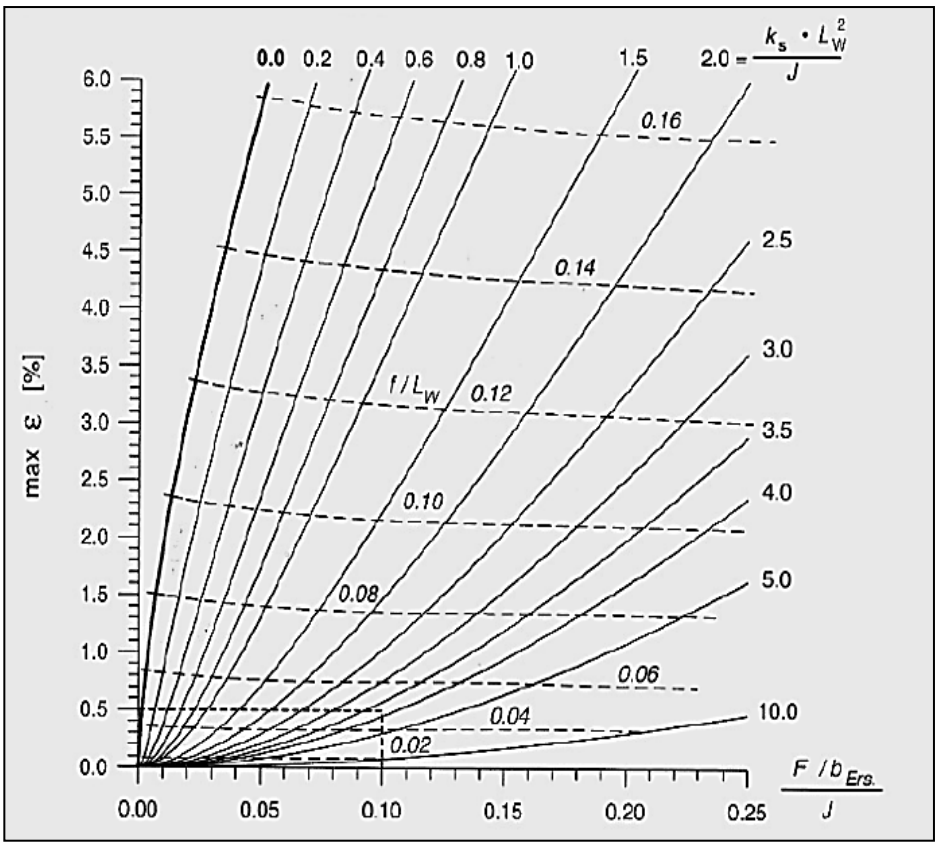

Figure 2.15. Maximum strain in the geosynthetic reinforcement (Kempfert *et al.*, 2004)

.

Figure 2.16 illustrates the terms used in Figure 2.15. Force F is a result of p_r acting on the geosynthetic layer over an influenced area of A_L. b_{Ers} is equal to $0.5d\sqrt{\pi}$ and L_w is equal to $(s_{x,y} - b_{Ers}) \times k_s$ is the modulus of subgrade reaction that is defined as the ratio of the elastic modulus of soft soil to the depth of the soft soil layer. J is the tensile stiffness of soft soil.

$$F_x = A_{Lx}p_r, F_y = A_{Ly}p_r, A_{Lx} = \frac{1}{2}s_x s_y - \frac{d^2}{2}\arctan\left(\frac{s_y}{s_x}\right)\frac{\pi}{180} \quad \text{and} \quad (2\text{-}42)$$

$$A_{Ly} = \frac{1}{2}s_x s_y - \frac{d^2}{2}\arctan\left(\frac{s_x}{s_y}\right)\frac{\pi}{180}$$

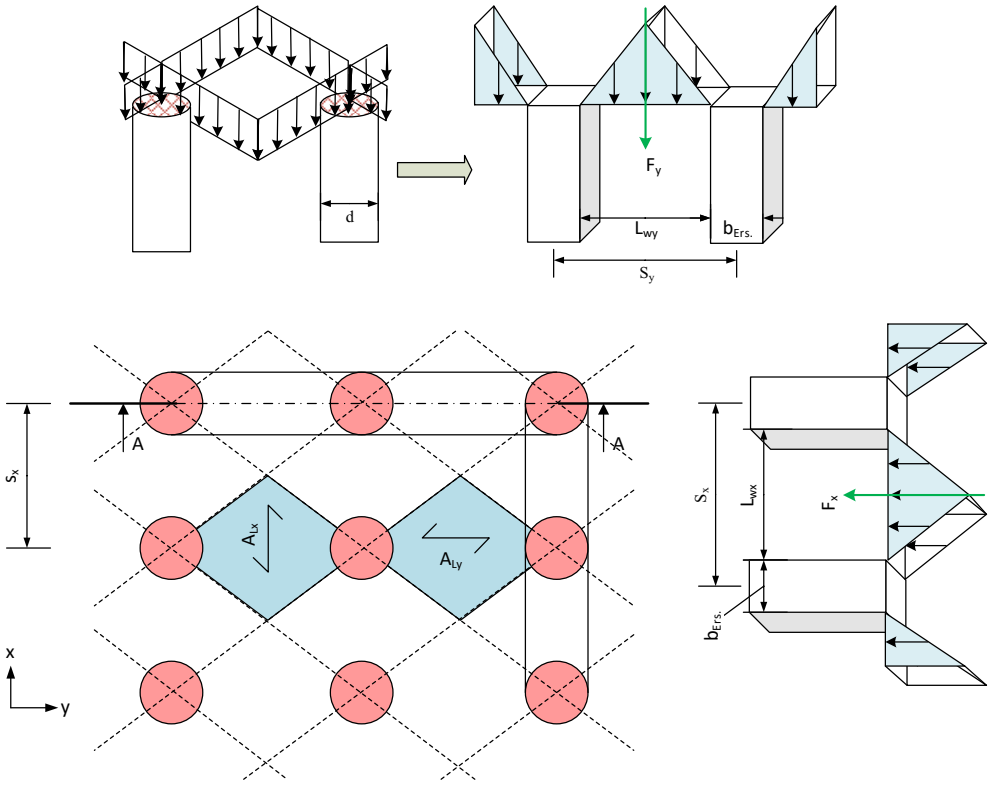

Figure 2.16. Calculation of the resulting force F assigned to the load influence area A_L (modified after Kempfert *et al.*, 2004).

Efficacy can be determined by:

$$E = \frac{A_p\sigma_c}{s_x s_y(\gamma h+q)} = 1 - \frac{SRR.(s_x s_y - A_p)}{s_x s_y} \quad (2\text{-}43)$$

In this study, first the magnitude of load transferred on the soft soil without inclusion of reinforcement is calculated. Then the tension in the reinforcement is estimated to support that load. This method allows the support from the foundation soil while calculating tension developed in geosynthetic. Applying the theory of elastically embedded membranes, the tension in the reinforcement is estimated.

According to this approach, the stress reduction ratio is:

$$\mathrm{SRR} = \frac{1}{\gamma h}\left\{\lambda_1^{\chi}\left(\gamma + \frac{q}{h}\right)\left[h\left(\lambda_1 + h_g^2\lambda_2\right)^{-\chi} + h_g\left(\left(\lambda_1 + \frac{h_g^2\lambda_2}{4}\right)^{-\chi} - \left(\lambda_1 + h_g^2\lambda_2\right)^{-\chi}\right)\right]\right\} \tag{2-44}$$

In addition, Stress Concentration Ratio can be determined by:

$$n = \frac{\sigma_c}{p_r} = \frac{s_x s_y(\gamma h + q) - p_r(s_x s_y - A_p)}{A_p p_r} \tag{2-45}$$

Russell and Pierpoint (1997) concluded from their study that the current design methods cannot be assuredly used for all embankment geometries. For example, BS8006-1 (2010) is not valid when embankment height is less than $0.7(s - a)$. Effect of frictional angle of fill, stiffness of piles, and tensile stiffness of geosynthetic was not considered in BS8006-1 (2010). Vertical equilibrium of forces is not satisfied in this standard. Due to double consideration of W_T, this method sometimes gives unrealistic result of stress reduction ratio (SRR). van Eekelen *et al.* (2013) method considers consolidation of subsoil but does not explain how load transfer mechanism will be affected by degree of consolidation.

2.9 Mechanical Behaviour of Geosynthetic Embedded Granular Fill Layer

Soft clays are usually affiliated with problems such as expansion, dispersion, and excessive settlement due to low shear strength, low bearing capacity, and high shrink-swell potential. Therefore, when heavy superstructures, such as high-rise buildings, fuel tanks, or high

embankments, are constructed on soft soil it is prone to excessive deformation (Azari *et al.*, 2016; Le and Fatahi, 2016; Parsa-Pajouh *et al.*, 2016). Thus, in combination with cautious field observations and laboratory tests, the use of several ground-improvement techniques using rigid or semirigid inclusions, such as stone columns, micropiles, jet grouting columns, deep soil mixing columns, and concrete injected columns (CICs), has grown substantially over the last two decades. For example, the Gerringong Upgrade Project (New South Wales) was one recent successful project in which CICs were used for soft soil improvement (Fulton-Hogan, 2015) (shown in Figure 2.17).

Figure 2.17. Gerringong upgrade project site (Roads and Maritime Services, 2015).

A layer of sand or gravel consisting of geosynthetic reinforcement is commonly placed on top of the columns to facilitate the load transfer from the superstructures to the columns, but soil behaviour becomes much more complex with the inclusion of geosynthetics. Because the entire system consists of more than one component, such as the granular layer, the geosynthetics, and the soft soils, the response of the system is both interdependent and complex. The interactions between the granular layer and geosynthetics, granular layer, and soft soil change their actual behaviour compared with what is obtained when considering each structure separately. This phenomenon is known as soil–structure interactions (SSIs).

In recent years many researchers have proposed several mechanical foundation models to simplify the analysis of the geosynthetic-reinforced granular layer on soft soil in SSI problems in which soft soil was idealized by the Winkler (1867) model, the Filonenko-Borodich (1940) model, the Pasternak (1954) model, the Horvath and Colasanti (2011), modified Kerr (1965) model, and so on. Whereas the granular layer with the geosynthetics or without the geosynthetics was idealized by the Euler-Bernoulli beam (deformation due to bending only), the Pasternak shear layer (deformation due to shear only), and the Timoshenko beam (deformation due to shear and bending). Figure 2.18a and b display a mechanistic idealisation of granular layer on soft soil where soft soil is simulated by Winkler springs, while granular layer is simulated by Euler-Bernoulli beam. In Figure 2.18a - b, $p(x)$ and $p_b(x)$ are the applied force and reaction force on the granular layer, respectively; while $V(x)$ and $M(x)$ are the shear force and the bending moment at the section-x, respectively. They also predicted the response of the granular layer under various applied loading, which may be limited to particular applications.

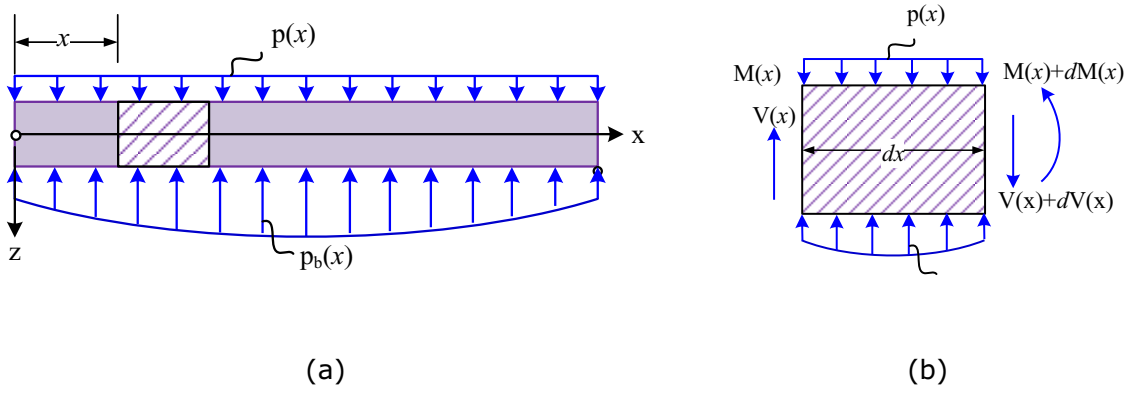

Figure 2.18. Beam on elastic foundation: (a) force acting along the length and (b) details of a finite section of the beam.

To represent the mechanistic behaviour of the granular layer with geosynthetics over soft soil, Madhav and Poorooshasb (1988) developed a new foundation model known as the modified

Pasternak model in which Winkler springs representing the soft soil were modified to introduce continuity through interaction among the spring elements by some structural elements representing the granular layer Figure 2.19a. Madhav and Poorooshasb (1988) modelled the soft soil, the granular layer, and the geofabric by a linear model using the Winkler springs, a Pasternak shear layer, and a rough membrane, respectively. They concluded that the granular material has a more significant effect than the geofabric on the deformation of soft soil. According to the Pasternak theory, the granular layer with geosynthetics experienced transverse shear deformation, as shown in Figure 2.19b. However, the deformation of the geosynthetic- reinforced granular layer on a soft soil system caused by bending was not considered in this model, and the settlement was completely controlled by shear.

Deb *et al.* (2007) and Deb (2010) proposed a mathematical model of the geosynthetic-reinforced granular layer on column-improved soft soil. They simulated the soft soil, the granular layer, the geosynthetics, and the columns by using a nonlinear springs-dashpot, Pasternak shear layer, rough membrane, and stiffer nonlinear Winkler springs, respectively, but did not consider the bending deformation of the geosynthetic reinforced granular layer in this proposed foundation model. Maheshwari and Khatri (2012) proposed a mechanical model to predict the response of the infinite beam on the geosynthetic-reinforced granular layer on column-improved soft soil under moving load. They modelled the granular layer as a Pasternak shear layer, the soft soil as a Kelvin-Voigt model, the geosynthetics as a rough elastic membrane, and the column as a Winkler spring. Maheshwari and Khatri (2012) found that any variation in applied load significantly influenced the response of the infinite beam with respect to its deflection and bending moment and tension mobilized in the geosynthetic layer. Similar to the Deb (2010) model, it did not consider the bending deformation of the geosynthetic-reinforced granular layer. The load-deflection relationship for the granular layer adopting the

Pasternak theory was obtained by considering the vertical stress equilibrium of an infinitesimal element of shear layer, as shown in Figure 2.20a.

Conversely, an attempt is made in literature to solve the classical problem of a geosynthetic-reinforced granular layer on an elastic foundation using the Euler-Bernoulli beam. In the Euler-Bernoulli beam, the shear deformation of a beam is omitted by assuming that plane sections remain plane and perpendicular to the neutral axis during bending, as shown in Figure 2.19c. Maheshwari and Viladkar (2009) developed a mechanical model of geosynthetic reinforced earth bed subjected to strip loading in which geosynthetic reinforcement was simulated with the Euler-Bernoulli beam while the finite bending stiffness of geosynthetics was assumed. The soil layers above and below this reinforcing layer were idealized by linear Winkler springs. Maheshwari and Viladkar (2009) obtained the differential equations for the flexural response of such a foundation system, but they did not consider its deformation due to shear. However, in reality, and particularly for deep beams, the cross section of the beam does not remain perpendicular to the neutral axis after deformation, as shown in Figure 2.19d. The Timoshenko (1921) beam considers shear deformation and the flexural deformation of a beam (as shown in Figure 2.19d), because in this beam rotation between the cross section and the bending line is allowed. This rotation is induced by the shear deformation that is not captured in the Euler-Bernoulli beam theory. Although the cross section in the Timoshenko beam is assumed to remain plane during bending, it does not remain perpendicular to the neutral axis. Therefore, in terms of rigidity the Euler-Bernoulli beam and the Pasternak shear layer are stiffer than the Timoshenko beam.

Adopting the Timoshenko beam theory Yin (2000a, 2000b) proposed an analytical model to simulate the granular layer with geosynthetics on soft soil and proposed the closed-form solutions for the differential equations for the point load and the uniformly distributed vertical

pressure. They idealized the soft soil, the granular layer, and the geosynthetics by linear Winkler springs, Timoshenko beam, and a rough membrane placed inside the Timoshenko beam, respectively. Based on an analytical solution for the reinforced Timoshenko beam on elastic medium, Yin (2000b) observed that larger settlement and less tension force occur near the location of point load compared with the pure bending beam theory. However, the model considered the linear behaviour of soft soil and the infinity tensile stiffness of the granular fill materials, whereas column supports were not considered.

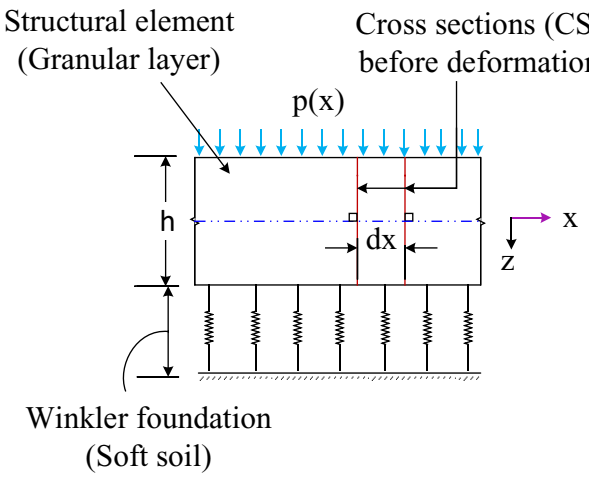

(a)

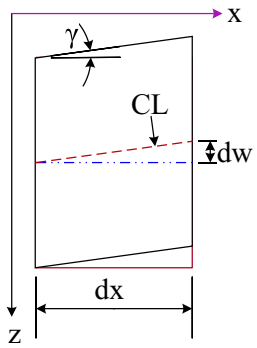

(b)

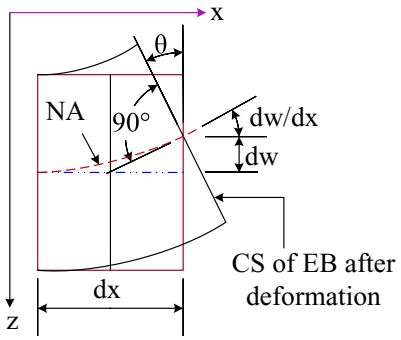

(c)

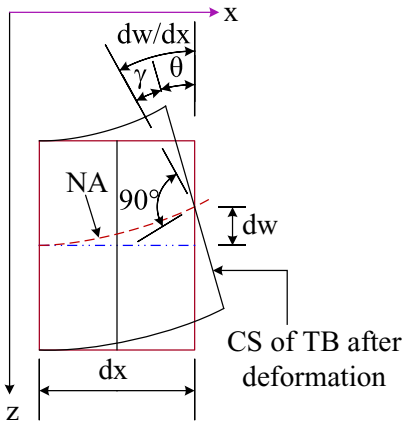

(d)

Figure 2.19. Different beam theories displaying: (a) beam on elastic foundation; (b) deformation due to shear only (Pasternak shear layer; CL = centreline); (c) deformation due to bending only (EB = Euler-Bernoulli beam; CS = cross section; NA = neutral axis); and (d) deformation due to bending and shear (TB = Timoshenko beam)

Similar to the Pasternak shear layer, the load-deflection relationship for a reinforced or unreinforced granular layer adopting the Euler-Bernoulli beam and the Timoshenko beam was obtained by considering the vertical force equilibrium of an infinitesimal beam element, as shown in Figure 2.20b. Indeed, most mechanical idealizations of soil foundation medium adopt the Winkler approach in which a linear load versus settlement relation is used. However, a nonlinear load versus settlement relationship for the soil is observed from the plate-load test (Chandra *et al.*, 1987); hence, it cannot be truly idealized by the linear Winkler model. Moreover, the settlements of soft soils are large even at working loads and because soil nonlinearity is more significant, it must be considered for more reliable predictions.

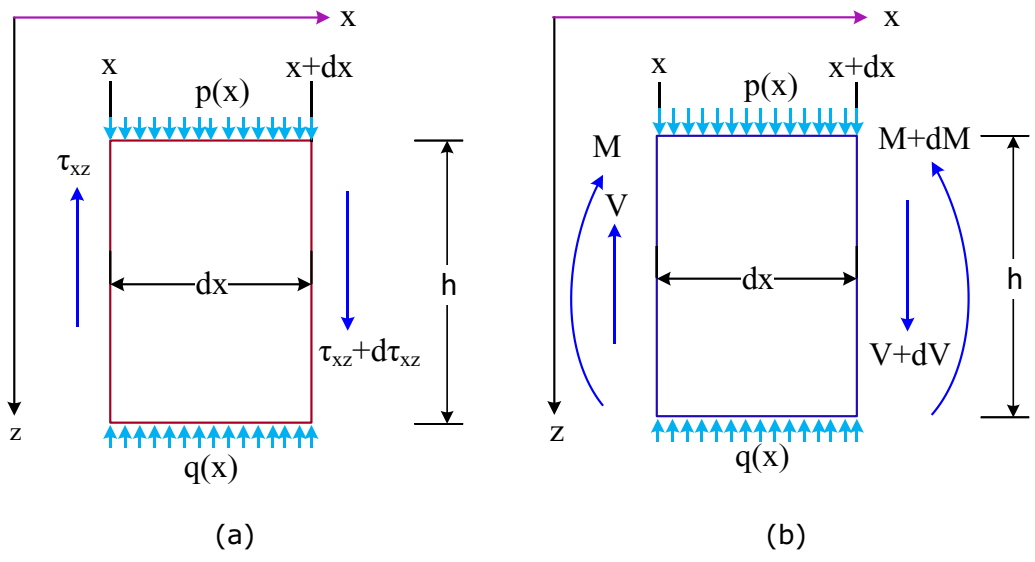

Figure 2.20. Free-body diagram of an infinitesimal beam element for (a) Pasternak shear layer and (b) Timoshenko and Euler-Bernoulli beams.

As discussed earlier, insufficient bearing capacity and excessive settlement are very common and severe issues of soft soils when heavy superstructures are constructed on the top of these soils. Thus, in combination with cautious field observations and laboratory tests, the use of ground improvement techniques using rigid (e.g. concrete injected columns, jet grouted columns, and piles) or semi-rigid inclusions (e.g. deep soil mixing columns and lime cement columns) has grown substantially over the last two decades (Bergado *et al.*, 1999; Han *et al.*, 2004). Load transfer platform (LTP), a layer of sand or gravel consisting of geosynthetic layers, is commonly placed over the columns (e.g. concrete injected columns, or piles) used for ground improvement to facilitate the load transfer from the superstructures to the columns (Russell and Pierpoint, 1997; Han and Gabr, 2002; Kempfert *et al.*, 2004).

Application of a load transfer platform resting on column improved soft soil is very common, particularly when highway embankments are built on improved ground. To analyse the column supported embankments, several analytical models have been proposed in the literature. van Eekelen *et al.* (2013) summarised and classified them as (a) frictional models (Terzaghi, 1943; McKelvey, 1994; Russell and Pierpoint, 1997; Naughton, 2007; McGuire *et al.*, 2012), (b) rigid arch models (Carlsson, 1987; Rogbeck *et al.*, 1998; Svanø *et al.*, 2000; van Eekelen *et al.*, 2003), (c) models using mechanical elements (Deb, 2010; Filz *et al.*, 2012; Zhang *et al.*, 2012b, 2012a; Deb and Mohapatra, 2013) and (d) limit-state equilibrium models (Marston and Anderson, 1913; Hewlett and Randolph, 1988; Jones *et al.*, 1990; Zaeske, 2001). British design guidelines BS8006-1 (2010), discussed by van Eekelen *et al.* (2011), adopted the empirical model proposed by Jones *et al.* (1990) to study the geosynthetic reinforced column supported embankments. Zaeske's model (2001) latter was adopted in the German design guidelines EBGEO (2010). van Eekelen *et al.* (2013) proposed a new limit-state equilibrium model for piled embankments which is an extension of the model proposed by Hewlett and Randolph (1988) and EBGEO (2010).

Several other researchers compared the results of existing analytical models with field or laboratory measurements (Chen *et al.*, 2008b; Briançon and Simon, 2012; Girout *et al.*, 2016). Chen *et al.* (2008b) conducted experiments both with and without geosynthetics and compared the results of their experiments with existing analytical models, namely Terzaghi (1943) and Low *et al.*, 1994 and the original 2D equation of Marston and Anderson, 1913. Zaeske (2001), Heitz (2006), and Farag (2008) compared the results of their laboratory model tests with their predictions from the calculations. Results of a predictive model to capture membrane behaviour of the geosynthetic reinforcement based on the results of twelve model tests have been reported by van Eekelen et al. (2012a, 2012b).

Several other studies have been conducted using two dimensional numerical models of geosynthetic reinforced column supported embankment structures adopting the finite element method (FEM) and finite difference method (FDM) (Han *et al.*, 2007; Huang *et al.*, 2009; Huang and Han, 2010; Yapage and Liyanapathirana, 2014). Furthermore, the predictions adopting full-width model were compared with unit cell model in numerical simulations by Bhasi and Rajagopal (2015b), Khabbazian *et al.* (2015), and Yu and Bathurst (2017). Collin *et al.* (2005) proposed a mechanical model of multiple layers of low strength geogrids within the LTP based on the concept of "beam" theory. But, the interrelationship between the embankment settlement and strain in the geosynthetics was ignored in that study. However, application of a load transfer platform is not limited to the column supported embankments. A load transfer platform is widely used for heavy superstructures such as fuel tanks and silos. The practical designs of LTP demand the simple yet accurate modelling of (i) the mechanical behaviour of the LTP, (ii) the mechanical behaviour of the underneath soft soil, and (iii) the interaction mechanism between the LTP and the soft soil.

While physically close and mathematically simple, idealisations of the mechanical behaviour of the geosynthetic reinforced granular fill or LTP can be established adopting Timoshenko (Yin 2000a; 2000b; Shukla and Yin, 2003; Zhao *et al.*, 2016) or the Euler-Bernoulli beam theories (Maheshwari *et al.*, 2004; Maheshwari and Viladkar, 2009; Zhang *et al*.2012a; 2012b) or even the Pasternak shear layer theory (Yin 1997b; 1997a; Deb *et al.*, 2007; Deb, 2010), the characteristics that represent the mechanical behaviour of the soft soil and its interaction with the granular layer are difficult to model. Since, the soft soil is heterogeneous, anisotropic and nonlinear in load-displacement response, the simple springs cannot simulate the soil response accurately. It should be noted that the most commonly used mechanical model to simulate the soil is the one developed by Winkler (1867). Although, the model proposed by van Eekelen *et al.* (2013) can be applicable for both full and partial arching which results in a better representation of the arching measured in the experiments than the other existing models such as EBGEO (2010), BS8006-1 (2010), especially when the embankment is relatively thin, van Eekelen *et al.* (2013) modelled the subsoil as an elastic spring with constant modulus of subgrade reaction which is comparable to linear Winkler's springs. Winkler's idealisation symbolises the soil medium as a series of identical but mutually independent, closely spaced, linearly elastic spring elements. Since according to the Winkler hypothesis, there is no interaction between adjacent springs, this model cannot account for the dispersion of the load with depth and distance from the loading area. However, it is a common phenomenon that the surface deflections occur not only immediately under the loaded region but also within certain limited regions beyond the loaded area. Therefore, Winkler's model has the inability to consider the continuity or shear strength of the soil. Hence, compressibility of the soil was considered in the model proposed by van Eekelen *et al.* (2013) while shear action in the soil was ignored.

To overcome the weaknesses of the Winkler's model (i.e. to achieve some degree of interaction between the individual spring elements), some modified foundation models have been

suggested in the literature. In these modified models, a second parameter was introduced to Winkler foundation to eliminate the discontinuous behaviour of soil by providing continuity through interaction between the individual spring elements with some structural elements (Filonenko-Borodich, 1940; Hetényi, 1946; Pasternak, 1954). To further improve the two-parameter foundation models, the third soil parameter was introduced, leading to the so-called "three-parameter" foundation model. Among several three parameter foundation models, the foundation model proposed by Kerr (1965) is of particular interest since it geneses from the well-known Pasternak foundation model for which several applications and solutions have been already available in the literature. Kerr foundation model consists of two spring layers, with varied spring constants, interconnected by a shear layer. Furthermore, Kerr concluded that for different types of foundation materials (e.g. soil and foam), the Winkler foundation model cannot realistically predict the interaction mechanisms between the beams and the contacting soil medium. Therefore, the most important task for practicing engineers is to simulate soft soil, which demands simple modelling but provides an accurate response of the soft soil.

In summary, mechanical behaviour of the geosynthetic reinforced granular fill or LTP can be theoretically established by adopting the Pasternak shear layer theory (Yin, 1997a; 1997b; Deb *et al.*, 2007; Deb, 2010), the Euler-Bernoulli beam theory (Maheshwari *et al.*, 2004; Maheshwari and Viladkar, 2009; Zhang et al.,2012a; 2012b), and the Timoshenko beam theory (Yin, 2000a; 2000b; Shukla and Yin, 2003; Zhao *et al.*, 2016). According to Pasternak theory, the cross-section of the LTP does not rotate and therefore, the granular layer experiences transverse shear deformation only. Thus, bending deformation of the granular layer was ignored in the developed models (Yin,1997a, 1997b; Deb *et al.*, 2007; Deb, 2010). For application of the Euler-Bernoulli theory in geosynthetic reinforced soil (Maheshwari *et al.*, 2004; Maheshwari and Viladkar, 2009; Zhang *et al.*, 2012a, 2012b), by considering the plane sections remain plane and perpendicular to the neutral axis after deformation, the shear

deformation of a geosynthetic reinforced soil was ignored. However, after deformation of beams with the small length - to depth ratio, the cross section of the beam is still not be perpendicular to the neutral axis. To overcome the shortcomings of Euler-Bernoulli and Pasternak theories, the well-known Timoshenko (1921) beam can be adopted to simulate the LTP (Yin, 2000a; 2000b). Yin (2000a, 2000b) idealised the soft soil, the granular layer, and the geosynthetics by linear Winkler springs, Timoshenko beam, and a rough membrane, respectively. Based on the Timoshenko (1921) beam assumption, Yin's model considers the shear and the flexural deformations of the granular layer since the rotation between the cross section and the bending line of the beam is acceptable (as shown in Figure 2.21a - b).

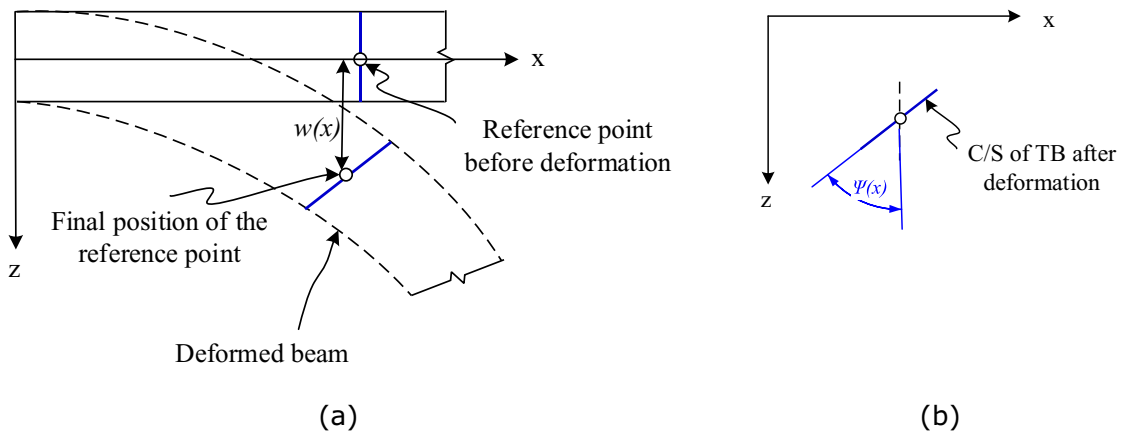

Figure 2.21. Structural illustration of a Timoshenko beam: (a) vertical deflection and (b) rotation of cross-section.

Zhao *et al.* (2016) proposed a new dual beam model for a geosynthetic-reinforced granular fill with an upper pavement. Zhao *et al.* (2016) modelled the upper pavement by an Euler-Bernoulli beam, while the geosynthetic reinforced granular fill was simulated by a reinforced Timoshenko beam. The explicit derivation process for the behaviour of this dual beam foundation system was presented in this study and an exact solution was suggested. However, effects of columns and negligible tensile strength of soil were not considered in that study as shown in Figure 2.22. When the granular material in LTP is dense to very dense (relative

density greater than 65%) due to the compaction process, idealisation of LTP as Timoshenko beam is more appropriate (Shukla and Yin, 2003). Indeed, the total settlement of LTP can occur due to the beam bending mechanism as well as the shear action, like the case of a reinforced concrete beam. After a few years of operation, LTP will become stiffer and behave like a concrete beam, deforming in shear as well as in bending. Hence, the settlement analysis of LTP in the construction stage or short time after may be conducted using the existing models (Deb , 2010; van Eekelen *et al.*, 2013), but the model proposed in this paper can be more suitable for the latter stages of LTP life as well as construction stage or short time after construction (by assuming lower shear or bending stiffness of LTP).

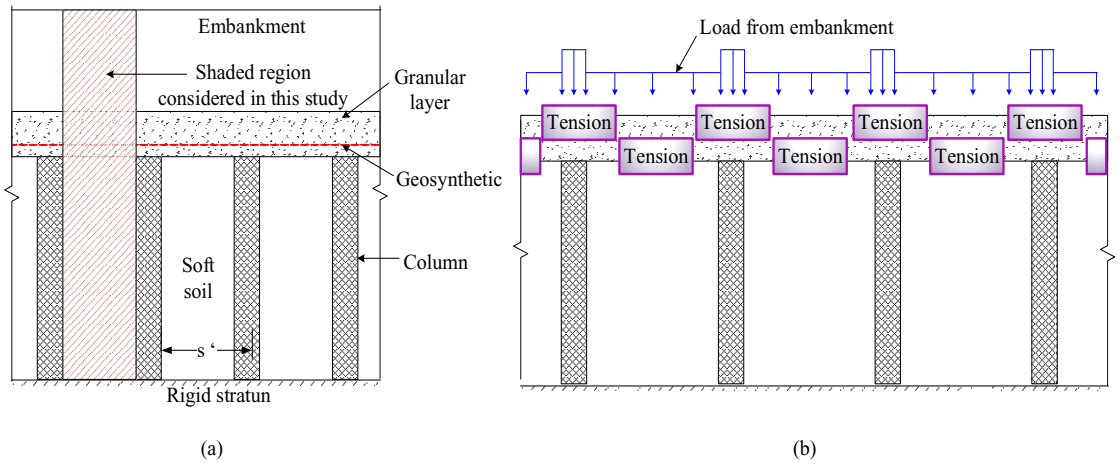

Figure 2.22. CIC-supported embankment: (a) sketch of a geosynthetic-reinforced CIC-supported embankment over soft soil system and (b) location of tension in the LTP.

Most of the analytical and numerical studies related to geosynthetic reinforced granular layer on soft soil have been conducted for a single layer geosynthetic reinforced soil system (Yin, 1997a, 1997b; Maheshwari *et al.*, 2004.; Huang and Han, 2009; Zhao *et al.*, 2016), while very limited number of studies have addressed multilayer geosynthetic reinforced arrangement (Nogami and Yong, 2003; Liu and Rowe, 2015; van Eekelen *et al.*, 2015; Borges and Gonçalves, 2016). Nogami and Yong (2003) proposed a mechanical model for a multilayer geosynthetic reinforced soil subjected to structural loading. Nogami and Yong (2003)

considered each soil layer by a system of an infinite number of closely spaced one-dimensional columns connected with horizontal springs. Governing differential equations were solved iteratively by the finite difference method. Therefore, this research is an attempt to suggest a generalised model that provides a closed-form solution to estimate the behaviour of multilayer reinforced granular fill. The key purpose of this work was to develop an accurate analytical model to predict behaviour of LTP on column reinforced soft soil by idealising the physical modelling of the LTP on the soil media as "membrane reinforced Timoshenko beam" on Kerr foundation. The analytical model developed in this work can be applied by practicing engineers to predict the deflection of the LTP and mobilised tension in the geosynthetic reinforcement. Then, an analytical solution for the governing differential equation was proposed. The suitability of the Kerr foundation model for engineering calculations of LTP were evaluated while LTP is subjected to symmetric loading. To solve the governing differential equations, the supports of column in the reinforced soft soil was counted in by considering the reaction force in the column locations. To validate the proposed model, the results obtained from the model, simulating the soft soil as the Kerr foundation model, were compared to the corresponding solutions when the soft soil is idealised by Winkler and Pasternak foundations. Similar approach to validate the analytical model was adopted by several other researchers, available in the literature (Maheshwari and Viladkar, 2009; Zhang *et al*., 2012b; Lei *et al*., 2016). Parametric studies were also carried out to assess the overall behaviour of the multilayer geosynthetic reinforced granular layer as well as that of the single layer geosynthetic reinforced granular layer.

Furthermore, most of the existing literature of mechanical design of the geosynthetic-reinforced granular platform in soil-structure-foundation system is based on classic thin beam/plate theory (Euler-Bernoulli beam, Pasternak shear layer). The modelling of foundation with Euler-Bernoulli beam theory becomes incorrect due to not considering the transverse

shear stress. This assumption, however, may be unrealistic for thicker geosynthetic reinforced granular platform in which shear deformations may be significant. According to Pasternak theory (1954) the foundation beam will deform under transverse shear force only. Therefore, neither Euler-Bernoulli (1933) nor Pasternak model (19544) considers both bending and shearing of beam. Timoshenko (1921) developed a model that takes into account shear deformation and bending effects, making it suitable for describing the behaviour of short and deep beams. Yin (2000a, 2000b) has derived the ordinary differential equations for a reinforced Timoshenko beam on elastic foundation excluding the stabilizing columns and provided the analytical solution. However, in Yin's model, geosynthetic in granular layer is assumed to be carry tension, soft soil behaviour is assumed to be linear, and there is no support from the column.

2.10 Summary

Several design methods and guidelines are available for the design of geosynthetic reinforced column-supported embankments, however there is no unanimously accepted design practice. Due to not considering subsoil support during arching, existing design guidelines may underestimate arching load on columns and overestimate tension developed in reinforcement. Due to not considering the reaction of the soft ground on the geosynthetic model proposed by Hewlett and Randolph may underestimate the efficacy and overestimate stress reduction ratio. Review of the existing literature also reveals that there is no mechanical foundation model for predicting the settlement of a geosynthetic-reinforced granular fill on a soft soil foundation that captures the negligible tensile strength compared with the compressive strength of granular materials, the bending and shear deformation of a granular layer with geosynthetics, and the nonlinear stress-strain behaviour of soft soil. Therefore, the need for a generalized model has been felt, and this research was also an effort in that direction. In this research, a mechanical

model was proposed for geosynthetic-reinforced granular fill on a soft soil foundation, which incorporates all these factors simultaneously. In this work, nonlinearity was included in the Winkler foundation by using a bilinear response of the soft soil, and the cracked cross section of the granular layer was considered to represent the negligible tensile strength compared with the compressive strength of granular materials. Moreover, the effect of column supports in composite ground was included by considering the reaction from the column supports, when solving the governing differential equations. For the sake of simplicity, only one-dimensional consolidation deformation was simulated.

Most of the existing two-dimensional and three-dimensional numerical models assume horizontal soil profiles underneath the embankment for simplicity (e.g. King et al., 2017; Liu et al., 2017; Yu and Bathurst, 2017), whereas this may not be the case in actual site conditions. Review of existing literature revealed that there are very limited studies with layered soil deposit of varying over consolidation ratio (OCR) along the depth. In addition, none of the existing numerical models were directly applicable to concrete injected columns needing consideration of a non-linear relationship between the major and minor effective principal stresses in the columns or piles. Since columns may experience significant lateral and vertical stresses as well as soil flow around the columns, more rigorous constitutive models considering yielding under axial, shear and tensile stresses would be preferred. Hence, this research is further effort toward three-dimensional finite element analysis where variations of soft soil OCR with depth in non-horizontal soil deposits and non-linear stress-dependent behaviour of columns are captured. Additionally, attempts are made to verify the three-dimensional finite element model by comparing the predictions with field measurements, while the interaction between the concrete injected columns (CICs) and the neighbouring zone improved with pre-fabricated vertical drains (PVDs) were also captured.

CHAPTER 3

3. ANALYTICAL SOLUTION OF LTP ON COLUMN-IMPROVED SOFT SOIL CONSIDERING SOIL NONLINEARITY

3.1. General

In this chapter, a mechanical model to idealise the settlement response of load transfer platform (LTP) on column improved soft soil is proposed. This model simultaneously considers the nonlinear and time-dependent stress-strain behaviour of soft soil, as well as the negligible tensile strength of the granular material in LTP. The reinforced Timoshenko beam is adopted to model LTP to consider the shear and flexural deformations. Soft soil is idealised by spring-dashpot system to include the time-dependent behaviour. The columns and geosynthetics are modelled with linear Winkler springs in the applied range of stresses and rough elastic membrane, respectively. The response function of LTP has been derived for distributed pressure loading in plane strain condition. The principle of superposition is used to solve the fourth order differential equations. Parametric studies indicate that the spacing of columns, thickness of LTP, degree of consolidation of soft soil, and tensile stiffness of geosynthetics significantly affect the behaviour of LTP. This study also evaluates the accuracy of using reinforced Timoshenko theory by comparing the results with Pasternak and Euler-Bernoulli theories.

3.2. Nonlinear Response of Soft Soil

The simplest and most conventional approach to model the load-displacement response of soil in soil-structure interactions problems is to assume that its behaviour is a linearly elastic Yin, 2000a; Maheshwari and Viladkar, 2009. However, a simplified linear load-displacement relationship for soil may not result in realistic and accurate predictions. Kravtchenko and Sirieys (1966), Parry (1972), Gudehus et al. (1977) have already established the stress-strain-time relationships for soil while capturing its nonlinearity. The measured data of vertical strains and stresses from oedometer tests on Hong Kong marine deposits, as presented by Yin 1999, is plotted in Figure 3.1a and shows the nonlinear nature of soil under applied stresses. One-dimensional consolidation tests on Ottawa lacustrine clay with differing load increment durations conducted by Graham et al. 1983 showed the soil as having a very obvious nonlinear stress-strain response. In addition, for seismic soil structure interaction analysis, effects of soil nonlinearity are very significant (Fatahi and Tabatabaiefar, 2014; Hokmabadi and Fatahi, 2015). On this basis, the nonlinear load-displacement response of soil should be considered in the problem of SSI to achieve more accurate and realistic predictions. However, it is understood that no closed-form solution is available for the differential equation of the Timoshenko beam on nonlinear elastic foundation. Therefore, to simplify the analysis in the SSI problem, a bilinear representation of the load-deflection relationship is used in this study.

In real cases the soft soil foundation often stiffens as the load increases, so one-dimensional stress-displacement response of soft soil is represented here by a bilinear relationship, as shown in Figure 3.1b. According to the bilinear behaviour of soft soil, the soft soil foundation deflects linearly under a transverse load with an initial foundation modulus (k_{0s}) and then reaches the transition deflection $\hat{w}$, beyond which soft soil again deflects linearly under a transverse load with a stiffened foundation modulus (k_{1s}) where $k_{1s} > k_{0s}$. Hence, the spring constant per

unit area representing the soft soil skeleton, known as the modulus of subgrade reaction (k_s), can be written as:

$$k_s = \begin{cases} k_{0s} & \text{when } w(x) \le \hat{w} \\ k_{1s} & \text{when } w(x) > \hat{w} \end{cases} \tag{3-1}$$

where $w(x)$ is the transverse deflection of underneath soft soil at any distance x.

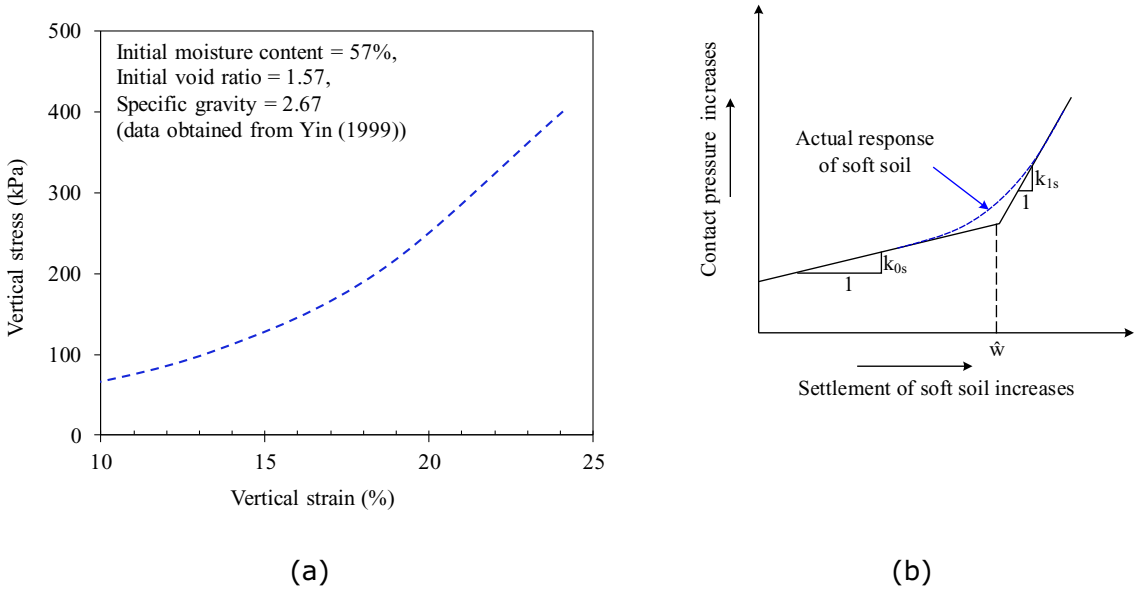

(a) (b)

Figure 3.1. Nonlinear response of soft soil: (a) stress-strain curve and (b) assumed bilinear response of soft soil.

3.3. Development of Analytical Model

Figure 3.2 demonstrates the deflection pattern of a load transfer platform (LTP) resting on a soft soil foundation improved by columns, and like a continuous concrete beam, there is tension at the bottom of LTP close to the mid-span and tension at the top of LTP close to the support under transverse loading. Since soil does not have strength to resist any significant tension due to negligible tensile strength, tension cracks initiate in LTP. Therefore, LTP should be designed using cracked section properties in flexural analysis. Since formation/initiation of tension

cracks and their propagation are varied in different locations, it would be more realistic to consider different cross section properties in different locations of LTP, depending on where the tension cracks are located.

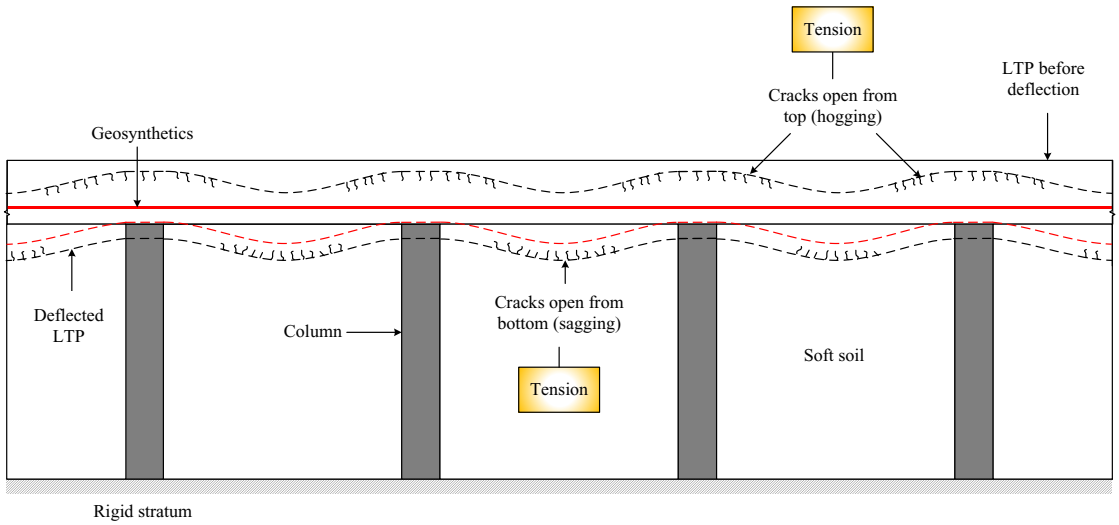

Figure 3.2. Deflection pattern and tension cracks in LTP supported on multiple columns improved soft soil foundation.

Figure 3.3a shows LTP on column improved soft soil foundation considered in this analytical model. The proposed mechanical model shown in Figure 3.3b idealises the behaviour of LTP-soft soil-column system. For simplicity, one layer of geosynthetic reinforcement between the two compacted granular layers is considered in this study. Geosynthetics, columns, and soft soil are idealised by a rough elastic membrane, linear Winkler springs within the applied stress range, and bilinear spring-dashpot system, respectively. The cracked reinforced Timoshenko beam is adopted to simulate LTP.

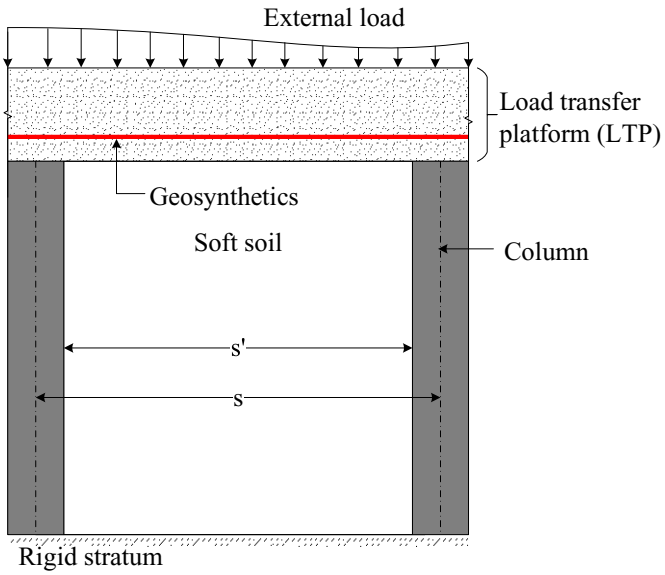

(a)

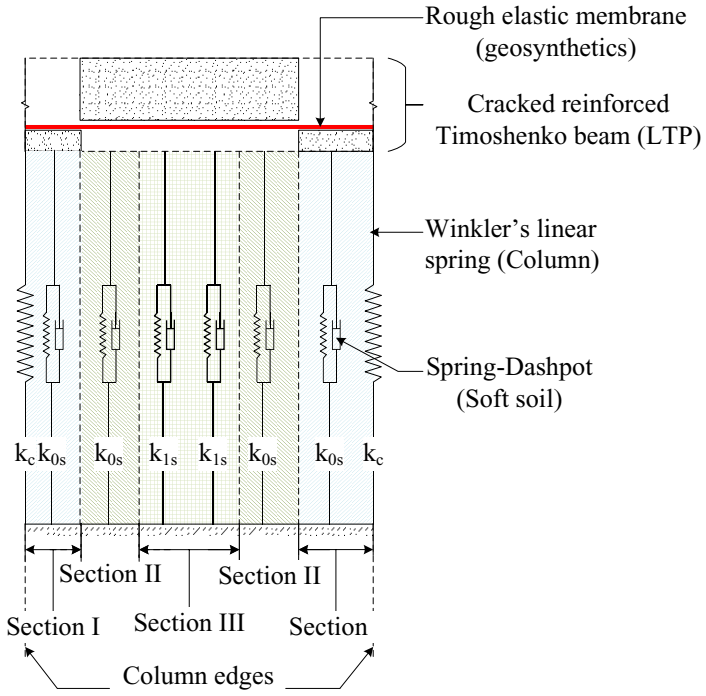

(b)

Figure 3.3. (a) Typical sketch of a geosynthetic reinforced column supported granular layer and (b) schematic diagram of the proposed foundation model.

According to the bilinear behaviour of the soft soil and locations of the tension cracks, the loaded LTP over soft soil is divided into three regions, as shown in Figure 3.5a. Figure 3.5b.

shows the various contact pressures of soft soil in a transverse direction under a distributed pressure loading at LTP-soil interface. When $x \in [0, r_1]$ or $x \in [r_4, s']$, tension cracks in LTP appear from the top fibre which means the top of LTP is under tension (hogging moment). Furthermore, considering the bilinear response of soft soil and the deflection of LTP $w(x)$ being less than or equal to $\hat{w}$; this region is called Section I. However, when $x \in [r_1, r_2]$ or $x \in [r_3, r_4]$ a sagging bending moment occurs in LTP, while the vertical deformation of LTP $w(x)$ is still less than or equal to $\hat{w}$; this area is called Section II. When $x \in [r_2, r_3]$ LTP has a sagging bending moment but the deflection of LTP beam $w(x)$ is greater than $\hat{w}$; this area is called Section III.

3.3.1. Equivalent Properties of Cracked Load Transfer Platform

It has been assumed here that granular fill material in the load transfer platform (LTP) has negligible tensile strength compare to compressive strength, so like a concrete beam McCormac and Brown, 2009, tension cracks are assumed to propagate from the tension face (bottom of LTP) to the neutral axis in the span, and since the granular layer is continuous over the column locations, the bending moment changes direction near the support. As a result, tension cracks generate at the top face of a granular layer and propagate towards the neutral axis at the column location. After cracking, it is still assumed that plane sections remain plane, but as the load increases, these cracks quickly spread towards the neutral axis, and then the neutral axis begins to move according to where the tension cracks are initiated in the granular layer. Since some parts of the granular layer are cracked, the soil in those cracked zones cannot resist tensile stresses and becomes weaker without any reinforcement. Therefore, the granular layer is strengthened by imbedding geosynthetic reinforcement. It is assumed that the geosynthetic reinforcement will not slide against the granular materials, so it is reasonable to assume that all the tension in LTP is taken by geosynthetic reinforcement and the compression

is carried by the granular materials. It is also assumed that the flexural cracks are developed vertically. Although in flexure, the soil below the neutral axis is omitted, but the same soil between the neutral axis and the cracks is needed for shear transfer between the geosynthetic reinforcement and the compression zone.

To carry out a flexural analysis, the cracked transformed section is obtained by replacing the area of geosynthetic reinforcement with an equivalent area of granular material equal to nA_r, where n is the ratio of the elastic modulus of geosynthetics (E_r) and granular material (E_g), known as the modular ratio $(n = E_r/E_g)$ and A_r is the cross sectional area of geosynthetics. To determine the stresses and moments in LTP, the neutral axis must be located first, and it is assumed to be located a distance (h_s) from the compression surface of LTP in the sagging moment regions. The equilibrium of first moment of the compression area of LTP cross section (A_s) and the transformed tensile area of geosynthetics (nA_r) about the neutral axis for the sagging region requires that $(A_s h_s)/2 = nA_r(y_r + y_s)$, which establishes the depth of the neutral axis (h_s). Similarly, from the equilibrium of the first moment of the compression area of LTP cross section (A_h) and the tensile area of geosynthetics (nA_r) about the neutral axis, the depth of the neutral axis (h_h) in the hogging region is determined. The solutions for the resulting quadratic equations to obtain the depth of the neutral axis (h_s or h_h) are obtained as follows:

$$h = \begin{cases} h_s = \sqrt{\left(\frac{S_r}{E_g}\right)\left(\frac{S_r}{E_g} + h + 2y_r\right)} - \frac{S_r}{E_g} & \text{in the sagging moment zone} \quad (3\text{-}2a) \\ h_h = \sqrt{\left(\frac{S_r}{E_g}\right)\left(\frac{S_r}{E_g} + h - 2y_r\right)} - \frac{S_r}{E_g} & \text{in the hogging moment zone} \quad (3\text{-}2b) \end{cases}$$

After locating the neutral axis the equivalent bending stiffness and shear stiffness of the granular layer with geosynthetics are calculated following the procedure proposed by Cowper 1966 and Yin 2000a.

$$D = \begin{cases} D_s = E_g I_s + S_r (y_r + y_s)^2 & \text{in the sagging moment zone} \quad (3\text{-}3a) \\ D_h = E_g I_h + S_r (y_h - y_r)^2 & \text{in the hogging moment zone} \quad (3\text{-}3b) \end{cases}$$

and

$$C = C_s = C_h = k_{sc} \left[\frac{E_g h}{2(1+\upsilon_g)} + \frac{S_r}{2(1+\upsilon_r)} \right] \text{in sagging and hogging moment zones} \quad (3\text{-}4)$$

where h is the thickness of LTP when LTP is not cracked; y_r is the location of geosynthetic reinforcement from the centroid axis as shown in Figure 3.4a; υ_g and υ_r are the Poisson's ratio of granular material and geosynthetics in LTP, respectively; S_r is the tensile stiffness of the geosynthetic reinforcement; D_s and D_h are the bending stiffness of LTP within the sagging and hogging bending moment sections, respectively; C_s and C_h are the shear stiffness of LTP for the sagging and hogging bending moment regions, respectively; $I_s \left(= {h_s}^3/3\right)$ and $I_h \left(= {h_h}^3/3\right)$ are the second moment of inertia of the granular materials about the neutral axis within the sagging and hogging bending moment sections, respectively; y_s and y_h are the distance between neutral axis and centroid axis of LTP within the sagging and hogging bending moment sections, respectively as shown in Figure 3.4b and Figure 3.4c; and k_{sc} is the shear correction coefficient suggested by Cowper 1966, Hutchinson 2001, Gere and Timoshenko 1961, and Wang 1995 for the rectangular cross section of a beam.

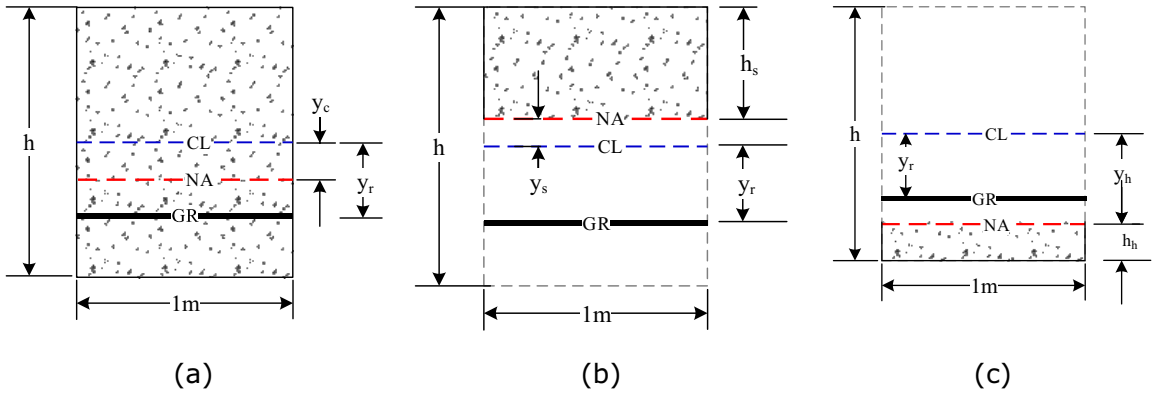

Figure 3.4. Different cross sections of LTP when: (a) uncracked; (b) tension at bottom (Sections II and III); and (c) tension at top (Section I).

3.3.2. Formulation for Load transfer Platform on Soft Soil

Figure 3.5b shows an infinitesimal LTP element with a constant cross section. LTP is supported by soil consisting of normal pressure of $q(x)$ at LTP-soil interface, while subjected to transverse pressure loading $p(x)$. From the equilibrium of vertical forces applied on an infinitesimal element, the followings basic differential equations can be obtained (Timoshenko, 1921).

$$D\frac{d^2\theta(x)}{dx^2} + C\frac{dw(x)}{dx} - C\theta(x) = 0 \tag{3-5}$$

and

$$C\frac{d\theta(x)}{dx} - C\frac{d^2w(x)}{dx^2} + q(x) = p(x) \tag{3-6}$$

Employing Eqs.(3-5) and (3-6), the differential equation governing the deflected shape of a transversely loaded LTP resting on soft soil foundation under the plane strain condition can be obtained as follows (Timoshenko, 1921):

$$D\frac{d^4w(x)}{dx^4} - \frac{D}{C}\frac{d^2q(x)}{dx^2} + q(x) \;= p(x) - \frac{D}{C}\frac{d^2p(x)}{dx^2} \tag{3-7}$$

where $w(x)$ is the transverse deformation of the centroid axis of LTP; $\theta(x)$ is the rotation angle of the cross section of LTP about its neutral axis; and D and C are the flexural and the transverse shear rigidity values for the uncracked LTP, respectively.

Fourier series is utilised to consider the most general case for the distribution of vertical loading. Hence, $p(x)$ considers the symmetric and asymmetric types of distributed loading on LTP over a length of s' between the two adjacent columns, so $p(x)$ can be described as:

$$p(x) = P_0 + \sum_{m=1}^{m=\infty}\left[P_m \cos\left(\frac{2m\pi x}{s'}\right) + Q_m \sin\left(\frac{2m\pi x}{s'}\right)\right] \tag{3-8}$$

where

$$P_0 = \frac{1}{s'}\int_0^{s'} f(x)\,dx \qquad \text{for} \quad m = 0 \tag{3-9a}$$

$$\left.\begin{aligned} P_m &= \frac{2}{s'}\int_0^{s'} f(x)\cos\left(\frac{2m\pi x}{s'}\right)dx \\ Q_m &= \frac{2}{s'}\int_0^{s'} f(x)\sin\left(\frac{2m\pi x}{s'}\right)dx \end{aligned}\right\} \qquad \text{for} \quad m \neq 0 \tag{3-9b}$$

According to the principal of Terzaghi's effective stress theory (1943) and considering the proposed nonlinear load-settlement response of the soft soil as stated in Eq. (3-1), the reaction of soft soil at LTP-soil interface $q(x)$ can be expressed as:

$$q(x) = \begin{cases} q_1(x) = q_2(x) = \dfrac{k_{0s}w(x,t)}{U} & \text{when} \quad x \in [0, r_2] \text{ or } x \in [r_3, s'] \quad (3\text{-}10a) \\ q_3(x) = \dfrac{(k_{0s}-k_{1s})\hat{w}}{U} + \dfrac{k_{1s}w(x,t)}{U} & \text{when} \quad x \in [r_2, r_3] \quad (3\text{-}10b) \end{cases}$$

where U is the average degree of consolidation of the soft soil; t is time; and $q_1(x)$, $q_2(x)$, and $q_3(x)$ are illustrated in Figure 3.5b.

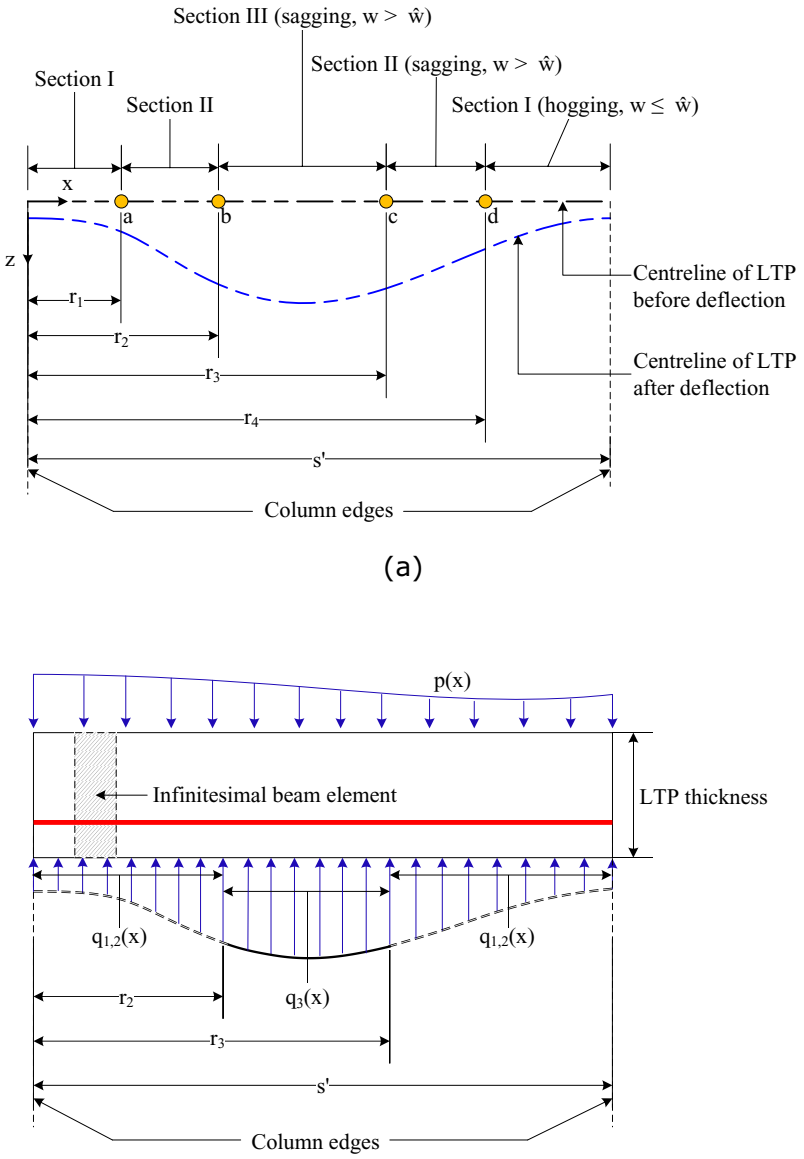

Figure 3.5. Load transfer platform showing: (a) different sections in LTP and (b) pressure distribution in LTP.

By substituting Eqs. (3-8) and (3-10a) into Eq. (3-7), the governing differential equation for the vertical displacement of LTP on a soft soil foundation, when $x \in [0, r_1]$ or $x \in [r_4, s']$ can be obtained as:

$$D_h \frac{d^4 w_1(x,t)}{dx^4} - \left(\frac{D_h k_{0s}}{C_h U}\right) \frac{d^2 w_1(x,t)}{dx^2} + \left(\frac{k_{0s}}{U}\right) w_1(x,t) = P_0 + \qquad (3\text{-}11a)$$

$$\sum_{m=1}^{m=\infty}\left\{P_m\left[1+\frac{D_h}{C_h}\left(\frac{2m\pi}{s\prime}\right)^2\right]\cos\left(\frac{2m\pi x}{s\prime}\right)+Q_m\left[1+\frac{D_h}{C_h}\left(\frac{2m\pi}{s\prime}\right)^2\right]\sin\left(\frac{2m\pi x}{s\prime}\right)\right\}$$

Similarly, the governing differential equation for LTP on a soft soil foundation when $x \in [r_1, r_2]$ or $x \in [r_3, r_4]$ can be expressed as:

$$D_s\frac{d^4w_2(x,t)}{dx^4}-\left(\frac{D_s k_{0s}}{C_s U}\right)\frac{d^2w_2(x,t)}{dx^2}+\left(\frac{k_{0s}}{U}\right)w_2(x,t)=P_0+$$

$$\sum_{m=1}^{m=\infty}\left\{P_m\left[1+\frac{D_s}{C_s}\left(\frac{2m\pi}{s\prime}\right)^2\right]\cos\left(\frac{2m\pi x}{s\prime}\right)+Q_m\left[1+\frac{D_s}{C_s}\left(\frac{2m\pi}{s\prime}\right)^2\right]\sin\left(\frac{2m\pi x}{s\prime}\right)\right\} \quad (3\text{-}11b)$$

Correspondingly, the governing differential equation for LTP on a soft soil foundation when $x \in [r_2, r_3]$ can be written as:

$$D_s\frac{d^4w_3(x,t)}{dx^4}-\left(\frac{D_s k_{0s}}{C_s U}\right)\frac{d^2w_3(x,t)}{dx^2}+\left(\frac{k_{1s}}{U}\right)w_3(x,t)=\frac{(k_{1s}-k_{0s})\hat{w}}{U}+P_0+$$

$$\sum_{m=1}^{m=\infty}\left\{P_m\left[1+\frac{D_s}{C_s}\left(\frac{2m\pi}{s\prime}\right)^2\right]\cos\left(\frac{2m\pi x}{s\prime}\right)+Q_m\left[1+\frac{D_s}{C_s}\left(\frac{2m\pi}{s\prime}\right)^2\right]\sin\left(\frac{2m\pi x}{s\prime}\right)\right\} \quad (3\text{-}11c)$$

3.4. Solutions of Governing Differential Equations

The governing differential equations (Eqs. (3-11a)-(3-11c)) are fourth order ordinary, linear, and nonhomogeneous equations with a number of constant coefficients. To obtain general solutions for the governing differential equations, first auxiliary or complementary equations to the homogeneous equations are solved. The auxiliary or complementary equations to the homogeneous equations can be expressed in a generalised form as stated in Eq. (3-12) and plays an important role in the solution of the original nonhomogeneous equations (Eqs. (3-11a)-(3-11c)) with roots λ_1, λ_2, λ_3, and λ_4.

$$D\lambda^4-\left(\frac{Dk_s}{CU}\right)\lambda^2+\frac{k_s}{U}=0 \quad (3\text{-}12)$$

where D and C are the flexural and the transverse shear rigidity values for LTP, respectively; U is the average degree of consolidation of the soft soil; and k_s is the modulus of subgrade reaction for the soft soil foundation. Since λ_1 to λ_4 are the four roots of Eq. (3-12), the roots are found by using the quadratic formula as follows:

$$\lambda_1 = +\sqrt{\frac{\frac{Dk_s}{CU} + \sqrt{\left(\frac{Dk_s}{CU}\right)^2 - \left(\frac{4Dk_s}{U}\right)}}{2D}}\ ; \qquad \lambda_2 = -\sqrt{\frac{\frac{Dk_s}{CU} + \sqrt{\left(\frac{Dk_s}{CU}\right)^2 - \left(\frac{4Dk_s}{U}\right)}}{2D}};$$

$$\lambda_3 = +\sqrt{\frac{\frac{Dk_s}{CU} - \sqrt{\left(\frac{Dk_s}{CU}\right)^2 - \left(\frac{4Dk_s}{U}\right)}}{2D}}\ ; \quad \text{and} \quad \lambda_4 = -\sqrt{\frac{\frac{Dk_s}{CU} - \sqrt{\left(\frac{Dk_s}{CU}\right)^2 - \left(\frac{4Dk_s}{U}\right)}}{2D}} \tag{3-13}$$

According to the sign of the discriminant shown in Eq. (3-13), there will be three distinguished cases, as stated in Eq. (3-14).

$$\left(\frac{Dk_s}{CU}\right)^2 - \left(\frac{4Dk_s}{U}\right) \gtreqless 0 \tag{3-14}$$

Thus, there will be three forms for the general solution of Eq. (3-12) that will correspond to the following three cases:

- λ_1 to λ_4 are real and distinct when $(Dk_s/CU)^2 - (4Dk_s/U) > 0$ i.e. $k_s > 4C^2U/D$,
- λ_1 to λ_4 are real and equal when $(Dk_s/CU)^2 - (4Dk_s/U) = 0$ i.e. $k_s = 4C^2U/D$, and
- λ_1 to $\lambda_4$are conjugate complex when $(Dk_s/CU)^2 - (4Dk_s/U) < 0$ i.e. $k_s < 4C^2U/D$.

Since in real cases the underneath soft soil is not as stiff as LTP, the solution corresponding to $k_s < 4C^2U/D$ would be applicable in this study so the roots can be expressed as: $\lambda_1 = \vartheta_j + i\delta_j$, $\lambda_2 = \vartheta_j - i\delta_j$, $\lambda_3 = -\vartheta_j + i\delta_j$, and $\lambda_4 = -\vartheta_j - i\delta_j$. where

$$\begin{Bmatrix} \vartheta_1 = \sqrt{\sqrt{\left(\frac{k_{0s}}{4D_hU}\right)} + \frac{k_{0s}}{4C_hU}} \\ \vartheta_2 = \sqrt{\sqrt{\frac{k_{0s}}{4D_sU}} + \frac{k_{0s}}{4C_sU}} \\ \vartheta_3 = \sqrt{\sqrt{\frac{k_{1s}}{4D_sU}} + \frac{k_{1s}}{4C_sU}} \end{Bmatrix} \quad \text{and} \quad \begin{Bmatrix} \delta_1 = \sqrt{\sqrt{\frac{k_{0s}}{4D_hU}} - \frac{k_{0s}}{4C_hU}} \\ \delta_2 = \sqrt{\sqrt{\frac{k_{0s}}{4D_sU}} - \frac{k_{0s}}{4C_sU}} \\ \delta_3 = \sqrt{\sqrt{\frac{k_{1s}}{4D_sU}} - \frac{k_{1s}}{4C_sU}} \end{Bmatrix} \tag{3-15}$$

j = 1 to 3 denotes Sections I to III, respectively. Considering that y_{a1} to y_{a4}, y_{b1} to y_{b4}, and y_{c1} to y_{c4} are the solutions for Eqs. Eqs. (3-11a)-(3-11c) and a_1 to a_4, b_1 to b_4, and c_1 to c_4 are constants, by using the superposition principle, the sum of four solutions would be the solution for the homogenous equation. Therefore, the solutions for the linear homogeneous equations for Section I to Section III can be expressed as:

$$y_{hj} = \begin{cases} a_1y_{a1} + a_2y_{a2} + a_3y_{a3} + a_4y_{a4} & \text{for} \quad x \in [0, r_1] \text{ or } x \in [r_4, s'] \quad (3\text{-}16a) \\ b_1y_{b1} + b_2y_{b2} + b_3y_{b3} + b_4y_{b4} & \text{for} \quad x \in [r_1, r_2] \text{ or } x \in [r_3, r_4] \quad (3\text{-}16b) \\ c_1y_{c1} + c_2y_{c2} + c_3y_{c3} + c_4y_{c4} & \text{for} \quad x \in [r_2, r_3] \quad (3\text{-}16c) \end{cases}$$

where

$$\begin{Bmatrix} y_{a1} = e^{+(\vartheta_1 + i\delta_1)x} \\ y_{a2} = e^{+(\vartheta_1 - i\delta_1)x} \\ y_{a3} = e^{-(\vartheta_1 + i\delta_1)x} \\ y_{a4} = e^{-(\vartheta_1 - i\delta_1)x} \end{Bmatrix}; \begin{Bmatrix} y_{b1} = e^{+(\vartheta_2 + i\delta_2)x} \\ y_{b2} = e^{+(\vartheta_2 - i\delta_2)x} \\ y_{b3} = e^{-(\vartheta_2 + i\delta_2)x} \\ y_{b4} = e^{-(\vartheta_2 - i\delta_2)x} \end{Bmatrix}; \text{ and } \begin{Bmatrix} y_{c1} = e^{+(\vartheta_3 + i\delta_3)x} \\ y_{c2} = e^{+(\vartheta_3 - i\delta_3)x} \\ y_{c3} = e^{-(\vartheta_3 + i\delta_3)x} \\ y_{c4} = e^{-(\vartheta_3 - i\delta_3)x} \end{Bmatrix} \tag{3-17}$$

To obtain general solutions to Eqs. (3-11a) - (11c), the particular solutions (y_p) of Eqs. (3-11a)-(11c) must be found, so in the next step, a trial forms for the particular integral indicated in Eqs.(3-18) are assumed for the three differential equations with different constants.

$$y_{pj} = \begin{cases} A_1 \cos(2m\pi x/s') + B_1 \sin(2m\pi x/s') & \text{for} \quad x \in [0, r_1] \text{ or } x \in [r_4, s'] \quad (3\text{-}18a) \\ A_2 \cos(2m\pi x/s') + B_2 \sin(2m\pi x/s') & \text{for} \quad x \in [r_1, r_2] \text{ or } x \in [r_3, r_4] \quad (3\text{-}18b) \\ A_3 \cos(2m\pi x/s') + B_3 \sin(2m\pi x/s') & \text{for} \quad x \in [r_2, r_3] \quad (3\text{-}18c) \end{cases}$$

These trial functions are then substituted into the corresponding differential equations and the constants that result in a particular solution (y_p) are obtained. Thus, the following expressions are obtained for the particular solutions:

$$y_{pj} = \begin{cases} \frac{UP_0}{k_{0s}} + \sum_{m=1}^{m=\infty} \left[p_{m1} \cos\left(\frac{2m\pi x}{s'}\right) + q_{m1} \sin\left(\frac{2m\pi x}{s'}\right) \right] & (3\text{-}19a) \\ \frac{UP_0}{k_{0s}} + \sum_{m=1}^{m=\infty} \left[p_{m2} \cos\left(\frac{2m\pi x}{s'}\right) + q_{m2} \sin\left(\frac{2m\pi x}{s'}\right) \right] & (3\text{-}19b) \\ \frac{\hat{w}(k_{1s} - k_{0s})}{k_{1s}} + \frac{UP_0}{k_{1s}} + \sum_{m=1}^{m=\infty} \left[p_{m3} \cos\left(\frac{2m\pi x}{s'}\right) + q_{m3} \sin\left(\frac{2m\pi x}{s'}\right) \right] & (3\text{-}19c) \end{cases}$$

where

$$\left.\begin{array}{l} p_{m1} = \dfrac{P_m\left[1+\left(\frac{2m\pi}{s'}\right)^2 \frac{D_h}{C_h}\right]}{D_h\left(\frac{2m\pi}{s'}\right)^4 + \left(\frac{2m\pi}{s'}\right)^2 \frac{D_h k_{0s}}{C_h U} + \frac{k_{0s}}{U}} \\ p_{m2} = \dfrac{P_m\left[1+\left(\frac{2m\pi}{s'}\right)^2 \frac{D_s}{C_s}\right]}{D_{b,s}\left(\frac{2m\pi}{s'}\right)^4 + \left(\frac{2m\pi}{s'}\right)^2 \frac{k_{0s} D_s}{U C_s} + \frac{k_{0s}}{U}} \\ p_{m3} = \dfrac{P_m\left[1+\left(\frac{2m\pi}{s'}\right)^2 \frac{D_s}{C_s}\right]}{D_s\left(\frac{2m\pi}{s'}\right)^4 + \left(\frac{2m\pi}{s'}\right)^2 \frac{k_{1s} D_s}{U C_s} + \frac{k_{1s}}{U}} \end{array}\right\}, \left\{\begin{array}{l} q_{m1} = \dfrac{Q_m\left[1+\left(\frac{2m\pi}{s'}\right)^2 \frac{D_h}{C_h}\right]}{D_h\left(\frac{2m\pi}{s'}\right)^4 + \left(\frac{2m\pi}{s'}\right)^2 \frac{D_h k_{0s}}{C_h U} + \frac{k_{0s}}{U}} \\ q_{m2} = \dfrac{Q_m\left[1+\left(\frac{2m\pi}{s'}\right)^2 \frac{D_s}{C_s}\right]}{D_s\left(\frac{2m\pi}{s'}\right)^4 + \left(\frac{2m\pi}{s'}\right)^2 \frac{k_{0s} D_s}{U C_s} + \frac{k_{0s}}{U}} \\ q_{m3} = \dfrac{Q_m\left[1+\left(\frac{2m\pi}{s'}\right)^2 \frac{D_s}{C_s}\right]}{D_s\left(\frac{2m\pi}{s'}\right)^4 + \left(\frac{2m\pi}{s'}\right)^2 \frac{k_{1s} D_s}{U C_s} + \frac{k_{1s}}{U}} \end{array}\right\} \quad (3\text{-}20)$$

By using the superposition principle, the homogeneous solution is combined with the particular solution to determine the following solutions for Eqs. (3-11a)-(3-11c):

$$w_j(x,t) = \begin{cases} y_{h1} + y_{p1} & \text{for} \quad x \in [0, r_1] \text{ or } x \in [r_4, s'] \quad (3\text{-}21a) \\ y_{h2} + y_{p2} & \text{for} \quad x \in [r_1, r_2] \text{ or } x \in [r_3, r_4] \quad (3\text{-}21b) \\ y_{h3} + y_{p3} & \text{for} \quad x \in [r_2, r_3] \quad (3\text{-}21c) \end{cases}$$

Once the deflections of LTP (w_j) are obtained using Eqs. (3-21a)- (3-21c), the rotational angles of cross sections of LTP (θ_j), the shear forces generated in LTP (V_j), the bending moments developed in LTP (M_j), and the tension mobilised in the geosynthetics (T_j) for each section can be obtained as set out in the following sections. It can be noted that j = 1 to 3 represents Sections I to III, respectively.

3.4.1. Rotation of LTP

By rearranging the two basic equations of Timoshenko beam on an elastic medium, as stated in Eqs. (3-5) and (3-6), the rotation of the cross section of the beam (θ) with respect to the neutral axis can be expressed as follows:

$$\theta(x) = \frac{D}{C}\left[\frac{d^3w(x)}{dx^3} + \frac{1}{C}\frac{dp(x)}{dx} - \frac{1}{C}\frac{dq(x)}{dx}\right] + \frac{dw(x)}{dx} \tag{3-22}$$

where D and C are the flexural and the transverse shear rigidity values for the beam, respectively; $p(x)$ and $q(x)$ are the transverse loading and the contact pressure, respectively.

By substituting Eqs.(3-8), (3-10), and (3-21) into Eq. (3-22), the governing equation for rotation of the cross section of LTP when $x \in [0, r_1]$ or $x \in [r_4, s']$ can be written as:

$$\begin{aligned}\theta_1(x,t) &= e^{\vartheta_1 x}(a_5 \cos\delta_1 x + a_6 \sin\delta_1 x) + e^{-\vartheta_1 x}(a_7 \cos\delta_1 x + a_8 \sin\delta_1 x) \\ &+ \sum_{m=1}^{m=\infty}\left\{\left[\frac{D_h}{C_h}\left(\frac{2m\pi}{s'}\right)^2 - \left(1 - \frac{k_{0s}D_h}{UC_h{}^2}\right)\right]p_{m1} - \frac{D_h}{C_h{}^2}P_m\right\}\left(\frac{2m\pi}{s'}\right)\sin\left(\frac{2m\pi x}{s'}\right) \\ &- \sum_{m=1}^{m=\infty}\left\{\left[\frac{D_h}{C_h}\left(\frac{2m\pi}{s'}\right)^2 - \left(1 - \frac{k_{0s}D_h}{UC_h{}^2}\right)\right]q_{m1} - \frac{D_h}{C_h{}^2}Q_m\right\}\left(\frac{2m\pi}{s'}\right)\cos\left(\frac{2m\pi x}{s'}\right)\end{aligned} \tag{3-23a}$$

In a similar way, the governing equation for the rotation of the cross section of LTP on soft soil when $x \in [r_1, r_2]$ or $x \in [r_3, r_4]$ can be expressed as:

$$\theta_2(x,t) = e^{\vartheta_2 x}(b_5 \cos\delta_2 x + b_6 \sin\delta_2 x) + e^{-\vartheta_2 x}(b_7 \cos\delta_2 x + b_8 \sin\delta_2 x)$$
$$+\sum_{m=1}^{m=\infty}\left\{\left[\frac{D_s}{C_s}\left(\frac{2m\pi}{s'}\right)^2 - \left(1-\frac{k_{0s}D_s}{UC_h{}^2}\right)\right]p_{m2} - \frac{D_s}{C_h{}^2}P_m\right\}\left(\frac{2m\pi}{s'}\right)\sin\left(\frac{2m\pi x}{s'}\right)$$
$$-\sum_{m=1}^{m=\infty}\left\{\left[\frac{D_s}{C_s}\left(\frac{2m\pi}{s'}\right)^2 - \left(1-\frac{k_{0s}D_s}{UC_s{}^2}\right)\right]q_{m2} - \frac{D_s}{C_s{}^2}Q_m\right\}\left(\frac{2m\pi}{s'}\right)\cos\left(\frac{2m\pi x}{s'}\right) \quad (3\text{-}23b)$$

Furthermore, the governing equation for the rotation of the cross section of LTP on soft soil when $x \in [r_2, r_3]$ can be stated as:

$$\theta_3(x,t) = e^{\vartheta_3 x}(c_5 \cos\delta_3 x + c_6 \sin\delta_3 x) + e^{-\vartheta_3 x}(c_7 \cos\delta_3 x + c_8 \sin\delta_3 x)$$
$$+\sum_{m=1}^{m=\infty}\left\{\left[\frac{D_s}{C_s}\left(\frac{2m\pi}{s'}\right)^2 - \left(1-\frac{k_{1s}D_s}{UC_h{}^2}\right)\right]p_{m3} - \frac{D_s}{C_h{}^2}P_m\right\}\left(\frac{2m\pi}{s'}\right)\sin\left(\frac{2m\pi x}{s'}\right)$$
$$-\sum_{m=1}^{m=\infty}\left\{\left[\frac{D_s}{C_s}\left(\frac{2m\pi}{s'}\right)^2 - \left(1-\frac{k_{1s}D_s}{UC_s{}^2}\right)\right]q_{m3} - \frac{D_s}{C_s{}^2}Q_m\right\}\left(\frac{2m\pi}{s'}\right)\cos\left(\frac{2m\pi x}{s'}\right) \quad (3\text{-}23c)$$

where

$$a_5 = a_1A_1 + a_2B_1\ ; a_6 = a_2A_1 - a_1B_1; a_7 = a_4B_1 - a_3A_1; a_8 = -a_3B_1 - a_4A_1; \quad (3\text{-}24a)$$
$$b_5 = b_1A_2 + b_2B_2; b_6 = b_2A_2 - b_1B_2; b_7 = b_4B_2 - b_3A_2; b_8 = -b_3B_2 - b_4A_2; \quad (3\text{-}24b)$$
$$c_5 = c_1A_3 + c_2B_3\ ; c_6 = c_2A_3 - c_1B_3;\ c_7 = c_4B_3 - c_3A_3; c_8 = -c_3B_3 - c_4A_3 \quad (3\text{-}24c)$$

The following equations can be used to obtain the parameters $A_1$to A_3, B_1 to B_3, C_1 to C_3, and $D_1$to D_3 in Eqs. (3-24a)-(3-24c).

$$\left.\begin{aligned} A_1 &= \vartheta_1\left(\frac{D_hC_1}{C_h} + 1 - \frac{D_hk_{0s}}{C_h{}^2U}\right)\\ A_2 &= \vartheta_2\left(\frac{D_sC_2}{C_s} + 1 - \frac{D_sk_{0s}}{C_s{}^2U}\right)\\ A_3 &= \vartheta_3\left(\frac{D_sC_3}{C_s} + 1 - \frac{D_sk_{1s}}{C_s{}^2U}\right)\end{aligned}\right\};\quad \left.\begin{aligned} B_1 &= \delta_1\left(\frac{D_hD_1}{C_h} + 1 - \frac{D_hk_{0s}}{C_h{}^2U}\right)\\ B_2 &= \delta_2\left(\frac{D_sD_2}{C_s} + 1 - \frac{D_sk_{0s}}{C_s{}^2U}\right)\\ B_3 &= \delta_3\left(\frac{D_sD_3}{C_s} + 1 - \frac{D_sk_{1s}}{C_s{}^2U}\right)\end{aligned}\right\} \quad (3\text{-}25a)$$

and

$$\left.\begin{matrix} C_1 = \vartheta_1{}^2 - 3\delta_1{}^2 \\ C_2 = \vartheta_2{}^2 - 3\delta_2{}^2 \\ C_3 = \vartheta_3{}^2 - 3\delta_3{}^2 \end{matrix}\right\}; \quad \left.\begin{matrix} D_1 = 3\vartheta_1{}^2 - \delta_1{}^2 \\ D_2 = 3\vartheta_2{}^2 - \delta_2{}^2 \\ D_3 = 3\vartheta_3{}^2 - \delta_3{}^2 \end{matrix}\right\} \tag{3-25b}$$

3.4.2. Bending Moment and Shear Force in LTP

Considering the variation of the rotation angle (θ) of the beam element with flexural rigidity D at any section-x, the bending moment (M) can be expresses as follows:

$$M(x) = -D\frac{d\theta(x)}{dx} \tag{3-26}$$

By substituting Eq. (3-23a) in Eq. (3-26), the governing equation for the bending moment in LTP on soft soil in Section I can be written as:

$$\begin{aligned} M_1(x,t) = -D_h[&e^{\vartheta_1 x}(a_9 \cos\delta_1 x + a_{10}\sin\delta_1 x) + e^{-\vartheta_1 x}(a_{11}\cos\delta_1 x + \\ &a_{12}\sin\delta_1 x) + \sum_{m=1}^{m=\infty}\left\{\left[\frac{D_h}{C_h}\left(\frac{2m\pi}{s'}\right)^2 - \left(1 - \frac{k_{0s}D_h}{UC_h{}^2}\right)\right]p_{m1} - \right. \\ &\left.\frac{D_h}{C_h{}^2}P_m\right\}\left(\frac{2m\pi}{s'}\right)^2\cos\left(\frac{2m\pi x}{s'}\right) - \sum_{m=1}^{m=\infty}\left\{\left[\frac{D_h}{C_h}\left(\frac{2m\pi}{s'}\right)^2 - \left(1 - \right.\right.\right. \\ &\left.\left.\left.\frac{k_{0s}D_h}{UC_h{}^2}\right)\right]q_{m1} - \frac{D_h}{C_h{}^2}Q_m\right\}\left(\frac{2m\pi}{s'}\right)^2\sin\left(\frac{2m\pi x}{s'}\right)\Bigg] \end{aligned} \tag{3-27a}$$

Similarly, the governing equation for the bending moment in LTP on soft soil in Section II can be stated as:

$$\begin{aligned} M_2(x,t) = -D_s[&e^{\vartheta_2 x}(b_9 \cos\delta_2 x + b_{10}\sin\delta_2 x) + e^{-\vartheta_2 x}(b_{11}\cos\delta_2 x + \\ &b_{12}\sin\delta_2 x) + \sum_{m=1}^{m=\infty}\left\{\left[\frac{D_s}{C_s}\left(\frac{2m\pi}{s'}\right)^2 - \left(1 - \frac{k_{0s}D_s}{UC_s{}^2}\right)\right]p_{m2} - \right. \end{aligned} \tag{3-27b}$$

$$\frac{D_s}{{C_s}^2}P_m\Big\}\left(\frac{2m\pi}{s\prime}\right)^2\cos\left(\frac{2m\pi x}{s\prime}\right)-\sum_{m=1}^{m=\infty}\left\{\left[\frac{D_s}{C_s}\left(\frac{2m\pi}{s\prime}\right)^2-\left(1-\frac{k_{0s}D_s}{U{C_s}^2}\right)\right]q_{m2}-\frac{D_s}{{C_s}^2}Q_m\right\}\left(\frac{2m\pi}{s\prime}\right)^2\sin\left(\frac{2m\pi x}{s\prime}\right)\Big]$$

Also, the governing equation for the bending moment in LTP on soft soil in Section III can be presented as:

$$M_3(x,t)=-D_s[e^{\vartheta_3 x}(b_9\cos\delta_3 x+b_{10}\sin\delta_3 x)+e^{-\vartheta_3 x}(b_{11}\cos\delta_3 x+b_{12}\sin\delta_3 x)+\sum_{m=1}^{m=\infty}\left\{\left[\frac{D_s}{C_s}\left(\frac{2m\pi}{s\prime}\right)^2-\left(1-\frac{k_{1s}D_s}{U{C_s}^2}\right)\right]p_{m3}-\frac{D_s}{{C_s}^2}P_m\Big\}\left(\frac{2m\pi}{s\prime}\right)^2\cos\left(\frac{2m\pi x}{s\prime}\right)-\sum_{m=1}^{m=\infty}\left\{\left[\frac{D_s}{C_s}\left(\frac{2m\pi}{s\prime}\right)^2-\left(1-\frac{k_{1s}D_s}{U{C_s}^2}\right)\right]q_{m3}-\frac{D_s}{{C_s}^2}Q_m\right\}\left(\frac{2m\pi}{s\prime}\right)^2\sin\left(\frac{2m\pi x}{s\prime}\right)\Big] \quad (3\text{-}27c)$$

If C is the transverse shear rigidity for a beam, then the relationship between the shear force (V) and the shear strain (γ) in LTP can be expressed as:

$$V(x)=-C\gamma(x)=C\left[\frac{dw(x)}{dx}-\theta(x)\right] \quad (3\text{-}28)$$

By substituting Eqs. (3-21a)-(3-21c) and (3-23a)-(3-23c) into Eq. (3-28), the governing equation of the shear force developed in LTP on soft soil in Section I can be written as:

$$V_1(x,t)=D_h\{e^{\vartheta_1 x}(a_{13}\cos\delta_1 x+a_{14}\sin\delta_1 x)+e^{-\vartheta_1 x}(a_{15}\cos\delta_1 x+a_{16}\sin\delta_1 x)-\sum_{m=1}^{m=\infty}\left\{\left[\left(\frac{2m\pi}{s\prime}\right)^2+\frac{k_{0s}D_h}{UC_h}\right]p_{m1}-\frac{P_m}{C_h}\right\}\left(\frac{2m\pi}{s\prime}\right)\sin\left(\frac{2m\pi x}{s\prime}\right)+\sum_{m=1}^{m=\infty}\left\{\left[\left(\frac{2m\pi}{s\prime}\right)^2+\frac{k_{0s}D_h}{UC_h}\right]q_{m1}-\frac{Q_m}{C_h}\right\}\left(\frac{2m\pi}{s\prime}\right)\cos\left(\frac{2m\pi x}{s\prime}\right)\Big\} \quad (3\text{-}29a)$$

Similarly, the governing equation of the shear force developed in LTP on soft soil in Section II can be expressed as:

$$V_2(x,t) = D_s\{e^{\vartheta_2 x}(a_{13}\cos\delta_2 x + a_{14}\sin\delta_2 x) + e^{-\vartheta_2 x}(a_{15}\cos\delta_2 x + a_{16}\sin\delta_2 x) - \sum_{m=1}^{m=\infty}\left\{\left[\left(\frac{2m\pi}{s\prime}\right)^2 + \frac{k_{0s}D_s}{UC_s}\right]p_{m2} - \frac{P_m}{C_s}\right\}\left(\frac{2m\pi}{s\prime}\right)\sin\left(\frac{2m\pi x}{s\prime}\right) + \sum_{m=1}^{m=\infty}\left\{\left[\left(\frac{2m\pi}{s\prime}\right)^2 + \frac{k_{0s}D_s}{UC_s}\right]q_{m2} - \frac{Q_m}{C_s}\right\}\left(\frac{2m\pi}{s\prime}\right)\cos\left(\frac{2m\pi x}{s\prime}\right)\right\} \quad (3\text{-}29b)$$

In addition, the governing equation of the shear force developed in LTP on soft soil in Section III can be determined using the equation below.

$$V_3(x,t) = D_s\{e^{\vartheta_3 x}(a_{13}\cos\delta_3 x + a_{14}\sin\delta_3 x) + e^{-\vartheta_3 x}(a_{15}\cos\delta_3 x + a_{16}\sin\delta_3 x) - \sum_{m=1}^{m=\infty}\left\{\left[\left(\frac{2m\pi}{s\prime}\right)^2 + \frac{k_{1s}D_s}{UC_s}\right]p_{m3} - \frac{P_m}{C_s}\right\}\left(\frac{2m\pi}{s\prime}\right)\sin\left(\frac{2m\pi x}{s\prime}\right) + \sum_{m=1}^{m=\infty}\left\{\left[\left(\frac{2m\pi}{s\prime}\right)^2 + \frac{k_{1s}D_s}{UC_s}\right]q_{m3} - \frac{Q_m}{C_s}\right\}\left(\frac{2m\pi}{s\prime}\right)\cos\left(\frac{2m\pi x}{s\prime}\right)\right\} \quad (3\text{-}29c)$$

where

$$a_9 = a_2E_1 - a_1F_1;\ a_{10} = -a_1E_1 - a_2F_1;$$
$$a_{11} = -a_3F_1 - a_4E_1;\ a_{12} = a_3E_1 - a_4F_1 \quad (3\text{-}30a)$$

$$b_9 = b_2E_2 - b_1F_2\ ;\ b_{10} = -b_1E_2 - b_2F_2;$$
$$b_{11} = -b_3F_2 - b_4E_2;\ b_{12} = b_3E_2 - b_4F_2 \quad (3\text{-}30b)$$

$$c_9 = c_2E_3 - c_1F_3\ ;\ c_{10} = -c_1E_3 - c_2F_3;$$
$$c_{11} = -c_3F_3 - c_4E_3;\ c_{12} = c_3E_3 - c_4F_3; \quad (3\text{-}30c)$$

$$a_{13} = -a_1H_1 - a_2G_1;\ a_{14} = a_1G_1 - a_2H_1;$$
$$a_{15} = a_3H_1 - a_4G_1;\ a_{16} = a_3G_1 + a_4H_1; \quad (3\text{-}30d)$$

$$b_{13} = -b_1H_2 - b_2G_2;\ b_{14} = b_1G_2 - b_2H_2;$$
$$b_{15} = b_3H_2 - b_4G_2;\ b_{16} = b_3G_2 + b_4H_2; \quad (3\text{-}30e)$$

$$c_{13} = -c_1H_3 - c_2G_3;\ c_{14} = c_1G_3 - c_2H_3; \quad (3\text{-}30f)$$
$$c_{15} = c_3H_3 - c_4G_3;\ \text{and}\ c_{16} = c_3G_3 + c_4H_3$$

The following equations can be used to obtain the parameters $E_1$to E_3, F_1 to F_3, G_1 to G_3, and $H_1$to H_3 in Eqs. (3-30a) - (3-30 f).

$$E_1 = 2\vartheta_1\delta_1;\ F_1 = \frac{k_{0s}}{2C_hU};\ G_1 = \delta_1\left(\frac{k_{0s}}{C_hU} - D_1\right);\ H_1 = \vartheta_1\left(\frac{k_{0s}}{C_hU} - C_1\right); \quad (3\text{-}31a)$$

$$E_2 = 2\vartheta_2\delta_2;\ F_2 = \frac{k_{0s}}{2C_sU};\ G_2 = \delta_2\left(\frac{k_{0s}}{C_sU} - D_2\right);\ H_2 = \vartheta_2\left(\frac{k_{0s}}{C_sU} - C_2\right); \quad (3\text{-}31b)$$

$$E_3 = 2\vartheta_3\delta_3;\ F_3 = \frac{k_{1s}}{2C_sU};\ G_3 = \delta_3\left(\frac{k_{1s}}{C_sU} - D_3\right);\ \text{and}\ H_3 = \vartheta_3\left(\frac{k_{1s}}{C_sU} - C_3\right) \quad (3\text{-}31c)$$

3.4.3. Tension Mobilised in the Geosynthetics

To obtain the tension mobilised in the geosynthetic reinforcement layer (T) embedded in the granular fill material when cracking phenomenon is not considered, Eq. (3-32) can be used.

$$T(x) = S_r\left\{\sqrt{\left[1 - (y_r - y_c)\frac{d\theta}{dx}\right]^2 + \left(\frac{dw}{dx}\right)^2} - 1\right\} \quad (3\text{-}32)$$

where y_r is the location of the geosynthetic reinforcement measured from the centroid axis of the granular layer; y_c is the distance between the neutral axis and the centroid axis of the granular layer as shown in Figure 3.4a; and S_r is the tensile stiffness of the geosynthetic reinforcement. Therefore, depending on whether the tension cracks are in sagging or hogging bending moment regions, and the modulus of the subgrade reaction of the soft soil, tension mobilised in the geosynthetics embedded in LTP can be expressed as follows.

$$T_j(x,t) = \begin{cases} S_r\left\{\sqrt{\left[1-(y_h-y_r)\frac{d\theta_1(x,t)}{dx}\right]^2+\left(\frac{dw_1(x,t)}{dx}\right)^2}-1\right\} \text{ for Section I} & (3\text{-}33a) \\ S_r\left\{\sqrt{\left[1-(y_s+y_r)\frac{d\theta_2(x,t)}{dx}\right]^2+\left(\frac{dw_2(x,t)}{dx}\right)^2}-1\right\} \text{ for Section II} & (3\text{-}33b) \\ S_r\left\{\sqrt{\left[1-(y_s+y_r)\frac{d\theta_3(x,t)}{dx}\right]^2+\left(\frac{dw_3(x,t)}{dx}\right)^2}-1\right\} \text{for Section III} & (3\text{-}33c) \end{cases}$$

where y_r is the location of the geosynthetic reinforcement measured from the centroid axis of the granular layer; y_s and y_h are the distances between neutral axis and centroid axis of LTP within the sagging and hogging bending moment sections, respectively as shown in Figure 3.4b and Figure 3.4c; S_r is the tensile stiffness of the geosynthetic reinforcement; θ and w are the rotation of the cross section and deflection of LTP, respectively.

3.5. Boundary and Continuity Conditions

There are twelve constants of integration (a_1 to a_4, b_1 to b_4, and c_1 to c_4) and 4 unknown lengths (r_1 to r_4) that should be evaluated using appropriate and sufficient numbers of boundary and continuity conditions. It is assumed that due to embedded geosynthetic reinforcement in LTP, the rotation of LTP at the column supports is zero at those two points. In addition, it is also assumed that at the column support, the shear force developed in LTP is equal to the reaction force, and therefore:

$$\theta_1(x,t)|_{x=0} = 0 \quad (3\text{-}34a)$$

$$V_1(x,t)|_{x=0} = -K_c w_1(x,t)|_{x=0} \quad (3\text{-}34b)$$

$$\theta_3(x,t)|_{x=s'} = 0 \quad (3\text{-}34c)$$

$$V_3(x,t)|_{x=s'} = +K_c w_3(x,t)|_{x=s'} \quad (3\text{-}34d)$$

On the other hand, the loading condition and the cross section of LTP for the left side of point "a" (as shown in Figure 3.5a) are not the same as the right side of point "a" so the deflection and internal forces in LTP beam should be represented by one function for the left side of point

"a" and another function for the right side of point "a". However, the deflection curve and internal forces of LTP is physically continuous at point "a" and therefore the continuity conditions for the deflections and moments are satisfied at "a". Similar continuity conditions are applied at points b, c, and d. Each of these continuity conditions yields to an equation for evaluating the unknowns. The continuity conditions can be summarised as below:

$$w_1(x,t)|_{x=r_1} = w_2(x,t)\big|_{x=r_1} \quad (3\text{-}35a)$$

$$M_1(x,t)|_{x=r_1} = 0 \quad (3\text{-}35b)$$

$$M_2(x,t)|_{x=r_1} = 0 \quad (3\text{-}35c)$$

$$w_2(x,t)|_{x=r_3} = \hat{w} \quad (3\text{-}35d)$$

$$w_3(x,t)|_{x=r_3} = \hat{w} \quad (3\text{-}35e)$$

$$M_2(x,t)|_{x=r_3} = M_3(x,t)|_{x=r_3} \quad (3\text{-}35f)$$

$$w_2(x,t)|_{x=r_2} = \hat{w} \quad (3\text{-}35g)$$

$$w_3(x,t)|_{x=r_2} = \hat{w} \quad (3\text{-}35h)$$

$$M_2(x,t)|_{x=r_2} = M_3(x,t)|_{x=r_2} \quad (3\text{-}35i)$$

$$w_1(x,t)|_{x=r_4} = w_2(x,t)|_{x=r_4} \quad (3\text{-}35j)$$

$$M_1(x,t)|_{x=r_4} = 0 \quad (3\text{-}35k)$$

$$M_2(x,t)|_{x=r_4} = 0 \quad (3\text{-}35l)$$

where K_c is the equivalent modulus of subgrade reaction for a column in a plane strain condition (kN/m). The equivalent modulus of subgrade reaction can be calculated as shown below.

$$K_c = \frac{(k_c)_{pl} A_p}{s} \tag{3-36}$$

where $A_p (= s \times d)$ is the plan area of the column wall; s and d are the spacing and the diameter of the column, respectively; and $(k_c)_{pl}$ is the equivalent spring constant of the columns in plane strain condition. Since in the field, discrete columns are placed in a square or triangular pattern, the equivalent plane strain material stiffness is determined using the relationship suggested by Tan *et al.* (2008) based on matching the stiffness of the column-soil composite system as expressed below:

$$(k_c)_{pl}(a_r)_{pl} = (k_c)_{ax}(a_r)_{ax} + (k_s)_{ax}\left[(a_r)_{pl} - (a_r)_{ax}\right] \tag{3-37}$$

Subscripts "pl" and "ax" denote plane-strain and axisymmetric conditions, respectively, while a_r is the area replacement ratio, and k_s is the spring constant corresponding to the soft soil. By replacing the expressions of deflections $w_j(x,t)$, rotation of the cross sections $\theta_j(x,t)$, and moments $M_j(x,t)$ from Eqs. (3-21a) - (3-21c), Eqs. (3-23a) - (3-23c), and Eqs. (3-27a) - (3-27 c) respectively into the boundary and the continuity conditions (Eqs.(3-34) - (3-35)) yields sixteen algebraic equations which are summarised in Appendix. Once all the constants of integration and unknown lengths are determined by solving the simultaneous equations, then the deflections $w_j(x,t)$, bending moments $M_j(x,t)$, shear forces $V_j(x,t)$, rotations of LTP $\theta_j(x,t)$, and mobilised tension in the geosynthetics $T_j(x,t)$ at any point in LTP can be determined using Eqs. (3-21a) - (3-21c), Eqs. (3-23a) - (3.23c), Eqs. (3-27a) - (3-27c), Eqs. (3-29a) - (3-29c), and Eqs. (3-33a) -(3-33c). For the sake of convenience and practical use, all the algebraic equations have been programmed in MATLAB R2014b (included in Appendix C) and the results can be presented graphically.

3.6. Model Evaluation and Parametric Study

In this section, a general evaluation of the proposed solution is presented through a parametric study. The effects of column spacing, the thickness of LTP, the degree of consolidation of soft soil, and the tensile stiffness of the geosynthetic reinforcement on the load-settlement response of LTP on column reinforced soft soil are also investigated using the proposed mechanical model. To evaluate the accuracy of the Timoshenko beam theory, the deflections and rotations of LTP beam, the bending moments and shear forces generated in LTP, the tension mobilised in the geosynthetics, and the stress concentration ratio, are compared with the predictions obtained from the Pasternak and Euler-Bernoulli theories. In this study, typical properties of soft estuarine clay similar to Gerringong clay (CH) is adopted to simulate the soft soil, while concrete injected columns (CIC) are used for ground improvement. The typical Oedometer test on this clay reveals the nonlinear stress vs. void ratio relationship as shown in Figure 3.6a. To obtain the modulus of the subgrade reaction of the soft soil, the initial elastic modulus (E_{0s}) and the stiffened elastic modulus (E_{1s}) are determined from the consolidation test data first, and then the initial subgrade modulus (k_{0s}) and stiffened subgrade modulus (k_{1s}) are determined using the procedures described by Selvadurai (1979) for one dimensional consolidation, which are plotted in Figure 3.6b. To make the results comparable, a baseline case with a typical configuration is selected. The design parameters used in this study for the baseline case are summarised in Table 3.1.

Table 3.1. Material properties used in the baseline case

Material	Mechanical element type	Parameters
Soft clay	Terzaghi's spring-dashpot	H_s = 4.5 m, $\hat{w}$ = 0.045 m, U = 100 %, k_{0s} = 225 kN/m^2/m, k_{1s} = 478 kN/m^2/m
CMC	Linear Winkler's springs	d = 0.45 m, s = 2.5 m, H_c = 4.5 m, ν_c = 0.25, E_c = 10,000 MPa
Geosynthetics	Rough elastic membrane	S_r = 2000 kN/m, ν_r = 0.3
Granular fill	Timoshenko beam	h = 0.75 m, E_g = 35 MPa, ν_g = 0.3

For the parametric study, one parameter is changed at one time from the baseline case to investigate the influence of that certain parameter. The variations in the ranges of the parameters mentioned in Table 3.2 are considered to cover the typical ranges observed in real projects for the CICs improved soft soil.

Table 3.2. Values of influencing factors used in the parametric study.

Material	Influencing factor	Range of value
Soft clay	Degree of consolidation, U (%)	10–100 (increment of 10%)
Columns	Spacing, s (m)	1.75–2.5 (increment of 0.15m)
Geosynthetics	Tensile stiffness, S_r (kN/m)	1000–4000 (increment of 1000)
Granular layer	Thickness, h (m)	0.75–1.25 (increment of 0.125m)

Table 3.3 summarizes key calculated parameters used in the study. Since uniformly distributed pressure is the commonly occurring loading condition with embankments, industrial silos, and water tank like structures, this study assumes 200 kPa of uniformly distributed pressure loading acting on LTP. The results of the parametric study are presented in Figure 3.7 to Figure 3.14.

Table 3.3. Calculated parameters of LTP for baseline case.

Parameters		Calculated values for different theories		
		Timoshenko	Euler-Bernoulli	Pasternak
Thickness of LTP in flexure (m)	Sagging (h_s)	0.203	0.203	0.75 (not cracked)
	Hogging (h_h)	0.1	0.1	0.75 (not cracked)
Bending stiffness of LTP (kN-m)	Sagging (D_s)	356	356	Infinity
	Hogging (D_h)	27	27	Infinity
Thickness of LTP in shear (m)	Sagging (h)	0.75	0.75	0.75
	Hogging (h)	10.75	0.75	0.75
Shear stiffness of LTP (kN/m)	Sagging (C_s)	9055	Infinity	9055
	Hogging (C_h)	9055	Infinity	9055

3.6.1. Comparison of Predictions Adopting Different Beam Theories

To evaluate the proposed mechanical model of LTP on columns improved soft soils, the results of the present analysis have been compared with the results simulated LTP as Euler-Bernoulli beam and Pasternak shear layer. Euler-Bernoulli beam theory is applicable to beams experiencing small deflections due to flexure only, which implies that the effect of transverse shear deformation is omitted. Therefore, by assuming the shear stiffness of the beam (C) as infinity, the reinforced Timoshenko beam theory will convert to the reinforced Euler-Bernoulli beam theory. Alternatively, Pasternak shear layer is better suited to structural elements that mainly deform due to shear with negligible flexural deformation. Therefore, by assuming the bending stiffness of the beam (D) as infinity, the reinforced Timoshenko beam theory will transform to the reinforced Pasternak beam theory. In this study, the Timoshenko beam model that considers transverse shear deflections and flexural deformations is used, while the differential equations presented here can readily cover the Euler-Bernoulli and Pasternak cases.

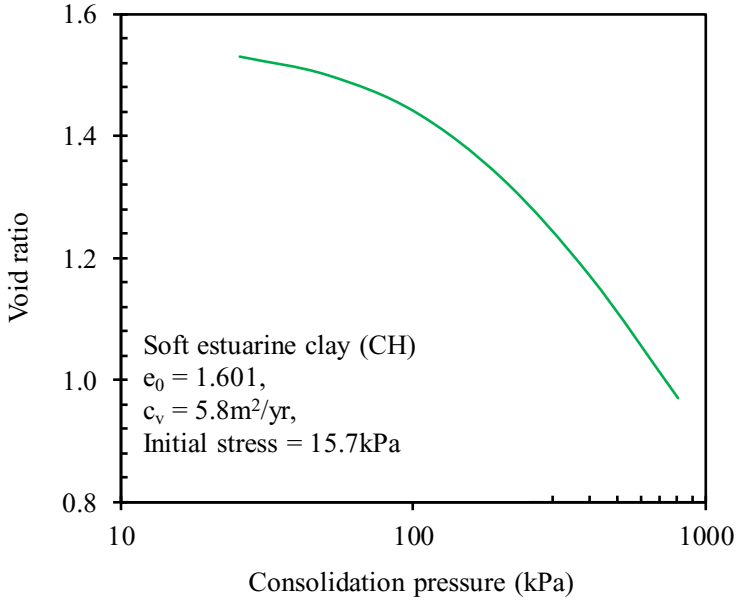

(a)

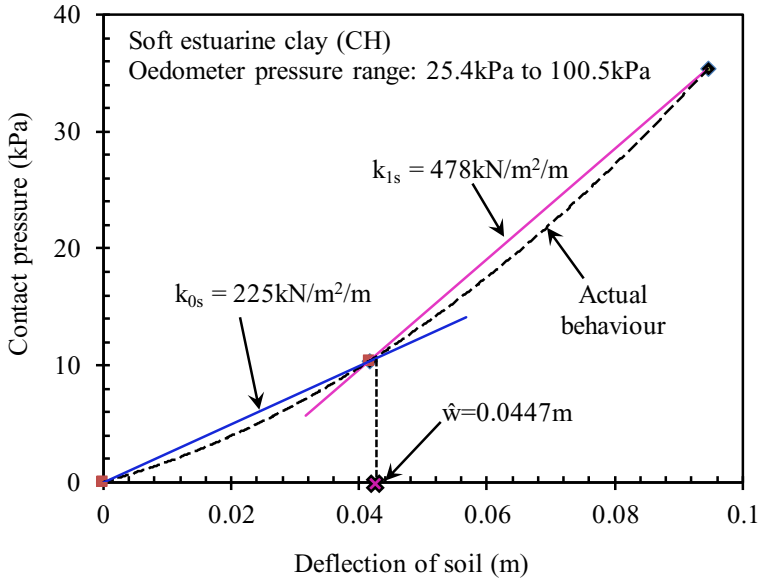

(b)

Figure 3.6. Stress-strain behaviour of soft estuarine clay (CH): (a) stress-displacement curve from Oedometer test and (b) calculated modulus of subgrade reaction for soft soil.

Figure 3.7a illustrates the parameters used for the baseline case. Figure 3.7b shows a comparison of results from the present study using Timoshenko beam theory with Euler-Bernoulli and Pasternak theories. There are notable variations between the results from the proposed model, using the Timoshenko, the Euler-Bernoulli, and the Pasternak theories, and

furthermore, adopting the Timoshenko theory results in the largest deflection of LTP compared to the Euler-Bernoulli and the Pasternak models. It should be noted that the tension cracks in LTP are propagated because of rotation of the cross section of LTP due to bending. Since the load transfer mechanism in the Pasternak shear layer is only due to transverse shear, the cracking phenomenon of LTP cannot be considered in this study for Pasternak model and therefore the actual thickness of LTP (h) is used for the analysis. Thus, properties of the cracked section of LTP cannot be considered in Pasternak model. Flexural deformation is also ignored due to the underlying assumption of infinite flexural rigidity in Pasternak theory, so with the Pasternak theory, the combined effect of uncracked LTP and the absence of deformation due to bending results in the smallest deflection of LTP between the three beam theories.

With the Euler-Bernoulli model, since LTP is deformed due to bending, the cracked section of LTP should be considered, however, the thickness of the cracked LTP in the absence of deformation due to transverse shear, results in higher and lower LTP deflection prediction compared to the Pasternak and Timoshenko models, respectively. Since LTP simulated with the Timoshenko beam allows the effect of transverse shear deformation, it relaxes the normality assumption where it is assumed that the plane sections remain perpendicular to the deformed centreline. The relaxation of this assumption allows for an additional rotation (γ) to the bending slope (θ). Therefore, the predicted displacements of LTP by adopting the Timoshenko theory are always somewhat greater than the corresponding predictions based on the traditional planar assumption (i.e. Euler-Bernoulli and Pasternak theories). In summary, in case of LTP idealised as Pasternak shear layer, the thickness of LTP (not cracked) and infinite flexural rigidity of LTP are the two governing factors which result in less deflection of LTP when compare to Timoshenko beam. Whereas, in case of LTP idealised as Euler-Bernoulli beam, the infinite shear rigidity of LTP is the only governing factor which results in less deflection of

LTP when compare to Timoshenko beam. However, in Timoshenko beam, bending and shear deformations of LTP are taken into account simultaneously with the cracked properties of LTP. Therefore, because of the cracking phenomenon, the combination of the deflections of LTP considering Pasternak shear layer and Euler-Bernoulli model would not be equal to that of Timoshenko beam. For example, at non-dimensional thickness of load transfer platform (h/s) equal to 0.3 and column spacing (s/d) equal to 5.5, the maximum predicted transverse deformation of LTP adopting the Timoshenko theory is approximately 1.2 and 3.4 times larger than corresponding values respectively, when the Euler-Bernoulli and the Pasternak theories are used.

Figure 3.7c shows the typical profiles of the slope of the centreline of deflected LTP (dw/dx) considering LTP as Timoshenko beam, Euler-Bernoulli beam, and Pasternak shear layer. In case of Timoshenko beam, slope of the centreline of deflected LTP or total angular displacement (dw/dx) are induced by bending and shear combined. Whereas, in Euler-Bernoulli beam, angular displacement occurs due to bending only and in Pasternak shear layer, angular displacement is due to shear only. Variations between the predictions from the different beam theories are noteworthy. For example, at non-dimensional thickness of load transfer platform (h/s) equal to 0.3 and column spacing (s/d) equal to 5.5, the maximum slope of the centreline of deflected LTP by adopting Timoshenko theory is almost 1.2 and 2.6 times greater than the corresponding values respectively, when Euler-Bernoulli and Pasternak theories are adopted because in the Timoshenko beam, internal shear stresses are developed within LTP along with bending action. These stresses cause the cross sections (initially perpendicular to the longitudinal axis of LTP) to distort as LTP beam deflects under a transverse loading. Thus, adopting the Timoshenko theory, the slope of the centreline of a deflected LTP is always somewhat greater than the predictions considering the traditional planar assumption (e.g. Euler-Bernoulli). This additional component of distortion is referred to as shear strain (γ), while the

primary component of rotation is called angular displacement (θ) due to bending. Therefore, the shear angle (or loss of slope) can be calculated as $\gamma = (dw/dx) - \theta$. In the case of Euler-Bernoulli beam model, since the deformed centreline of LTP is perpendicular to the cross section, rotation of the cross section due to bending is equal to the slope of the centreline (i.e. $dw/dx = \theta$). Similarly, for Pasternak shear layer, rotation of the cross section due to shear (γ) is equal to the slope of the centreline of the deflected LTP (i.e. $dw/dx = \gamma$). However, implementing the Timoshenko theory means that the rotation of the centreline would no longer be equal to the slope of the centreline (i.e. $dw/dx \neq \theta$; $dw/dx \neq \gamma$).

Figure 3.8a illustrates the parameters adopted for the baseline case. A comparison of predicted bending moments, when LTP is simulated as Timoshenko beam, Euler-Bernoulli beam, and Pasternak shear layer for an applied uniformly distributed load of 200 kPa is shown in Figure 3.8b. It should be noted that since the Pasternak theory omits flexural deformation, the stresses and distortion in the cross section due to flexure would also be omitted. However, the moment is recovered from the equilibrium: $M = \int V\,dx$, while V is the shear force in LTP. As expected, the diagrams in Figure 3.8b showing the shape of the bending moment for all three beam theories are parabolic and are symmetric about the line of symmetry. Maximum negative bending moments (hogging) occur at the support locations whereas the maximum positive bending moments (sagging) occur at the middle of the span. It is observed that at non-dimensional thickness of load transfer platform (h/s) equal to 0.3 and column spacing (s/d) equal to 5.5, the maximum positive bending moment at the mid-span of two CICs for the Pasternak shear layer is almost half of the corresponding values for the Timoshenko and the Euler-Bernoulli beam models. Similarly, at the column location, the maximum negative bending moment in the Pasternak shear layer case is almost twice higher than the corresponding values for the Euler-Bernoulli and the Timoshenko models. Moreover, the Timoshenko and the Euler-Bernoulli beam theories predict a similar bending moment developed in LTP.

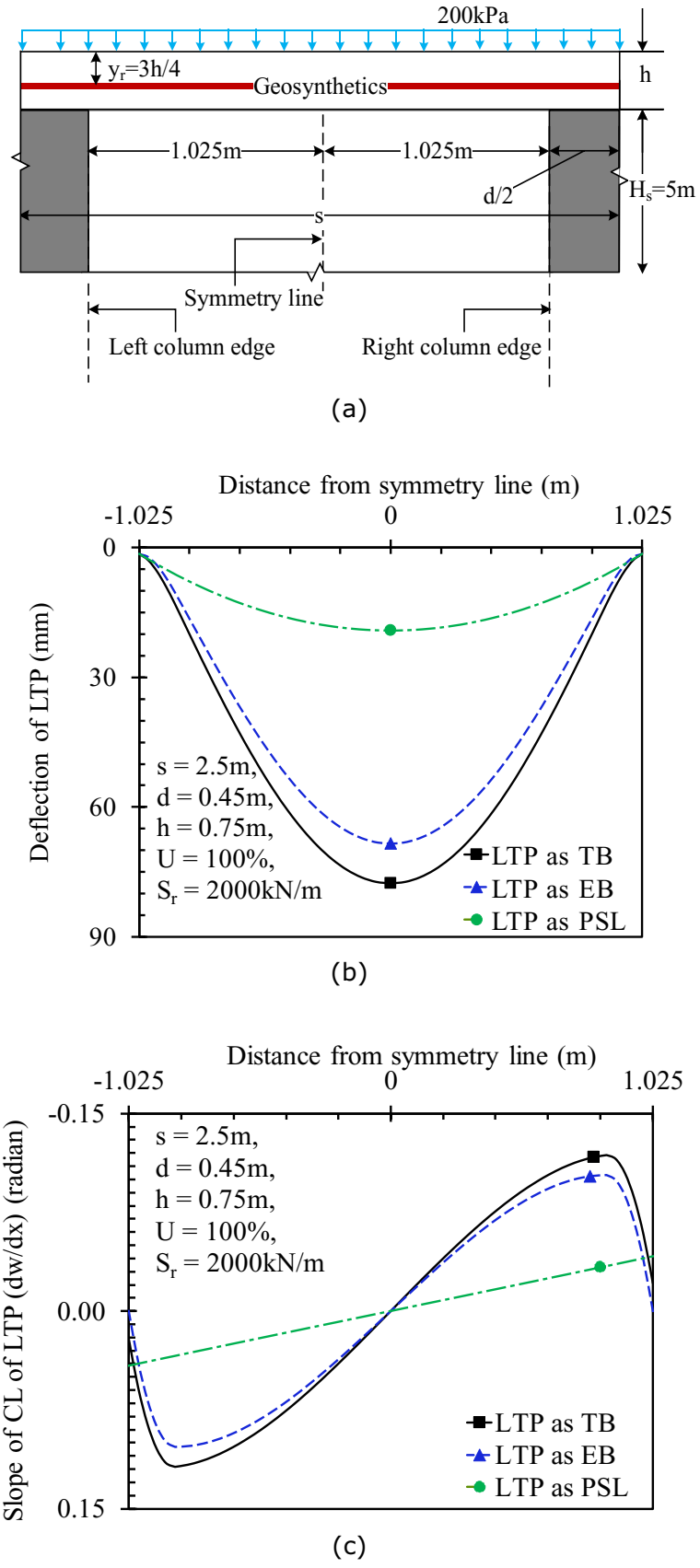

Figure 3.7. Illustration of: (a) LTP on soft soil for baseline case; (b) variation of deflection; and (c) variation of slope of CL of LTP (dw/dx) at the end of consolidation.

A comparison of shear forces in LTP, while considering the three different beam theories for a uniformly distributed load of 200 kPa is shown in Figure 3.8c. Although the cracked section is used to calculate the deformations induced by bending, the full thickness of LTP is used to calculate the shear forces because soil between the cracks can still take shear. Since Euler-Bernoulli beam theory assumes the shear stiffness of LTP as infinity ($C \to \infty$), shear deformations are disregarded but the shear force is recovered due to equilibrium from $V = dM/dx$, while M is the bending moment in LTP. As the shear force diagram indicates, at the column locations (i.e. where $x = 0$ and $x = s'$) the shear force in LTP is equal to the column reaction while there is no shear force at the line of symmetry. Note that at non-dimensional thickness of LTP (h/s) equal to 0.3 and column spacing (s/d) equal to 5.5, the maximum shear force in LTP at the column location for Pasternak model is approximately 5% greater than the corresponding shear forces in Timoshenko and Euler-Bernoulli models. Moreover, the Timoshenko and the Euler-Bernoulli beam theories predict a similar shear force generated in LTP.

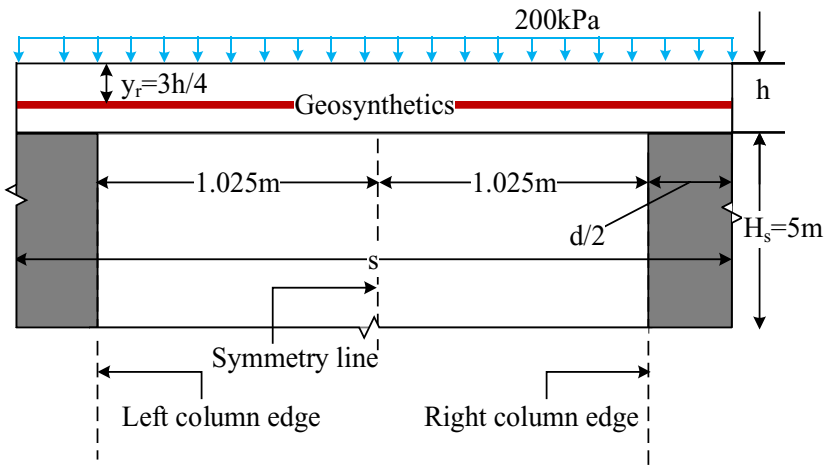

(a)

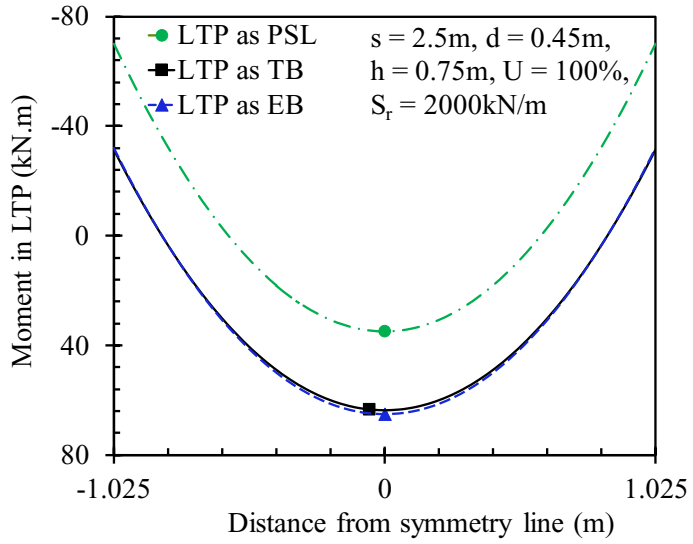

(b)

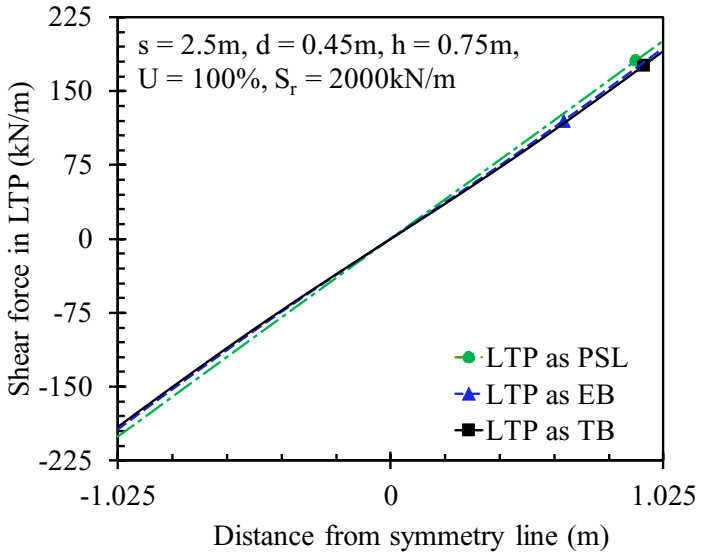

(c)

Figure 3.8. Illustration of: (a) LTP on soft soil for baseline case; (b) variation of bending moment; and (c) shear force at the end of consolidation.

Figure 3.9a shows the parameters used for the baseline case. Figure 3.9b displays a comparison of the rotations of the cross section of LTP (θ) using the Timoshenko, Euler-Bernoulli, and Pasternak theories. It has been observed that Euler-Bernoulli beam theory results in the

maximum rotation of the cross section whereas zero rotation occurs when LTP is simulated with Pasternak model. Since in the Timoshenko model the plane cross section does not need to be perpendicular to the neutral axis (as considered in Euler-Bernoulli theory), the comparison of the rotation of the cross section between the Timoshenko and the Euler-Bernoulli beams indicates that there is less rotation in Timoshenko model. Since the Pasternak shear layer deflects due to transverse shear only, the rotation of the cross section is always zero which is shown in Figure 3.9b. Figure 3.9c shows the profiles of shear strain developed in LTP (γ) using Timoshenko, Euler-Bernoulli, and Pasternak theories. It has been noticed that Pasternak shear layer results in the maximum shear strain in LTP whereas zero shear strain occurs when LTP is simulated with an Euler-Bernoulli beam. Since the load transfer mechanism in the Timoshenko model is due to bending and shear combined while in the Pasternak shear layer is due to shear only, the comparison of the rotation of the cross section between the Timoshenko beam and the Pasternak shear layer indicates that there is less shear strain in Timoshenko model. Since the shear stiffness of Euler-Bernoulli beam is assumed to be infinity, no shear strain generates in LTP which is shown in Figure 3.9c. Figure 3.9d shows the profiles of tension mobilised in the geosynthetics embedded in granular layer resting on a concrete injected column improved soft soil foundation simulating LTP using different beam theories including Timoshenko, Euler-Bernoulli, and Pasternak theories. It is observed that the maximum tension generated in the geosynthetics occurs at the column locations in the three cases. Although a similar trend of mobilised tension occurs in the Timoshenko and Euler-Bernoulli models, a different trend of tension distribution in geosynthetics is predicted for Pasternak case. It is noticed again that at non-dimensional thickness of load transfer platform (h/s) equal to 0.3 and column spacing (s/d) equal to 5.5, the maximum mobilised tension in the geosynthetics at the column locations for Euler-Bernoulli beam is significantly greater than the corresponding

tension when LTP is idealised as Pasternak shear layer, whereas the Timoshenko and the Euler-Bernoulli theories result in similar predictions.

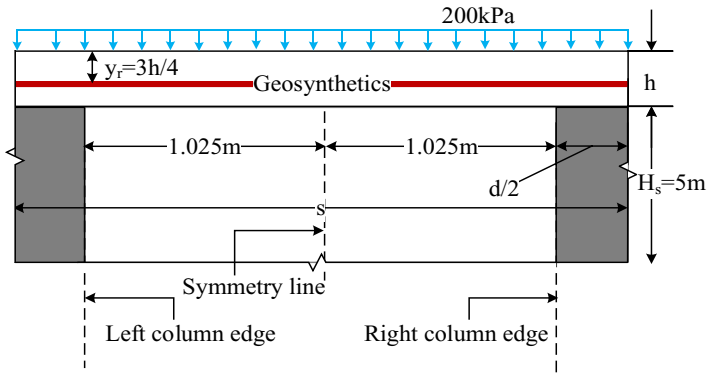

(a)

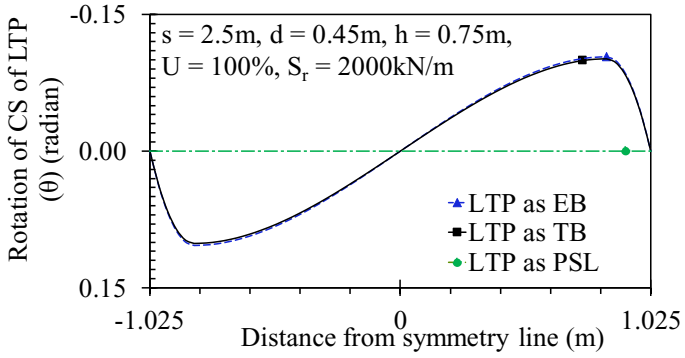

(b)

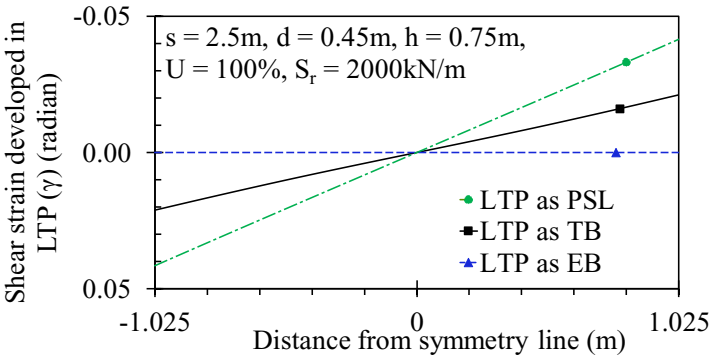

(c)

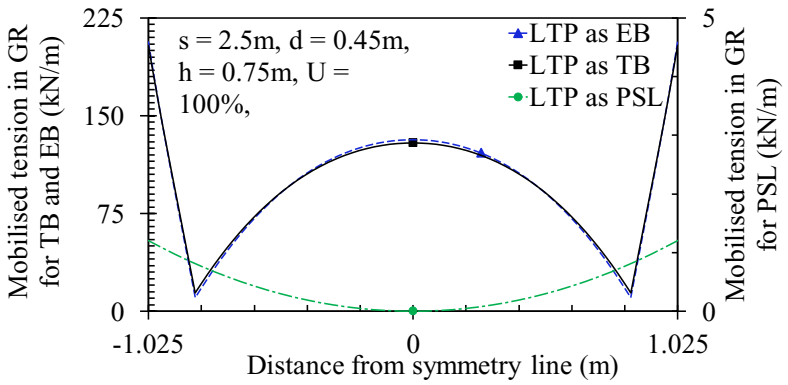

(d)

Figure 3.9. Illustration of: (a) LTP on soft soil for baseline case; (b) variation of rotation of CS of LTP due to bending (θ); (c) variation of shear strain developed in LTP (γ); and (d) variation of mobilised tension in geosynthetics at the end of consolidation.

Figure 3.10 shows a comparison between the stress concentration ratios when LTP is idealised as Timoshenko, Euler-Bernoulli, and Pasternak models. The stress concentration ratio is usually used to analyse the load distribution between the columns and the soil. The higher the stress concentration ratio, the more stress is transferred onto the columns. Since the stress distribution at the interface of LTP and soft soil is not uniform, the stress concentration ratio is presented for two cases; Case 1: stress concentration ratio for the average stress transferred to the soil and Case 2: stress concentration ratio for the maximum stress transferred to the soil which is at the middle of two columns. The stress concentration ratio (SCR) can be defined as Han and Gabr, 2002:

$$(SCR)_{avg} = \frac{\sigma_c}{\overline{\sigma}_s} = \frac{(k_c)_{pl} w_c}{\overline{k}_s \overline{w}_s} \qquad \text{for Case 1} \qquad (3\text{-}38a)$$

and

$$(SCR)_{min} = \frac{\sigma_c}{(\sigma_s)_{max}} = \frac{(k_c)_{pl} w_c}{k_{1s}(w_s)_{max}} \qquad \text{for Case 2} \qquad (3\text{-}38b)$$

where σ_c is the stress transferred to the columns; $\overline{\sigma}_s$ and $(\sigma_s)_{max}$ are the average and maximum stresses transferred to soil, respectively; $(k_c)_{pl}$ is the modulus of subgrade reaction for the columns in plane strain condition; $\overline{k}_s$ and k_{1s} are the average and stiffened modulus of subgrade reactions for the soil, respectively; w_c is the deflection of the column; and $\overline{w}_s$ and $(w_s)_{max}$ are the average and maximum displacement of soil, respectively. In this study, it is assumed that there is a continuity of the deflection of the soil at the locations of the columns. As Figure 3.10 shows, the stress concentration ratio for the Pasternak shear layer case is much higher than the Timoshenko and Euler-Bernoulli cases. Excluding the bending deformation of the granular materials in LTP (due to an assumption of infinity bending stiffness in Pasternak theory) transferred less stress to the soil. This contribution from bending stiffness occurs because the load transfer platform becomes stiffer and reduces the deflection of LTP in the region of soft soil, and hence less pressure is transferred to the soil. Figure 3.10 also indicates that the value of SCR using the maximum stress transferred to soil is less than the corresponding value for the average stress transferred to soft soil for the proposed Timoshenko model.

By comparing the Timoshenko beam to traditional theories (i.e. Euler-Bernoulli and Pasternak), it is evident that the combined effects of shear and flexural stiffnesses decrease the overall stiffness of LTP and increases LTP deflection. Since in reality, shear and flexural stiffnesses are simultaneously present (i.e. $C \neq \infty$ and $D \neq \infty$), the simplified theories including Euler-Bernoulli and Pasternak (assuming $C \to \infty$ or $D \to \infty$) always underestimates the deflection of LTP. Particularly the Pasternak shear layer (assuming $D \to \infty$) results in insignificant tension in the geosynthetics.

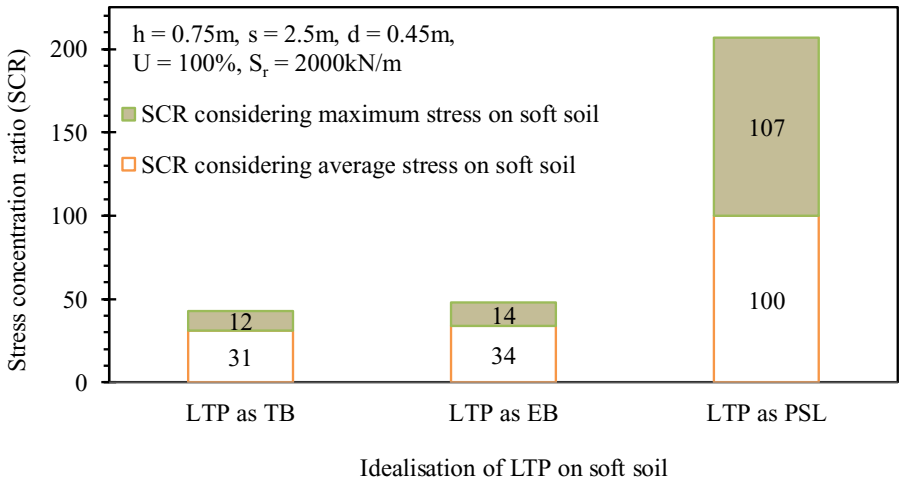

Figure 3.10. Comparison of stress concentration ratio considering LTP as TB, EB, and PSL.

3.6.2. Effect of Column Spacing

Figure 3.11a shows the influence of the column spacing on the maximum settlement of LTP. In this study, the diameter of CIC (d) and the thickness of LTP (h) are 0.45 m and 0.75 m, respectively. The maximum settlement of LTP is calculated at the mid-span of columns. The results from the parametric study show that as the spacing increases, the maximum settlement of LTP also increases, that is, smaller spacing between the CICs reduces the settlement of LTP. For example, using the Timoshenko theory, where the non-dimensional thickness of the load transfer platform (h/d) is equal to 1.6 when the column spacing (s) is equal to 1.75 m, the maximum deflection of LTP occurring at the middle of two columns (at Point B in Figure 3.11a) decreases by almost 78% compared to a prediction corresponding to 2.5 m of column spacing. This is due to the fact that for smaller spacing, total load applied to LTP section between columns is less, causing less deformation of LTP, but as the spacing of the columns increases, more loads are accumulated within LTP on soft soil regions which results in more deformation of LTP. Moreover, since the area replacement ratio decreases with an increase in the spacing, the equivalent subgrade reaction of column (K_c) decreases, and therefore the

rigidity of the column support also decreases, directing more stresses onto the soil rather than the columns. Figure 3.11b illustrates the effect of column spacing on the maximum tension in the geosynthetic layer. It is observed that the maximum mobilised tension in the geosynthetics (at the column edge location i.e. Point A in Figure 3.11b) increases as the column spacing increases because as the settlement of LTP increases with the column spacing, axial strains in the geosynthetics also increase resulting in more tension being mobilised in the geosynthetics. Therefore, tension generated in the geosynthetics increases as the spacing of the columns increases. It is observed that the maximum mobilised tension in the geosynthetics increases by approximately 2.5 times as the spacing of the columns increases from 1.75 m to 2.5 m. Similar results were reported by Abusharar et al. 2009 during an empirical analysis of an embankment supported on piles. It should be noted that similar trends occur for Euler-Bernoulli and Pasternak models, where the maximum settlement of LTP and mobilised tension in the geosynthetics are greater with larger column spacing compared to smaller column spacing.

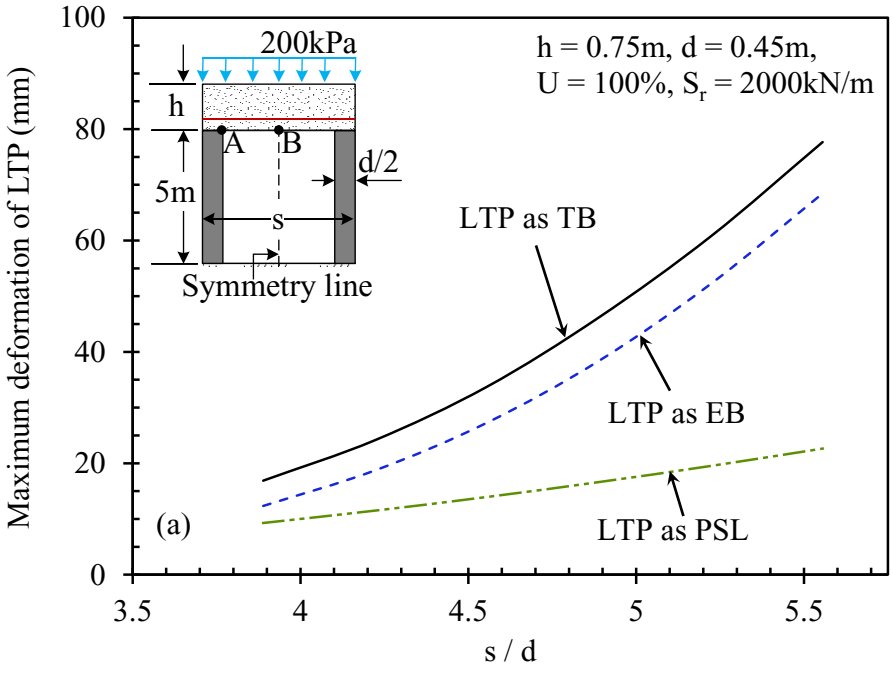

(a)

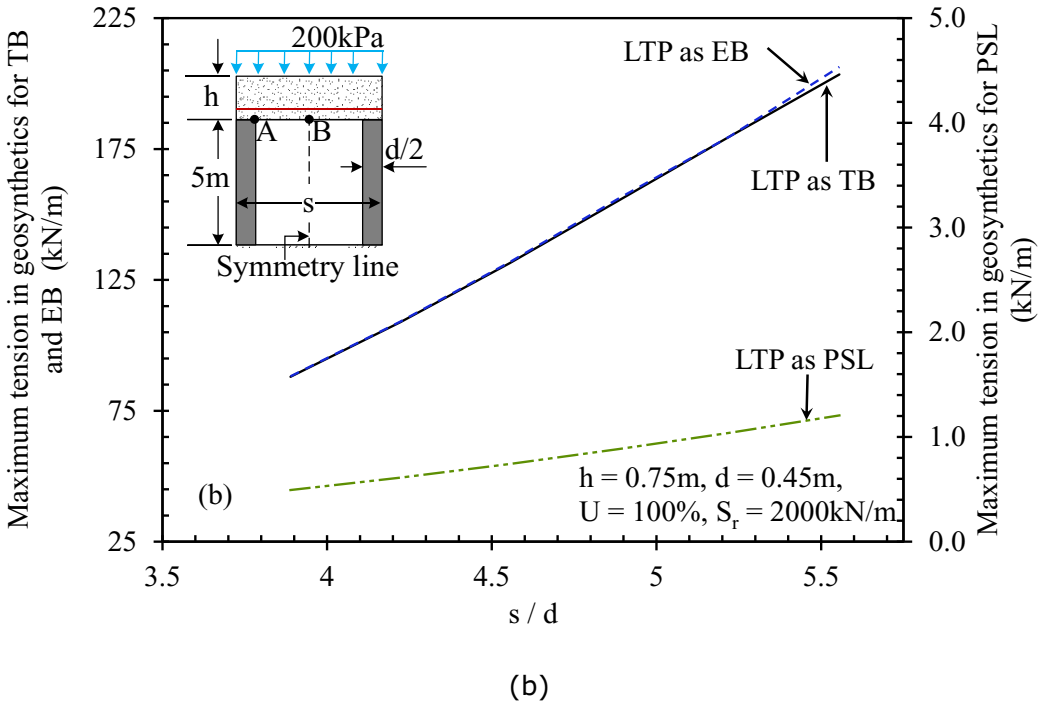

(b)

Figure 3.11. Effect of column spacing on: (a) maximum settlement of LTP and (b) maximum mobilised tension in geosynthetics.

3.6.3. Effect of LTP Thickness

Figure 3.12a shows the effect of LTP thickness on the maximum settlement of LTP. It is observed that the maximum settlement at the mid span (i.e. Point B in Figure 3.12a) decreases as LTP becomes thicker. This occurs because as LTP thickness increases from 0.75 m to 1.25 m, the equivalent bending stiffness (D_s) and shear stiffness (C_s) of LTP increase in the sagging section by about 3 and 1.5 times, respectively (in the case of Timoshenko model). Thus, as LTP becomes thicker, it becomes more rigid, resulting in less settlement. Considering the Timoshenko beam theory, for a particular LTP thickness h =1.25 m, the maximum settlement of LTP is almost 60% less compared to h = 0.75 m. Furthermore, the maximum mobilised tension in the geosynthetics at the edge of the column (i.e. Point A in Figure 3.12b) decreases as LTP becomes thicker. This is due to the fact that as LTP becomes thicker it settles less, and thus the axial strain in the geosynthetics decreases causing less tension in the geosynthetics.

The parametric study also shows that the axial strains in the geosynthetics decreases by 1.6 times as the thickness of LTP increases from 0.75 m to 1.25 m (i.e. a 37% reduction in mobilised tension). As Figure 3.12b shows, the trends in Euler-Bernoulli and Pasternak models are similar.

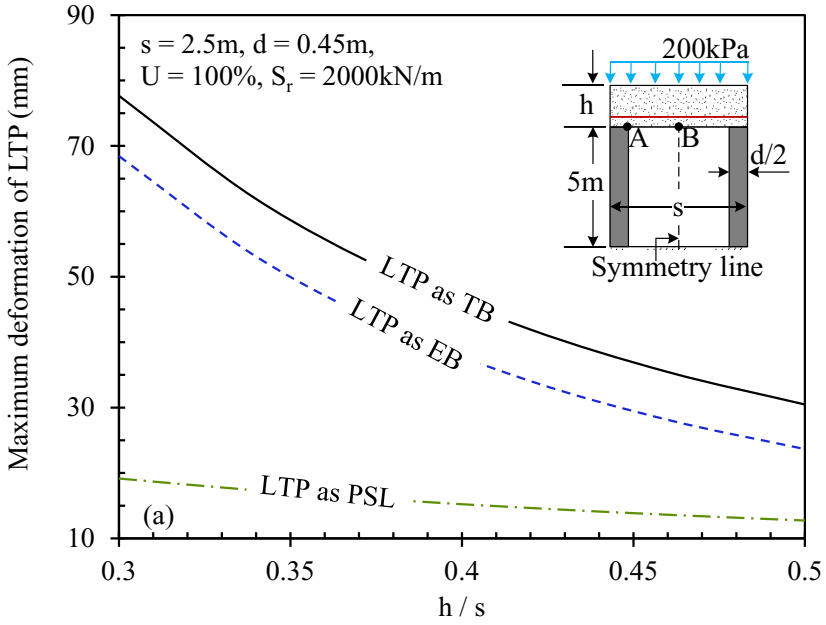

(a)

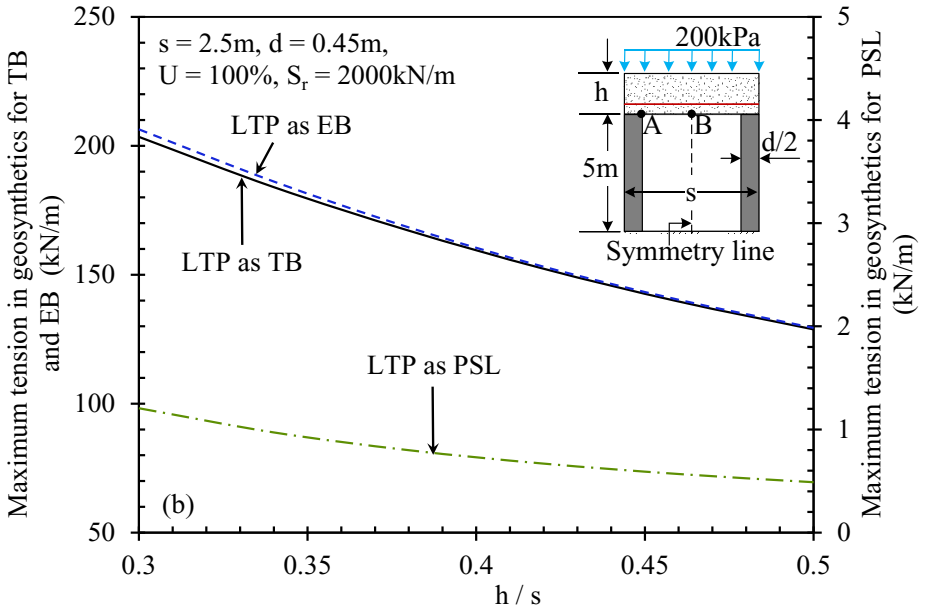

(b)

Figure 3.12. Effect of thickness of LTP on: (a) maximum settlement of LTP and (b) maximum mobilised tension in geosynthetics.

3.6.4. Effect of Tensile Stiffness of Geosynthetics

The tensile stiffness of geosynthetics varies according to its type. For this study, the tensile stiffness of geosynthetics (geogrids in this study) varied from 1000 kN/m to 4000 kN/m. Figure 3.13a shows the effect of the tensile stiffness of geosynthetics on the maximum deflection of LTP beam at the mid span of two columns. Since it is assumed that the geosynthetic layer takes tension as well as shear, the equivalent bending (D_s) and shear stiffness (C_s) of LTP depend on the tensile stiffness of the geosynthetics (see Eqs. (3-3a) and (3-4)). Adopting the Timoshenko beam theory, it is noticed that as the tensile stiffness of geosynthetics increases from 1000 kN/m to 4000 kN/m, the bending and shear stiffnesses of LTP in the sagging section increase by about 2.2 and 1.1 times, respectively. Therefore, using geosynthetics with a higher tensile stiffness increases the rigidity of LTP beam and causes less settlement. For example, when non-dimensional thickness of the load transfer platform (h/s) is equal to 0.3 and tensile stiffness of the geosynthetics is 1000 kN/m, the maximum deflection of LTP (i.e. Point B in Figure 3.13a) decreases by approximately 51% compared to using geosynthetics of 4000 kN/m tensile stiffness. Furthermore, as the geosynthetics becomes stiffer, the maximum mobilised tension in the geosynthetics also increases. Although, when the stiffness of the geosynthetics increases from 1000 kN/m to 4000 kN/m, the strain in the geosynthetics decreases 1.2 times, the tension mobilised in the geosynthetics increases by 12% (in the case of Timoshenko model) as shown in Figure 3.13b; this is occurred because mobilised tension is the product of tensile stiffness and strain in the geosynthetics layer so as the geosynthetics becomes stiffer, its maximum tension also increases. Similar results were reported by Huang and Han 2010, and Bhasi and Rajagopal (2015a) for geosynthetic-reinforced embankments constructed on columns where a numerical analysis were carried out. Similar relationships between the tensile

stiffness of geosynthetics, the maximum settlement of LTP, and the maximum tension mobilised in geosynthetics are also observed when Euler-Bernoulli and Pasternak theories are used.

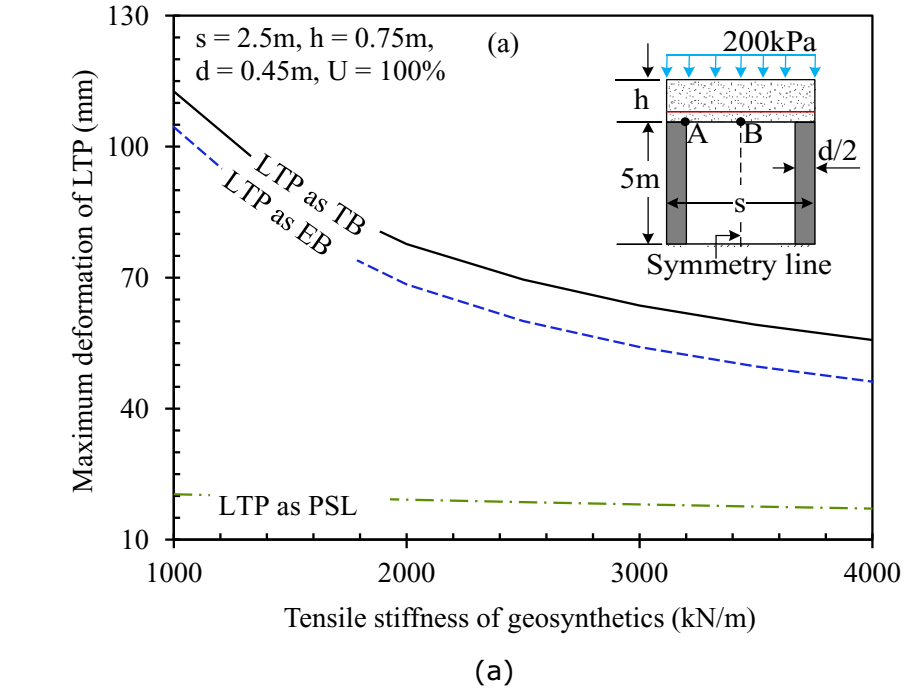

(a)

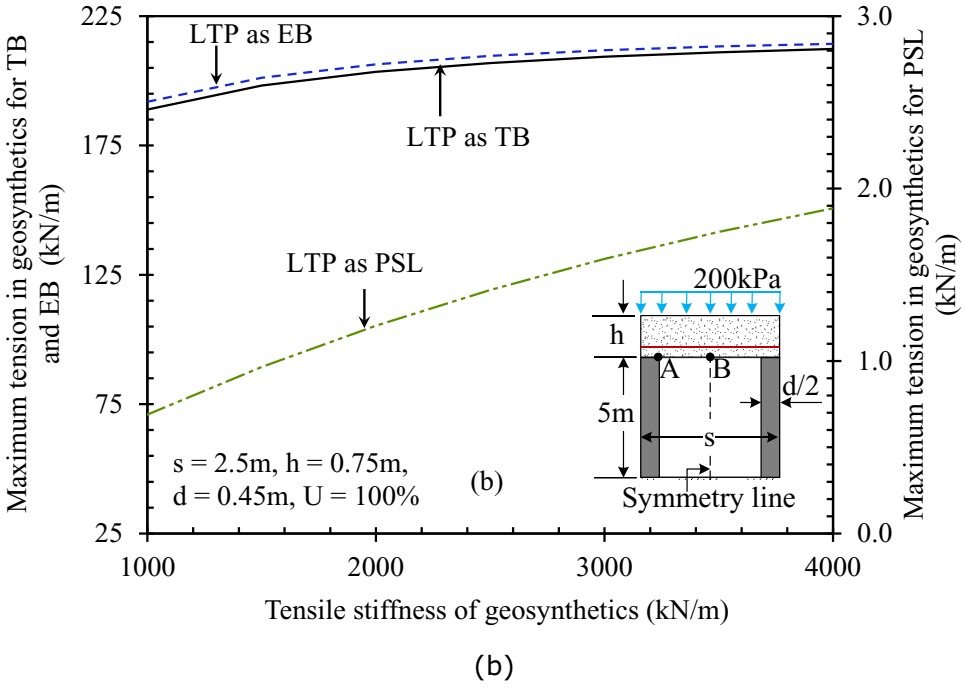

(b)

Figure 3.13. Effect of tensile stiffness of geosynthetics on: (a) maximum settlement of LTP and (b) maximum mobilised tension in geosynthetics.

3.6.5. Effect of Degree of Consolidation (U)

Figure 3.14a shows the effect of consolidation of soft soil on the maximum deflection of LTP in the middle of two columns (i.e. Point B in Figure 3.14a). As expected, as the degree of consolidation increases, the maximum deflection of LTP also increases. For example, by using Timoshenko beam theory, at a non-dimensional thickness of LTP (h/d) equal to 1.6 and column spacing (s/d) equal to 5.5, the maximum deflection of LTP increases by 29% as the degree of consolidation increases from 20% to 80%. This is due to the fact that as the degree of consolidation increases, the reaction of the soft soil at the soil-LTP interface decreases which contributes to further deflection. It is obvious that as the deflection of LTP increases, the mobilised tension in the geosynthetics also increases. Figure 3.14b shows the variation of maximum mobilised tension with the degree of consolidation of the underlying soft soils. At a non-dimensional thickness of load transfer platform (h/d) equal to 1.6 and column spacing (s/d) equal to 5.5, the maximum mobilised tension increases by 24% as the degree of consolidation increases from 20% to 80% in case of Timoshenko beam.

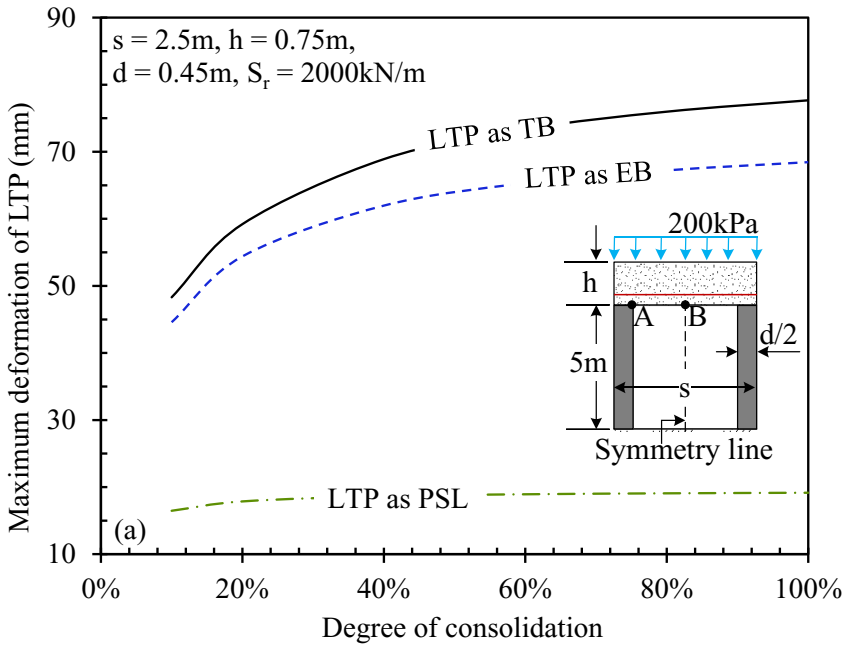

(a)

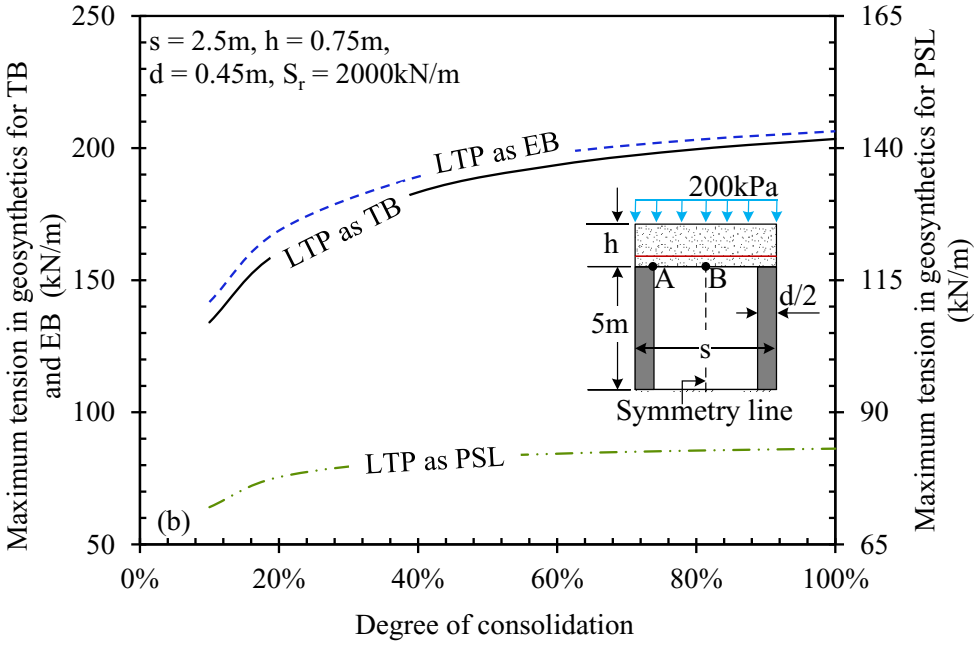

(b)

Figure 3.14. Effect of degree of consolidation of soft soil on: (a) maximum settlement of LTP and (b) maximum mobilised tension in geosynthetics.

Although the overall behaviour of LTP due to bending and shear actions on a nonlinear soft soil foundation can be predicted using the proposed cracked reinforced Timoshenko beam model, there are several limitations for the proposed analytical solution namely: (1) columns rest on a rigid stratum; (2) possible pull-out resistance force of geosynthetics from the surrounding granular material is omitted; (3) the friction between the column and the surrounding soft soil is ignored for simplicity; and (4) shear deformation of soft soil has been ignored (i.e. Winkler model). The authors are currently working on a solution to address some of the above-mentioned limitations. Although the time dependent behaviour of the soft soil is considered in the present model, it should be noted that soil cementation and creep can significantly affect the performance of soft soil and may be considered in future research (Le et al., 2015; Nguyen and Fatahi, 2016).

3.7. Summary

The analytical solutions to predict the response of the load transfer platform (LTP) on column stabilised soft soil subjected to pressure loadings have been presented in this chapter. The effect of the bending and shear deformations of LTP and the nonlinear stress strain behaviour of soft soil were incorporated into the present mechanical model. The influence of negligible tensile strength compared to the compressive strength of granular materials in LTP was also considered in the model. The effect of column supports was treated as boundary conditions. For the analytical development, the principle of superposition was used to obtain the exact solutions to the fourth order nonhomogeneous differential equations. Furthermore, a parametric study was carried out to investigate how parameters such as the spacing of columns, the thickness of LTP, the tensile stiffness of geosynthetics, and the degree of consolidation affect the response of LTP on soft soil. It was observed that smaller spacing between the columns and thicker LTP reduce the maximum settlement of LTP and tension mobilised in the geosynthetics. Although use of stiffer geosynthetics reduces the maximum settlement of LTP but increases the mobilised tension in the geosynthetics. Moreover, the Euler-Bernoulli and the Pasternak theories in addition to Timoshenko beam theory were used to evaluate the accuracy of existing beam theories to analyse LTP on column reinforced soft soil. The results from the proposed Timoshenko theory (capturing the combined shear and bending stiffness of LTP) were compared with results from the Euler-Bernoulli model (capturing deflection due to bending only) and the Pasternak model (capturing deformation due to shear only). Moreover, the Timoshenko model outperformed the Euler-Bernoulli model and Pasternak model, while simultaneously considering bending and shear deformations of granular materials and reinforcement. Therefore, it was concluded that simulating LTP as Euler-Bernoulli beam or Pasternak shear layer resulted in an aggressive design in terms of the prediction of the deflection of LTP. It is therefore recommended that practising engineers use the Timoshenko

beam for design purposes. The proposed mechanical model and its analytical solutions for LTP on a soft soil foundation can be used to calculate the settlement/deflection of LTP and tension in the reinforcement for any shape of loading, as well as the linear and nonlinear stress strain responses of soft soil.

CHAPTER 4

4. ANALYTICAL STUDY FOR DOUBLE-LAYER GEOSYNTHETIC REINFORCED LOAD TRANSFER PLATFORM ON COLUMN IMPROVED SOFT SOIL

4.1. General

The objective of this study is to propose a reasonably accurate mechanical model for double-layer geosynthetic reinforced load transfer platform (LTP) on column reinforced soft soil which can be used by practicing engineers. The developed model is very useful to study the behaviour of LTP resting on soft soil improved with conventional columns such as concrete columns, piles, and deep soil mixing columns. The negligible tensile strength of granular material in LTP, bending and shear deformations of LTP, compressibility and shearing of soft soil have been incorporated in the model. Furthermore, the results from the proposed model simulating the soft soil as Kerr foundation model are compared to the corresponding solutions when the soft soil is idealised by Winkler and Pasternak foundation models. It is observed from the comparison that the presented model can be used as a tool for a better prediction of the LTP behaviour with multi layers of geosynthetics, in comparison with the situation that soft soil is modelled by Winkler and Pasternak foundations. Furthermore, parametric studies show that as the column spacing increases, the maximum deflection of LTP and normalised tension in the geosynthetics also increase. Whereas, the maximum deflection of LTP and normalised tension in the geosynthetics decrease with increasing LTP thickness, stiffness of subsoil, and stiffness of geosynthetic reinforcement. In addition, it is observed that the use of one stronger geosynthetic layer (e.g. 1×2000 kN/m) with the equivalent stiffness of two geosynthetic layers

(e.g. 2×1000 kN/m) does not result in the same settlement of LTP and the tension of the geosynthetic reinforcement when compared to two weaker geosynthetic layers.

4.2. Formulation of the problem

The proposed mechanical model that idealises the mechanistic behaviour of a load transfer platform (LTP) on column improved soft soil in plane strain condition is presented in Figure 4.1a. The free body diagrams of the small segments in LTP (i.e. element A) and shear layer (i.e. element B) of length dx are shown in Figure 4.1b−c, respectively. In this study, double layers of geosynthetic reinforcement embedded within compacted granular layers are considered (whereas in the previous chapter, single layer of geosynthetics was considered). The geosynthetic reinforcement is modelled as a rough elastic membrane, placed inside the Timoshenko beam representing the granular fill materials. Thus, the combined representation of the geosynthetic-reinforced granular layer is a structural element named as "membrane-reinforced Timoshenko beam". Columns and soft soil are idealised by Winkler springs and Kerr foundation model, respectively.

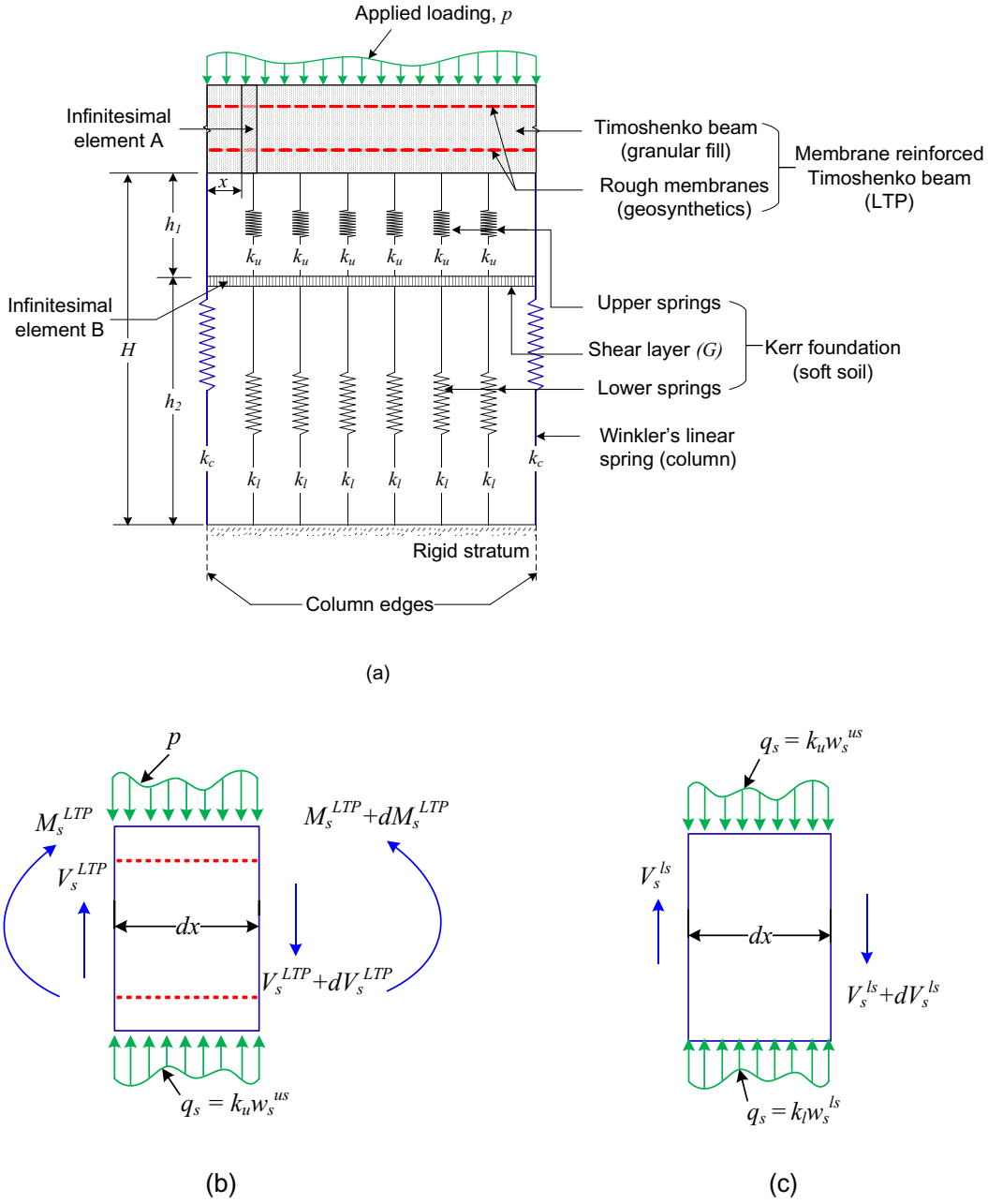

Figure 4.1. Illustration of: (a) proposed mechanical model of load transfer platform on column improved soft soil in plane strain condition; (b) free-body diagram of element A in sagging part; and (c) free-body diagram of element B in sagging part.

It is implicit here that granular fill material in the load transfer platform (LTP) has insignificant tensile strength compared to compressive strength, so similar to a concrete beam, tension cracks are expected to spread from the tension face (bottom edge of LTP) in the direction of the neutral axis in the span. In contrast, since the granular layer is continuous over the column positions,

the direction of the bending moment changes adjacent to the columns. Accordingly, tension cracks are produced at the top edge of the granular layer and spread towards the neutral axis. A typical profile of deflection of the LTP assumed for the analytical development is shown in Figure 4.2a. After cracking, it may be presumed that plane sections continue to be plane, but as the load increases, these cracks spread towards the neutral axis, and then the neutral axis starts to change its position depending on tension cracks propagation. It is assumed here that the flexural cracks are developed vertically. Since some parts of the granular layer are cracked, the soil in those fractured zones cannot sustain tensile stresses and becomes weaker. Therefore, geosynthetic reinforcement is embedded to strengthen the granular fill. Similar approach (i.e. cracked load transfer platform) was considered previously by Ghosh et al. (2017) while load transfer platform was analysed on Winkler foundation considering the non-linear behaviour of soft soils. For the sake of obtaining an analytical solution and following one of the basic assumptions used for flexural design of reinforced concrete beams, it is presumed that the geosynthetic reinforcement is attached to the granular material, thus it is reasonable to assume that the tensile and compressive forces mobilised in LTP are carried by geosynthetic reinforcement and granular material, respectively. This means the strain in the geosynthetic reinforcement is equal to the strain in the granular fill at the same level. It should be noted that by making this simplifying assumption, possible gap or slip between the geosynthetics and the granular fill materials is ignored. A similar assumption was adopted by several other researchers to study the mechanical behaviour of LTP (Yin, 2000a, b; Shukla and Yin, 2003). Hence, section properties of a cracked LTP should be adopted for flexural design. Since the initiation of the tension cracks and their propagation are varied in different locations, the design of LTP would be more accurate if different cross section properties in different locations of LTP are considered, depending on the locations of the tension cracks. Considering the position of the tension cracks, the loaded LTP is divided into two sections, as shown in Figure 4.2a.

Region I (when $-r \leq x \leq +r$) where tension cracks in the LTP appear from the bottom edge; which means the bottom of LTP is under tension (sagging moment). In contrast, in Region II (when $\pm r \leq x \leq \pm s/2$), tension cracks in the LTP develop from the top edge (hogging moment). Figure 4.2b−c illustrates the effective cross sections of the LTP in Regions I and II, respectively. The cracked transformed section to carry out the flexural analysis is attained by substituting the area of geosynthetic reinforcement with an equivalent area of granular fill material equal to nA_r, where $n\left(n = E_r/E_g\right)$ is the modular ratio with the elastic modulus of geosynthetic reinforcement (E_r) and granular fill material $\left(E_g\right)$ and A_r is the cross sectional area of geosynthetic reinforcement. To analyse the response of LTP, the neutral axis is located first, positioned at a distance (h_s) from the compression end of LTP in the sagging bending moment region which is indicated in Figure 4.2b. The first moment of the compression area in the LTP (A_s) above the neutral axis with respect to neutral axis must be equal that of the tension area in the transformed geosynthetic layer $\left(nA_r^b\right)$ under the neutral axis; that is $A_s h_s/2 = nA_r^b\left(y_r^b + y_s\right)$. where A_r^b is the cross-section area of bottom geosynthetic reinforcement; y_r^b is the locations of bottom geosynthetic layer from the centroid axis; and y_s is the distance between neutral axis and centroid axis of LTP within the sagging bending moment section. The above-mentioned equation is a quadratic equation in terms of h_s, the value of which determines the location of the neutral axis. Similarly, to establish the neutral axis (h_h) in the hogging region, first moment of the compression area in the LTP (A_h) above the neutral axis with respect to neutral axis must be equal that of the tension area in the transformed geosynthetic layer (nA_r^t) below the neutral axis. To acquire the depth of the neutral axis $(h_s \text{ or } h_h)$, the solutions of the resulting quadratic equations are found as follows:

$$h = \begin{cases} h_s = \sqrt{\left(\frac{S_r^b}{E_g}\right)^2 + \left[\frac{S_r^b}{E_g}\left(2y_r^b + h\right)\right]} - \left(\frac{S_r^b}{E_g}\right), & -r \le x \le +r \\ h_h = \sqrt{\left(\frac{S_r^t}{E_g}\right)^2 + \left[\frac{S_r^t}{E_g}\left(2y_r^t + h\right)\right]} - \left(\frac{S_r^t}{E_g}\right), & \pm r \le x \le \pm\frac{s}{2} \end{cases} \quad (4\text{-}1)$$

where h is the thickness of LTP before cracking; h_s and h_h are the locations of neutral axis in sagging moment and hogging moment zones, respectively; y_r^t and y_r^b are the locations of top and bottom geosynthetic layer from the centroid axis, respectively; $S_r^t(= A_r^t E_r^t)$ and $S_r^b(= A_r^b E_r^b)$ are the tensile stiffness of top and bottom geosynthetic layers, respectively; E_r^t and E_r^b are the Young's moduli of top and bottom reinforcements, respectively; E_g is the Young's modulus of the granular material; and A_r^t and A_r^b are the cross-sectional area of top and bottom geosynthetic reinforcements, respectively.

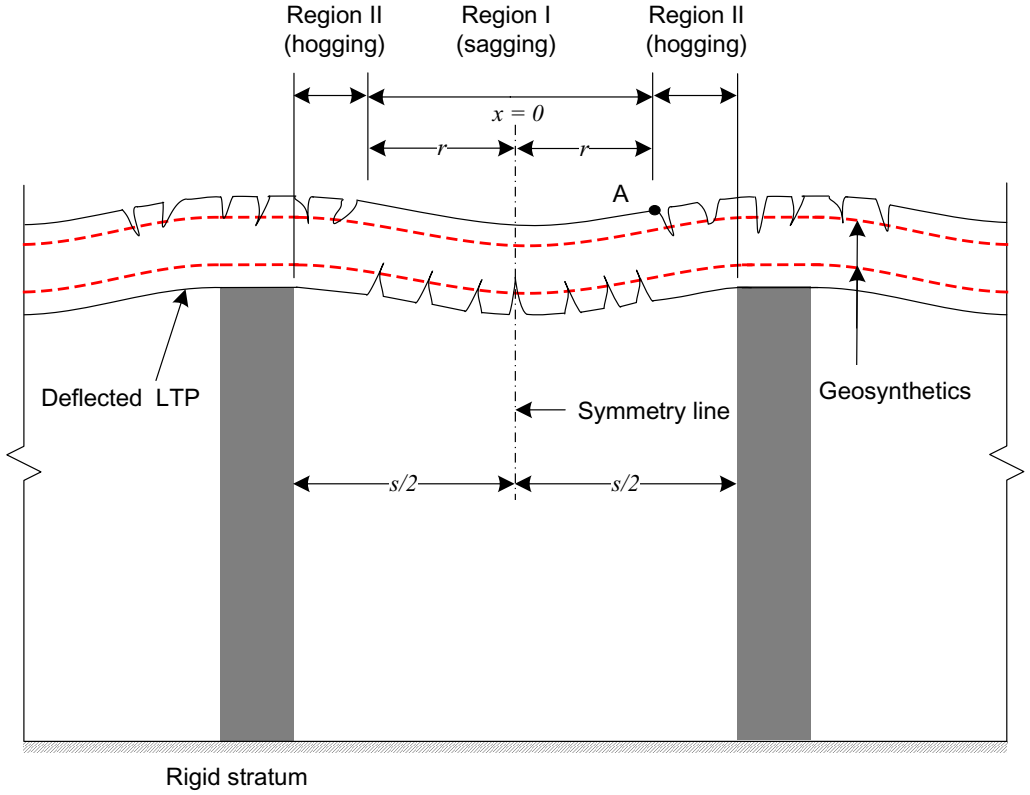

(a)

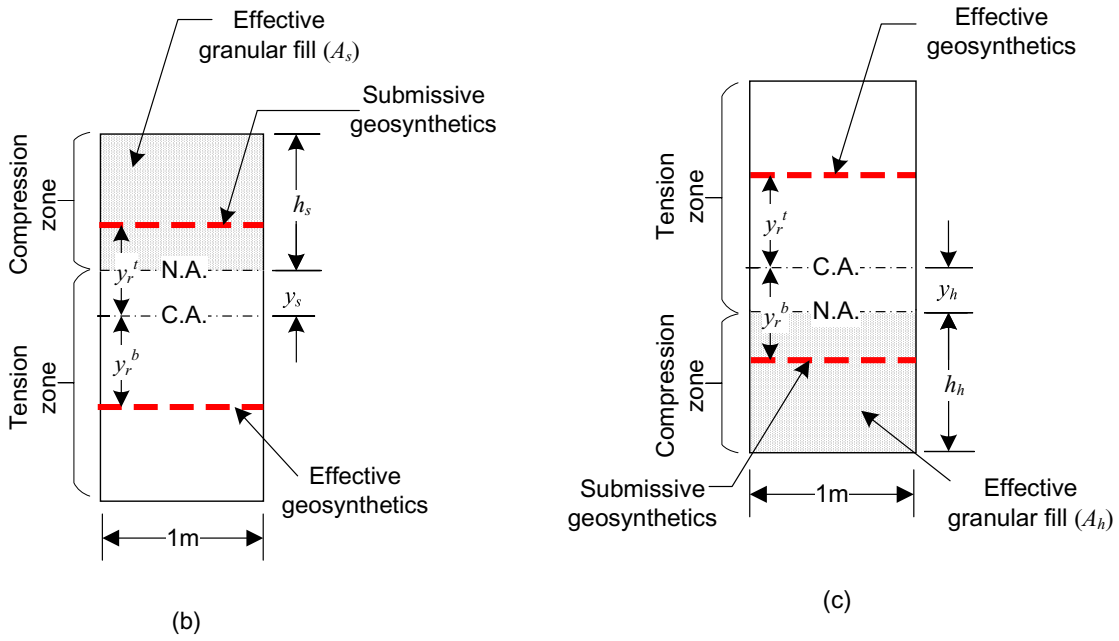

Figure 4.2. Typical diagram of: (a) deflection profile of load transfer platform (LTP), (b) effective cross-section of LTP in sagging region, and (c) effective cross-section of LTP in hogging region.

After locating the neutral axis, the equivalent bending stiffness of the granular layer with geosynthetic reinforcement (D_s and D_h) is calculated as follows.

$$D = \begin{cases} D_s = E_g I_s + S_r^b \left(y_s + y_r^b\right)^2, & -r \le x \le +r \\ D_h = E_g I_h + S_r^t (y_h + y_r^t)^2, & \pm r \le x \le \pm \frac{s}{2} \end{cases} \tag{4-2}$$

Although in flexure, the existence of granular materials below/above the neutral axis is omitted, but the same granular material between the neutral axis and the cracks is needed for shear transfer between the geosynthetic reinforcement and the compression zone. Hence, the shear stiffness of the granular fill including geosynthetic reinforcement (C) can be calculated as follows.

$$C = k_{sc} \left\{ \frac{E_g h}{2(1+\nu_g)} + \frac{S_r^t}{2(1+\nu_r^t)} + \frac{S_r^b}{2(1+\nu_r^b)} \right\}, \quad -\frac{s}{2} \le x \le +\frac{s}{2} \tag{4-3}$$

where y_s and y_h are the distances between neutral axis and centroid axis of LTP within the sagging and hogging bending moment sections, respectively; ν_g , ν_r^t, and ν_r^b are the Poisson's ratios of granular material, top and bottom geosynthetic layers, respectively; D_s and D_h are the equivalent bending stiffness of LTP within the sagging and hogging bending moment sections, respectively; C is the shear stiffness of LTP irrespective of the sagging and hogging bending moments; I_s and I_h are the second moment of inertias of the granular materials within the sagging and hogging bending moment sections, respectively ($I_s = {h_s}^3/3$ and $I_h = {h_h}^3/3$); and k_{sc} is the shear factor suggested by Cowper (1966) and Hutchinson (2001) for the rectangular cross section of a beam.

As the LTP settles on the column improved soft soil, shear stresses are generated in the soft soil. Thus, Winkler foundation model to simulate the soft soil under the LTP would not be suitable in this case as the differential settlement occurs underneath the granular layer. Because of the discontinuity amongst the spring elements, Winkler foundation model cannot consider the shear stress transfer in the soil. Hence, for the sake of realistic modelling of the soft soil, the connectivity of the individual Winkler springs must be achieved through a structural element such as a beam, a shear layer, or a plate. However, this structural element cannot be introduced just below the granular layer. Since the differential settlement of soft soil just underneath the granular layer is very high, large shear stresses are generated in this region. However, since soil is a continuum medium, the differential settlement dissipates over the soil depth, resulting in less shear stresses generated in the soft soil. Therefore, structural elements such as a shear layer must be introduced in combination with the Winkler springs at some distance below the granular layer. Hence, the Kerr foundation model which consists of two spring layers interconnected by a shear layer is adopted to simulate the soft soil. The three-parameter Kerr foundation model consists of two linear spring layers with modulus of subgrade reactions k_u and k_l, interconnected by a shear layer with shear modulus G (as shown in Figure

4.1a). Plane strain condition allowing the consideration of a LTP strips of finite length "s" and unit width, is considered. To analyse the LTP, the equilibrium equations (i.e. externally applied loads equal to the sum of the internal element forces at all nodes of a structure) and the compatibility equations (i.e. one or more equations which state either that no gaps exist internally, or deflections are consistent with the geometry imposed by the supports) which are the most fundamental equations in structural analysis. Therefore, the concept of "Load-Displacement compatibility method" in the present research is adopted from fundamental laws of physics. Similar concept was implemented by Smith (2005) and Filz and Smith (2007) for design of bridging layers in geosynthetics reinforced embankments. Hence, to satisfy the vertical deformation continuity, the following conditions should be satisfied.

$$w_{LTP} = \begin{cases} w_s^{LTP} = w_s^{us} + w_s^{ls}, & -r \le x \le +r \\ w_h^{LTP} = w_h^{us} + w_h^{ls}, & \pm r \le x \le \pm\frac{s}{2} \end{cases} \tag{4-4}$$

where w_s^{LTP} and w_h^{LTP} are the deflections of the LTP in the sagging and hogging regions, respectively; w_s^{us} and w_s^{ls} are the contractions or extensions of the upper and lower springs layers in the sagging region, respectively; w_h^{us} and w_h^{ls} are the contraction or extension of the upper and lower spring layers in the hogging region, respectively. The contact pressures (q) under the LTP as shown in Figure 4.1b can be expressed as:

$$q = \begin{cases} q_s = k_u w_s^{us}, & -r \le x \le +r \\ q_h = k_u w_h^{us}, & \pm r \le x \le \pm\frac{s}{2} \end{cases} \tag{4-5}$$

The governing equation for the Pasternak shear layer as displayed in Figure 4.1c is given by:

$$q = \begin{cases} q_s = k_l w_s^{ls} - G w_s^{ls''}, & -r \le x \le +r \\ q_h = k_l w_h^{ls} - G w_h^{ls''}, & \pm r \le x \le \pm\frac{s}{2} \end{cases} \tag{4-6}$$

where k_u and k_l are the spring constants for upper and lower layers, respectively and G is the shear modulus of soft soil. According to Lagrange's notation, a prime mark denotes a derivative (e.g. $w_s^{ls\prime\prime} = \frac{d^2 w_s^{ls}}{dx^2}$).

Rearranging Eq. (3-5), the relationship between the deflection of the upper soil layer and the contact pressure at the interface of LTP and soft soil can be obtained as below:

$$\frac{k_l}{k_u} q_s - \frac{G}{k_u} q_s'' = k_l w_s^{us} - G w_s^{us\prime\prime}, \qquad -r \le x \le +r \tag{4-7a}$$

and

$$\frac{k_l}{k_u} q_h - \frac{G}{k_u} q_h'' = k_l w_h^{us} - G w_h^{us\prime\prime}, \qquad \pm r \le x \le \pm \frac{s}{2} \tag{4.7b}$$

Combining Eqs. (4-6) and (4-7a) and then substituting the resulting equation in Eq. (4-4), leads the relationship between the deflection of the LTP and the contact pressure at the interface of LTP and soft soil in sagging region which is stated in Eq. (4-8a) (similar steps are applied for Eq. (4-8b)):

$$\left(1 + \frac{k_l}{k_u}\right) q_s - \frac{G}{k_u} q_s'' = k_l w_s^{LTP} - G w_s^{LTP\prime\prime}, \qquad -r \le x \le +r \tag{4-8a}$$

and

$$\left(1 + \frac{k_l}{k_u}\right) q_h - \frac{G}{k_u} q_h'' = k_l w_h^{LTP} - G w_h^{LTP\prime\prime}, \qquad \pm r \le x \le \pm \frac{s}{2} \tag{4.8b}$$

The differential equations for LTP in the plane strain condition adopting membrane reinforced Timoshenko (1921) beam can be rewritten as:

$$D_s w_s^{LTP\,iv} - \frac{D_s}{C} q_s'' + q_s = p - \frac{D_s}{C} p'', \qquad -r \le x \le +r \tag{4-9a}$$

and

$$D_h w_h^{LTP\,iv} - \frac{D_h}{C} q_h'' + q_h = p - \frac{D_h}{C} p'', \qquad \pm r \le x \le \pm \frac{s}{2} \tag{4.9b}$$

Combining Eqs. (4-8a) and (4-9a) yields the governing differential equation of the deflection of the LTP for sagging region (i.e. for $-r \le x \le +r$) which is expressed as below.

$$\left(\frac{GD_s}{k_u}\right) w_s^{LTP\,vi} - D_s\left(1 + \frac{k_l}{k_u} + \frac{G}{C}\right) w_s^{LTP\,iv} + \left(\frac{D_s k_l}{C} + G\right) w_s^{LTP\,''} - k_l w_s^{LTP} =$$
$$-\left(\frac{GD_s}{Ck_u}\right) p^{iv} + \left(\frac{D_s}{C} + \frac{D_s k_l}{Ck_u} + \frac{G}{k_u}\right) p'' - \left(1 + \frac{k_l}{k_u}\right) p \tag{4-10a}$$

where Roman numerals, as in $w_s^{LTP\,vi}$, $w_s^{LTP\,iv}$, and $w_s^{LTP\,''}$ denote sixth, fourth, and second order derivatives with respect to x, respectively.

Similarly, combining Eqs. (4-8b) and (4-9b), the response of LTP in the hogging region (i.e. for $\pm r \le x \le \pm s/2$) can be represented as:

$$\left(\frac{GD_h}{k_u}\right) w_h^{LTP\,vi} - D_h\left(1 + \frac{k_l}{k_u} + \frac{G}{C}\right) w_h^{LTP\,iv} + \left(\frac{D_h k_l}{C} + G\right) w_h^{LTP\,''} - k_l w_h^{LTP} =$$
$$-\left(\frac{GD_h}{Ck_u}\right) p^{iv} + \left(\frac{D_h}{C} + \frac{D_h k_l}{Ck_u} + \frac{G}{k_u}\right) p'' - \left(1 + \frac{k_l}{k_u}\right) p \tag{4.10b}$$

4.3. The Analytical Solutions

In the present study, two-dimensional plane strain analysis has been carried out for column-supported structures. Analytical solutions are obtained for calculating the settlement of the load transfer platform at any arbitrary point for the symmetric loading condition. Fourier series is utilised to consider the symmetric distribution of vertical loading (p) on LTP between the two adjacent columns. Hence, p can be described as:

$$p = P_0 + \sum_{n=1}^{n=\infty} P_n \cos\left(\frac{2n\pi x}{s}\right) \tag{4-11}$$

where

$$P_0 = \frac{1}{s}\int_{-s/2}^{s/2} f(x)\,dx \text{ and } P_n = \frac{2}{s}\int_{-s/2}^{s/2} f(x)\cos\left(\frac{2n\pi x}{s}\right) \tag{4-12}$$

Combining Eqs. (4-10a) and (4-11), the following differential equation is governed for Region I (i.e. for $-r \le x \le +r$).

$$w_s^{LTP^{vi}} + X_s w_s^{LTP^{iv}} + Y_s w_s^{LTP''} + Z_s w_s^{LTP} = -\left(\frac{k_u+k_l}{GD_s}\right)P_0 - \sum_{n=1}^{n=\infty}\left[\left(\frac{k_u+k_l}{GD_s}\right) + \left(\frac{k_u}{GC}+\frac{k_l}{GC}+\frac{1}{D_s}\right)\left(\frac{2n\pi}{s}\right)^2 + \frac{1}{C}\left(\frac{2n\pi}{s}\right)^4\right]P_n\cos\left(\frac{2n\pi x}{s}\right) \tag{4-13a}$$

Similarly, by substituting Eq. (4-11) into Eq. (4-10b), the following differential equation for Region II (i.e. for $\pm r \le x \le \pm s/2$) can be derived:

$$w_h^{LTP^{vi}} + X_h w_h^{LTP^{iv}} + Y_h\, w_h^{LTP''} + Z_h w_h^{LTP} = -\left(\frac{k_u+k_l}{GD_h}\right)P_0 - \sum_{n=1}^{n=\infty}\left[\left(\frac{k_u+k_l}{GD_h}\right) + \left(\frac{k_u}{GC}+\frac{k_l}{GC}+\frac{1}{D_h}\right)\left(\frac{2n\pi}{s}\right)^2 + \frac{1}{C}\left(\frac{2n\pi}{s}\right)^4\right]P_n\cos\left(\frac{2n\pi x}{s}\right) \tag{4-13b}$$

where

$$\left\{\begin{matrix} X_s = -\frac{1}{G}\left(k_u + k_l + \frac{k_u G}{C}\right) \\ X_h = -\frac{1}{G}\left(k_u + k_l + \frac{k_u G}{C}\right)\end{matrix}\right\};\ \left\{\begin{matrix} Y_s = \frac{k_u k_l}{GC} + \frac{k_u}{D_s} \\ Y_h = \frac{k_u k_l}{GC} + \frac{k_u}{D_h}\end{matrix}\right\};\ \text{and}\ \left\{\begin{matrix} Z_s = -\frac{k_u k_l}{GD_s} \\ Z_h = -\frac{k_u k_l}{GD_h}\end{matrix}\right\} \tag{4-14}$$

The governing differential equations (i.e. Eqs. (4-13a) and (4-13b)) are sixth order, linear, and nonhomogeneous equations with constant coefficients. To obtain general solutions for the governing differential equations, auxiliary or complementary equations corresponding to the homogeneous equations are solved. The auxiliary equations to the homogeneous equations can be expressed in a generalised form as stated in Eqs. (4-15a) and (4-15b) sourcing the solution

for the original nonhomogeneous equations with roots a_{s1} to a_{s6} and a_{h1} to a_{h6}. The auxiliary equations corresponding to Eqs. (4-13a) and (4-13b) are:

$$a_s{}^6 + X_s a_s{}^4 + Y_s a_s{}^2 + Z_s = 0\,, \qquad -r \le x \le +r \tag{4-15a}$$

and

$$a_h{}^6 + X_h a_h{}^4 + Y_h a_h{}^2 + Z_h = 0\,, \qquad \pm r \le x \le \pm\frac{s}{2} \tag{4-15b}$$

For the sake of thesis length, detailed calculation steps for the sagging section are explained in details and readers can simply use the same method to obtain the solution for the hogging region. Eq. (4-15a) is a polynomial equation of degree 6. Therefore, Eq. (4-15a) has 6 real and/or complex roots (not necessarily distinct). Considering $a_s{}^2 = \mu_s$, the following relation is obtained from Eq. (4-15a):

$$\mu_s{}^3 + X_s \mu_s{}^2 + Y_s \mu_s + Z_s = 0 \tag{4-16}$$

Considering $\mu_s = b_s - (X_s/3)$, Eq. (4-16) can be rewritten as

$$b_s{}^3 + 3\alpha_s b_s + 2\beta_s = 0 \tag{4-17}$$

where

$$\alpha_s = \frac{1}{3}\left(Y_s - \frac{X_s{}^2}{3}\right) \text{ and } \beta_s = \frac{1}{2}\left(\frac{2X_s{}^3}{27} - \frac{X_s Y_s}{3} + Z_s\right) \tag{4-18}$$

There are many solution types to Eq. (4-13a) depending on the auxiliary parameter Δ_s, where:

$$\Delta_s = -108\left(\alpha_s{}^3 + \beta_s{}^2\right) \tag{4-19}$$

It is well established in the literature (Avramidis and Morfidis, 2006; Morfidis, 2007) that the most common solution case corresponding to the positive sign of the auxiliary parameter Δ_s is

when $\Delta_s < 0$. Thus Eq. (4-19) converts to ${\alpha_s}^3 + {\beta_s}^2 > 0$ with one real and two conjugate complex roots. The real root (μ_{s1}) is as following:

$$\mu_{s1} = -\frac{X_s}{3} + \sqrt[3]{-\beta_s + \sqrt{\Delta_s}} + \sqrt[3]{-\beta_s - \sqrt{\Delta_s}} \tag{4-20a}$$

and the two complex roots (μ_{s2} and μ_{s3}) are as below:

$$\mu_{s2} = -\frac{X_s}{3} - \frac{1}{2}\left(\sqrt[3]{-\beta_s + \sqrt{\Delta_s}} + \sqrt[3]{-\beta_s - \sqrt{\Delta_s}}\right) + i\frac{\sqrt{3}}{2}\left(\sqrt[3]{-\beta_s + \sqrt{\Delta_s}} - \sqrt[3]{-\beta_s - \sqrt{\Delta_s}}\right) \tag{4-20b}$$

and

$$\mu_{s3} = -\frac{X_s}{3} - \frac{1}{2}\left(\sqrt[3]{-\beta_s + \sqrt{\Delta_s}} + \sqrt[3]{-\beta_s - \sqrt{\Delta_s}}\right) - i\frac{\sqrt{3}}{2}\left(\sqrt[3]{-\beta_s + \sqrt{\Delta_s}} - \sqrt[3]{-\beta_s - \sqrt{\Delta_s}}\right) \tag{4-20c}$$

If six roots of Eq. (4-15a) are known as a_{sj} where $j = 1-6$, then the solution of the homogeneous equation (Eq. (4-15a)) can be tabulated as:

$$a_{sj} = \begin{cases} +\sqrt{\mu_{s1}} = e^{\delta_s x}, & \text{Real root} \\ -\sqrt{\mu_{s1}} = e^{-\delta_s x}, & \text{Real root} \\ +\sqrt{\mu_{s2}} = e^{-\varepsilon_s x}\cos\sigma_s x, & \text{Complex root} \\ +\sqrt{\mu_{s3}} = e^{-\varepsilon_s x}\sin\sigma_s x, & \text{Complex root} \\ -\sqrt{\mu_{s2}} = e^{\varepsilon_s x}\cos\sigma_s x, & \text{Complex root} \\ -\sqrt{\mu_{s3}} = e^{\varepsilon_s x}\sin\sigma_s x, & \text{Complex root} \end{cases} \tag{4-21}$$

where

$$\begin{cases} \delta_s = \pm\sqrt{-\frac{X_s}{3} + \sqrt[3]{-\beta_s + \sqrt{\Delta_s}} + \sqrt[3]{-\beta_s - \sqrt{\Delta_s}}} \\ \varepsilon_s = \sqrt{\frac{1}{2}\left(\sqrt{{m_s}^2 + {n_s}^2} + m_s\right)} \\ \sigma_s = \sqrt{\frac{1}{2}\left(\sqrt{{m_s}^2 + {n_s}^2} - m_s\right)} \end{cases} \tag{4-22}$$

Following equations can be used to obtain m_s and n_s required in Eq.(4-22).

$$m_s = -\frac{1}{2}\left(\frac{2X_s}{3} + \sqrt[3]{-\beta_s + \sqrt{\Delta_s}} + \sqrt[3]{-\beta_s - \sqrt{\Delta_s}}\right) \tag{4-23a}$$

and

$$n_s = \frac{\sqrt{3}}{2}\left(\sqrt[3]{-\beta_s + \sqrt{\Delta_s}} - \sqrt[3]{-\beta_s - \sqrt{\Delta_s}}\right) \tag{4-23b}$$

To obtain the general solutions for Eqs. (4-13a) and (4-13b), the particular solutions (y_p) must be found. Thus, trial forms for the particular integral are assumed for the two differential equations with different constants which are presented in Eq. (4-24).

$$y_p = \begin{cases} y_{ps} = W_s \cos\left(\frac{2n\pi x}{s}\right), & -r \le x \le +r \\ y_{ph} = W_h \cos\left(\frac{2n\pi x}{s}\right), & \pm r \le x \le \pm\frac{s}{2} \end{cases} \tag{4-24}$$

where W_s and W_h are the arbitrary constants for the sagging and hogging regions, respectively. These trial functions are then substituted into the corresponding differential equations (i.e. Eqs. (4-13a) and (4-13b)) and the constants resulting in particular solutions are obtained. Subsequently, the following expressions are obtained for the particular solutions:

$$y_p = \begin{cases} y_{ps} = \left(\frac{k_u+k_l}{k_u k_l}\right) P_0 + \sum_{n=1}^{n=\infty} p_{ns} \cos\left(\frac{2n\pi x}{s}\right), & -r \le x \le +r \\ y_{ph} = \left(\frac{k_u+k_l}{k_u k_l}\right) P_0 + \sum_{n=1}^{n=\infty} p_{nh} \cos\left(\frac{2n\pi x}{s}\right), & \pm r \le x \le \pm\frac{s}{2} \end{cases} \quad (4\text{-}25)$$

where

$$p_{ns} = \frac{P_n\left[\frac{1}{k_u}\left(\frac{2n\pi}{s}\right)^4 + \frac{k_u}{GD_s}\left(\frac{D_s}{C} + \frac{D_s k_l}{k_u C} + \frac{G}{k_u}\right)\left(\frac{2n\pi}{s}\right)^2 + \frac{(k_u+k_l)}{GD_s}\right]}{\left(\frac{2n\pi}{s}\right)^6 + \frac{1}{G}\left(k_u+k_l+\frac{k_u GD_s}{C}\right)\left(\frac{2n\pi}{s}\right)^4 + \frac{k_u}{D_s}\left(1+\frac{k_l D_s}{GC}\right)\left(\frac{2n\pi}{s}\right)^2 + \frac{k_u k_l}{GD_s}} \quad (4\text{-}26a)$$

and

$$p_{nh} = \frac{P_n\left[\frac{1}{k_u}\left(\frac{2n\pi}{s}\right)^4 + \frac{k_u}{GD_h}\left(\frac{D_h}{C} + \frac{D_h k_u}{k_1 C} + \frac{G}{k_u}\right)\left(\frac{2n\pi}{s}\right)^2 + \frac{(k_u+k_l)}{GD_h}\right]}{\left(\frac{2n\pi}{s}\right)^6 + \frac{1}{G}\left(k_u+k_l+\frac{k_u GD_h}{C}\right)\left(\frac{2n\pi}{s}\right)^4 + \frac{k_u}{D_h}\left(1+\frac{k_l D_h}{GC}\right)\left(\frac{2n\pi}{s}\right)^2 + \frac{k_u k_l}{GD_h}} \quad (4\text{-}26b)$$

Finally, using the superposition principle, the solution of the governing differential equation (i.e. Eq. (4-13a)) for the settlement of the LTP with symmetric loading in the sagging region (i.e. for $-r \le x \le +r$) can be written as follows:

$$w_s^{LTP} = c_1 e^{-\delta_s x} + c_2 e^{\delta_s x} + e^{-\varepsilon_s x}(c_3 \cos\sigma_s x + c_4 \sin\sigma_s x) + e^{\varepsilon_s x}(c_5 \cos\sigma_s x + c_6 \sin\sigma_s x) + \left(\frac{k_u+k_l}{k_u k_l}\right) P_0 + \sum_{n=1}^{n=\infty} p_{ns} \cos\left(\frac{2n\pi x}{s}\right) \quad (4\text{-}27a)$$

Similarly, the solution of the governing differential equation for the deflection of the LTP with symmetric loading in the hogging region (i.e. for $\pm r \le x \le \pm s/2$) is given by:

$$w_h^{LTP} = d_1 e^{-\delta_h x} + d_2 e^{\delta_h x} + e^{-\varepsilon_h x}(d_3 \cos\sigma_h x + d_4 \sin\sigma_h x) + e^{\varepsilon_h x}(d_5 \cos\sigma_h x + d_6 \sin\sigma_h x) + \left(\frac{k_u+k_l}{k_u k_l}\right) P_0 + \sum_{n=1}^{n=\infty} p_{nh} \cos\left(\frac{2n\pi x}{s}\right) \quad (4\text{-}27b)$$

where δ_h, ε_h, and σ_h for the hogging section can be calculated following the similar procedures as described for the sagging region in Eqs. (4-22) and (4-23a). Once the deflections of LTP at different locations are obtained using Eqs. (4-27a) and (4-27b), the rotational angles of cross

sections of LTP, the shear forces generated in LTP, the bending moments developed in LTP, and the tension mobilised in the geosynthetic reinforcement for each section can be obtained as set out in the following sections.

Deflection of the shear layer embedded in the Kerr foundation can be expressed in terms of w_{LTP}. According to Eqs. (4-4) and (4-5):

$$q_s = k_u\left(w_s^{LTP} - w_s^{ls}\right), \qquad -r \le x \le +r \tag{4-28}$$

Then combination of Eqs. (4-28) and (4-9a) yields the following equation.

$$w_s^{ls} = U_1 w_s^{LTP\,iv} - \left(\frac{U_1 k_u}{C}\right) w_s^{LTP\,\prime\prime} + \left(\frac{U_1 k_u k_l}{CG} + 1\right) w_s^{LTP} - \left(\frac{U_1}{D_s}\right) p + \left(\frac{U_1}{C}\right) p'', \quad -r \le x \le +r \tag{4-29a}$$

Similarly, for the hogging region, deflection of the shear layer within the Kerr foundation is given by:

$$w_{h^{ls}} = U_2 w_h^{LTP\,iv} - \left(\frac{U_2 k_u}{C}\right) w_h^{LTP\,\prime\prime} + \left(\frac{U_2 k_u k_l}{CG} + 1\right) w_h^{LTP} - \left(\frac{U_2}{D_h}\right) p + \left(\frac{U_2}{C}\right) p'', \quad \pm r \le x \le \pm\frac{s}{2} \tag{4-29b}$$

where

$$U_1 = \frac{D_s CG}{k_u[CG - D_s(k_u + k_l)]} \text{ and } U_2 = \frac{D_h CG}{k_u[CG - D_h(k_u + k_l)]} \tag{4-30}$$

4.3.1. Rotation of LTP

According to the direction of bending moment (i.e. sagging or hogging), the rotation of the cross section of LTP (reinforced Timoshenko beam model) on the Kerr foundation model is given by:

$$\theta_{LTP} = \begin{cases} \theta_s^{LTP} = \frac{D_s}{C} w_s^{LTP'''} + w_s^{LTP'} - \frac{D_s}{C^2} q_s{}' + \frac{D_s}{C^2} p' , \ -r \le x \le +r \\ \theta_h^{LTP} = \frac{D_h}{C} w_h^{LTP'''} + w_h^{LTP'} - \frac{D_h}{C^2} q_h{}' + \frac{D_h}{C^2} p' , \ \pm r \le x \le \pm \frac{s}{2} \end{cases} \quad (4\text{-}31)$$

Substituting Eqs. (4-5) and (4-11) into Eq. (4-31) and then utilising Eq. (4-27a) lead to the governing equation for rotation of the cross section of LTP in sagging region which is written below.

$$\theta_s^{LTP} = -c_1 A_1 \delta_s e^{-\delta_s x} + c_2 A_1 \delta_s e^{\delta_s x} - c_3 e^{-\varepsilon_s x}(B_1 \sin \sigma_s x - C_1 \cos \sigma_s x) +$$
$$c_4 e^{-\varepsilon_s x}(C_1 \sin \sigma_s x + B_1 \cos \sigma_s x) - c_5 e^{\varepsilon_s x}(B_1 \sin \sigma_s x + C_1 \cos \sigma_s x) -$$
$$c_6 e^{\varepsilon_s x}(C_1 \sin \sigma_s x - B_1 \cos \sigma_s x) - \sum_{n=1}^{n=\infty} \left\{ \left[D_1 + E_1 \left(\frac{2n\pi}{s}\right)^4 - F_1 \left(\frac{2n\pi}{s}\right)^2 \right] p_{ns} + \right.$$
$$\left. \left[\left(\frac{GF_1 {D_s}^2}{C^2}\right) \left(\frac{2n\pi}{s}\right)^2 + \left[\left(\frac{GF_1 D_s}{C}\right) + \frac{D_s}{C^2} \right] \right] P_n \right\} \left(\frac{2n\pi}{s}\right) \sin\left(\frac{2n\pi x}{s}\right) \quad (4\text{-}32a)$$

In the same way, combining Eqs. (4-5), (4-11), (4-27b), and (4-31), the governing equation for rotation of the cross section of LTP in hogging region can be expressed as:

$$\theta_h^{LTP} = -d_1 A_2 \delta_h e^{-\delta_h x} + d_2 A_2 \delta_h e^{\delta_h x} - d_3 e^{-\varepsilon_h x}(B_2 \sin \sigma_h x - C_2 \cos \sigma_h x) +$$
$$d_4 e^{-\varepsilon_h x}(C_2 \sin \sigma_h x + B_2 \cos \sigma_h x) - d_5 e^{\varepsilon_h x}(B_2 \sin \sigma_h x + C_2 \cos \sigma_h x) -$$
$$d_6 e^{\varepsilon_h x}(C_2 \sin \sigma_h x - B_2 \cos \sigma_h x) - \sum_{n=1}^{n=\infty} \left\{ \left[D_2 + E_2 \left(\frac{2n\pi}{s}\right)^4 - \right. \right.$$
$$\left. \left. F_2 \left(\frac{2n\pi}{s}\right)^2 \right] p_{nh} + \left[\left(\frac{GF_2 {D_h}^2}{C^2}\right) \left(\frac{2n\pi}{s}\right)^2 + \left[\left(\frac{GF_2 D_h}{C}\right) + \frac{D_h}{C^2} \right] \right] P_n \right\} \left(\frac{2n\pi}{s}\right) \sin\left(\frac{2n\pi x}{s}\right) \quad (4\text{-}32b)$$

where

$$\begin{Bmatrix} A_1 = \delta_s \left({\delta_s}^4 E_1 + {\delta_s}^2 F_1 + D_1 \right) \\ A_2 = \delta_h \left({\delta_h}^4 E_2 + {\delta_h}^2 F_2 + D_2 \right) \end{Bmatrix}$$

$$\begin{cases} B_1 = \sigma_s[E_1(\sigma_s{}^4 - 10\varepsilon_s{}^2\sigma_s{}^2 + 5\varepsilon_s{}^4) + F_1(3\varepsilon_s{}^2 - \sigma_s{}^2) + D_1] \\ B_2 = \sigma_h[E_2(\sigma_h{}^4 - 10\varepsilon_h{}^2\sigma_h{}^2 + 5\varepsilon_h{}^4) + F_2(3\varepsilon_h{}^2 - \sigma_h{}^2) + D_2] \end{cases}$$

$$\begin{cases} C_1 = -\varepsilon_s[E_1(\varepsilon_s{}^4 - 10\varepsilon_s{}^2\sigma_s{}^2 + 5\sigma_s{}^4) + F_1(\varepsilon_s{}^2 - 3\sigma_s{}^2) + D_1] \\ C_2 = -\varepsilon_h[E_2(\varepsilon_h{}^4 - 10\varepsilon_h{}^2\sigma_h{}^2 + 5\sigma_h{}^4) + F_2(\varepsilon_h{}^2 - 3\sigma_h{}^2) + D_2] \end{cases}$$

$$\begin{cases} D_1 = 1 - \left(\frac{k_u k_l G_1 D_s{}^2}{C^2}\right) \\ D_2 = 1 - \left(\frac{k_u k_l G_2 D_h{}^2}{C^2}\right) \end{cases}$$

$$\begin{cases} E_1 = -\frac{G G_1 D_s{}^2}{C} \\ E_2 = -\frac{G G_2 D_h{}^2}{C} \end{cases}$$

$$\begin{cases} F_1 = \frac{D_s}{C}\left(1 + \frac{G k_u G_1 D_s}{C}\right) \\ F_2 = \frac{D_h}{C}\left(1 + \frac{G k_u G_2 D_h}{C}\right) \end{cases}$$

and

$$\begin{cases} G_1 = \frac{D_s}{C} - \frac{D_s}{C^2}\frac{G k_u}{k_u + k_l} \\ G_2 = \frac{D_h}{C} - \frac{D_h}{C^2}\frac{G k_u}{k_u + k_l} \end{cases} \quad (4\text{-}33)$$

4.3.2. Bending Moment and Shear Force in LTP

According to the theory of Timoshenko beam (1921), the relationship between moment and the rate of rotation angle change can be written as:

$$M_{LTP} = \begin{cases} M_s^{LTP} = -D_s \theta_s^{LTP\prime}, & -r \le x \le +r \\ M_h^{LTP} = -D_h \theta_h^{LTP\prime}, & \pm r \le x \le \pm\frac{s}{2} \end{cases} \quad (4\text{-}34)$$

By substituting Eq. (3-23a) into Eq.(4-34), the governing equations for the bending moments in the LTP can be obtained as:

$$M_s^{LTP} = -D_s\left\{c_1A_1{\delta_s}^2e^{-\delta_s x} + c_2A_1{\delta_s}^2e^{\delta_s x} + c_3e^{-\varepsilon_s x}(J_1\sin\sigma_s x - I_1\cos\sigma_s x) - \right.$$

$$c_4e^{-\varepsilon_s x}(I_1\sin\sigma_s x + J_1\cos\sigma_s x) - c_5e^{\varepsilon_s x}(J_1\sin\sigma_s x + I_1\cos\sigma_s x) -$$

$$c_6e^{\varepsilon_s x}(I_1\sin\sigma_s x - J_1\cos\sigma_s x) - \sum_{n=1}^{n=\infty}\left\{\left[D_1 + E_1\left(\frac{2n\pi}{s}\right)^4 - F_1\left(\frac{2n\pi}{s}\right)^2\right]p_{ns} + \right.$$

$$\left.\left.\left[\left(\frac{GF_1{D_s}^2}{C^2}\right)\left(\frac{2n\pi}{s}\right)^2 + \left[\left(\frac{GF_1D_s}{C}\right) + \frac{D_s}{C^2}\right]\right]P_n\right\}\left(\frac{2n\pi}{s}\right)^2\cos\left(\frac{2n\pi x}{s}\right)\right\} \quad (4\text{-}35a)$$

The following can be derived from Eqs. (4-32b) and (4-34):

$$M_h^{LTP} = -D_h\left\{d_1A_2{\delta_h}^2e^{-\delta_2 x} + d_2A_2{\delta_h}^2e^{\delta_h x} + d_3e^{-\varepsilon_h x}(J_2\sin\sigma_h x - I_2\cos\sigma_h x) - \right.$$

$$d_4e^{-\varepsilon_h x}(I_2\sin\sigma_h x + J_2\cos\sigma_h x) - d_5e^{\varepsilon_h x}(J_2\sin\sigma_h x + I_2\cos\sigma_h x) -$$

$$d_6e^{\varepsilon_h x}(I_2\sin\sigma_h x - J_2\cos\sigma_h x) - \sum_{n=1}^{n=\infty}\left\{\left[D_2 + E_2\left(\frac{2n\pi}{s}\right)^4 - F_2\left(\frac{2n\pi}{s}\right)^2\right]p_{nh} + \right.$$

$$\left.\left.\left[\left(\frac{GF_2{D_h}^2}{C^2}\right)\left(\frac{2n\pi}{s}\right)^2 + \left[\left(\frac{GF_2D_h}{C}\right) + \frac{D_h}{C^2}\right]\right]P_n\right\}\left(\frac{2n\pi}{s}\right)^2\cos\left(\frac{2n\pi x}{s}\right)\right\} \quad (4\text{-}35b)$$

According to the direction of bending moment (i.e. sagging or hogging) the shear force in LTP can be expressed as:

$$V_{LTP} = \begin{cases} V_s^{LTP} = C\left(w_s^{LTP\prime} - \theta_s^{LTP}\right), & -r \le x \le +r \\ V_h^{LTP} = C\left(w_h^{LTP\prime} - \theta_h^{LTP}\right), & \pm r \le x \le \pm\frac{s}{2} \end{cases} \quad (4\text{-}36)$$

By substituting Eqs. (4-27a) and (4-32a) into Eq. (4-36), the shear forces developed in the LTP can be obtained as:

$$V_s^{LTP} = C\left\{c_1K_1\delta_s e^{-\delta_s x} - c_2K_1\delta_s e^{\delta_s x} - c_3e^{-\varepsilon_s x}(M_1\sin\sigma_s x + L_1\cos\sigma_s x) - \right.$$

$$c_4e^{-\varepsilon_s x}(L_1\sin\sigma_s x - M_1\cos\sigma_s x) - c_5e^{\varepsilon_s x}(M_1\sin\sigma_s x - L_1\cos\sigma_s x) + \quad (4\text{-}37a)$$

$$c_6 e^{\varepsilon_s x}(L_1 \sin \sigma_s x + M_1 \cos \sigma_s x) + \sum_{n=1}^{n=\infty} \left[D_1 + E_1 \left(\frac{2n\pi}{s}\right)^4 - F_1 \left(\frac{2n\pi}{s}\right)^2 - 1 \right] p_{ns} +$$

$$\left[\left(\frac{GF_1 {D_s}^2}{C^2}\right) \left(\frac{2n\pi}{s}\right)^2 + \left[\left(\frac{GF_1 D_s}{C}\right) + \frac{D_s}{C^2} \right] \right] P_n \left(\frac{2n\pi}{s}\right) \sin \left(\frac{2n\pi x}{s}\right) \Bigg\}$$

Correspondingly, substituting Eqs. (4-27b) and (4-32b) into Eq.(4-36), the shear forces developed in the LTP in hogging region can be obtained as:

$$V_h^{LTP} = C \Bigg\{ d_1 K_2 \delta_h e^{-\delta_h x} - d_2 K_2 \delta_h e^{\delta_h x} - d_3 e^{-\varepsilon_h x}(M_2 \sin \sigma_h x + L_2 \cos \sigma_h x) -$$

$$d_4 e^{-\varepsilon_h x}(L_2 \sin \sigma_h x - M_2 \cos \sigma_h x) - d_5 e^{\varepsilon_h x}(M_2 \sin \sigma_h x - L_2 \cos \sigma_h x) +$$

$$d_6 e^{\varepsilon_h x}(L_2 \sin \sigma_h x + M_2 \cos \sigma_h x) + \sum_{n=1}^{n=\infty} \left[D_2 + E_2 \left(\frac{2n\pi}{s}\right)^4 - F_2 \left(\frac{2n\pi}{s}\right)^2 - 1 \right] p_{nh} \cdot$$

$$\left[\left(\frac{GF_2 {D_h}^2}{C^2}\right) \left(\frac{2n\pi}{s}\right)^2 + \left[\left(\frac{GF_2 D_h}{C}\right) + \frac{D_h}{C^2} \right] \right] P_n \left(\frac{2n\pi}{s}\right) \sin \left(\frac{2n\pi x}{s}\right) \Bigg\} \quad (4\text{-}37b)$$

where

$$\left\{ \begin{matrix} I_1 = \varepsilon_s C_1 + \sigma_s B_1 \\ I_2 = \varepsilon_h C_2 + \sigma_h B_2 \end{matrix} \right\}$$

$$\left\{ \begin{matrix} J_1 = \varepsilon_s B_1 - \sigma_s C_1 \\ J_2 = \varepsilon_h B_2 - \sigma_h C_2 \end{matrix} \right\}$$

$$\left\{ \begin{matrix} K_1 = \delta_s - A_1 \\ K_2 = \delta_s - A_2 \end{matrix} \right\}$$

$$\left\{ \begin{matrix} L_1 = \varepsilon_s + C_1 \\ L_2 = \varepsilon_h + C_2 \end{matrix} \right\} \quad (4\text{-}38)$$

and

$$\left\{ \begin{matrix} M_1 = \sigma_s - B_1 \\ M_2 = \sigma_h - B_2 \end{matrix} \right\}$$

4.3.3. Tension in Geosynthetic Reinforcement

Tension mobilised in the geosynthetic reinforcement is the product of axial strain in the geosynthetic reinforcement (which is assumed to be equal to the strain developed in the LTP at the location of geosynthetic reinforcement) and the tensile stiffness of the geosynthetic reinforcement. Following the Timoshenko beam theory and depending on the bending moment directions, the tension mobilised in the geosynthetic reinforcement can be expressed as follows:

$$T = \begin{cases} -S_r^b\left(y_r^b + y_s\right)\theta_s^{LTP'}, & -r \le x \le +r \\ -S_r^t\left(y_r^t + y_h\right)\theta_h^{LTP'}, & \pm r \le x \le \pm\frac{s}{2} \end{cases} \quad (4\text{-}39)$$

where y_r^t and y_r^b are the distances from the top and bottom geosynthetic layer to the centroid axis, respectively as shown in Figure 4.2b; y_s and y_h are the distances between neutral axis and centroid axis of LTP within the sagging and hogging moment sections, respectively as shown in Figure 4.2b−c; and S_r^t and S_r^b are the tensile stiffnesses of top and bottom geosynthetic reinforcements, respectively.

4.3.4. Pressure Distribution under LTP

Combining Eqs. (4-4), (4-7a), and (4-9a), the pressure distribution under the LTP for $-r \le x \le +r$ can be obtained as below:

$$q_s = \frac{GCD_s}{[D_s(k_u+k_l)-GC]} w_s^{LTP^{iv}} - \frac{k_u D_s G}{[D_s(k_u+k_l)-GC]} w_s^{LTP''} + \frac{k_u k_l D_s}{[D_s(k_u+k_l)-GC]} w_s^{LTP} - \frac{GC}{[D_s(k_u+k_l)-GC]} p + \frac{D_s GC}{[D_s(k_u+k_l)-GC]} p'' \quad (4\text{-}40a)$$

Similarly, from Eqs. (4-4), (4-7b), and (4-9b), the pressure distribution under the LTP for $\pm r \le x \le \pm s/2$ can be expressed as:

$$q_h = \frac{GCD_h}{[D_h(k_u+k_l)-GC]} w_h^{LTP^{iv}} - \frac{k_u D_h G}{[D_h(k_u+k_l)-GC]} w_h^{LTP''} + \frac{k_u k_l D_h}{[D_h(k_u+k_l)-GC]} w_h^{LTP} - \frac{GC}{[D_h(k_u+k_l)-GC]} p + \frac{D_h GC}{[D_h(k_u+k_l)-GC]} p'' \quad (4\text{-}40b)$$

4.3.5. Boundary and Continuity Conditions

Referring to Eqs. (4-27a) and (4-27b), there are twelve constants of integration (c_1 to c_6 and d_1 to d_6) and one unknown length (r) that can be estimated using the boundary and continuity conditions. Due to symmetric loading, at the middle of loaded region, the shear force and the slope of the deflected LTP are zero. Additionally, it is presumed that at the column location, the shear force produced in LTP is equivalent to the reaction force from the column. It is also assumed here that due to inclusion of the geosynthetic reinforcement in LTP and continuity of LTP above the column, LTP will not be rotating at the column support. Summary of the above-mentioned boundary conditions are expressed in Eq. (4-41).

$$\text{at } x = 0, \begin{cases} V_s^{LTP} = 0 \\ w_s^{LTP'} = 0 \end{cases} \quad \text{and} \quad \text{at } x = \frac{s}{2}, \begin{cases} V_h^{LTP} = -(K_c)_{eq} w_h^{LTP} \\ \theta_h^{LTP} = 0 \end{cases} \quad (4\text{-}41)$$

where $(K_c)_{eq}$ is the equivalent modulus of subgrade reaction for a column in a plane strain condition (kN/m) which can be calculated as Eq. (4-42).

$$(K_c)_{eq} = \frac{(E_c)_{eq}}{H_c} \times \frac{A_c}{s} \quad (4\text{-}42)$$

where A_c is the area of the column in plane strain condition (i.e. $A_c = s \times d$); s and d are the clear spacing and the diameter of the column, respectively as shown in Figure 4.3a; H_c is the length of column; and $(E_c)_{eq}$ is the equivalent elastic modulus of the column wall in plane strain condition. Since in the field, discrete columns are placed in a square or triangular pattern, the equivalent plane strain material stiffness must be determined for the two-dimensional plane

strain modeling. In the literature, there are two approaches for plane strain equivalent conversion (Tan *et al.*, 2008). In the first approach, the width of the column (in plane-strain condition) can be taken equal to the diameter of the column (in axisymmetric condition). However, the material stiffness in axisymmetric model should be converted to equivalent plane-strain material stiffness by the suggested relationship based on the matching of the column–soil composite stiffness. This approach was adopted by Huang and Han (2009) where the equivalent elastic modulus and cohesion of the deep mixing walls of geosynthetic-reinforced column-supported embankments were calculated during the investigation of coupled mechanical and hydraulic mechanism. In the second approach, geometrical conversion can be done to obtain similar response in both axisymmetric and plane-strain conditions as adopted by Tan *et al.* (2008). In this study, first approach to convert a 3D or axisymmetric model into an equivalent plane-strain model is adopted. The equivalent modulus of columns is calculated using the area replacement ratio as stated by Huang et al. (2009) as follows:

$$(E_c)_{eq} = E_c a_r + E_s(1 - a_r) \tag{4-43}$$

where E_c and E_s denote the elastic moduli of the column and soft soil, respectively; while a_r is the area replacement ratio. Similar approach (i.e. first approach) was adopted by Huang et al. (2009) and Deb and Mohapatra (2013) where deep mixing columns and stone columns supported embankments were analysed in plane-strain condition in which the equivalent plane-strain material stiffness of column was determined using the suggested relationship based on the matching of the column–soil composite stiffness.

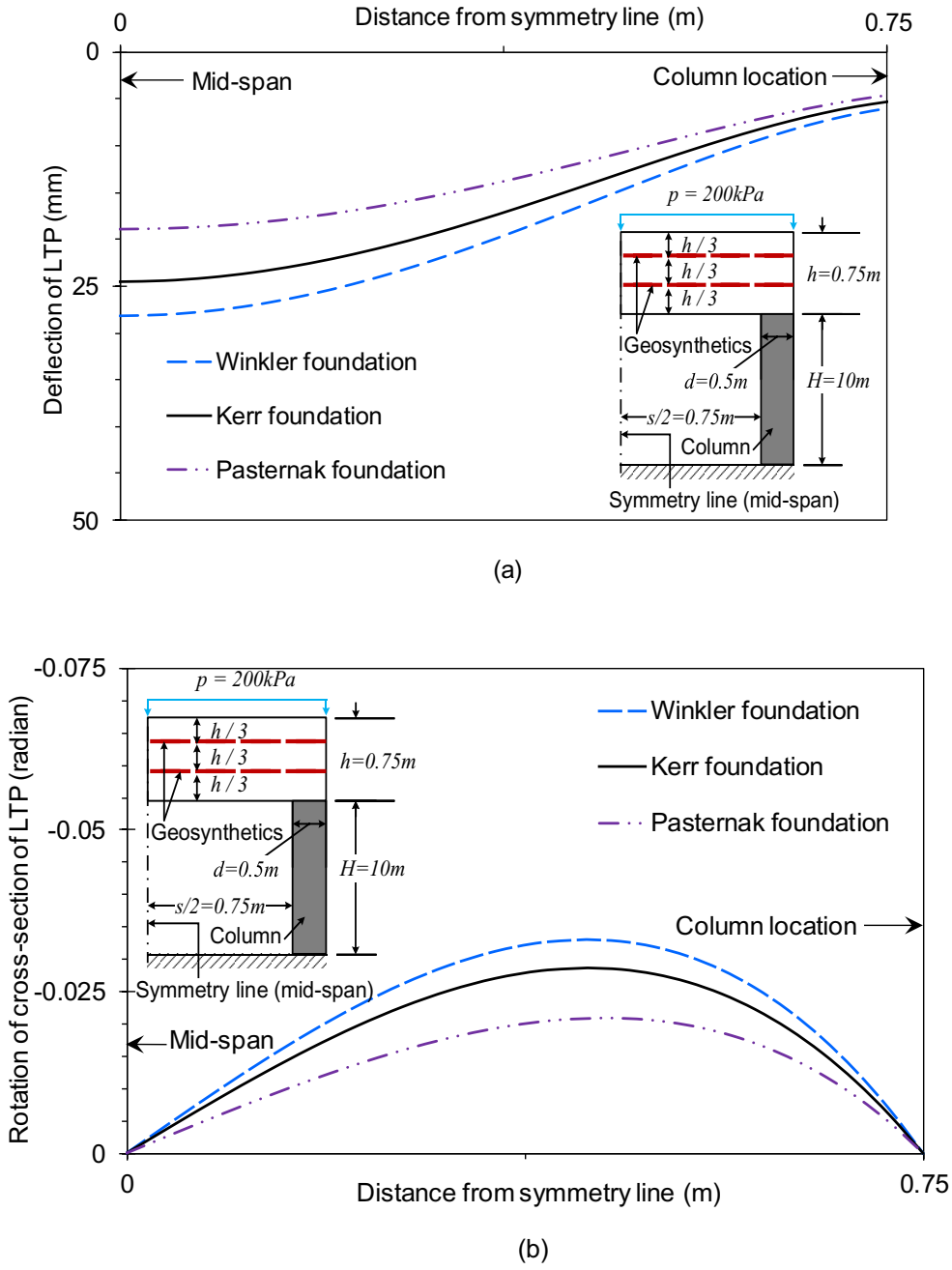

Figure 4.3. Comparison of: (a) settlement and (b) rotation profiles of LTP considering soft soil as Kerr, Pasternak, and Winkler foundation models.

On the other hand, the effective cross section of the LTP in the sagging region (the left side of point "A" as shown in Figure 4.2a) is not the same as the hogging region (right side of point "A"). Hence, the deformations and internal forces in the LTP beam should be represented by two separate functions. However, the deflection curve and internal forces of LTP are physically

continuous at point "A" and therefore the continuity conditions for the deformations and moments must be satisfied at point "A". Each of these continuity conditions yields to an equation for evaluating the unknowns. The continuity conditions can be summarised as below:

$$\text{at } x = r \text{ (Point "A")}, \begin{cases} w_s^{LTP} = w_h^{LTP} \\ \theta_s^{LTP} = \theta_h^{LTP} \\ M_s^{LTP} = 0 \\ M_h^{LTP} = 0 \\ V_s^{LTP} = V_h^{LTP} \end{cases} \quad (4\text{-}44)$$

To obtain the continuity conditions for the shear layer in Kerr model, similar continuity conditions can be applied at a distance “r” (i.e. at point “A”) from the symmetry line since in this study 1-D settlement of soft soil has been considered.

$$\text{at } x = r, \begin{cases} w_s^{ls} = w_h^{ls} \\ w_s^{ls'} = w_h^{ls'} \end{cases} \quad (4\text{-}45)$$

Similar to LTP, at the column location, it is assumed that the shear force developed in shear layer is equal to the reaction force from the column. Hence, the varied shear strain along the column length is considered in this study. In addition, as a result of symmetricity, at the mid span shear force in the shear layer should be zero. Thus, the boundary conditions of the shear layer can be summarised as below.

$$\text{at } x = \frac{s}{2} (\text{i. e. at column location}),\ V_h^{ls} = (K_c)_{eq} \left(\frac{G}{C}\right) w_h^{ls} \quad \text{and}$$

$$\text{at } x = 0 (\text{i. e. at mid} - \text{span}),\quad w_s^{ls'} = 0 \quad (4\text{-}46)$$

Replacing the expressions for deflection, rotation of the cross section, moment, and shear force of LTP and the shear layer from Eqs. (4-27), (4-29), (4-32), (4-35), and (4-37) respectively into the boundary and the continuity conditions (Eqs.(4-41), (4-44) and (4-46)) yields thirteen algebraic equations which are summarised in Appendix B. Once all the constants of integration and unknown lengths are determined by solving the simultaneous equations, then the deflections, bending moments, shear forces, rotations of the LTP, and mobilised tension in the geosynthetic reinforcement at any point in the LTP can be determined.

Although the overall behaviour of LTP due to bending and shear actions on a soft soil foundation can be predicted using the proposed mechanical model, it should be noted that possible pull-out resistance force of geosynthetic reinforcement, permeability of soft soil, and cyclic loading can significantly affect the performance of soft soil (Indraratna et al., 2005; Suksiripattanapong et al., 2012; Indraratna et al., 2013b).

4.4. Results and Discussions

Due to symmetry, only half of the problem is considered for the parametric study. Based on the formulations and for the sake of convenience and practical use, all the algebraic equations have been programmed in MATLAB R2016b (MathWorks) (shown in Appendix C) and the results are presented graphically. Similar to Maheshwari and Viladkar (2009), Zhang et al. (2012b), and Lei et al. (2016), to evaluate the accuracy of implementation of the Kerr foundation model as the soft soil model, the response of double layer geosynthetic reinforced LTP, the tension mobilised in the geosynthetic reinforcement, and stress concentration ratio are compared with the results gained from the Pasternak and the Winkler foundation models. Maheshwari and Viladkar (2009) developed a mechanical model for geosynthetic reinforced soil–foundation system subjected to strip loading and carried out a parametric study to understand the effect of various parameters influencing the response of such a system without validating the proposed model with

field or experimental results. Zhang et al. (2012b) proposed a mechanical model of geocell mattress subjected to symmetric loads and the presented solution was verified through comparison with the other existing published solutions namely Zhang et al. (2010) and Qu (2009). Lei et al. (2016) derived an analytical solution to predict consolidation with vertical drains under impeded drainage boundary conditions and multi-ramp surcharge loading. To verify the validity and accuracy of the proposed analytical solution, the results calculated from the proposed solution were compared to those given by the analytical solution of Gray (1944). As far as the maximum settlement of LTP and tension mobilised in the geosynthetic reinforcement (GR) are concerned, the parametric studies have been carried out to show the effects of various parameters on the maximum settlement of LTP and tension mobilised in the geosynthetic reinforcement when the soft soil is idealised by the Kerr foundation model. In this study, mobilised tension in the reinforcement is expressed as a normalised form (T/T_y) assuming ultimate or yield strength of geosynthetic reinforcement is 10% of tensile stiffness of geosynthetic (i.e. $T_y = 10\% \times S_r$). Additionally, the results of a double layer geosynthetic reinforced granular fill are compared with a single layer geosynthetic reinforced granular fill. Most of the guidelines adopt single layer of geosynthetics, whereas in practice, it is often common to use two or three layers of geosynthetics. However, to reduce the thickness of LTP, use of single layer but stronger geosynthetic reinforcement may be a good option. Thus, the intention of this parametric study is to investigate whether the use of one stronger geosynthetic layer (e.g. 1×2000 kN/m) with the equivalent stiffness of two weaker geosynthetic layers (e.g. 2×1000 kN/m), results in the same settlement of LTP and the tension of the geosynthetic reinforcement when compared to two weaker geosynthetic layers or not. For the sake of reasonable comparison, similar overall tensile stiffness due to the geosynthetic layers is adopted. For example, 2×1000 kN/m tensile stiffness of geosynthetics for the double layer is compared with 1×2000 kN/m tensile stiffness of a single layer geosynthetics. For two layers' case, geosynthetic reinforcement is placed such

that the reinforcement layers equally divide the granular fill layer while the one layer of geosynthetic layer is simply placed at the centre of granular layer for the single layer case. It has been noticed in the literature that many researchers placed the single layer of geosynthetic reinforcement at the mid-level of LTP in their studies (Liu et al., 2007; Nunez et al., 2013). However, it should be noted that geosynthetics can be placed at any level of LTP in case of single layer analysis in the proposed mechanical model. For practical application purposes, the spring constants and the shear modulus of soft soil can be estimated following the procedures proposed by Jones and Xenophontos (1976) for the Kerr foundation model which are summarised as below:

$$k_u = \frac{E_1(1-\nu_1)}{h_1(1-\nu_1-2\nu_1{}^2)}\ ;\ k_l = \frac{E_2\gamma(1-\nu_2)(\sinh\gamma h_2\cosh\gamma h_2+\gamma h_2)}{2(1-\nu_2-2\nu_2{}^2)\sinh^2\gamma h_2};\ \text{and}$$

$$G = \frac{E_2(\sinh\gamma h_2\cosh\gamma h_2-\gamma h_2)}{4\gamma(1+\nu_2)\sinh^2\gamma h_2} \tag{4-47}$$

where Jones and Xenophontos (1976) assumed a foundation consisting of two layers with elastic coefficients (E_1, ν_1) and (E_2, ν_2) and thicknesses h_1 and h_2 as illustrated in Figure 4.1a, respectively. The term γ is a constant, governing the vertical deformation profile. In this study, it is assumed that $\gamma = 0.46$ at the mid-depth of the second layer with thickness h_2 as Kneifati (1985) assumed in his study. Since the analytical solution for homogeneous soil deposit is obtained for one layer only (i.e. $H = 10$ m), and in order to determine the corresponding parameters for the Kerr foundation, (see Eq. (4-47)), it is assumed that $h_1 = 1$ m; $h_2 = 9$ m; $E_1 = E_2 = E_s = 1000$ kPa; $\nu_1 = \nu_2 = \nu_s = 0.3$. Following the Kerr foundation model, it is presumed that the upper layer of soft soil experiences significant shear deformations (exceeding the shear strength of the soft soil) as commonly modelled by the Winkler foundation. While the lower layer in Kerr foundation model is subjected to both compressive

and shear stresses without exceeding the shear strength. Therefore, h_1 and h_2 have been selected in such a way that the maximum shear stress generated in the top section of the soft soil (h_1) reaches the shear strength of the soil, while the shear strength of the soft soil is not exceeded in the bottom part (h_2). It has been noticed that decreasing the depth of upper layer results in larger shear stresses generated in the bottom part of the soft soil (h_2) which exceeds the shear strength of the soft soil. The foregoing solution is evaluated for a uniform load of 200 kPa which includes the self-weight of LTP. The proposed analytical model is a generalised model to analyse the ground stabilised using columns (such as concrete injected columns, piles, deep soil mixing columns) where load transfer platform is used to enhance the distribution of the load from the super-structures (such as silos, and fuel tanks) to the columns. However, typical properties of concrete injected columns (CICs) from a real project in Australia (Highway upgrade, approximately 100 km south of Sydney), is adopted in this study. The material properties used in this study for the reference case are summarised in Table 4.1.

Table 4.1. Properties of materials used in the baseline analysis.

Material	Parameters	
Soft soil	Stiffness (E_s) = 1000 kPa, Poisson's ratio (ν_s) = 0.3	
CIC	Stiffness (E_c) = 10,000 MPa, Poisson's ratio (ν_c) = 0.25	
Geosynthetics	Multilayer	Tensile stiffness ($S_r^t = S_r^b$) = 1000 kN/m, Poisson's ratio ($\nu_r^t = \nu_r^b$) = 0.3
	Single layer	Tensile stiffness (S_r) = 2000 kN/m, Poisson's ratio (ν_r) = 0.3
Granular fill	Stiffness (E_g) = 35 MPa, Poisson's ratio (ν_g) = 0.3	

For the parametric study, one parameter is changed at one time to investigate the influence of that particular parameter. The adopted range of the parameters for the parametric study

summarised in Table 4.2 is considered to cover the typical ranges observed in real projects for the column improved soft soil.

Table 4.2. Adopted range of parameters used in the parametric study.

Influencing factor	Range of value
Stiffness of soft soil, E_s (kPa)	1000*, 2000, 3000, 4000
Centre to centre spacing of columns, S (m)	1.75, 2.0*, 2.25, 2.5
Tensile stiffness of geosynthetics, (kN/m)	S_r^t: 1000*, 2000, 3000, 4000
	S_r^b : 1000*, 2000, 3000, 4000
	S_r: 2000*, 4000, 6000, 8000
Thickness of granular layer, h (m)	0.625, 0.75*, 0.875, 1
Loading, p (kPa)	125, 150, 175, 200*

∗Parameters used for baseline analysis.

In addition, the calculated LTP parameters for double and single layer cases for the baseline case are summarised in Table 4.3.

4.4.1. Predictions of Kerr Foundation Versus Other Foundation Models

In order to verify the validity and accuracy of the proposed analytical solution, the results calculated from the proposed solution for load transfer platform are compared with those given by the analytical solution of the same LTP resting on the Winkler (1867) and the Pasternak (1954) foundations. It is noted that when the shear modulus is equal to zero (i.e. $G = 0$), Eqs. (4-10a) and (4-10b) reduce to fourth-order governing differential equations which simulates the response of LTP on Winkler foundation model. Additionally, when the upper spring modulus approaches infinite (i.e. $k_u \rightarrow \infty$), Eqs. (4-10a) and (4-10b) are reduced to a fourth-

order governing differential equations of the LTP on Pasternak foundation model. For the Winkler model, according to Horvath (1983)

$$k_w = \frac{E_s}{H} \tag{4-48}$$

Table 4.3. Calculated parameters of reinforced granular layer for baseline case.

Parameters	Double layer	Single layer
h_s (m)	0.14	0.16
h_h (m)	0.14	0.16
y_s (m)	0.23	0.22
y_h (m)	0.23	0.22
D_s (kN.m)	161	140
D_h (kN.m)	161	140
C (kN/m)	9.2×10^3	9.2×10^3

For the Pasternak model, according to Kerr (1964)

$$k_p = \frac{E_s}{H} \quad \text{and} \quad G_p = \frac{E_s H}{6(1+\nu_s)} \tag{4-49}$$

Figure 4.3a shows a comparison of the deflection of the LTP adopting the Kerr foundation model to simulate the soft soil against the Winkler and the Pasternak models. There are notable variations in the predictions considering different foundation models. As evident, adopting the Winkler foundation model results in larger deflection of LTP compared to the Kerr foundation model. In contrast, Pasternak model results in less deflection of LTP than the Kerr foundation model. For example, the maximum deflection of LTP adopting the soft soil as Winkler foundation model is about 29 mm, while in Kerr foundation model case the value drops to 25 mm, shown in Figure 4.3a. Winkler model only considers the compressibility of the soft soil

without any shear resistance. Therefore, the soft soil which is idealised by the Winkler foundation model is prone to an excessive settlement resulting in the largest deformation of the LTP. In contrast, Pasternak foundation model predicts the maximum deflection of LTP of 18 mm, which is 28% less than the corresponding value from the Kerr foundation model as given in Figure 4.3a. Since the Pasternak shear layer beneath the LTP is a continuous layer deforming based on elastic shear only, minimum settlement of soil and consequently LTP is occurred. In case of the soft soil idealised by the Kerr foundation, the soil just below the LTP (from the ground surface up to h_1) deforms due to the compressibility of the soft soil only, while in deeper areas both shear resistance and compressibility of the soft soil are contributing to the deformation. Therefore, soft soil simulated with the Kerr foundation behaves stiffer than the Winkler foundation while being softer than the Pasternak foundation. Hence, the Kerr foundation model predicts the deformations more realistically between two upper and lower bounds which are the Winkler and the Pasternak foundation models, respectively.

Figure 4.3b shows the predictions of the variation of the rotations of the LTP adopting the soft soil as Kerr, Winkler, and Pasternak foundation models. It is noticed that the Winkler foundation predicts larger LTP rotation compared to the Kerr foundation model. In contrast, the Pasternak model calculates less rotation of LTP compared to the Kerr model. For example, the maximum rotation of LTP when the Kerr foundation model is adopted for the soft soil is -0.03 radians, which increases to -0.04 radians for the Winkler foundation model (i.e. 33% increase) and decreases to -0.019 radians for the Pasternak foundation model (i.e. 37% decrease) as displayed in Figure 4.3b. This is since implementing the Winkler model predicts the largest deformation of the LTP (see Figure 4.3a); hence the largest rotation of LTP is achieved in the Winkler model. In contrast, adopting the Pasternak model predicts the smallest deformation of LTP (see Figure 4.3a), it results in the least rotation of LTP. Accordingly, the

Kerr foundation model predicts the rotations more precisely which is between two upper and lower bounds corresponding to the Winkler and the Pasternak foundation models, respectively.

In Figure 4.4a, the distribution of the bending moment along the length of the LTP is presented. It is observed that the maximum positive and negative moments in the LTP adopting the Winkler foundation model are approximately 6% and 12% more, respectively, than the corresponding values when the Kerr foundation model is used to simulate the soft soil. In contrast, Pasternak model predicts smaller positive (sagging) and negative (hogging) bending moments in the LTP compared to the Kerr foundation model. As an illustration, the Pasternak foundation model estimates the maximum positive and negative moments in the LTP approximately 35% and 21% less than the corresponding values when the Kerr foundation model is used to simulate the soft soil, respectively, as illustrated in Figure 4.4a. Referring to Figure 4.3a, since implementing the Winkler model results in the largest deformation of the LTP, the largest moments in the LTP are developed correspondingly. In contrast, the Pasternak model predicts the smallest deformation of LTP (see Figure 4.3a), hence it predicts the least moments in the LTP. Accordingly, similar to the deformations reported, the Kerr foundation model calculates the moments more accurately, which are between the upper (i.e. Winkler foundation) and lower bounds (i.e. Pasternak foundation).

Figure 4.4b shows a comparison of the shear forces developed in the LTP using the Kerr foundation model to pretend the soft soil against the Winkler and the Pasternak foundation models. From Figure 4.4b it is depicted that the Winkler model estimates larger shear force in LTP as compared to the Kerr model. Whereas, the Pasternak model predicts less shear force in the LTP incomparision to the Kerr model. For example, the maximum shear force in LTP adopting the Kerr foundation model is 131 kN/m, which increases to 140 kN/m and reduces to 128 kN/m in the Winkler and the Pasternak foundation models, respectively. Since adopting

the Winkler model predicts larger deflection of LTP compared to the Kerr model (refer to Figure 4.3a), shear force induced in the LTP is also greater. On the other hand, adopting the Pasternak model predicts less deflection of LTP incomparision to the Kerr model (see Figure 4.3a); hence predicted shear force induced in LTP is also smaller.

Figure 4.4c represents the variation of shear forces developed in the soft soil between two columns. As expected, at the mid span, the shear force in the soil is zero due to the symmetric condition while the Kerr and the Pasternak foundation models are used to idealise the soft soil. As evident in Figure 4.4c, the shear forces generated in the soft soil for the Pasternak model are greater than those of the Kerr model. Simulating the soft soil as Winkler foundation model, the shear modulus of soft soil is assumed to be zero; therefore, no shear stresses can be predicted in the soft soil as shown in Figure 4.4c. When the soft soil is idealised by the Pasternak shear layer, a shear layer is attached to the bottom of the load transfer platform at the ground surface. Hence the soft soil layer underneath the LTP is exposed to shear stresses which may unrealistically exceed the shear strength of the soft soil (violating the elastic assumption used in Pasternak shear layer theory) as shown in Figure 4.4c.

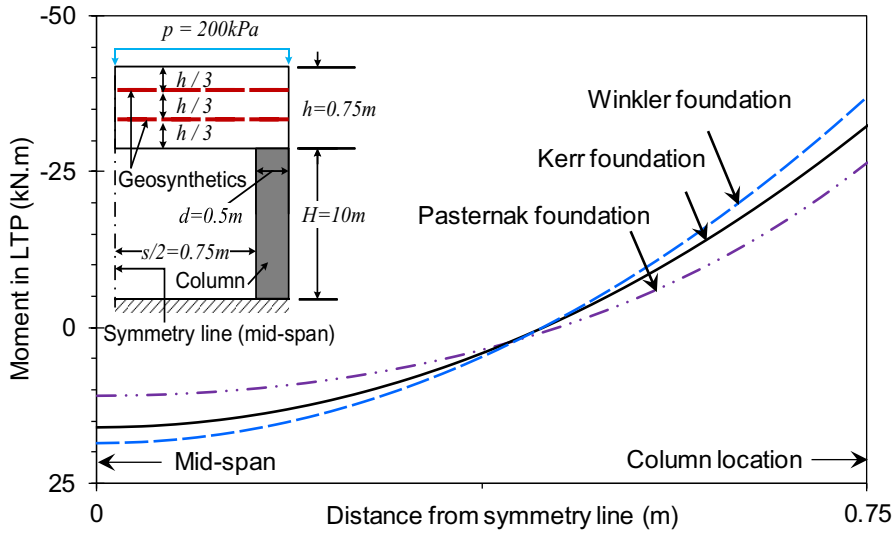

(a)

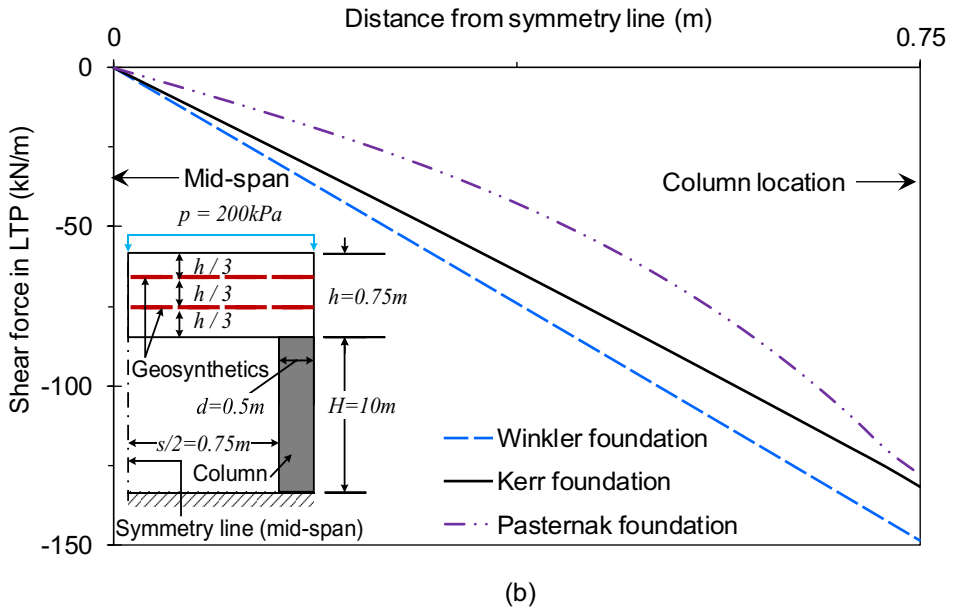

(b)

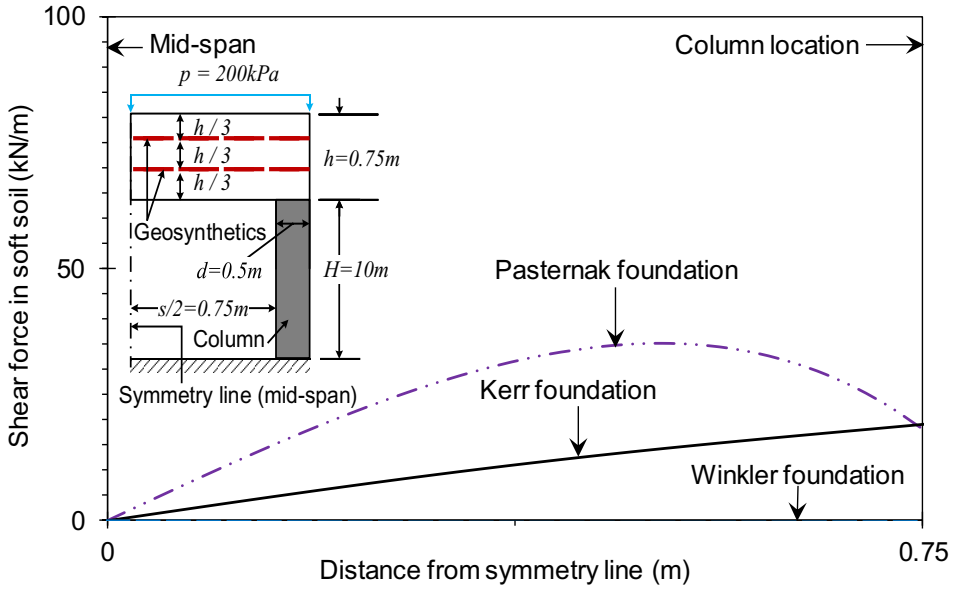

(c)

Figure 4.4. Comparison of: (a) bending moment of LTP, (b) shear force in LTP, and (c) shear force developed in soft soil considering soft soil as Kerr, Pasternak, and Winkler foundation models.

Figure 4.5a shows the mobilised tension in the top geosynthetic layer adopting the Kerr, Winkler, and Pasternak foundation models to simulate the soft soil. The predicted maximum normalised tensions mobilised in the top geosynthetic layer simulating the soft soil adopting the Kerr and the Winkler foundation models are found to be 0.53 and 0.47 kN/m (i.e. 13%

larger than corresponding value when the Kerr model is used); while in the Pasternak foundation case that value is 0.38 (i.e. 20% less than corresponding value while the Kerr model is adopted). Referring to Figure 4.3a, as the LTP resting on Winkler foundation deflects greater than the Kerr foundation model, more axial strains and tensions are mobilised in the geosynthetic reinforcement than the Kerr foundation model. In contrast, the Pasternak model results in the smaller deformation of LTP when compare to the Kerr model (see Figure 4.3a), hence less axial strains and tensions are mobilised in the geosynthetic reinforcement than the Kerr foundation model. Similarly, the maximum tension in the bottom geosynthetic reinforcement at the mid-span is achieved when the Winkler foundation is adopted while the minimum tension in the bottom geosynthetic reinforcement corresponding to the Pasternak foundation case, which is demonstrated in Figure 4.5b. The predicted maximum normalised tension generated in the bottom geosynthetic layer, simulating the soft soil adopting the Kerr, is 0.23, which rises to 0.27 (i.e. 15% increase) and drops to 0.15 (i.e. 44% decrease) while the Winkler and the Pasternak foundation models are adopted to idealise the soft soil, respectively. Figure 4.5a–b also display that larger tensions hence larger strains are generated at the column edge than in the mid-span. van Eekelen et al. (2015) reported that strains are larger at the edges of the pile caps than in the centre of the GR strips while validating the limit equilibrium models for the arching of basal reinforced piled embankments. However, like a continuous reinforced beam, bottom layer would be under compression at the column location (due to the assumption of small cracks propagation), and since, the geosynthetics only carries tension, there would be no forces mobilised in the geosynthetics. However, when geosynthetics is not stiff enough and granular material is very stiff, then the tension cracks can open and go through low layers of geosynthetics. In that case, the bottom geosynthetic may also attract tension. To consider cracks propagating deep inside the LTP, putting both geosynthetic layers under tension, Eq. (4-1) can be used. However, for the selected case study and parametric study, cracks only cross

one layer of geosynthetics due to the geometry and material properties used. Hence, bottom geosynthetic was not subjected to tension.

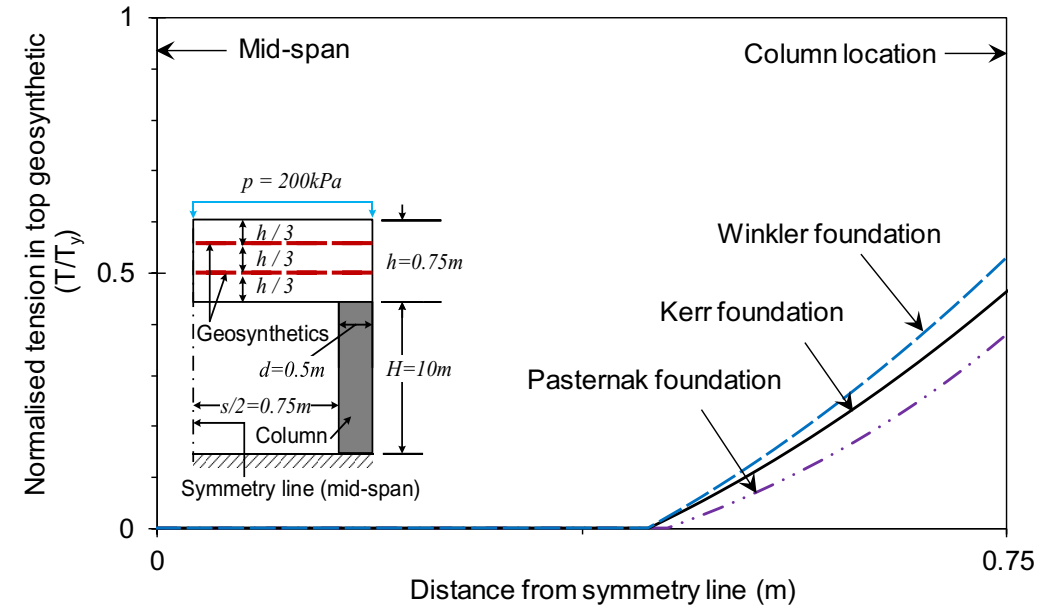

(a)

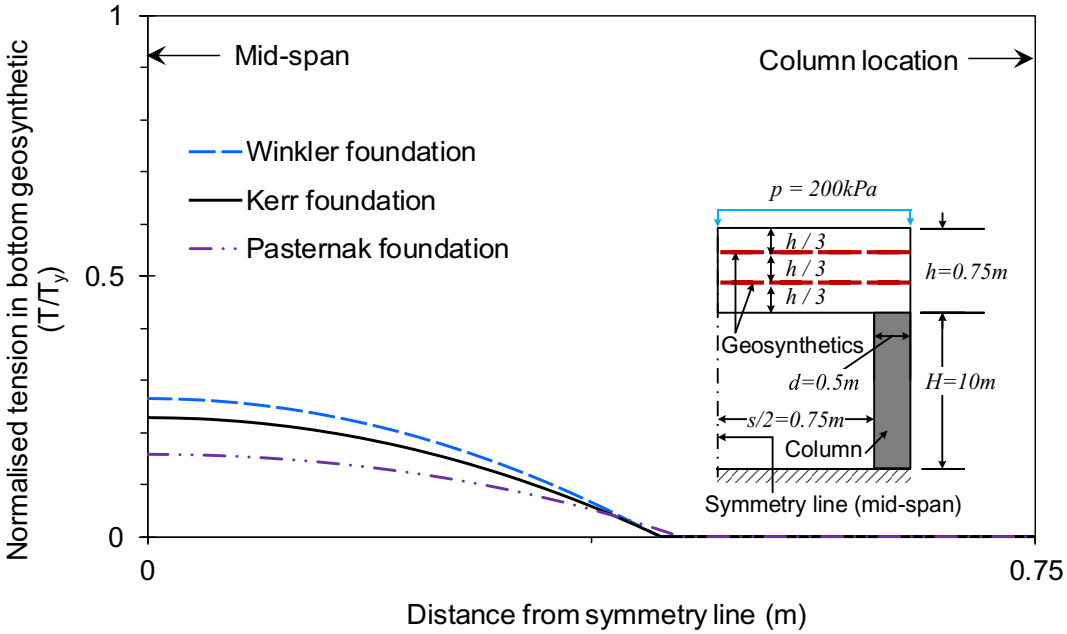

(b)

Figure 4.5. Comparison of mobilised tensions in: (a) top and (b) bottom geosynthetic layers considering soft soil as Kerr, Pasternak, and Winkler foundation models.

The stress concentration ratios (SCR) when the soft soil is simulated with the Kerr, the Pasternak, and the Winkler foundation models have also been examined in this study. The stress concentration ratio is usually used to analyse the load distribution between the columns and the soil. The higher the stress concentration ratio, the more stress is transferred onto the columns. Since the stress distribution at the interface of LTP and soft soil is not uniform, average stress transferred to the soil is used to determine the stress concentration ratio. The stress concentration ratio can be stated as (Han and Gabr, 2002; Indraratna et al., 2013a):

$$(\mathrm{SCR})_{\mathrm{avg}} = \frac{\sigma_c}{\overline{\sigma}_s} \tag{4-50}$$

where σ_c is the stress distributed to the columns and $\overline{\sigma}_s$ is the average stress transferred to the soil on the surface. The stress concentration ratio for the soft soil idealised as the Winkler foundation is larger than that of the Kerr foundation. Since the behaviour of soft soil under applied load simulated with the Winkler foundation is softer than that of the Kerr foundation model, almost entire applied loads transferred to the column. Very less stresses transferred to the soft soil. Hence very large SCR (SCR = 90) is observed for the Winkler foundation model case. In contrast, the stress concentration ratio for the soft soil idealised as the Pasternak foundation (SCR = 6) is less than that of the Kerr foundation (SCR = 15). Inclusion of the shear layer just beneath the LTP reduces the load transfer to the columns. In other words, soft soil simulated with the Pasternak foundation model behaves stiffer than that of the Kerr foundation model and results in the reduction of the stresses transferred to the column; hence least stress concentration ratio is observed. Similar ranges of stress concentration ratios (as Kerr and Pasternak foundation models) were reported by Han (2001) while stone column reinforced soft soil was analysed.

By comparing the Kerr model to the Winkler and the Pasternak models, it is evident that the combined effect of shear and compression of soft soil results in the most accurate prediction of

the response of LTP on soft soil. Since significant differential settlement is expected near the ground surface (i.e. zone h_1 in Figure 4.1a), Winkler springs would be more appropriate for simulating the soil near the ground surface. However, in deeper soil layers, experiencing the stress distribution and reduction in the differential settlements, Pasternak shear layer attached to the springs considering both shear and compressive deformations would be more appropriate. Therefore, among these, Kerr foundation model is the most suitable soil foundation model to idealise the mechanistic behaviour of the soft soil beneath LTP. The simplified Winkler model always overpredicts the response of LTP due to the assumption of no shear resistance of soft soil. Whereas, the Pasternak model always underpredicts the deflection of LTP due to large shear resistance near the ground surface.

4.4.2. Effects of Column Spacing

Figure 4.6a represents the effect of column spacing on the maximum settlement of LTP with one layer (1×1000 kN/m) and two layers (2×1000 kN/m) of geosynthetic reinforcement. It is evident from Figure 4.6a that as the column spacing increases the maximum settlement of LTP which occurs at the middle of two adjacent columns also increases (as shown in Figure 4.3a and as reported by Liu et al., 2015). For example, as the non-dimensional column spacing (s/d) increases from 3 to 3.5 the maximum settlement is increased from 25 mm to 37 mm (i.e. 48% increase) for the granular layer with two geosynthetic layers (i.e. 2×1000 kN/m) which is shown in Figure 4.6a. This is due to the accumulation of more loads on the LTP in the soft soil region for larger column spacing. Furthermore, since the area replacement ratio reduces as the spacing rises, the equivalent subgrade reaction of column decreases, and therefore the equivalent rigidity of the column supports also decreases, resulting in more settlement of LTP. Fig 6a also illustrates that the maximum settlement of the single layer geosynthetic reinforced LTP (i.e. 1×2000 kN/m) is higher than that of the double layer geosynthetic reinforced LTP

(i.e. 2×1000 kN/m). For example, at $s/d = 3$, the maximum settlement of LTP with single geosynthetic reinforcement (i.e. 1×2000 kN/m) is 27 mm which decreases to 25 mm while the LTP is reinforced with double geosynthetic layers (i.e. 2×1000 kN/m). As Table 3 indicates that the bending stiffness of the LTP with the single geosynthetic layer is less than that of double layer geosynthetic reinforcement. As a result, settlement is higher for single layer case. Figure 4.6b shows the influence of column spacing on tension of geosynthetic reinforcement. It is observed that tension increases with the increase in column spacing. For example, the maximum normalised tensions in the top and the bottom geosynthetic layers increase from 0.46 to 0.57 (i.e. 24% rise) and from 0.22 to 0.28 (i.e. 27% growth), respectively, as s/d increases from 3 to 3.5. Referring to Figure 4.6a, it is obvious that as the settlement of LTP increases with the increasing column spacing, the axial strain of the geosynthetic reinforcement also increases causing more tension in the geosynthetic reinforcement. Abusharar et al. (2009) also observed similar trend during an empirical analysis of a pile supported embankment. Similar ranges of strains developed in the geosynthetics were reported by Rowe and Liu (2015) while a finite element modelling of a full-scale geosynthetic-reinforced, pile-supported embankment was presented. It can be seen that the change in the tensile force with column spacing for one geosynthetic reinforcement follows the similar trend as double layers' case reported in Figure 4.6b. Furthermore, for $s/d = 3$, it is displayed that the one layer of geosynthetic reinforcement (i.e. 1×2000 kN/m) attracts 8% and 55% more normalised tension than the top and the bottom layer of geosynthetics, respectively in case of two layers geosynthetic reinforcement.

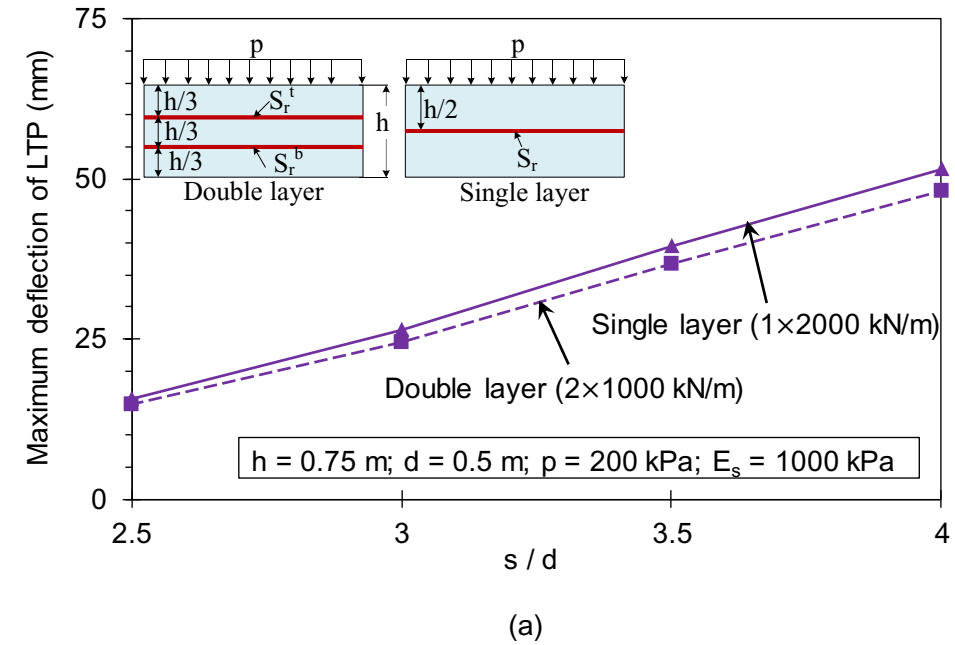

(a)

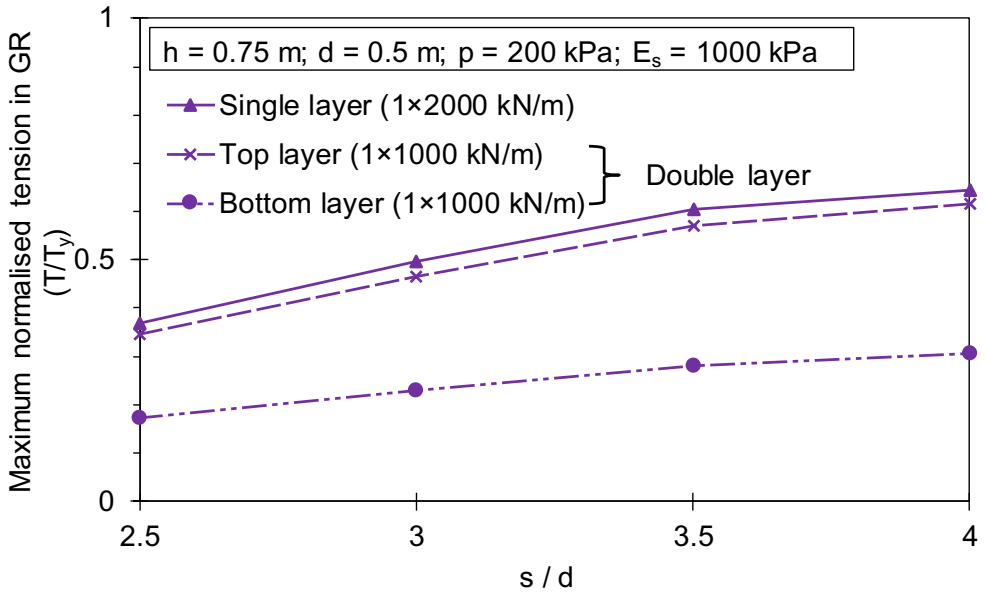

(b)

Figure 4.6. Effect of column spacings for the case of LTP on Kerr foundation model on: (a) the maximum deflections of LTP and (b) the maximum normalised tensions in the geosynthetics.

4.4.3. Effects of LTP Thickness

As anticipated, increase in the LTP thickness results in the reduced maximum settlement of LTP which is displayed in Figure 4.7a. For example, when the granular layer is reinforced with

two geosynthetic layers (i.e. 2×1000 kN/m), the maximum settlement of LTP decreases 20% (i.e. from 25 mm to 20 mm) as the non-dimensional LTP thickness (h/d) increases from 1.5 to 1.75, which is presented in Figure 4.7a. Parametric study reveals that as the thickness of LTP increases the equivalent bending stiffness and shear stiffness of LTP also increase. For example, as the non-dimensional thickness of LTP (h/d) increases from 1.5 to 1.75, the equivalent bending stiffness and shear stiffness of LTP with two geosynthetic layers (i.e. 2×1000 kN/m) increase by 33% and 14%, respectively. Thus, as the LTP becomes thicker, it becomes more inflexible which results in reduced settlement as visualised in Figure 4.7a. Referring to Figure 4.7a, the maximum settlement of LTP decreases when a single layer geosynthetic layer (i.e. 1×2000 kN/m) is replaced by two geosynthetics layers (i.e. 2×1000 kN/m). In addition, it is also noticed that this reduction in the maximum settlement is more noticeable for thinner LTP as compared to thicker LTP. For example, at the non-dimensional LTP thickness $h/d = 1.25$, 9% reduction in the maximum settlement of LTP is observed when a single layer of geosynthetic reinforcement (i.e.1×2000 kN/m) is replaced by two layers of geosynthetic reinforcement (i.e. 2×1000 kN/m) as shown in Figure 4.7a. On the other hand, when the non-dimensional LTP thickness $h/d = 2$ is adopted, only 4% drop in the maximum settlement of LTP is perceived when a single layer of geosynthetic reinforcement (i.e. 1×2000 kN/m) is replaced by two layers of geosynthetic reinforcement (i.e. 2×1000 kN/m). The effect of LTP thickness on the maximum tension in the geosynthetic reinforcement is captured in Figure 4.7b. This figure shows that the maximum mobilised tension in the geosynthetic reinforcement decreases with the thickness of LTP. The reason is that as LTP becomes thicker, it settles less (refer to Figure 4.7a), and thus the axial strain of the geosynthetic reinforcement decreases, mobilising less tension in the geosynthetic reinforcement. As shown in Figure 4.7b, for the granular layer with two geosynthetic layers (2×1000 kN/m), the maximum normalised mobilised tension in the top and the bottom geosynthetic layers are reduced by 13% and 9%,

respectively, when h/d increases from 1.5 to 1.75. It should be noted that similar trends occur for granular fill with a single geosynthetic layer (i.e. 1×2000 kN/m) in which the maximum mobilised tension in the geosynthetics is smaller with thicker LTP compared with thinner LTP which is shown in Figure 4.7b.

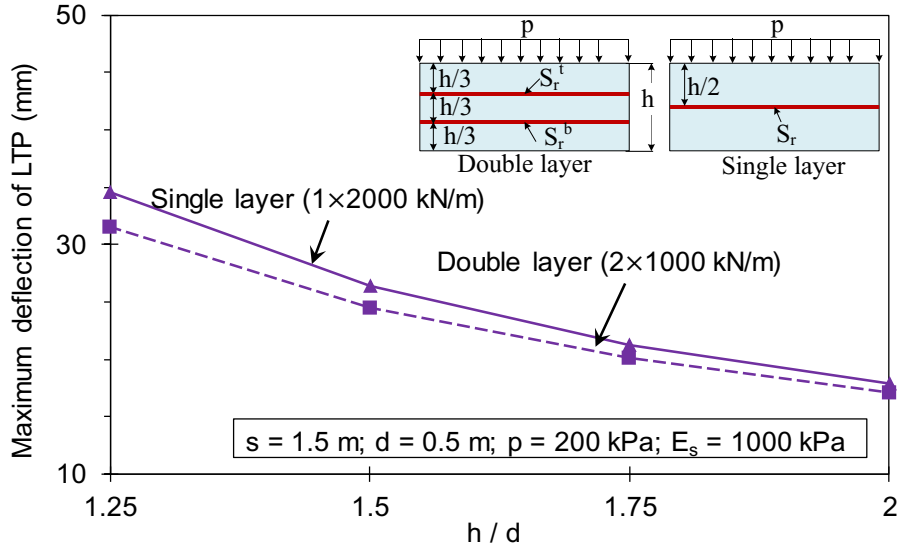

(a)

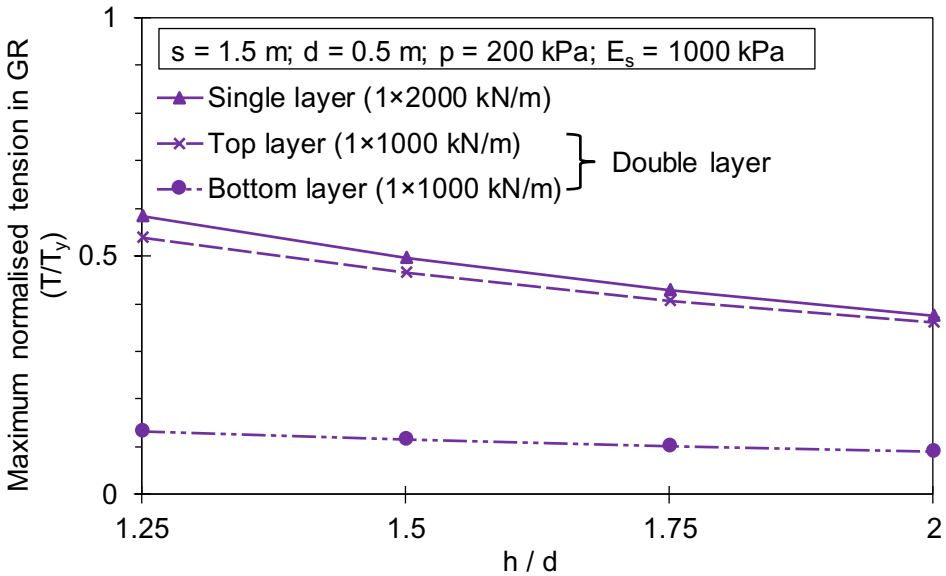

(b)

Figure 4.7. Effect of LTP thicknesses for the case of LTP on Kerr foundation model on: (a) the maximum deflections of LTP and (b) the maximum normalised tensions in the geosynthetics.

4.4.4. Effects of Soft Soil Stiffness

Effects of the soft soil stiffness on the maximum settlement of LTP are demonstrated in Figure 4.8a. As evident in Figure 4.8a, the maximum settlement of LTP decreases as the stiffness of soft soil increases. For example, the maximum deflection of LTP is reduced by 30% as elastic modulus of the soft soil (E_s) increases from 1000 kPa to 4000 kPa for LTP with double geosynthetics (i.e. 2×1000 kN/m). This can be explained by the fact that when soil is stiffer (i.e. soil with higher E_s value), the spring constants (k_u and k_l) and shear modulus (G) of the soil are also larger resulting in less deflection predictions for the soil. Hence, as the soil stiffness increases, the soft soil experiences less settlement, reflected in the LTP deformation. Obviously, similar relationship between the maximum deflection of LTP and the stiffness of the soft soil is observed when only one geosynthetic layer (i.e. 1×2000 kN/m) is adopted. Figure 4.8b shows the effect of soft soil stiffness on mobilised tension in geosynthetic reinforcement. It is observed that as the stiffness of soft soil increases tension in geosynthetic reinforcement decreases. This is due to the fact that the increase in stiffness of soft soil causes less settlement of LTP and due to this reason less axial strain and tension are induced in the geosynthetic layer. For example, as the elastic modulus of the soft soil increases from 1000 kPa to 4000 kPa, the maximum normalised tension in the top and the bottom geosynthetic layers decreases from 0.46 to 0.3 (i.e. 35% reduction) and from 0.23 to 0.16 (i.e. 30% fall), respectively. A similar trend is observed for the case with single layer of geosynthetic as presented in Figure 4.8b.

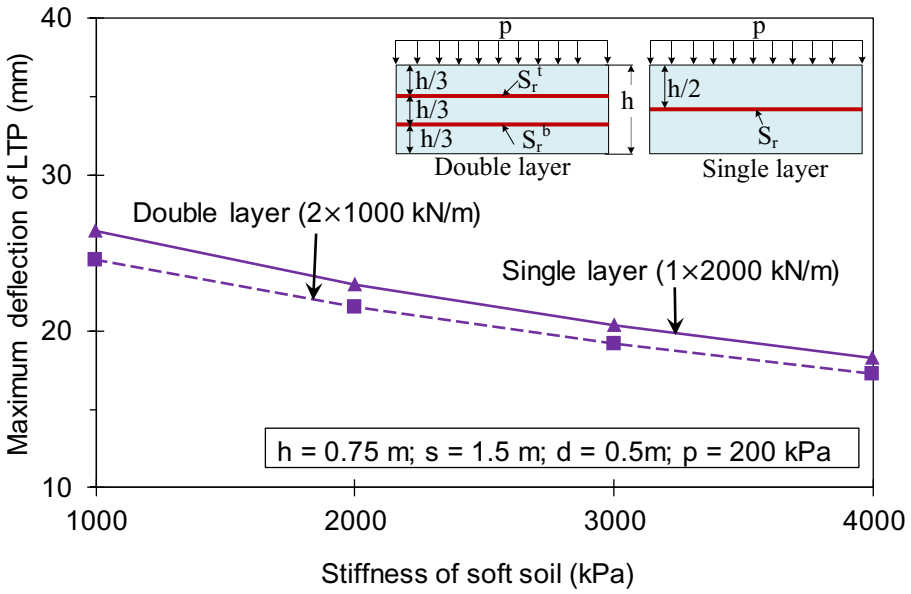

(a)

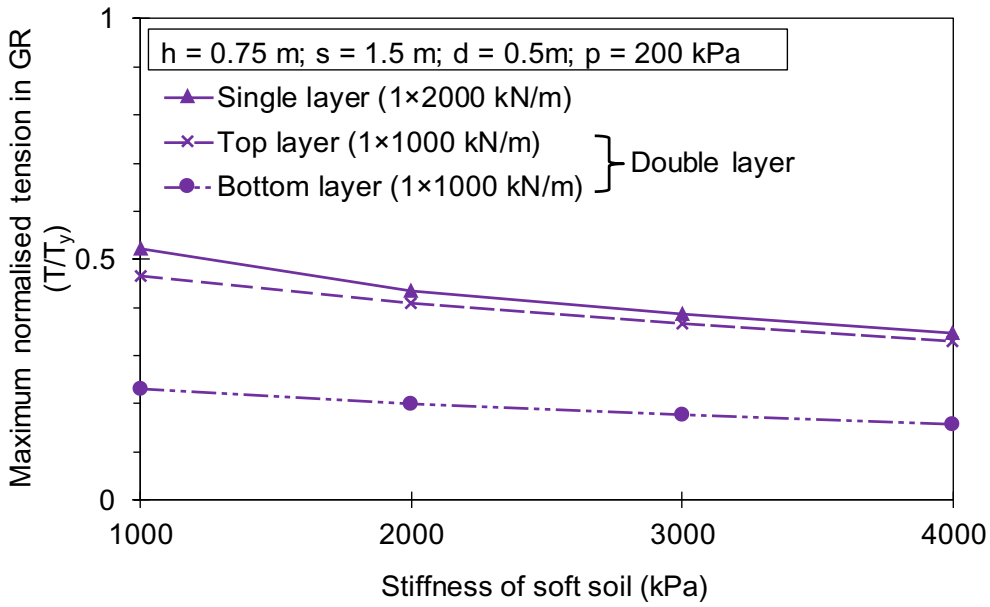

(b)

Figure 4.8. Effect of soft soil stiffnesses for the case of LTP on Kerr foundation model on: (a) the maximum deflections of LTP and (b) the maximum normalised tensions in the geosynthetics.

4.4.5. Effects of Tensile Stiffness of Geosynthetic Reinforcement

Figure 4.9a displays the effect of tensile stiffness of geosynthetic reinforcement on the maximum settlement of LTP. As shown in Figure 4.9a, the maximum settlement of LTP decreases as the tensile stiffness of geosynthetic reinforcement increases. For example, as the tensile stiffness of the each geosynthetic reinforcement for double layer case increases from 1000 kN/m to 2000 kN/m (i.e. from 2×1000 kN/m to 2×2000 kN/m), the maximum deflection of LTP decreases 24% (i.e. from 25 mm to 19 mm) which is plotted in Figure 4.9a. This can be clarified by the point that as the tensile stiffness of geosynthetic reinforcement increases from 2×1000 kN/m to 2×2000 kN/m, the equivalent bending and shear stiffness of LTP becomes almost double (see Eqs.(4-2) and (4-3)) which results in less deflection of LTP. Similar patterns were also observed in the literature during the numerical analysis of a geosynthetic-reinforced embankments over soft foundation (Rowe and Li, 2005; Han et al., 2007). Referring to Figure 4.9b, due to the increase in the tensile stiffness of geosynthetic reinforcement, the maximum normalised tension in the geosynthetic reinforcement decreases. For example, as the tensile stiffness of the each geosynthetic reinforcement increases from 1000 kN/m to 2000 kN/m for the case of double layer, the maximum normalised tension in the top layer decreases 50% (i.e. from 0.46 to 0.23) (see Figure 4.9b). As the tensile stiffness of the geosynthetic reinforcement increases, the settlement of the LTP decreases (see Figure 4.9a), and consequently the axial strain of the geosynthetic reinforcement decreases. Liu and Rowe (2015) also observed similar trend during a numerical analysis of a deep-mixing column supported embankment. However, the tension mobilised in the geosynthetic reinforcement increases. This increase in the mobilised tension is due to the fact that the mobilised tension is the product of the tensile stiffness and the axial strain of the geosynthetic layer (see Eqs. (4-39)). Therefore, as the tensile stiffness of the geosynthetic reinforcement increases the maximum mobilised tension also increases. Similar results were reported by Huang and Han

(2010), and Bhasi and Rajagopal (2015a) for geosynthetic reinforced embankments constructed on columns where numerical simulations were carried out. However, normalised tension is the ratio of mobilised tension in the geosynthetic (T) and ultimate strength (T_y) of the geosynthetics. It is observed that as the tensile stiffness of the geosynthetic reinforcement increases this ratio is decreased. Similar trends of the maximum deformations and normalised tensions are observed for the case with single layer of geosynthetic as presented in Figure 4.9a–b.

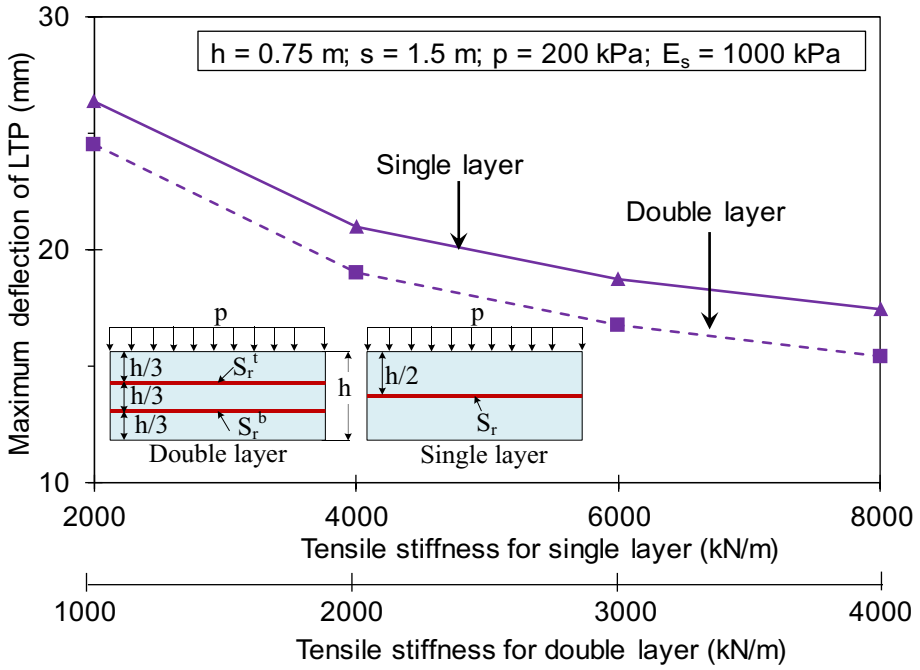

(a)

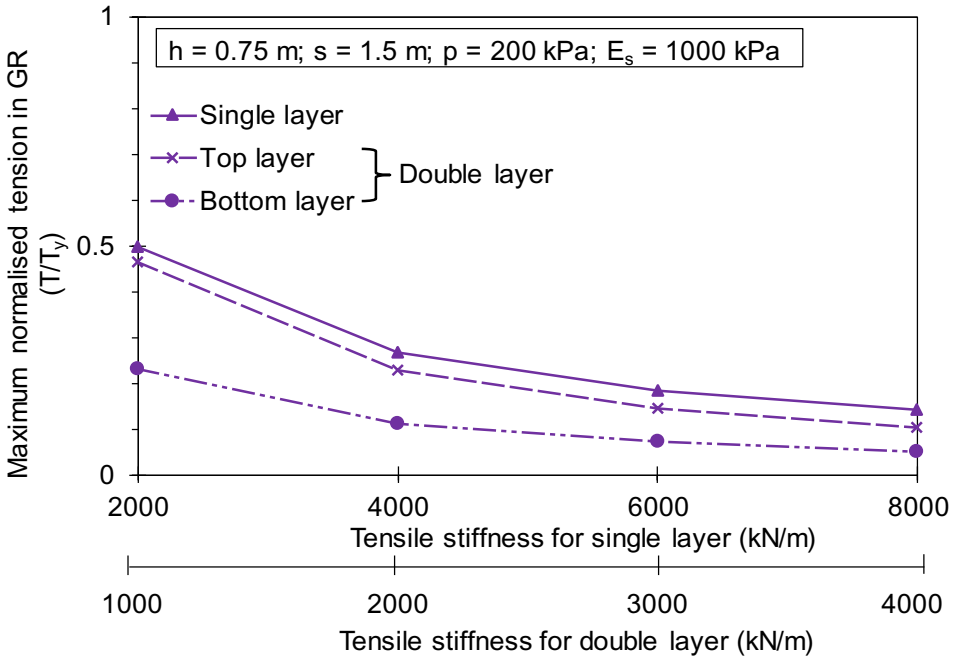

(b)

Figure 4.9. Effect of tensile stiffnesses of geosynthetic reinforcement for the case of LTP on Kerr foundation model on: (a) the maximum deflections of LTP and (b) the maximum normalised tensions in the geosynthetics.

It is mention worthy that the variations of deflection of LTP or tension in the geosynthetic reinforcement with the distance between two geosynthetic layers can be predicted using the proposed analytical solution in this study. It has been noticed that as the distance between two layers of geosynthetic reinforcements reduces, more deflection of LTP as well as the tension in geosynthetics are observed. Indeed, when the geosynthetic layers are positioned closely, the effective bending stiffness of the LTP (cracked LTP) is reduced contributing to more deflection of LTP and hence more tension in the geosynthetics. For example, for the baseline case, when the distance between two layers of geosynthetics is $2\,h/3$, the equivalent bending stiffness of LTP in sagging and hogging regions is equal to 263 kN.m. However, when the distance between two layers of geosynthetics is $h/3$, the equivalent bending stiffness of LTP in sagging and hogging regions is reduced to 161 kN.m. Therefore, deflection of LTP as well as mobilised

tension in geosynthetics reinforcement increase as the spacing between geosynthetic layers decreases.

Indeed, in this work a simple analytical model to predict the settlement behaviour of LTP on soft soil, reinforced by column inclusions such as unreinforced concrete columns and reinforced piles, has been presented. To achieve the objective of the study, a closed-form solution has been developed to assess the performance of the load transfer platform for a general symmetric loading pattern. Therefore, the proposed model can be applied for any shape of symmetric loads from super structures such as embankments, silo, or fuel tanks where LTP over the columns is used. Indeed, since a general form of symmetric external loading has been adopted in this study (see Eq. (11)), user can adjust the model parameters to simulate different patterns of applied loading including those obtained from existing arching theories for embankments. It can be noted that a similar scenario of uniform loading was adopted by other researchers (Yin, 2000a, b; Zhang et al., 2012a; Borges and Gonçalves, 2016) to investigate the behaviour of load transfer platform on soft soil. Although, the loading due to arching can be symmetric close to middle of the embankments, but close to the batter or slopes, the loading due to arching would not be symmetric. The proposed model cannot be used for asymmetric loads such as arching below batters of embankments. Thus, this is one of the limitations of the proposed model.

4.5. Summary

The present study makes an attempt to suggest a reasonably accurate mechanical model for LTP reinforced with double layers of geosynthetics on column reinforced soft soil, which can be used by practicing engineers to investigate the flexural and shear behaviours of the LTP. The response function of the system has been derived for symmetric loading in plane strain conditions. This has been achieved by developing governing differential equations for the

proposed model and its solutions. In order to develop analytical equations, the basic differential equations of a Timoshenko beam subjected to a distributed transverse load and a foundation interface pressure, generated from the Kerr foundation model were adopted. The homogeneous solution of the governing sixth order nonhomogeneous differential equation was found from the roots of the characteristic polynomial equation. Then adopting the method of Undetermined Coefficients, the particular solution was obtained. The proposed mechanical model can be beneficial for practicing engineers in analysing the settlement response of the multilayer geosynthetic reinforced granular bed overlying column improved soft soil.

Furthermore, soft soil idealised by the Winkler and the Pasternak foundations were used to evaluate the accuracy of the adopted Kerr foundation model to detail study of LTP on column improved soft soil. In general, the Winkler model produced higher values of displacements, rotations, bending moments, shear forces, and tensions than the reference solutions adopting the Kerr foundation model. However, the values of the displacements, rotations, bending moments, shear forces, and tensions obtained from Pasternak foundation model were smaller than the respective reference values adopting the Kerr foundation model. Kerr foundation model predicted the response of the soft soil more accurately, which were between two upper and lower bounds corresponding to the Winkler and the Pasternak foundation models. Therefore, it can be concluded that the Kerr foundation model is superior to the Winkler and the Pasternak models for the representation of the soil response. It should be noted that this theoretical model with its closed form solution may simulate the exact performance of the LTP under loading. However, the presented model can be used as a tool for a better estimation of the LTP behaviour with multi layers of geosynthetics, in comparison with the situation that soft soil is modelled by Winkler and Pasternak foundations.

Furthermore, using the proposed mechanical model, response of double layer geosynthetic reinforced LTP was compared with a single layer geosynthetic reinforced LTP. It was observed that inclusion of the two geosynthetic layers (i.e. 2×1000 kN/m) further reduced the maximum deflection of the LTP when compared to a single layer (i.e. 1×2000 kN/m). However, for the double layer case, the strength of geosynthetics was less utilised than that of the single layer case. It was also revealed that in the double layer reinforcement, the top geosynthetic layer was more effective at the column location (in the hogging region), whereas the bottom geosynthetic layer was more effective in the middle span (in the sagging region). It was also noticed that top geosynthetic layer was subjected to higher mobilised tension than the bottom layer. Moreover, it can be concluded that the use of one stronger geosynthetic layer (e.g. 1×2000 kN/m) with the equivalent stiffness of two geosynthetic layers (e.g. 2×1000 kN/m), does not result in the same settlement of LTP and the tension of the geosynthetic reinforcement when compared to two weaker geosynthetic layers (e.g. 2×1000 kN/m).

CHAPTER 5

5. REINFORCED TIMOSHENKO BEAM TO SIMULATE LOAD TRANSFER MECHANISM IN CIC SUPPORTED EMBANKMENT

5.1. General

CICs are sustainable and cost-effective ground improvement technology that transmit the load from the traffic and the embankment to a lower bearing stratum through a composite CIC/soil matrix. The key influencing components of the load transfer mechanism include embankment fill, load transfer platform (LTP) with one or more layers of geosynthetics, CIC and the foundation soils. The use of LTP enhances the load transfer mechanism in the CIC improved soft ground and minimises the post construction settlement of the ground. In this chapter, reinforced Timoshenko beam theory is adopted to simulate the LTP with one layer of geosynthetics that is resting on elastic foundation with columns. A parametric study is conducted to investigate the importance of the LTP on the load transfer mechanism for the CIC supported embankment. Special attentions are given to the thickness of the LTP, the use of geosynthetics and its influence on deflection of the LTP, the shear force developed in the LTP and the tension developed in geosynthetics. The parametric study reveals that the thickness of the LTP has a significant effect on the behaviour of LTP up to a certain limit.

In addition, a new mechanical model of columns-supported embankment is suggested to study the effects of multilayer geosynthetics on the settlement response of the granular layer. A notable reduction of the settlement has been observed as a result of the using multilayer weaker geosynthetic reinforcement system when compare to one stronger geosynthetics layer. It is also

observed that the top reinforcement layer is subjected to maximum mobilised tension at the column edge whereas bottom reinforcement layer is more effective in controlling the deflection in the middle of two columns.

Furthermore, this chapter proposes a mechanical model for idealising the response of LTP-soft soil-column system, by representing each sub-system using commonly used mechanical elements such as rough-elastic membrane, beam, and spring. The soil arching effect is incorporated in the model to determine the deflection of the soft soil as well as mobilised tension in the geosynthetics more accurately. The effects of the column stiffness and consolidation of saturated soft soils are also incorporated in the model. Moment and shear force in the LTP, tension developed in the geosynthetics, and settlements of the improved soft ground are predicted using the proposed model. To evaluate the proposed model, a parametric study is conducted to investigate the influence of different pressure distribution due to different arching theories. It is observed that the pattern of distribution of the arching loads affect the performance of concrete injected column-supported embankments significantly.

5.2. Reinforced Timoshenko Beam Theory to Simulate Load Transfer Mechanism in CIC-Supported Embankments

Since the composite system comprises of more than one component the response of the system is complex. The flexibility of the soft soil results in varied responses of LTP and the embankment. In a similar way, the presence of LTP and embankment causes varied responses of the ground, the collective phenomena of which is called soil-structure interactions (SSI). Practicing geotechnical engineers recognise the importance of SSI to analyse the impact of the heavier structures on soft soil. To represent the soil medium in the SSI problems, Winklerian approach is the basic classic and the most popular approach which is used by most practicing engineers due to its simplicity. According to Winkler's idealization (1867), deformation of

foundation in bending due to applied load is confined to the loaded regions only and stress–strain behaviour of soil is assumed linear; which are the two serious demerits of the model. In order to overcome the shortcomings of Winklerian approach, some modified foundation models have been proposed in the literature, such as Filonenko-Borodich (1940), Hetenyi's foundation (1946), Pasternak foundation (1954), and Kerr foundation (1965). Pasternak (1954) proposed a model where the foundation settles due to the shear only. As a new foundation model to represent the geosynthetic reinforced soil, a modified Pasternak model has been proposed by Madhav and Poorooshasb (1988), where Pasternak shear layer was combined with Winkler's springs. However, neither Winkler nor Pasternak model considers both bending and shearing. Euler-Bernoulli beam on elastic foundation model has been attempted to solve the SSI problem considering the bending only. However, very little attention is paid to Timoshenko beam model on elastic foundation considering bending and shearing to represent the engineered granular layer. Yin (2000a) has derived the ordinary differential equations for a reinforced Timoshenko beam on elastic foundation excluding the stabilizing columns and provided the analytical solution for point load on an infinite beam and for uniformly distributed vertical pressure for a finite beam. This study extends Yin (2000a) work to take into account the effect of rigid inclusions on LTP design as well as the pressure due to arching in the embankment.

5.2.1. Basic Differential Equations for Timoshenko Beam on Elastic Foundation

Yin (2000a) has proposed the following basic differential equations for a reinforced Timoshenko beam on elastic foundation excluding the column reinforcement.

$$D\frac{d^2\psi}{dx^2} + C\frac{dw}{dx} - C\psi = 0 \tag{5-1}$$

and

$$C\frac{d\psi}{dx} - C\frac{d^2w}{dx^2} + k_s w = q \tag{5-2}$$

Eqs. (5-1) and (5-2) results in Eq. (5-3)

$$D\frac{d^4w}{dx^4} - \frac{Dk_s}{C}\frac{d^2w}{dx^2} + k_s w = q - \frac{D}{C}\frac{d^2q}{dx^2} \tag{5-3}$$

where w and ψ are vertical deflection and rotation angle of the reinforced Timoshenko beam, respectively; q is the pressure; D and C are bending stiffness and shear stiffness of the reinforced beam, respectively; and k_s is the modulus of subgrade reaction for soft soil. Figure 5.1a illustrates the 2D foundation model to simulate the LTP that has been presented by Yin (2000a). Figure 5.1b shows the forces acting on a finite beam element of the reinforced granular layer. If w is known, the rotational angle (ψ) can be determined, using Eqs. (5-1) and (5-2), as follows:

$$\psi = \left(1 - \frac{D}{C^2}\right)\frac{dw}{dx} + \frac{D}{C}\frac{d^3w}{dx^3} + \frac{D}{C^2}\frac{d^2q}{dx^2} \tag{5-4}$$

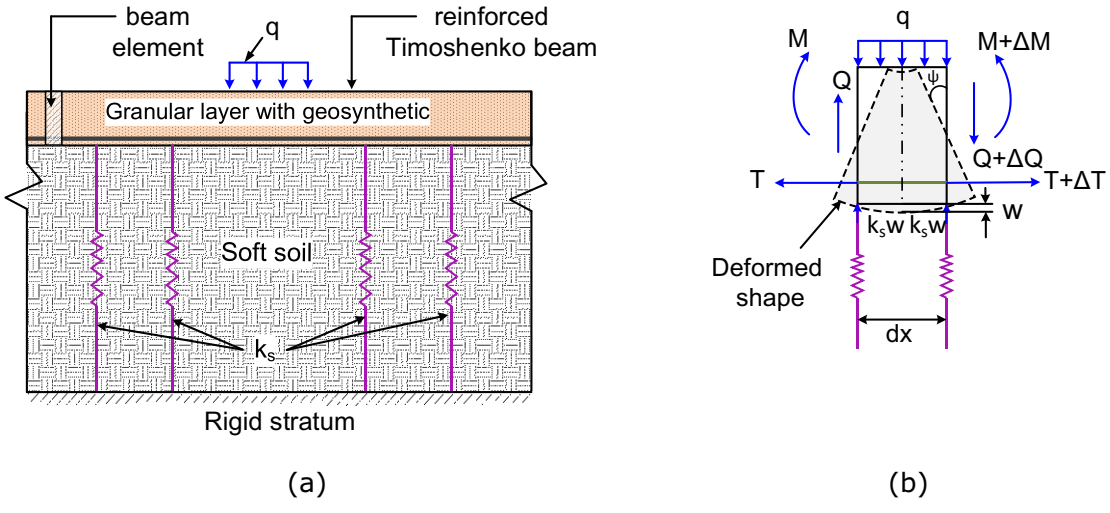

Figure 5.1. Modified model of Yin's (2000a) model showing: (a) foundation model for the geosynthetic reinforced granular layer on soft soil proposed by and (b) forces acting on a finite element of reinforced granular layer.

This study considers BS8006-1 (2010) to calculate stresses acting on LTP. Thus, in plane strain condition, distribution of the vertical stresses on LTP can be calculated as below:

$$p_c' = \sigma_v' \left(\frac{C_c a}{H}\right)^2 \tag{5-5}$$

and

$$p_r' = \begin{cases} 1.4\gamma \dfrac{s^2 - a^2\left(\frac{p_c'}{\sigma_v'}\right)}{(s+a)}, & H > 1.4\,(s-a) \\ \sigma_v' \dfrac{s^2 - a^2\left(\frac{p_c'}{\sigma_v'}\right)}{s^2 - a^2}, & 0.7(s-a) \leq H \leq 1.4(s-a) \end{cases} \tag{5-6}$$

where p_c' is the vertical stress on top of LTP above the CIC; p_r' is the vertical stress on top of LTP above the soft soil region; a and s are the width and spacing of the column, respectively; σ_v' is the factored average vertical stress on top of LTP without arching ($\sigma_v' = f_{fs}\gamma H + f_q w_s$); w_s is the uniformly distributed surcharge loading; f_{fs} and f_q are the partial load factors (refer to BS 8006-1, 2010); H and γ are height and unit weight of the embankment fill, respectively; and C_c is the arching coefficient (refer to BS 8006-1, 2010). Figure 5.2 demonstrates the two-dimensional foundation model of a CIC supported embankment.

5.2.2. Closed Form Solution

Yin (2000a) considered a finite beam with length L that is subjected to uniformly distributed pressure in the form of a polynomial without any column supports. Yin expressed the applied pressure as the Fourier cosine series function and proposed an analytical solution considering the both ends of the beam are free. The solution for deformation (w) given by Yin (2000a) for soft soil without the columns support is:

$$w = e^{\alpha x}(c_1 \cos \beta x + c_2 \sin \beta x) + e^{-\alpha x}(c_3 \cos \beta x + c_4 \sin \beta x) + \frac{A_0}{k_s} + \sum_{n=1}^{n=\alpha} a_n \cos\left(\frac{n\pi}{L} x\right) \quad (5\text{-}7)$$

where c_1 to c_4 are the four constants of integration and can be obtained from the boundary conditions.

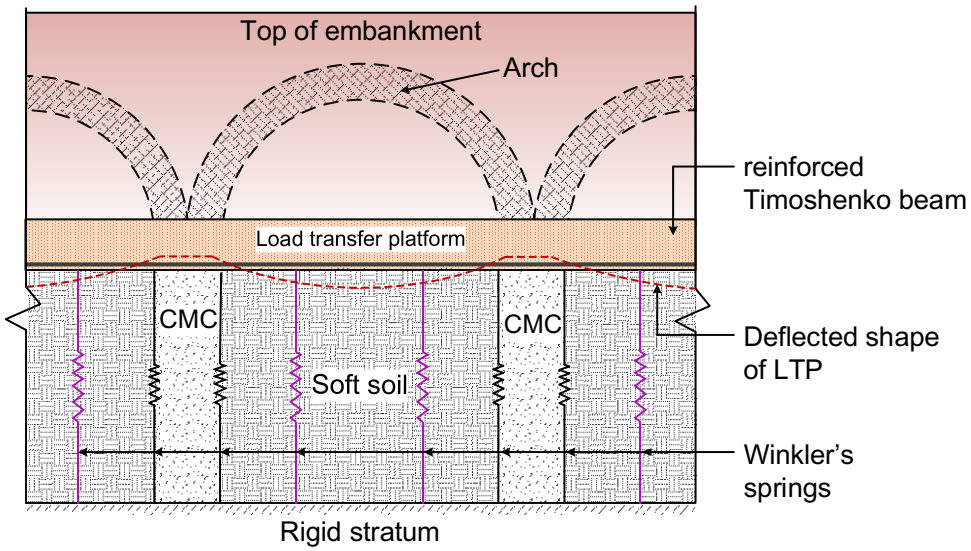

Figure 5.2. Schematic diagram of the proposed foundation model for CIC supported embankment.

Timoshenko (1921) has proposed the relationship between the shear force (Q) and the shear strain (γ) as follows:

$$Q = C\gamma = C\left(\frac{dw}{dx} - \psi\right) \quad (5\text{-}8)$$

Timoshenko (1921) has also reported the relationship between the moment (M) and the rate of rotation angle $\left(\frac{d\psi}{dx}\right)$ as follows:

$$M = -D\frac{d\psi}{dx} \quad (5\text{-}9)$$

According to Yin (2000a), the tension (T) developed in the reinforcement can be expressed as follows:

$$T = -E_r(y_r - y_c)\frac{d\psi}{dx} \tag{5-10}$$

Supporting equations and additional details are presented by Yin (2000a).

To obtain c_1, c_2, c_3 and c_4 for reinforced Timoshenko beam on elastic foundation with columns, the following simplifications are made in addition to the basic assumptions for Timoshenko beam theory: (1) The response of CIC and soft soil are assumed to be linearly elastic and (2) Friction between CIC and surrounding soft soil is ignored for simplicity. Clear spacing (L) between two CIC is considered as the region loaded with embankment weight below the arch and resisted with the underneath soft soil as shown in Figure 5.3a.

Four boundary conditions to be adopted in Eq. (5-7) to obtain the constants are as following:

$$\text{at } x = 0: M = 0 \tag{5-11a}$$

$$\text{at } x = 0: Q = \left(P_c - K_{c,eq}w\right) \tag{5-11b}$$

$$\text{at } x = L: M = 0 \tag{5-11c}$$

$$\text{at } x = L: Q = -\left(P_c - K_{c,eq}w\right) \tag{5-11d}$$

where P_c is the concentrated force on LTP due to arching at the edge of CIC (kN); M is the moment at CIC edge (kN.m); Q is the shear force at support as shown in Figure 5.3b (kN/m); and $K_{c,eq}$ is the equivalent modulus of subgrade reaction for CIC (kN/m) estimated as follows:

$$K_{c,eq} = k_c A_p + k_s\left(A_w - A_p\right) \tag{5-12}$$

where A_p is the cross-section area of CIC (m^2); A_w is the plan area of CIC wall in plane strain (m^2); k_s and k_c are the modulus of subgrade reaction for soft soil and CIC, respectively (kN/m^3).

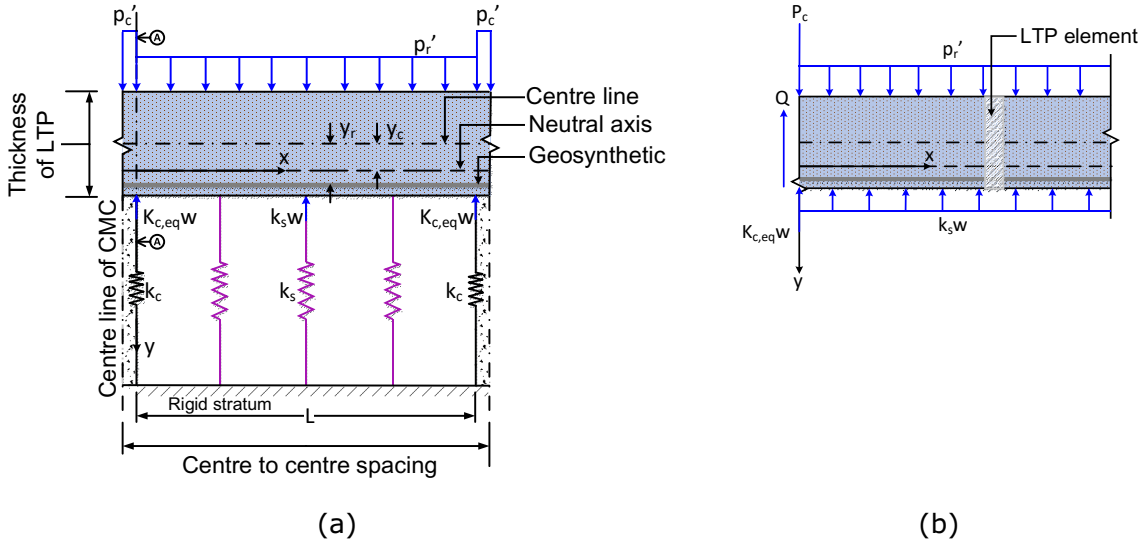

Figure 5.3. Illustration of: (a) stresses acting on proposed 2-dimensional foundation model for geosynthetic reinforced CIC supported embankment and (b) free body diagram of LTP cut at a section A-A.

Considering the boundary condition as presented in Eq. (5-11a), the following equation can be obtained:

$$c_1\left(\alpha^2-\beta^2-\frac{k_s}{C}\right)+2c_2\alpha\beta+c_3\left(\alpha^2-\beta^2-\frac{k_s}{C}\right)-2c_4\alpha\beta=R_1 \tag{5-13}$$

According to the boundary condition as indicated in Eq. (5-11b), the following equation can be derived:

$$c_1D\left[\frac{\alpha k_s}{C}-\alpha^3+3\alpha\beta^2+\frac{K_{c,eq}}{D}\right]+c_2D\left[\frac{\beta k_s}{C}-3\alpha^2\beta+\beta^3\right]+c_3D\left[-\frac{\alpha k_s}{C}+\alpha^3-3\alpha\beta^2+\frac{K_{c,eq}}{D}\right]+c_4D\left[\frac{\beta k_s}{C}-3\alpha^2\beta+\beta^3\right]=R_2 \tag{5-14}$$

The following equation can be derived from the boundary condition as presented in Eq. (5-11c):

$$e^{\alpha L}c_1\left[\left(\alpha^2-\beta^2-\frac{k_s}{C}\right)\cos\beta L-2\alpha\beta\sin\beta L\right]+e^{\alpha L}c_2\left[2\alpha\beta\cos\beta L+\left(\alpha^2-\beta^2-\frac{k_s}{C}\right)\sin\beta L\right]+e^{-\alpha L}c_3\left[\left(\alpha^2-\beta^2-\frac{k_s}{C}\right)\cos\beta L+2\alpha\beta\sin\beta L\right]+e^{-\alpha L}c_4\left[\left(\alpha^2-\beta^2-\frac{k_s}{C}\right)\sin\beta L-2\alpha\beta\cos\beta L\right]=R_3 \quad (5\text{-}15)$$

The following equation can be obtained from the boundary condition presented in Eq. (5-11d):

$$c_1e^{\alpha L}\left[D\cos\beta L\left\{\frac{\alpha k_s}{C}-\alpha^3+3\alpha\beta^2+\frac{K_{c,eq}}{D}\right\}-D\sin\beta L\left\{\frac{\beta k_s}{C}+\beta^3-3\alpha^2\beta\right\}\right]+c_2e^{\alpha L}\left[D\cos\beta L\left\{\frac{\beta k_s}{C}+\beta^3-3\alpha^2\beta\right\}+D\sin\beta L\left\{\frac{\alpha k_s}{C}-\alpha^3+3\alpha\beta^2+\frac{K_{c,eq}}{D}\right\}\right]+c_3e^{-\alpha L}\left[D\cos\beta L\left\{-\frac{\alpha k_s}{C}+\alpha^3-3\alpha\beta^2+\frac{K_{c,eq}}{D}\right\}-D\sin\beta L\left\{\frac{\beta k_s}{C}+\beta^3-3\alpha^2\beta\right\}\right]+c_4e^{-\alpha L}\left[D\cos\beta L\left\{\frac{\beta k_s}{C}-3\alpha^2\beta+\beta^3\right\}+D\sin\beta L\left\{-\frac{\alpha k_s}{C}+\alpha^3-3\alpha\beta^2+\frac{K_{c,eq}}{D}\right\}\right]=R_4 \quad (5\text{-}16)$$

where

$$R_1=\sum_{n=1}^{\alpha}\left[a_n\left(\frac{n\pi}{L}\right)^2+a_n\frac{k_s}{C}-\frac{A_n}{C}\right] \quad (5\text{-}17a)$$

$$R_2=P_c-K_{c,eq}\left[\frac{A_0}{k_s}+\sum_{n=1}^{n=\alpha}a_n\right] \quad (5\text{-}17b)$$

$$R_3=\sum_{n=1}^{\alpha}\left[a_n\left(\frac{n\pi}{L}\right)^2+a_n\frac{k_s}{C}-\frac{A_n}{C}\right]\cos(n\pi) \quad (5\text{-}17c)$$

$$R_4=-P_c+K_{c,eq}\frac{A_0}{k_s}+K_{c,eq}\sum_{n=1}^{n=\alpha}a_n\cos(n\pi)+C\sum_{n=1}^{n=\alpha}a_n\left(\frac{n\pi}{L}\right)\sin(n\pi)+C\sum_{n=1}^{\alpha}\left\{\left[\frac{D}{C}\left(\frac{n\pi}{L}\right)^3-\left(1-\frac{Dk_s}{C^2}\right)\left(\frac{n\pi}{L}\right)\right]a_n-\frac{n\pi D}{LC^2}A_n\right\}\sin(n\pi) \quad (5\text{-}17d)$$

Eqs.(5-13), (5-14), (5-15) and (5-16) can be expressed in a matrix form as presented below:

$$[M]\{c\} = \{R\} \tag{5-18}$$

where $\{c\} = [c_1, c_2, c_3, c_4]^{-1}$ and $\{R\} = [R_1, R_2, R_3, R_4]^{-1}$. In [M], the coefficient M_{ij} $(i = 1 - 4, j = 1 - 4)$ can be determined using the basic parameters α, β, D, C, k_s and k_c. Then, the solution to Eq. (5-18) is:

$$\{c\} = [M]^{-1}\{R\} \tag{5-19}$$

5.2.3. Parametric Study

Typical parameters for geosynthetic reinforced (GR) CIC supported embankment will be used for the parametric study in this study. Modulus of subgrade reaction for the soft soil and the CIC can be estimated using the following equations proposed by Selvadurai (1979):

$$k_s = E_s/[H_s(1 + \upsilon_s)(1 - 2\upsilon_s)] \tag{5-20}$$

and

$$k_c = E_c/[H_c(1 + \upsilon_c)(1 - 2\upsilon_c)] \tag{5-21}$$

where E, H and υ are the Young's modulus, depth (length) and Poisson's ratio, respectively; suffixes "s" and "c" represent the soft soil and the column, respectively. Figure 5.4 shows a typical geometry of a geosynthetic reinforced CIC supported embankment adopted in this study. In this study, geosynthetic used in the load transfer platform is considered to be geogrid. In practice geosynthetic reinforcement is designed under tension only, but shear modulus can be considered in case of geogrid. γ_e and ϕ_e are the unit weight and friction angle of the embankment fill, respectively; γ_g, E_g and ν_g are the unit weight, Young's modulus and Poisson's ratio of the granular material in LTP, respectively; E_r and ν_r are the tensile stiffness and Poisson's ratio of GR, respectively; $E_r = E_r' A_r$, where E_r' is the Young's modulus of GR

and A_r is the cross-sectional area of GR. In this study, thickness of the LTP varies between 0.2m to 1.0m. Effect of geosynthetics with varied thickness of the LTP has been investigated. In this study, it is assumed that the location of GR is always at quarter of the depth of the LTP below the centerline of the LTP. A cracked section of reinforced Timoshenko beam (or LTP) is assumed since the soil in the LTP does not carry tension. Therefore, the second moment of inertia and the shear modulus of the beam have been reduced by 0.25 and 0.5 times, respectively.

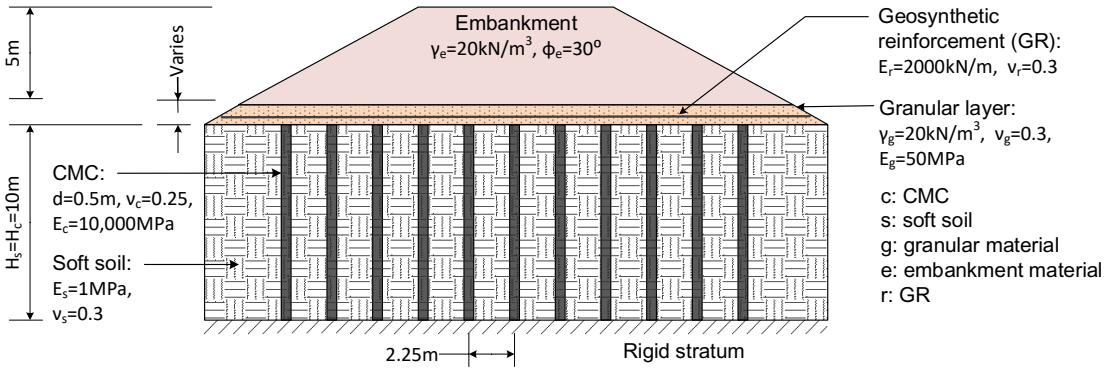

Figure 5.4. Typical cross section of a geosynthetic reinforced CIC supported embankment.

5.2.4. Results and Discussions

Key calculated parameters and geometry of soil and geosynthetics are summarised in Table 1. for 0.3m and 0.5m thick LTP. After calculating the matrices $[M]$ and $\{R\}$ with the value of α, β, D, C, k_s and k_c, constant $\{c\}$ is determined. The differential settlement is assessed at the bottom of the LTP between the edge of column and the midpoint of two columns. It can be observed from Figure 5.5a that while the thickness of LTP increases from 0.2m to 0.6m, the maximum settlement and the differential settlement decrease notably. However, when the thickness of LTP with geosynthetic reinforcement increases further above 0.6m, changes in the maximum settlement and the differential settlement are not significant. It has been observed from the parametric study that the bending stiffness (D) and the shear stiffness (C) of LTP

increase when the thickness of the LTP increases as shown in Figure 5.5b. It is obvious that the settlement of the LTP beam with geosynthetic reinforcement is less than that without the geosynthetic reinforcement as shown in Figure 5.6a. Inclusion of the geosynthetic reinforcement increases the bending stiffness (D) and the shear stiffness (C) of reinforced LTP which increases the rigidity of the LTP resulting in less settlement. Influence of the thickness of LTP on the tension developed in GR is illustrated in Figure 5.6b. Since the increase in the thickness of LTP results in less differential settlement in LTP, the tension developed in the geosynthetic reinforcement decreases. Figure 5.7a illustrates the comparison of shear force with and without the geosynthetic reinforcement for 0.3m and 0.5m thick LTP. Figure 5.7a indicates that shear force generated in the reinforced LTP beam at two supports is maximum but with opposite sign. Then the shear force decreases resulting in zero shear force at the midpoint of the LTP, which satisfies the boundary conditions assumed in this study. Figure 5.7b demonstrates that the thicker LTP (0.5m in this example) with geosynthetic reinforcement rotates less than that of without GR due to more rigidity of the LTP. It is also displayed in Figure 5.7b that the maximum rotation of the cross section of the LTP occurs at the two supports. Then the rotation angle decreases resulting in zero rotation of the LTP at the mid-point.

Table 5.1. Calculated material properties and geometry of 0.3m and 0.5m thick LTP.

Parameters	0.3m thick LTP	0.3m thick LTP	0.5m thick LTP	0.5m thick LTP
	With GR	Without GR	With GR	Without GR
D in kN.m	37	28	158	130
C in kN/m	3044	2403	4646	4005
G_e in kPa	12179	9615	11154	9615
y_c in m	0.009	0.0	0.009	0.0
k_s in kN/m^3	192	192	192	192
k_c in kN/m^3	1600000	1600000	1600000	1600000
p_c' in kPa	374	374	374	374
p_r' in kPa	45	45	45	45

Although the overall behaviour of LTP due to bending and shear can be predicted using the above-mentioned reinforced Timoshenko beam model, there are several limitations for the proposed model as follows: (1) CIC rests on rigid stratum; (2) pull-out resistance force of GR from the surrounding granular material is neglected; (3) although the reduced stiffness of the cracked LTP is considered in this study, the actual behaviour of the cracked LTP beam section has not been captured; (4) although it is assumed that the connection between LTP beam and CIC will not carry any moment and LTP is free to rotate at the column connection, in reality this support may have some moment resistance restraining the rotation. Therefore, further investigation on the possibility of moment capacity and rotational resistance at this connection is required; and (5) in this study, the settlement of LTP beam has been predicted at a particular time. However, to simulate the consolidation of soft-clay, time-dependent settlement of the LTP has to be considered. It should be noted that soil cementation and creep can significantly influence time dependent behaviour of clays (Nguyen et al., 2014; Fatahi et al., 2013).

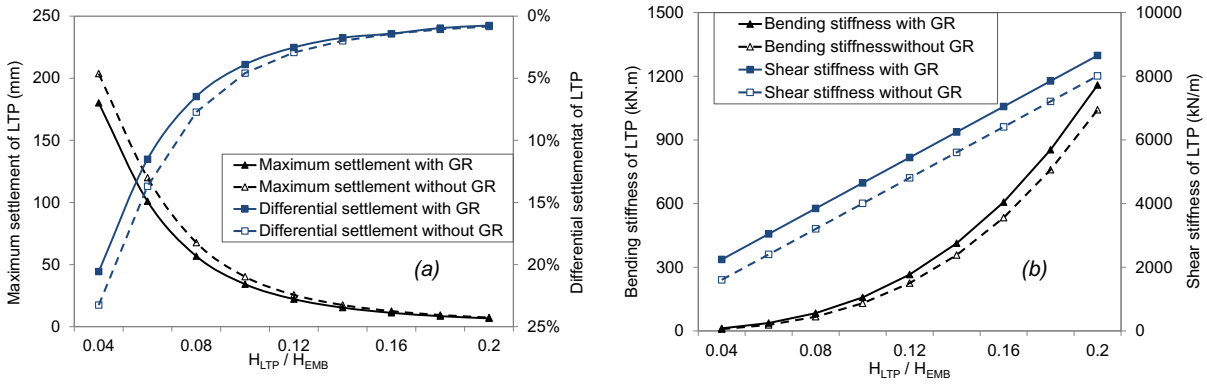

Figure 5.5. Effects of the thickness of LTP with GR and without GR on: (a) maximum settlement and differential settlement of the LTP and (b) bending stiffness and shear stiffness of the LTP.

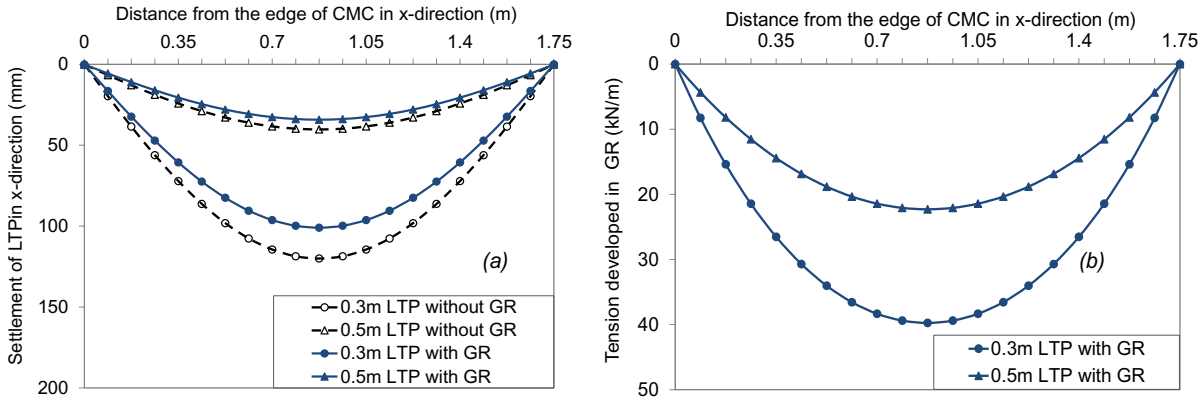

Figure 5.6. Variations in: (a) settlement of the LTP in x-direction and (b) tension generated in the geosynthetic reinforcement in x-direction.

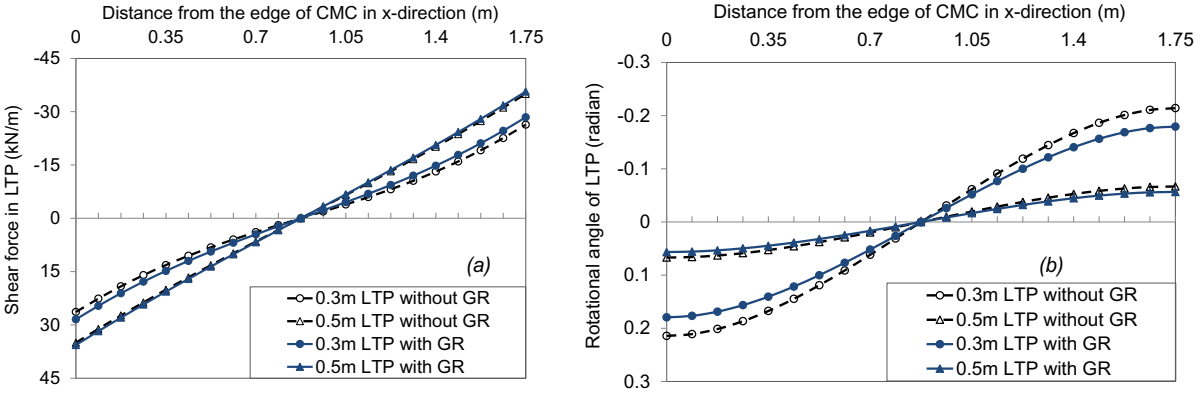

Figure 5.7. Variations in: (a) shear force developed in the reinforced LTP and (b) rotation angle of the LTP with geosynthetic reinforcement and without geosynthetic reinforcement in x-direction.

5.3. Mechanical Model to Analyse Multilayer Geosynthetic-Reinforced Granular Layer in Column-Supported Embankments

In this section, a mechanical model is proposed for a multilayer geosynthetic reinforced granular layer on column stabilised soft soil, which incorporates the deformation of the granular fill due to both bending and shear. Using the proposed model, the load transfer mechanism in terms of deflection and rotation of the granular layer and tension mobilised in

the geosynthetics with one stronger layer of geosynthetics and with two layers of weaker geosynthetics are compared.

5.3.1. Analytical Model

A granular layer with multilayer of geosynthetics on CIC improved soft soil system at the base of the embankment is shown in Figure 5.8a. The behaviour of such a system may be idealised in terms of the proposed mechanical model shown in Figure 5.8b. In this model, the geosynthetic reinforced granular fill has been idealised as a reinforced Timoshenko beam. The CICs and the soft soil have been idealised as a layer of linear springs with different stiffness. Two geosynthetic layers are considered in the model. It is assumed that there will be no slippage between the geosynthetic reinforcement layers and granular fill materials. The assumed deformed shape of the LTP and the co-ordinate axes for a unit cell are shown in Figure 5.9a. The deformation of the column is assumed to remain unchanged over its width. The CIC and the soft soil are loaded with different distributed loading intensities of p_s and p_c, respectively due to soil arching. Since in the field, discrete columns are placed in a square or triangular pattern, the equivalent plane-strain material stiffness is determined by the relationship suggested by Tan *et al.* (2008) based on matching the column-soil composite stiffness as: $k_{c,pl}a_{r,pl} = k_{c,ax}a_{r,ax} + k_{s,ax}(a_{r,pl} - a_{r,ax})$. Subscripts ″pl″ and ″ax″ denote plane-strain and axisymmetric conditions, respectively, while a_r is the area replacement ratio. Deformation of the CIC reinforced composite ground can be expressed as:

$$w = \begin{cases} w_{cz} & \text{when } 0 \le \xi \le d/2 \\ w_{cz} + w_{sz} & \text{when } 0 \le x \le s'/2 \end{cases} \quad (5\text{-}22)$$

where s' is the clear spacing between the CICs, w_{sz} is the displacement of the LTP on soft soil region at a horizontal distance x, and w_{cz} is the displacement of the LTP over column region at a horizontal distance ξ.

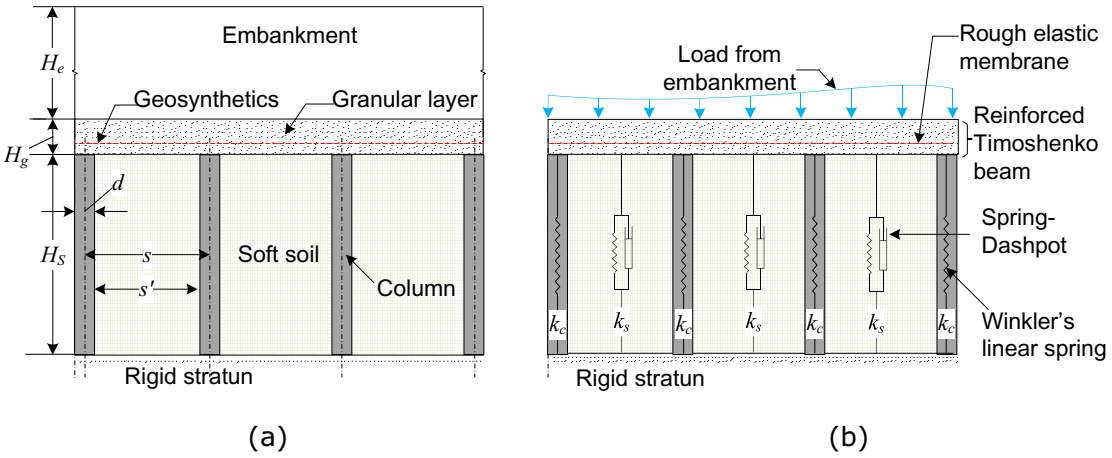

Figure 5.8. Illustration of: (a) embankment on CIC-improved soft soil and (b) proposed foundation model.

To obtain the differential equation, governing the deflected shape of a transversely loaded LTP beam resting on elastic foundation, the LTP is divided into infinitesimal beam elements in the horizontal direction having equal thickness Δx within the soft soil region and $\Delta\xi$ within the column. Typical LTP elements over the soft soil and the columns and the stresses acting on LTP are shown in Figure 5.9b. The equilibrium of the vertical forces and moments of a typical element of LTP for $0 \leq x \leq s'/2$ under plain strain conditions yield the following equations:

$$\left.\begin{aligned} D_b \frac{d^2\theta_{sz}}{dx^2} + C_b \frac{dw_{sz}}{dx} - C_b\theta_{sz} = 0 \\ C_b \frac{d\theta_{sz}}{dx} - C_b \frac{d^2 w_{sz}}{dx^2} + q_s = p_s \end{aligned}\right\} \quad (5\text{-}23)$$

Similar set of equations can be governed within the CIC region ($0 \leq \xi \leq d/2$) replacing θ_{sz}, w_{sz}, p_s, and q_s by θ_{cz}, w_{cz}, p_c, and q_c, respectively. In Eq. (5-23), w is the transverse deformation of the centroid axis of the beam, θ is the rotation angle of the cross section of beam about its neutral axis, D_b and C_b are the un-cracked bending rigidity and shear rigidity of the LTP with geosynthetics (Yin, 2000), respectively. Considering linear stress-displacement relation proposed by Winkler, 1867 and consolidation effect of the soft soil suggested by Deb

et al., 2007, normal pressure at the LTP-soil (q_s) and LTP-column interfaces (q_c) can be written as:

$$q_s = \frac{k_s w_{sz}}{U} \tag{5-24a}$$

$$q_c = k_{c,pl} w_{cz} \tag{5-24b}$$

where U is the degree of consolidation of the soft soil. Although the time dependent behaviour of the soft soil is considered in the present study, it should be noted that soil cementation and creep can significantly affect the behaviour of soft soil (Azari et al., 2016; Le et al., 2015; Nguyen et al., 2014).

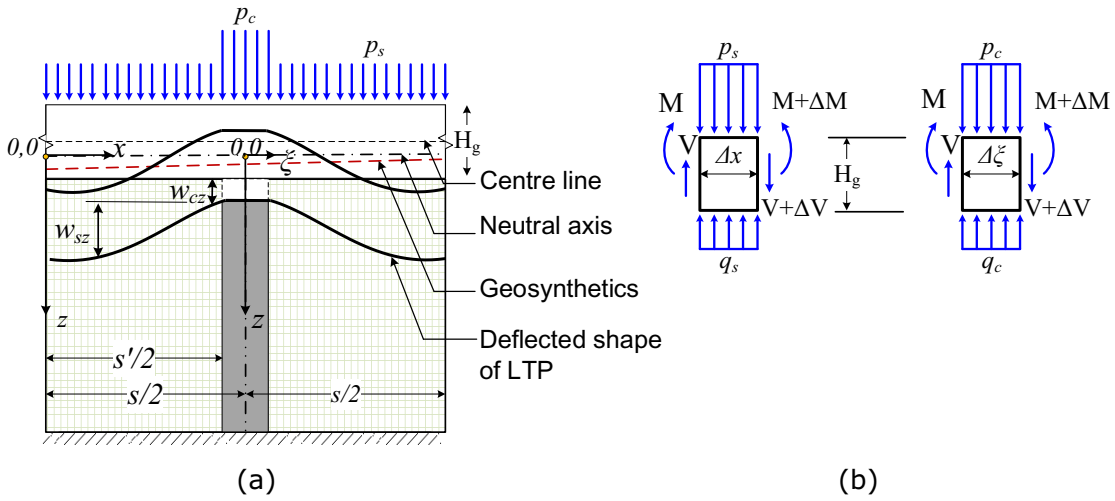

Figure 5.9. Proposed mechanical model demonstrating: (a) multilayer geosynthetic-reinforced granular fill soft soil column system and (b) stress application in different infinitesimal LTP section.

Combining Eqs. (5-23) and (5-24) and assuming Fourier cosine series which considers the symmetric embankment loading on the LTP, the ordinary fourth-order differential equations of the deflection for the LTP for $0 \leq x \leq s'/2$ and $0 \leq \xi \leq d/2$ can be written as:

$$D_s \frac{d^4 w_1}{dx^4} - \frac{D_s k_s}{C_s U} \frac{d^2 w_1}{dx^2} + \left(\frac{k_s}{U}\right) w_1 = S_0 + \sum_{m=1}^{m=\infty} S_m \left[1 + \frac{D_s}{C_s}\left(\frac{2m\pi}{s'}\right)^2\right] \cos\left(\frac{2m\pi x}{s'}\right) \quad (5\text{-}25)$$

$$D_h \frac{d^4 w_2}{dx^4} - \frac{D_h k_s}{C_h U} \frac{d^2 w_2}{dx^2} + \left(\frac{k_s}{U}\right) w_2 = S_0 + \sum_{m=1}^{m=\infty} S_m \left[1 + \frac{D_h}{C_h}\left(\frac{2m\pi}{s'}\right)^2\right] \cos\left(\frac{2m\pi x}{s'}\right) \quad (5\text{-}26)$$

$$D_b \frac{d^4 w_{cz}}{d\xi^4} - \frac{D_b k_{c,pl}}{C_b} \frac{d^2 w_{cz}}{d\xi^2} + k_{c,pl} w_{cz} = C_0 + \sum_{m=1}^{m=\infty} C_m \left[1 + \frac{D_b}{C_b}\left(\frac{2m\pi}{d}\right)^2\right] \cos\left(\frac{2m\pi\xi}{d}\right) \quad (5\text{-}27)$$

where D_s and C_s are the bending and shear rigidity of LTP, respectively when the LTP is subjected to sagging moment; D_h and C_h are the bending and shear rigidity of LTP, respectively when the LTP is subjected to hogging moment (tension cracks appear above the neutral axis); and D_b and C_b are the bending and shear rigidity of LTP, respectively when the LTP is considered as an un-cracked on top of the column.

5.3.2. Analytical Solution

The solution of the fourth order nonhomogeneous differential equation Eq. (5-25) governing the deflected shape of a transversely loaded LTP beam resting on foundation soil which is subjected to hogging moment can be expressed as:

$$w_1 = e^{\vartheta x}(s_1 \cos \delta x + s_2 \sin \delta x) + e^{-\vartheta x}(s_3 \cos \delta x + s_4 \sin \delta x) + \frac{S_0}{k_s} + \sum_{m=1}^{m=\infty} s_s \cos\left(\frac{2m\pi x}{s'}\right) \quad (5\text{-}28)$$

The solution for LTP beam when it is subjected to sagging moment (Eq. (5-26)) is written below.

$$w_2 = e^{\alpha x}(t_1 \cos \beta x + t_2 \sin \beta x) + e^{-\alpha x}(t_3 \cos \beta x + t_4 \sin \beta x) + \frac{S_0}{k_s} + \sum_{m=1}^{m=\infty} s_h \cos\left(\frac{2m\pi x}{s'}\right) \quad (5\text{-}29)$$

Correspondingly, for $0 \leq \xi \leq d/2$, the analytical solution of Eq. (5-27) can be expressed as:

$$w_{cz} = d_1 e^{r_1 \xi} + d_2 e^{r_2 \xi} + d_3 e^{-r_1 \xi} + d_4 e^{-r_2 \xi} + \frac{C_0}{k_{c,pl}} + \sum_{m=1}^{m=\infty} c_m \cos\left(\frac{2m\pi\xi}{d}\right) \quad (5\text{-}30)$$

where

$$\vartheta = \left(\sqrt{\frac{k_s}{4D_s U}} + \frac{k_s}{4C_s U}\right)^{1/2}; \quad \alpha = \left(\sqrt{\frac{k_s}{4D_h U}} + \frac{k_s}{4C_h U}\right)^{1/2};$$
$$\delta = \left(\sqrt{\frac{k_s}{4D_s U}} - \frac{k_s}{4C_s U}\right)^{1/2}; \quad \beta = \left(\sqrt{\frac{k_s}{4D_h U}} - \frac{k_s}{4C_h U}\right)^{1/2}; \quad (5\text{-}31)$$
$$r_1 = \frac{k_{c,pl}}{2C_b} + \sqrt{\left(\frac{k_{c,pl}}{2C_b}\right)^2 - \frac{k_{c,pl}}{D_b}}$$
$$r_2 = \frac{k_{c,pl}}{2C_b} - \sqrt{\left(\frac{k_{c,pl}}{2C_b}\right)^2 - \frac{k_{c,pl}}{D_b}}$$

$$S_0 = \frac{1}{s'}\int_{-\frac{s'}{2}}^{\frac{s'}{2}} p_s \, dx \quad S_m = \frac{1}{s'}\int_{-\frac{s'}{2}}^{\frac{s'}{2}} p_s \cos\left(\frac{2m\pi x}{s'}\right) dx \quad ; \text{ and}$$
$$C_0 = \frac{1}{d}\int_{-\frac{d}{2}}^{\frac{d}{2}} p_c \, d\xi \quad C_m = \frac{1}{d}\int_{-\frac{d}{2}}^{\frac{d}{2}} p_c \cos\left(\frac{2m\pi\xi}{d}\right) d\xi$$

$$s_s = \frac{S_m\left[1+\left(\frac{2m\pi}{s'}\right)^2\frac{D_s}{C_s}\right]}{D_s\left(\frac{2m\pi}{s'}\right)^2\left[\left(\frac{2m\pi}{s'}\right)^2+\frac{k_s}{C_s U}\right]+\frac{k_s}{U}} \quad (5\text{-}32)$$
$$s_h = \frac{S_m\left[1+\left(\frac{2m\pi}{s'}\right)^2\frac{D_h}{C_h}\right]}{D_h\left(\frac{2m\pi}{s'}\right)^2\left[\left(\frac{2m\pi}{s'}\right)^2+\frac{k_s}{C_h U}\right]+\frac{k_s}{U}}$$
$$c_m = \frac{C_m\left[1+\left(\frac{2m\pi}{d}\right)^2\frac{D_b}{C_b}\right]}{D_b\left(\frac{2m\pi}{d}\right)^2\left[\left(\frac{2m\pi}{d}\right)^2+\frac{k_{c,pl}}{C_b U}\right]+k_{c,pl}}$$

In practice, the stiffness of the LTP beam is greater than the stiffness of the soft soil and less than the stiffness of the CIC. Hence, the given solutions Eq. (5-28) to Eq. (5-30) are valid for $k_s < 4{C_{h,s}}^2 U/D_{h,s}$ (for soft soil region) and $k_c > 4{C_b}^2/D_b$(for column region). It can be noted that s_1 to s_4, t_1 to t_4, and r_1 and r_2 are the constants of integration which can be determined by applying the boundary and continuity conditions. Once deflection (w) of the LTP beam is obtained, rotational angle (θ), shear force (V), bending moment (M) of the LTP, and tension (T) in the geosynthetics can be obtained using the following equations:

$$\theta = \frac{D}{C}\left(\frac{d^3w}{dx^3} + \frac{1}{C}\frac{dp}{dx} - \frac{1}{C}\frac{dq}{dx}\right) + \frac{dw}{dx};\ M = -D\frac{d\theta}{dx};\ V = C\left(\frac{dw}{dx} - \theta\right);\ \text{and}$$
$$T = -S_{gr}(y_n - y_r)\frac{d\theta}{dx} \tag{5-33}$$

where S_{gr} is the tensile stiffness of GR, y_n and y_r are the location of neutral axis and GR from the centreline of the LTP, respectively.

5.3.3. Boundary and Continuity Conditions

Due to symmetry, at the outside boundary of the unit cell, the shear stresses and the slope of the deflection are assumed to be zero. It is assumed that there will be no rotation and transverse deformation of the LTP at the column location. In addition, continuity conditions are satisfied at unknown distance R. For column region, at the column support, shear stress is equal to the reaction from the column support. Since the deformation of the column is constant through the width, the slope of the deflection will be zero. Boundary conditions for $0 \le x \le s'/2$ and $0 \le \xi \le d/2$ are as follows:

Within soft soil region:

$$\text{at } x = 0 \rightarrow \begin{cases} \frac{dw_1}{dx} = 0 \\ \tau_1 = 0 \end{cases}, x = \frac{s'}{2} \rightarrow \begin{cases} \theta_2 = 0 \\ w_2 = 0 \end{cases} \text{and } x = R \rightarrow \begin{cases} w_1 = w_2 \\ M_1 = 0 \\ M_2 = 0 \\ V_1 = V_2 \\ \theta_1 = \theta_2 \end{cases} \tag{5-34a}$$

Within column region:

$$\text{at } \xi = 0 \rightarrow \frac{dw_c}{d\xi} = 0 \text{ and } \xi = \frac{d}{2} \rightarrow \tau_c = k_{c,pl} w_c \tag{5-34b}$$

Following the boundary and continuity conditions as stated in Eq.(5-34), and using Eq. (5-33) (for θ_s, θ_c, τ_s, and τ_c) constants of integrations and unknown R can be determined. Due to the page limitation, calculation steps are not provided in detail.

5.3.4. Results and Discussions

Parametric study is conducted to predict the vertical deflection of LTP, bending, and rotation in the LTP and tension developed in the geosynthetic reinforcement (GR) using the proposed analytical model. This study considers the typical parameters for CIC supported geosynthetic reinforced embankments which are presented in Table 5.2. Modulus of subgrade reaction for the soft soil (k_s) and the CIC (k_c) are estimated using the equations suggested by (Selvadurai, 1979). The stresses acting on top of the LTP layer is determined by considering the soil arching in the embankment in plane-strain condition using the expressions proposed by Low et al. (1995). In this study, two layers of geosynthetics are used for multilayer case.

Table 5.2. Material properties adopted in parametric study.

Material	Parameters
Embankment fill	H_e = 2m and 5m, γ_e = 18.3kN/m^3, φ_e = 30°
Granular fill	H_g = 0.85m, E_g = 35MPa, ν_g = 0.3
Soft soil	H_s = 5m, E_s = 1MPa, ν_s = 0.3
CMC	H_c = 5m, d = 0.45m, s = 2.5m (square arrangement), E_c = 10000MPa, ν_c = 0.25
Geogrids (two layers but	S_{gr} = 1000kN/m, S_{gr} /T_y=10, ν_{gr} = 0.3, y_{gr1} = 0.05m (location of top layer below the C.L. of LTP) y_{gr2} = 0.30m (location of bottom layer below the C.L. of LTP)
Geogrids (one layer but stronger)	S_{gr} = 2000kN/m, S_{gr} /T_y=10, ν_{gr} = 0.3, y_{gr} = 0.175m (location of one GR layer below the C.L. of LTP)

Note: H: height/depth/thickness; γ: unit weight; φ: frictional angle; E: Young's modulus; d: diameter; s: spacing; ν: Poisson's ratio; S: tensile stiffness. Suffices "e", "g", "s", "c", and "gr" are used to designate embankment fill, granular fill, soft soil, CIC, and geosynthetic reinforcement (GR), respectively; T_y: yield strength of geosynthetics.

Comparison of Multilayer and One Layer of Geosynthetics:

The results of multilayer weaker geosynthetics are compared with the results with the one layer of stronger geosynthetics using the proposed mechanical model. Figure 5.10a shows the settlement profiles of a LTP on soft soil and column region for different embankment heights. For 5m embankment height, as the number of geosynthetic layers reduces from two (weaker) to one (stronger), the maximum settlement in the middle of the two columns (Point B in Figure 5.10a) increases by 13%, whereas for 2m embankment this increase is 9%. Thus, for higher embankment, multiple geosynthetic reinforcements reduce the vertical settlement more effectively than for shallow embankment. This is due to the fact that the tension mobilisation of geosynthetic reinforcements increases with increasing load. However, on top of the column, since the CIC is 10000 times stiffer than the soft soil, the effect of embankment height and the geosynthetics reinforcement is very minimal on the corresponding settlement of LTP. In addition, as shown in Figure 5.10b, adopting two layers of weaker geosynthetic reinforcements reduces the maximum rotation of the LTP by about 16% when the embankment height is 5m as shown in Figure 5.10b.

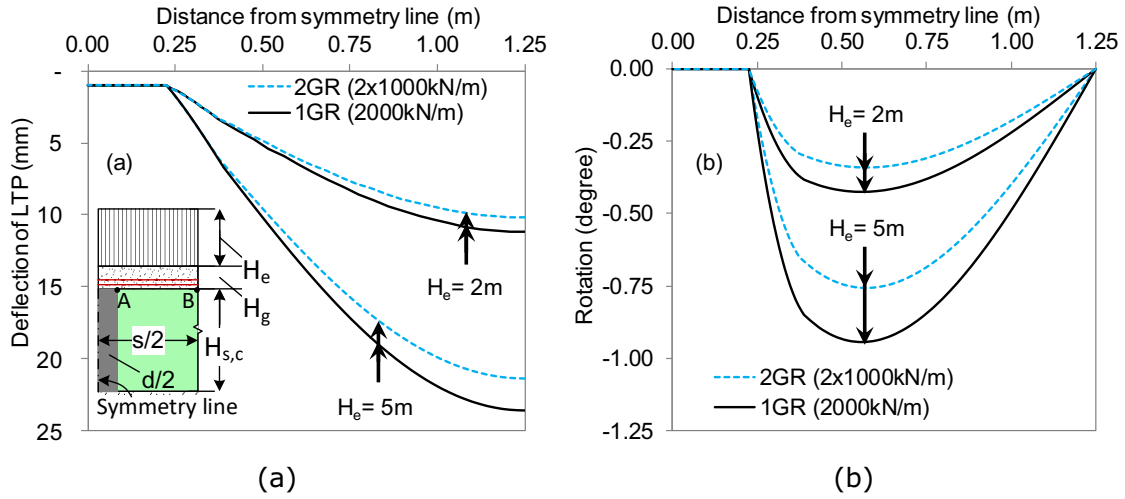

Figure 5.10. Effect of embankment height with multilayer geosynthetic reinforcements on: (a) settlement profiles and (b) rotation of the LTP.

Figure 5.11 demonstrates the variation of the normalised mobilised tension T/T_y in the reinforcement (normalised against the yield strength of geosynthetics) with distance from the CIC centreline for both cases (i.e. the two layers of weaker geosynthetics and one stronger geosynthetics layer) for 5 m high embankment. Results presented in Figure 5.10b show that the maximum negative bending moment (hogging) occurs at the column edge (Point A in Figure 5.11), whereas the maximum positive moment (sagging) occurs at the middle of two columns (Point B in Figure 5.11). Figure 5.11 illustrates that the top geosynthetic layer is subjected to a higher tension in the hogging region, whereas beyond this region the mobilised tension in the bottom geosynthetic layer is greater. Additionally, at the column location (Point A in Figure 5.11), one stronger layer of GR carries 30% less normalised tension than the top layer of GR. On the other hand, at Point B in Figure 5.11, it is displayed that the one layer of GR attracts 22% less normalised tension than the bottom layer of GR and 37% higher normalised tension than the top layer GR in case of two layers geosynthetic reinforcement. Therefore, one stronger layer of GR is not the equivalent of two weaker layers of geosynthetic reinforcement.

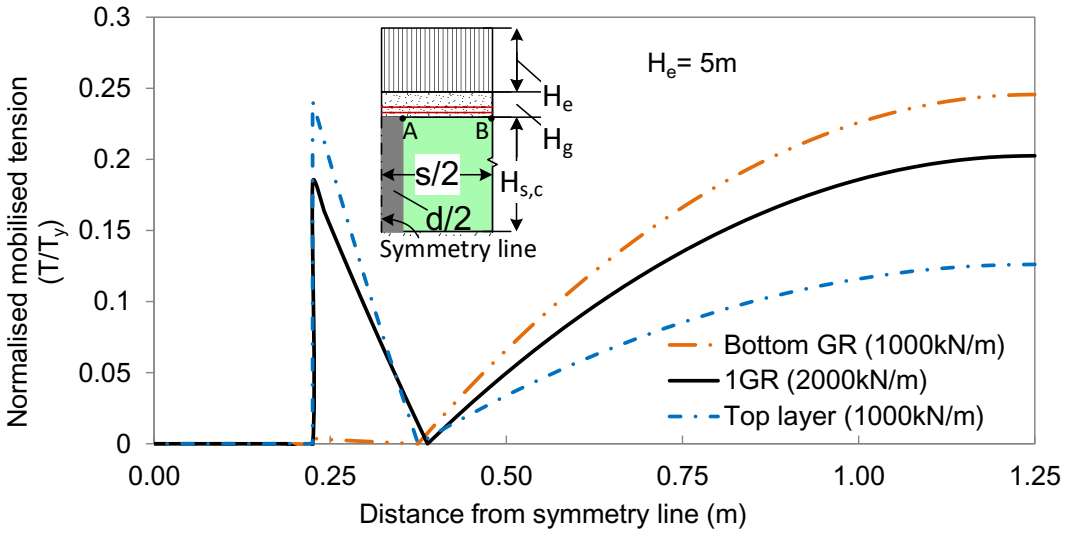

Figure 5.11: Typical profile of normalised mobilised tension in the geosynthetic reinforcement along the length of the LTP from the centreline of CIC.

5.4. Analysis of CIC-Supported Embankments Considering Soil Arching

In this work, a mechanical model has been developed to study the behaviour of CIC-supported geosynthetic-reinforced embankments by considering the effect of soil arching within the embankments, depth of soft soil, stiffness of soft soil and reinforcement layer. The effect of stiffness of the CIC has also been incorporated in the present model. Parametric studies have also been conducted to quantify the effect of different load distribution due to arching on the deflection, bending moment, shear force, and rotation of the LTP as well as the tension developed in the geosynthetic reinforcement.

5.4.1. Mechanical Model Development

Figure 5.12a shows geosynthetic-reinforced embankment resting on CIC-improved soft soil. The model proposed by Yin (2000a) for beam on elastic foundation has been modified to simulate the CIC-improved ground by including the effect of CIC. Furthermore, the effects of different soil arching theories within the embankment fill have been incorporated in the analysis. The geosynthetic reinforced granular layer and the soft soil have been simulated with the reinforced Timoshenko beam and the spring-dashpot system, respectively. The CICs are idealised by stiffer linear springs and the geosynthetics is assumed to be rough elastic membrane as illustrated in Figure 5.12b. The assumed deformed shape of the LTP and the co-ordinate axes for a unit cell are shown in Figure 5.13a. The deformation of the column is assumed to remain unchanged over its width. The CIC and the soft soil are loaded with different distributed loading intensities of p_s and p_c, respectively due to soil arching. In the present study, a 2-D plane strain analysis has been carried out for CIC-supported embankments. Since in the field, discrete columns are placed in a square or triangular pattern, the equivalent plane-strain material stiffness is determined by the relationship suggested by () based on matching the column-soil composite stiffness as: $k_{c,pl}a_{r,pl} = k_{c,ax}a_{r,ax} + k_{s,ax}(a_{r,pl} - a_{r,ax})$. Subscripts

″pl″ and ″ax″ denote plane-strain and axisymmetric conditions, respectively, while a_r is the area replacement ratio. Deformation of the CIC-reinforced composite ground as shown in Figure 5.13a can be expressed as:

$$w_{xz} = w_{cz} + w_{sz} \qquad \text{for} \qquad 0 \le x \le s'/2 \qquad (5\text{-}35)$$

where s' is the clear spacing between the CICs, w_{sz} is the displacement of the LTP on soft soil region at a horizontal distance x, and w_{cz} is the displacement of the LTP over column region at a horizontal distance ξ.

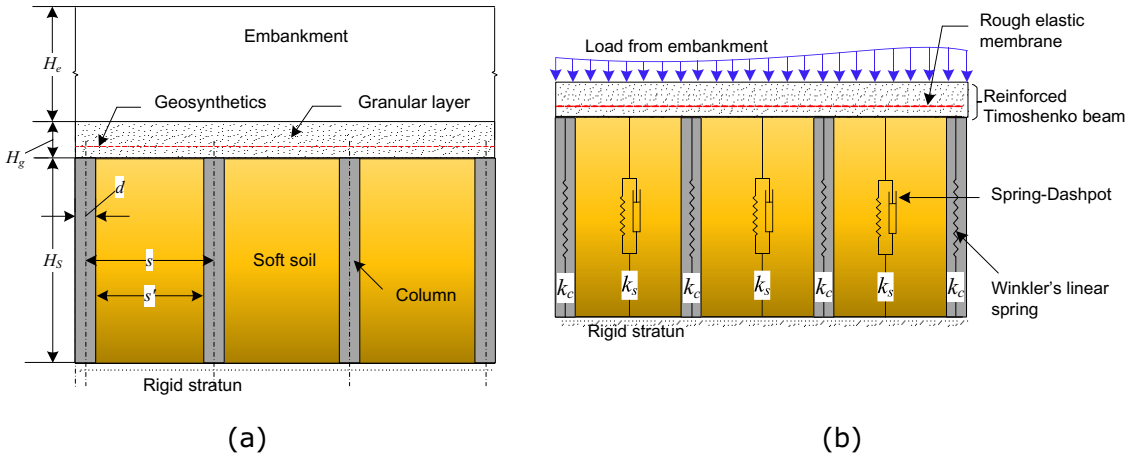

Figure 5.12. Sketch of: (a) embankment resting on CIC-improved soft soil and (b) proposed foundation model.

To obtain the differential equation, governing the deflected shape of a transversely loaded LTP beam resting on elastic foundation, the LTP is divided into infinitesimal beam elements in the horizontal direction having equal thickness Δx within the soft soil region and $\Delta\xi$ within the column. Typical LTP elements over the soft soil and the columns and the stresses acting on LTP are shown in Figure 5.13b. The equilibrium of the vertical forces and moments of a typical element of LTP for $0 \le x \le s'/2$ under plain strain conditions yield the following equations:

$$\left.\begin{aligned} D_b\frac{d^2\theta_{sz}}{dx^2}+C_b\frac{dw_{sz}}{dx}-C_b\theta_{sz}=0 \\ C_b\frac{d\theta_{sz}}{dx}-C_b\frac{d^2w_{sz}}{dx^2}+q_s=p_s \end{aligned}\right\} \quad (5\text{-}36)$$

Similar set of equations can be governed within the CIC region ($0 \le \xi \le d/2$) replacing θ_{sz}, w_{sz}, p_s, and q_s by θ_{cz}, w_{cz}, p_c, and q_c, respectively. In Eq. (5-36), w is the transverse deformation of the centroid axis of the beam, θ is the rotation angle of the cross section of beam about its neutral axis, D_b and C_b are the bending rigidity and shear rigidity of the LTP with geosynthetics (Yin, 2000a). Considering linear stress-displacement relation proposed by Winkler (1867) and consolidation effect of the soft soil suggested by Deb (2007), normal pressure at the LTP-soil (q_s) and LTP-column interfaces (q_c) can be written as:

$$\left.\begin{aligned} q_s=\frac{k_s w_{sz}}{U} \\ q_c=k_{c,pl}w_{cz} \end{aligned}\right\} \quad (5\text{-}37)$$

where U is the degree of consolidation of the CIC-improved soft soil. Although the time dependent behaviour of the soft soil is considered in the proposed model, it should be noted that soil cementation and creep can significantly influence the behaviour of soft soil (Nguyen et al., 2014; Azari et al., 2016).

Combining Eqs. (5-36) and (5-37) and assuming Fourier cosine series which considers the symmetric embankment loading on the LTP, the ordinary fourth-order differential equations of the deflection for the LTP on the soil and column areas can be written as:

$$\left.\begin{aligned} D_b\frac{d^4w_{sz}}{dx^4}-\frac{D_b k_s}{C_b U}\frac{d^2w_{sz}}{dx^2}+\left(\frac{k_s}{U}\right)w_{sz}=S_0+\sum_{m=1}^{m=\infty}S_m\left[1+\frac{D_b}{C_b}\left(\frac{2m\pi}{s'}\right)^2\right]\cos\left(\frac{2m\pi x}{s'}\right) \\ D_b\frac{d^4w_{cz}}{d\xi^4}-\frac{D_b k_{c,pl}}{C_b}\frac{d^2w_{cz}}{d\xi^2}+k_{c,pl}w_{cz}=C_0+\sum_{m=1}^{m=\infty}C_m\left[1+\frac{D_b}{C_b}\left(\frac{2m\pi}{d}\right)^2\right]\cos\left(\frac{2m\pi\xi}{d}\right) \end{aligned}\right\} \quad (5\text{-}38)$$

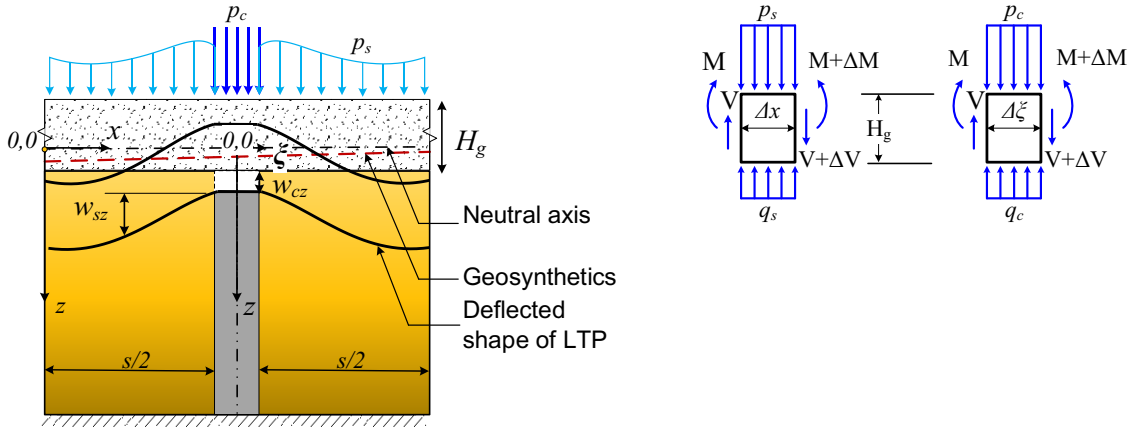

Figure 5.13. Illustration of: (a) assumed deformation shape of CIC-improved ground and (b) stresses on the LTP elements within the soil and column region.

The solution of the fourth order nonhomogeneous differential equation governing the deflected shape of a transversely loaded LTP beam resting on foundation soil for $0 \le x \le s'/2$ can be expressed as:

$$w_{sz} = e^{\vartheta x}(s_1 \cos \delta x + s_2 \sin \delta x) + e^{-\vartheta x}(s_3 \cos \delta x + s_4 \sin \delta x) + \frac{S_0}{k_s} + \sum_{m=1}^{m=\infty} s_m \cos\left(\frac{2m\pi x}{s'}\right) \quad (5\text{-}39)$$

Correspondingly, for $0 \le \xi \le d/2$, the governing equation can be expressed as:

$$w_{cz} = d_1 e^{r_1 \xi} + d_2 e^{r_2 \xi} + d_3 e^{-r_1 \xi} + d_4 e^{-r_2 \xi} + \frac{C_0}{k_{c,pl}} + \sum_{m=1}^{m=\infty} c_m \cos\left(\frac{2m\pi\xi}{d}\right) \quad (5\text{-}40)$$

where

$$\begin{cases} \vartheta = \left(\sqrt{\frac{k_s}{4D_b U}} + \frac{k_s}{4C_b U}\right)^{1/2} \\ \delta = \left(\sqrt{\frac{k_s}{4D_b U}} - \frac{k_s}{4C_b U}\right)^{1/2}, \end{cases} \quad \begin{cases} r_1 = \frac{k_{c,pl}}{2C_b} + \sqrt{\left(\frac{k_{c,pl}}{2C_b}\right)^2 - \frac{k_{c,pl}}{D_b}} \\ r_2 = \frac{k_{c,pl}}{2C_b} - \sqrt{\left(\frac{k_{c,pl}}{2C_b}\right)^2 - \frac{k_{c,pl}}{D_b}}, \end{cases} \quad \begin{cases} S_0 = \frac{1}{s'} \int_{-s'/2}^{s'/2} p_s \, dx \\ C_0 = \frac{1}{d} \int_{-d/2}^{d/2} p_c \, d\xi \end{cases} \quad (5\text{-}41)$$

and

$$\begin{cases} S_m = \frac{1}{s'}\int_{-\frac{s'}{2}}^{\frac{s'}{2}} p_s \cos\left(\frac{2m\pi x}{s'}\right) dx \\ C_m = \frac{1}{d}\int_{-\frac{d}{2}}^{\frac{d}{2}} p_c \cos\left(\frac{2m\pi \xi}{d}\right) d\xi \end{cases} \quad \text{and} \quad \begin{cases} s_m = \frac{S_m\left[1+\left(\frac{2m\pi}{s'}\right)^2\frac{D_b}{C_b}\right]}{D_b\left(\frac{2m\pi}{s'}\right)^2\left[\left(\frac{2m\pi}{s'}\right)^2+\frac{k_s}{C_b U}\right]+\frac{k_s}{U}} \\ c_m = \frac{C_m\left[1+\left(\frac{2m\pi}{d}\right)^2\frac{D_b}{C_b}\right]}{D_b\left(\frac{2m\pi}{d}\right)^2\left[\left(\frac{2m\pi}{d}\right)^2+\frac{k_{c,pl}}{C_b U}\right]+k_{c,pl}} \end{cases} \tag{5-42}$$

In practice, the stiffness of the LTP beam is greater than the stiffness of the soft soil and less than the stiffness of the CIC. Hence, the given solutions Eq. (5-39) and Eq. (5-40) are valid for $k_s < 4{C_b}^2 U/D_b$ (for soft soil region) and $k_c > 4{C_b}^2 U/D_b$(for column region). It can be noted that s_1 to s_4 and r_1 and r_2 are the constants of integration which can be determined by applying the boundary conditions. Once deflection (w) of the LTP beam is obtained, rotational angle (θ), shear force (V), bending moment (M) of the LTP, and tension (T) in the geosynthetics can be obtained using the following equations:

$$\left.\begin{aligned} \theta = \frac{D_b}{C_b}\left(\frac{d^3 w}{dx^3} + \frac{1}{C_b}\frac{dp}{dx} - \frac{1}{C_b}\frac{dq}{dx}\right) + \frac{dw}{dx}, \quad M = -D_b\frac{d\theta}{dx}, \\ V = C_b\left(\frac{dw}{dx} - \theta\right), \quad T = -S_{gr}(y_n - y_r)\frac{d\theta}{dx} \end{aligned}\right\} \tag{5-43}$$

where S_{gr} is the tensile stiffness of GR, y_n and y_r are the location of neutral axis and GR from the centreline of the LTP, respectively.

Due to symmetry, at the outside boundary of unit cell, the shear stress and the slope are assumed to be zero. It is assumed that there will be no rotation and transverse deformation at the connection between the LTP beam and the column. Within column region, at the column support, shear stress is equal to the reaction from the column support. Since the deformation of the column is constant through the width, the slope will be zero.

Boundary conditions for $0 \le x \le s'/2$ and $0 \le \xi \le d/2$ are as follows:

$$\left\{\left.\frac{dw_s}{dx}\right|_{x=0} = 0, \quad \tau_s|_{x=0} = 0, \quad \theta_s|_{x=\frac{s'}{2}} = 0, \quad w_s|_{x=\frac{s'}{2}} = 0\right\}$$
$$\left\{\left.\frac{dw_c}{d\xi}\right|_{\xi=0} = 0, \quad \tau_c|_{\xi=\frac{d}{2}} = -p_c + k_{c,pl} w_c|_{\xi=\frac{d}{2}}\right\} \tag{5-44}$$

Following the boundary conditions in Eq. (5-44), and using Eq. (5-43) (for θ_s, θ_c, τ_s, and τ_c) constants of integrations can be determined using simple Excel spread sheet. Due to the page limitation, calculation steps are not provided in detail.

5.4.2. Geometry and Material Properties of a CIC-Supported Embankments

Parametric study is conducted to predict the vertical deflection of LTP-soft soil-CIC system, bending and shear force in the LTP and tension developed in the geosynthetics using the proposed analytical model. This study considers the typical parameters for CIC-supported geosynthetic-reinforced embankments which are presented in Table 5.3. Modulus of subgrade reaction for the soft soil (k_s) and the CIC (k_c) are estimated using the equations suggested by Selvadurai (1979, Eq. 7.9) for one dimensional settlement.

Table 5.3. Material properties used in parametric study.

Material	Parameters
Embankment fill	H_e = 4.5m, γ_e = 18.3kN/m^3, φ_e = 43°
Granular fill	H_g = 0.75m, E_g = 35MPa, ν_g = 0.3
Foundation soil	H_s = 5m, E_s = 1MPa, ν_s = 0.3
CMC	H_c = 5m, d = 0.45m, s = 2.5m (square arrangement) ,
	E_c = 10000MPa, ν_c = 0.25
Geogrids	S_{gr} = 1000kN/m, ν_{gr} = 0.3

Note: H: height/depth/thickness; γ: unit weight; φ: frictional angle; E: Young's modulus; d: diameter; s: spacing; ν: Poisson's ratio; S: tensile stiffness. Suffices e, g, s, c, and gr are used to designate embankment fill, granular fill, soft soil, CIC, and geosynthetic reinforcement (GR).

In this study, it is assumed that the location of GR is always at quarter of the depth of the LTP below the centreline of the LTP. Similar to a concrete beam, a cracked section of reinforced Timoshenko beam (or LTP) is assumed since the soil in the LTP does not carry tension. Therefore, the second moment of inertia and the shear modulus of the beam have been reduced by 25% and 50%, respectively.

5.4.3. Results and Discussion

The stresses acting on top of the LTP layer placed at the base of the embankment can be determined by considering soil arching in the embankment in plane-strain condition using the expressions proposed by BS8006-1 (2010), EBGEO (2010), and van Eekelen *et al.* (2013). According to BS8006-1 (2010) and EBGEO (2010), stresses are distributed uniformly and in triangular shape on the geosynthetics, respectively. In contrast, van Eekelen *et al.* (2013) suggested an inverse triangular distribution of stresses on the geosynthetics. Since, van Eekelen et al. provides the minimum load intensity on the LTP within the column as displayed in Figure 5.14a, the minimum downward movements of LTP are observed on the column for this theory as plotted in Figure 5.14b. Whereas BS8006-2010 provides the minimum load intensity on the LTP within the soil region. Hence the minimum downward movements of LTP are observed for BS8006 on the soil area as plotted in Figure 5.14b.

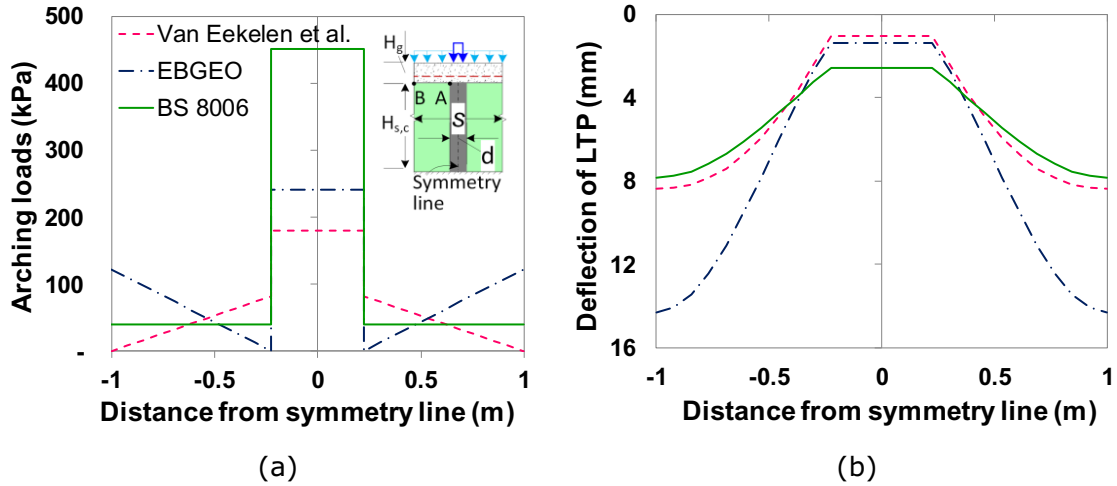

(a) (b)

Figure 5.14. Effect of arching on: (a) stresses on LTP and (b) deflection of LTP.

Since van Eekelen et al. concept results the maximum load at the column-soil interface (Point A in Figure 5.14a) shear force generated in the LTP at the column location is the maximum as shown in Figure 5.15a. In contrast, the maximum negative bending moment occurs at the column location in case of triangular distribution of load (EBGEO, 2010) whereas, the uniformly distribution pattern (BS8006-1, 2010) results in the minimum negative bending moment as plotted in Figure 5.15b.

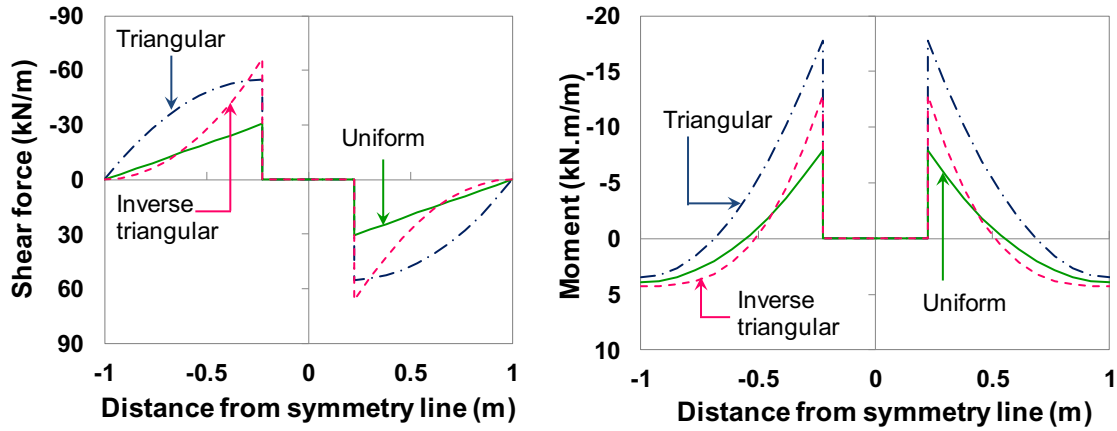

(a) (b)

Figure 5.15. Effect of arching on: (a) shear force and (b) moment in the LTP.

Figure 5.16a shows the variation of the magnitude of the rotation angle of the cross-section of LTP due to the bending. Figure 5.16b demonstrates the variation of the geosynthetics tension. It can be seen that the maximum tension occurs at the column edge and then continues to decrease away from the column for all the cases until reaches zero. This is because of the assumption of Timoshenko beam theory that a plane section remains plane after bending. Since, EBGEO (2010) predicts the greatest negative moment at the column edge, the maximum mobilised tension occurs for the case of EBGEO (2010).

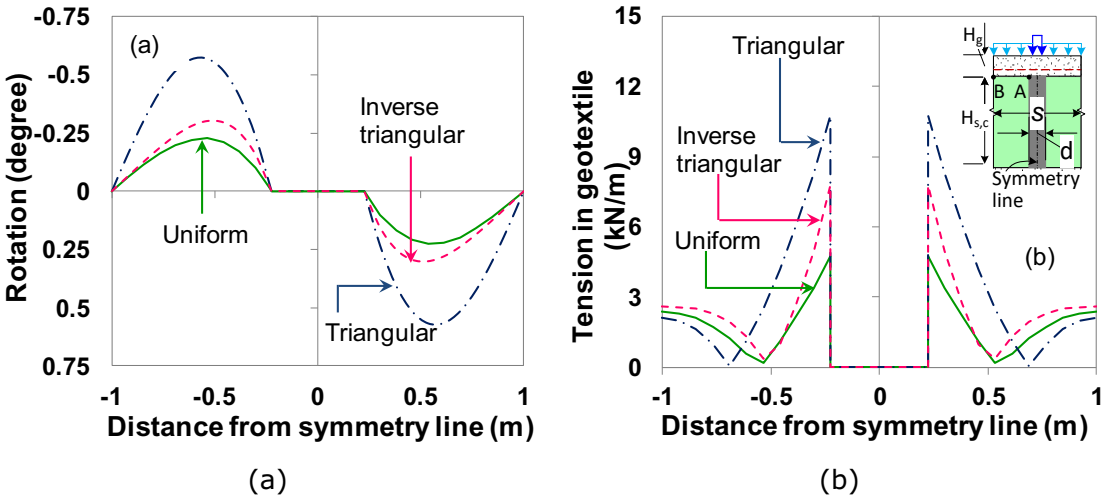

Figure 5.16. Effect of arching on: (a) rotation of LTP and (b) tension in GR.

5.5. Summary

This study has investigated the effects of thickness of load transfer platform (LTP) and geosynthetic reinforcement on concrete injected column (CIC) supported embankment simulating the LTP as a "reinforced Timoshenko beam". Results show that the geosynthetics can significantly affect the settlement of LTP when the thickness of LTP is between 0.2 m to 0.6 m, as the geosynthetics enhances the bending stiffness and shear stiffness of the composite LTP. The use of geosynthetics when LTP is thicker than 0.6 m has insignificant effect on load transfer mechanism in the column supported embankment. Although the material properties of

CIC have been used in this study, the outcomes can be applicable to other types of columns supporting embankment loads.

In addition, a new mechanical model with corresponding closed form analytical solutions have been proposed to study the settlement response of a granular fill layer with multilayer of geosynthetics for column stabilised soft soils. It can be concluded from this study that the use of multiple geosynthetic layers is more effective for higher embankment. Application of multiple geosynthetics reduces the maximum settlement of LTP. In case of two layers of geosynthetics, the top layer is more effective at the column location (in hogging region), whereas bottom layer is more effective in the middle of two columns (sagging region) in the column supported embankments. In addition, it is also observed that the use of one layer of stronger geosynthetics with equivalent stiffness of two layers of geosynthetics, does not results in the same settlement of LTP and tension in the GR compared to two layers of weaker GR. Therefore, it can be concluded that the load transfer mechanism in the column supported embankments with one stronger layer of geosynthetics is not equivalent to the load transfer mechanism with two weaker geosynthetics layers. Thus, the practicing geotechnical engineers should be cautious in since detailed design and construction drawings arrangement of GR in the LTP can have a severe consequence on the performance of the composite system. It should be noted that although the material properties of CIC have been used in this study, the proposed model can be used to analysis the behaviour of any type of column supported embankment with load transfer platform.

Furthermore, this study has investigated the effects of different stress distributions patterns on the load transfer platform (LTP) on the behaviour of geosynthetic-reinforced concrete injected column (CIC) supported embankment simulating the LTP as a “reinforced Timoshenko beam”. Results show that the load-settlement response of the LTP-soil-CIC system can significantly

be affected by the different arching theories. Uniformly distributed loading on the LTP following the British Standard predicts the smallest settlement, rotation, shear force and negative moment in the LTP within the soft soil region and the smallest mobilised tension as compared with the triangular and inverse triangular distribution of loading. These analysis results certainly raise question mark on the use of British Standard for designing the LTP in particular for the determination of tension capacity of the geosynthetics and settlement of the LTP for CIC improved embankment application.

CHAPTER 6

6. FIELD STUDY AND NUMERICAL MODELLING FOR A ROAD EMBANKMENT BUILT ON SOFT SOIL IMPROVED WITH CONCRETE INJECTED COLUMNS

6.1. General

Generally numerical modelling can provide an accurate and cost-effective approach to understand the behaviour of geosynthetic-reinforced column-supported embankment. Compared to two-dimensional plane-strain finite element modelling widely used in practice, full scale three-dimensional modelling while being more accurate for simulation of composite ground, is computationally intensive and hence is not widely adopted. When the problem geometry cannot be simplified to the two-dimensional plane-strain or axisymmetric, a full three-dimensional solution is required to obtain sensible results. This study presents a modelling of the geosynthetic-reinforced composite ground supporting a road embankment. Response of soft soil is captured by adopting Modified Cam-Clay model. In addition, Hoek-Brown constitutive model is considered to simulate non-linear stress-dependent yield criterion for Concrete Injected Columns that describes shear failure and tensile failure by a continuous function. A full-scale 3D finite element analysis is carried out to predict the time dependent settlement of embankment and generation and dissipation of excess pore water pressure in the soft soil during and after the construction.

To assess whether the proposed numerical model can capture real behaviour of composite ground, field monitoring data of deep soft clay deposit improved by CIC from Gerringong Upgrade is used to validate the model. The settlement and lateral displacements of ground,

stress transferred to column, and pore water pressure results for the embankment during and after the construction, measured using the field instrumentations including settlement plates, inclinometers, earth pressure cells on CIC, and pore pressure transducers, are compared with numerical predictions. The results show that there is a reasonable agreement between the field measurements and the numerical predictions. In addition, the numerical results provide insights to investigate load transfer mechanism in the composite ground capturing response of soil – column - embankment system.

6.2. Overview of the Case Study

This study presents the field measurements and the numerical predictions for the ground treatment works for the northern bridge approach embankment, corresponding to the 24 m long Northbound Twin Bridge at Omega Flat as a part of Gerringong Upgrade Project in NSW, Australia. The twin bridge was located between Station 1885 and Station 1909 of the main carriageway M110, approximately 140 km south of Sydney. The maximum fill height was 3.9 m. For the general embankment areas, a maximum total settlement of 100 mm was required in 40 years following the construction of the pavement. However, under the bridge approach slabs, the maximum total settlement should have been limited to 18 mm in 40 years post construction. Without any special ground treatment, the estimated post construction settlement would have exceeded 400 mm in 40 years.

For the above reasons, ground improvement works including preloading with pre-fabricated vertical drains (PVD) along with concrete injected columns (CICs) were adopted for the northern and southern bridge approach embankments of the Twin Bridge. The field results of the northern bridge approach embankment are reported in this study. The northern bridge approach with PVD and preloading extended from Station 1690 to Station 1867 (177 m) while the embankment section improved by CICs extended from Station 1867 to Station 1884 (17 m)

as shown in Figure 6.1. The adopted ground treatment zoning to provide the transition from the bridge abutment to the normal road embankment is also shown in Figure 6.1.

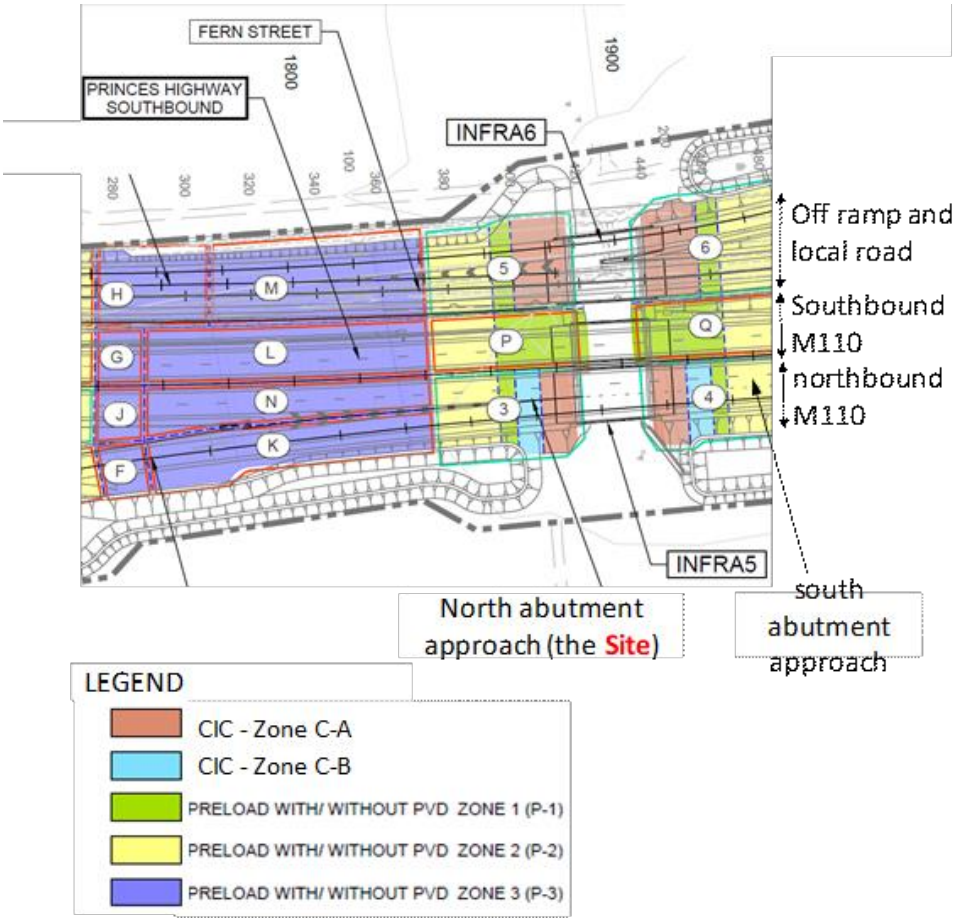

Figure 6.1. Ground improvement zones for the northbound bridge abutment approach leading to the north abutment of the Infra 5 bridge.

The details of the ground treatment zoning adopted in this project as shown in Figure 6.1 are as below:

- CIC Zone C-A: behind the bridge abutments with column spacings of 1.75 m and 2 m.
- CIC Zone C-B: directly behind zone A, with column spacing of 2.5 m.
- Preloading Zone P-1: where post construction settlement of 18 mm over 40 years was targeted.

- Preloading Zone P-2: transition between zone P-1 and P-3 to satisfy the requirement of maximum differential settlement.
- Preloading Zone P-3: general embankment area, where a PCS of 100 mm over 40 years was targeted.

The depth of the concrete injected columns ranged from 9 m to 12 m. The CICs were used in this instance to limit the ground settlement to within the design criteria of less than 18 mm over 40 years. The CICs were designed to increase the strength of the ground, which was composed of soft to firm clay. The CIC columns were 450 mm in diameter and 1.75 m, 2.0 m and 2.5 m in spacing. The design included both 40 MPa and 20 MPa strength columns for Zones C-A and C-B, respectively. Referring to Figure 6.2, a load transfer platform 750 mm in thickness was constructed above the CICs with two embedded layers of geotextile in the transverse and longitudinal directions.

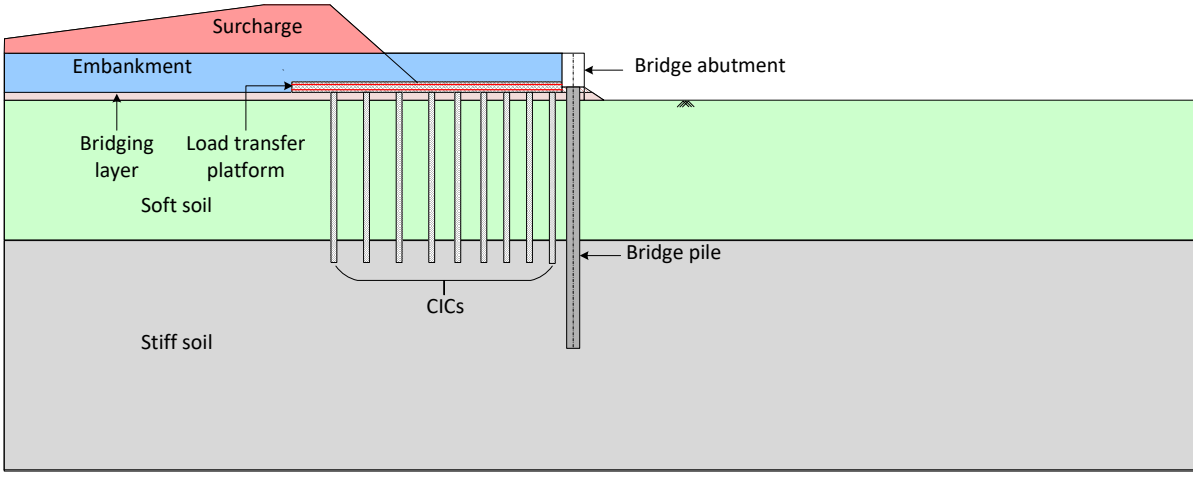

Figure 6.2. A schematic cross-sectional 2-D view of the CIC improved ground near the bridge abutment.

In this project, CICs were formed by lean concrete grout without reinforcement. As shown in Figure 6.3, CICs were installed into strong soil by achieving a minimum 500 mm embedment in the medium dense to very dense granular strata. The base of the socket was determined not

only by the available geotechnical data but also on the torque pressure displayed during the penetration process while installing CICs.

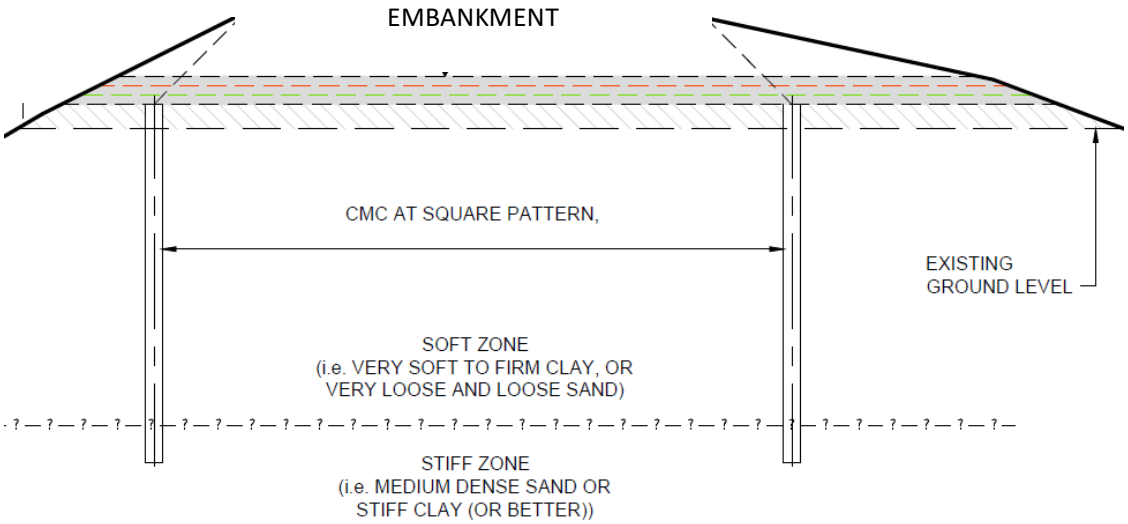

Figure 6.3. The requirement of termination depth during installing CIC.

6.3. Site Conditions and Soil Properties

The project area lies within the southern part of the Sydney Basin, consisting of the volcanic sedimentary sequences of the Shoalhaven Group bedrocks, overlain by unconsolidated Quaternary sediments deposited on the Broughton Creek and Crooked River Floodplains. The twin bridge is located within a low-lying area, where the Quaternary sediments including the alluvial and estuarine soils are present. The soil conditions were derived from the available geotechnical investigation data at INFRA-5 location as displayed in Figure 6.4a. Boreholes, K15, BH136, and BH141 and CPT205 were used to derive the soil strata and relevant geotechnical parameters as displayed in Figure 6.4b.

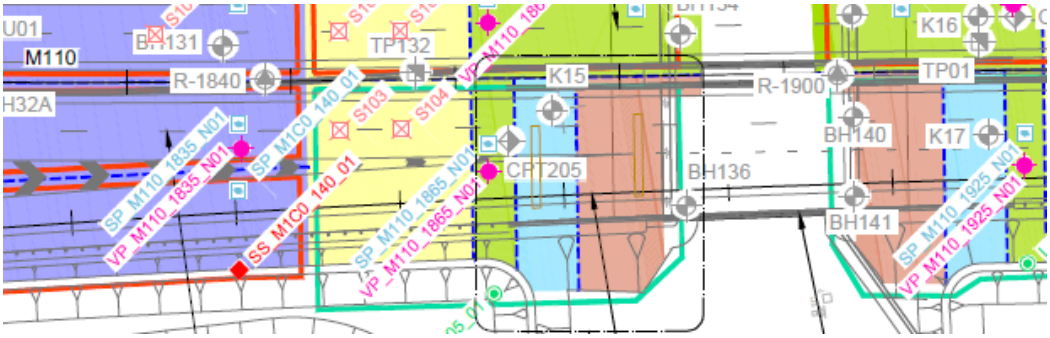

(a)

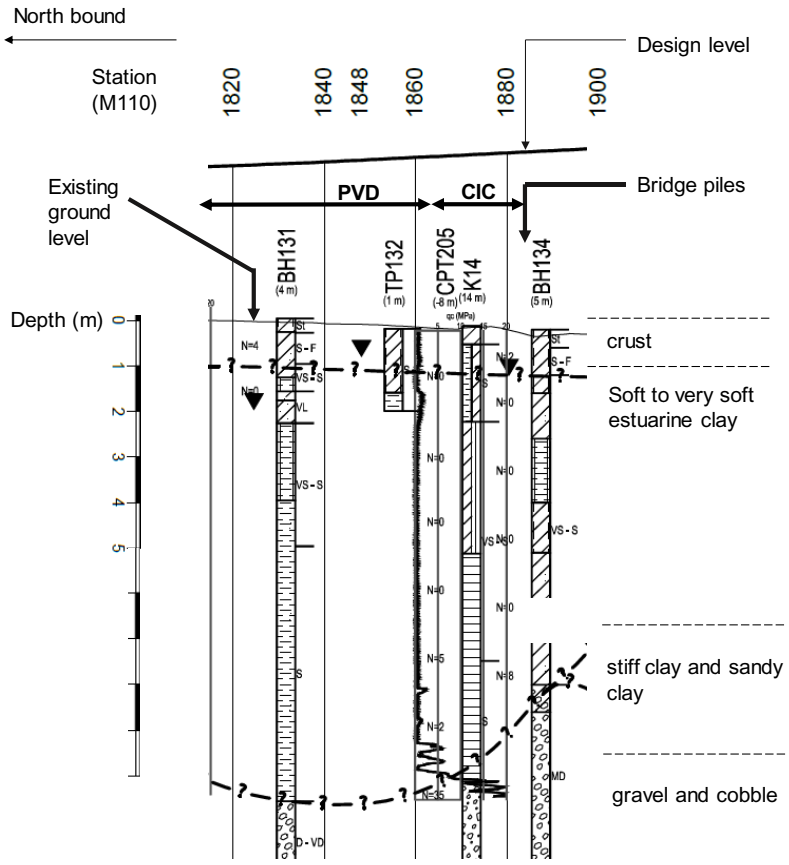

(b)

Figure 6.4. Geotechnical investigation at the site: (a) The investigation locations; and (b) geotechnical long section at the section of the northern bridge approach embankment.

The ground conditions in the soft soil treatment area consisted of the upper crust layer, overlying approximately 7.5 m of very soft to soft medium to high plasticity alluvial/estuarine clay, 2.7 m of soft alluvial clay, 3.9 m of dense alluvial gravel, which are underlain by 0.7 m

of medium to high strength sandstone rock. The groundwater level was at a depth of approximately 0.8 m. Table 6.1 summarises the model parameters for the soil layers. It should be noted that the soil properties were derived from the available site investigation and laboratory data.

The Modified Cam-Clay (MCC) material model (Muir Wood, 1990) was used to represent the behaviour of the very soft to soft estuarine clay and the alluvial firm to stiff clay and sandy clay. The underlying medium dense to dense gravel and cobbles were characterised by the linearly elastic-perfectly plastic material model with a Mohr-Coulomb (MC) yield criterion, which is controlled by both the effective friction angle ϕ' and the effective cohesion c'. The linear elastic and perfectly plastic MC model was also used to model the LTP and the embankment materials.

It is noted that the lateral earth pressure coefficient at rest (K_0) values for the soft clay and stiff clay were estimated using Eq. (6-1) as recommended by Mayne and Kulhawy (1982).

$$K_0 = (1 - \sin\phi') \times OCR^{0.5} \tag{6-1}$$

where ϕ' is the effective friction angle and OCR is over consolidation ratio of the soil deposit.

It should be noted that OCR (see Figure 6.5) were correlated to the undrained shear strength (s_u) measured through adopting the following equation (Ladd, 1991):

$$s_u / \sigma'_{v,o} = 0.22 \times OCR^{0.8} \tag{6-2}$$

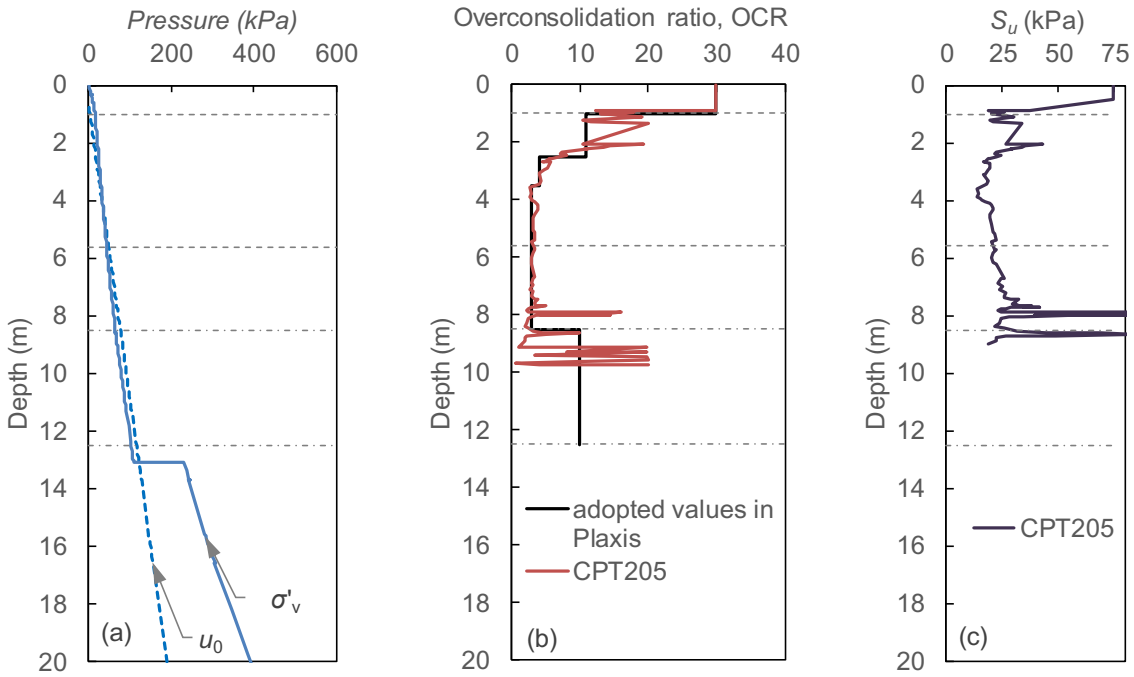

Figure 6.5. Soil profiles and properties.

The initial ground conditions adopted are: (i) the initial hydrostatic pore water pressure u_o, (ii) the groundwater table to be at the 0.8 m below the ground surface, and (iii) the initial in-situ vertical effective stresses ($\sigma'_{v,o}$) to be induced by the weight of the soil, while the horizontal effective stresses ($\sigma'_{h,o}$) were directly proportional to the vertical stresses (σ'_{vo}) using the K_0 values presented in Table 6.1.

Table 6.1. Soil model parameters used in the numerical modelling.

Soil layers	Thickness (m)	Model	γ (kN/m^3)	c' (kPa)	ϕ'(°)	ψ'(°)	E' (MPa)	ν	e_0	λ	κ	OCR	M	k_x (m/day)	k_y (m/day)	k_y (m/day)
Unit 1b without PVD	1	MCC	16	1	32			0.15	1.1	0.2289	0.0144	30	1.720	0.0796E-3	0.0796E-3	0.0398E-3
Unit 1b with PVD	1	MCC	16	1	32			0.15	1.1	0.2289	0.0144	30	1.720	0.0968E-3	0.0968E-3	0.0398E-3
Unit 2a without PVD	4	MCC	16	1	28			0.15	1.9	0.3161	0.0144	4	1.535	0.0796E-3	0.0796E-3	0.0398E-3
Unit 2a without PVD	1.5-3.5	MCC	16	1	28			0.15	1.9	0.3161	0.0144	2	1.535	0.0796E-3	0.0796E-3	0.0398E-3
Unit 2a with PVD	4	MCC	16	1	28			0.15	1.9	0.3161	0.0144	4	1.535	0.0968E-3	0.0968E-3	0.0398E-3
Unit 2a with PVD	1.5-3.5	MCC	16	2	28			0.15	1.9	0.3161	0.0144	2	1.535	0.0968E-3	0.0968E-3	0.0398E-3
3a/3b without PVD	4.5-8.1	MCC	17.5	3	28			0.15	1.5	0.1625	0.0138	2	1.497	0.249E-3	0.249E-3	0.125E-3
3a/3b with PVD	4.5-8.1	MCC	17.5	3	28			0.15	1.5	0.1625	0.0138	2	1.497	0.146E-3	0.146E-3	0.125E-3
3c/3d	0.75	MC	20	0.1	35	0	100E3	0.3								
Bridging layer	0.6	MC	22	5	45	0	60E3	0.3								
Embankment	4	MC	20	5	30	0	30E3	0.3								
Surcharge	3	MC	20	5	30	0	30E3	0.3								
LTP	0.75	MC	22	5	35	0	90E3	0.15								
R5/R6	2.6-5.4	MC	21	20	30	0	800E3	0.3								
R3/R4	3.5-14.3	MC	23	30	33	0	4E6	0.25								
Pile	17	Linear elastic	27				40E6	0.25								

Note: MC: Linear elastic – Perfectly Plastic Mohr-Coulomb model, MCC: Modified Cam Clay model, γ is the unit weight, c' is the effective cohesion, ϕ' is the effective friction angle, $\psi'$is the effective dilatancy angle, E' is the effective stiffness, υ is the Poisson's ratio, e_0 is the initial void ratio, λ is the slope of normal consolidation line, κ is the Slope of elastic swelling line, OCR is the over consolidated ratio, M is the slope of critical line which is function of K_0^{NC}($M \approx 3.0 - 2.8K_0^{NC}$), and k_x, k_y, k_z are the initial permeability of soil in x, y, and z directions, respectively.

6.4. Instrumentation

The instrumentation and monitoring plan (IMP) prepared for the monitoring of the performance of the proposed earthworks within this area is shown in Figure 6.6. One settlement plate (ID SP_M110_1865_N01) was installed to monitor total vertical soil movement in area of preloading and surcharge. This settlement plate was installed at the base of embankment to measure the settlement of the natural ground with the varying loads during and after the construction of the embankments. The settlement plate was placed on the founding material prior to placement of the first fill layer. Near the settlement plate, a vibrating wire piezometer (ID VP_M110_1865_N01) was installed inside a borehole to measure the evolution of the pore water pressure in the soft soil. The piezometer had a pressure range of 100 - 250 kPa.

Referring to Figure 6.6, one earth pressure cell (ID PC_M110_1870_N01) was installed in the CICs region to monitor the vertical stresses transmitted to the CICs. This earth pressure cell had a pressure range of 50 – 100 kPa, which was installed on top of the selected CIC head to measure the vertical stress transferred from the embankment fill to the CIC. The capacity of the cell was selected based on the overburden pressure at proposed locations. It should be noted that an earth pressure cell consists of two stainless steel plates welded together around their periphery and separated by a narrow gap filled with hydraulic fluid. External pressures increase the fluid pressure, which is converted into an electrical signal transmitted by cable to the readout location. The exact position of the earth pressure cell is shown in Figure 6.6.

As shown in Figure 6.6, two inclinometers (i.e. I_M110_1885_N01 and I_M110_1865_N01) were used to investigate lateral displacement of soil deposit during the embankment construction. The inclinometers were installed after CICs installation

and before the construction of the load transfer platform. Inclinometer ID I_M110_1885_N01 was installed to monitor the expected lateral ground movement near the bridge pile due to the embankment fill behind the bridge abutment. Inclinometer ID I_M110_1865_N01 was located at the interface of the PVD and CIC improved areas to monitor lateral stability of the embankment as well as the soil surrounding the CICs. As evident in Figure 6.6, this inclinometer was located between the two adjacent CICs nearby and orientated perpendicular to the CMC - PVD interface.

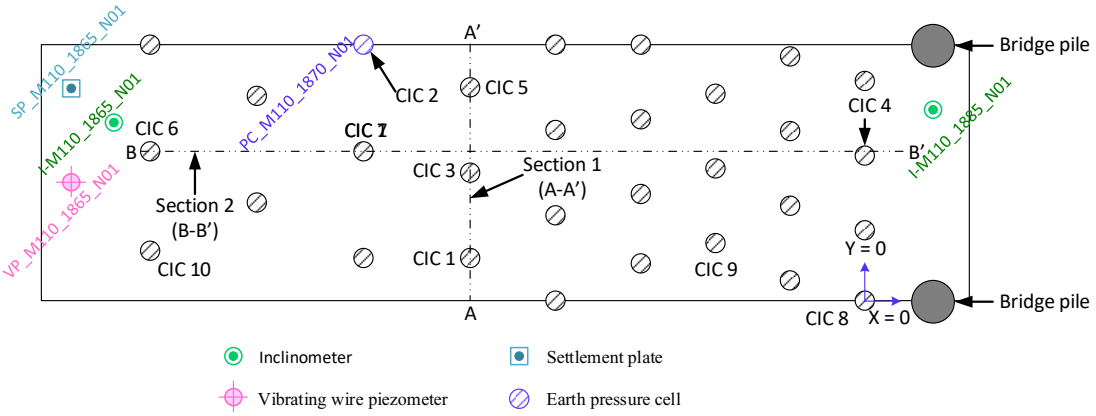

Figure 6.6. Layout of instrumentation for the section at the Infra-5 close to the North bound North abutment.

6.5. Numerical Modelling Details

Three-dimensional numerical modelling of concrete injected column supported embankment was carried out with total embankment length of 80 m as shown in Figure 6.7 using finite element software package PLAXIS 3D (AE). The finite element mesh with 5,30,181 number of elements and 7,31,947 number of nodes in the three-dimensional model is shown in Figure 6.8a and Figure 6.8b. To improve the thick soft soil deposit (which is approximately 10 m deep as shown in Figure 6.7), concrete injected

columns (CICs) 450 mm in diameter at varied centre-to-centre spacing (1.75 m, 2.0 m, and 2.5 m) in a square arrangement as illustrated in Figure 6.8a, were adopted.

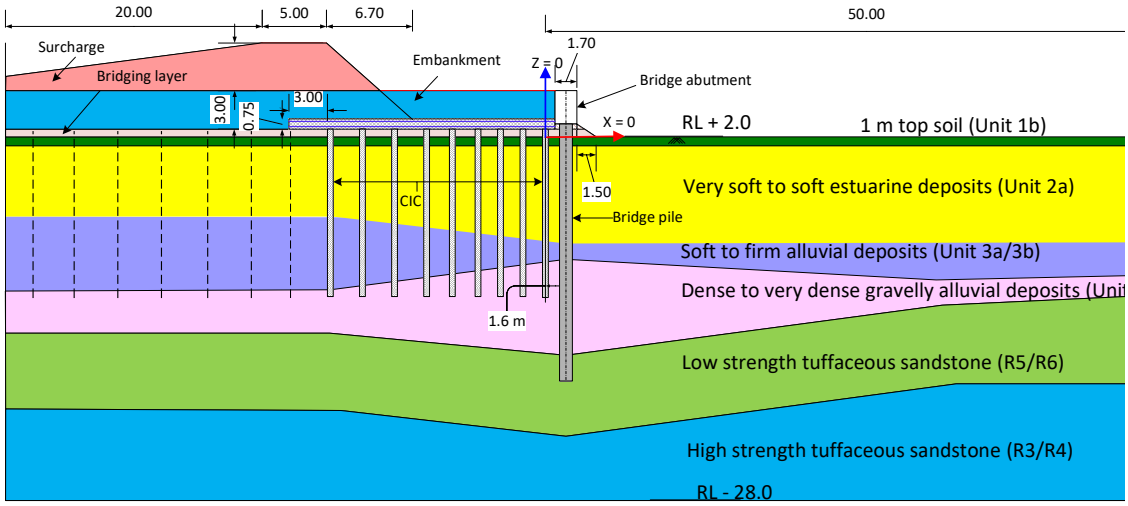

Figure 6.7. Schematic diagram of the section adopted for finite element modelling (all dimensions are in metre and not necessarily to scale).

Once the geometry of the entire column-soil-embankment system was fully defined in three dimensions following the site conditions, the geometry was meshed into finite elements to perform the numerical calculations. The adopted mesh was sufficiently fine to ensure the mesh size did not impact the predictions and accurate numerical results were achieved without excessive calculation time. Indeed, 10-node tetrahedral solid elements with a second order interpolation of displacements were adopted to simulate the soil layers and CICs. In addition, 6-node membrane-geogrid elements were used to simulate the behaviour of geosynthetics. Moreover, to simulate the soil-structure interaction between geosynthetics and granular fill material, 12-node triangular interface elements were used. Three translational degrees of freedom of interface elements allowed the differential displacements between the node pairs.

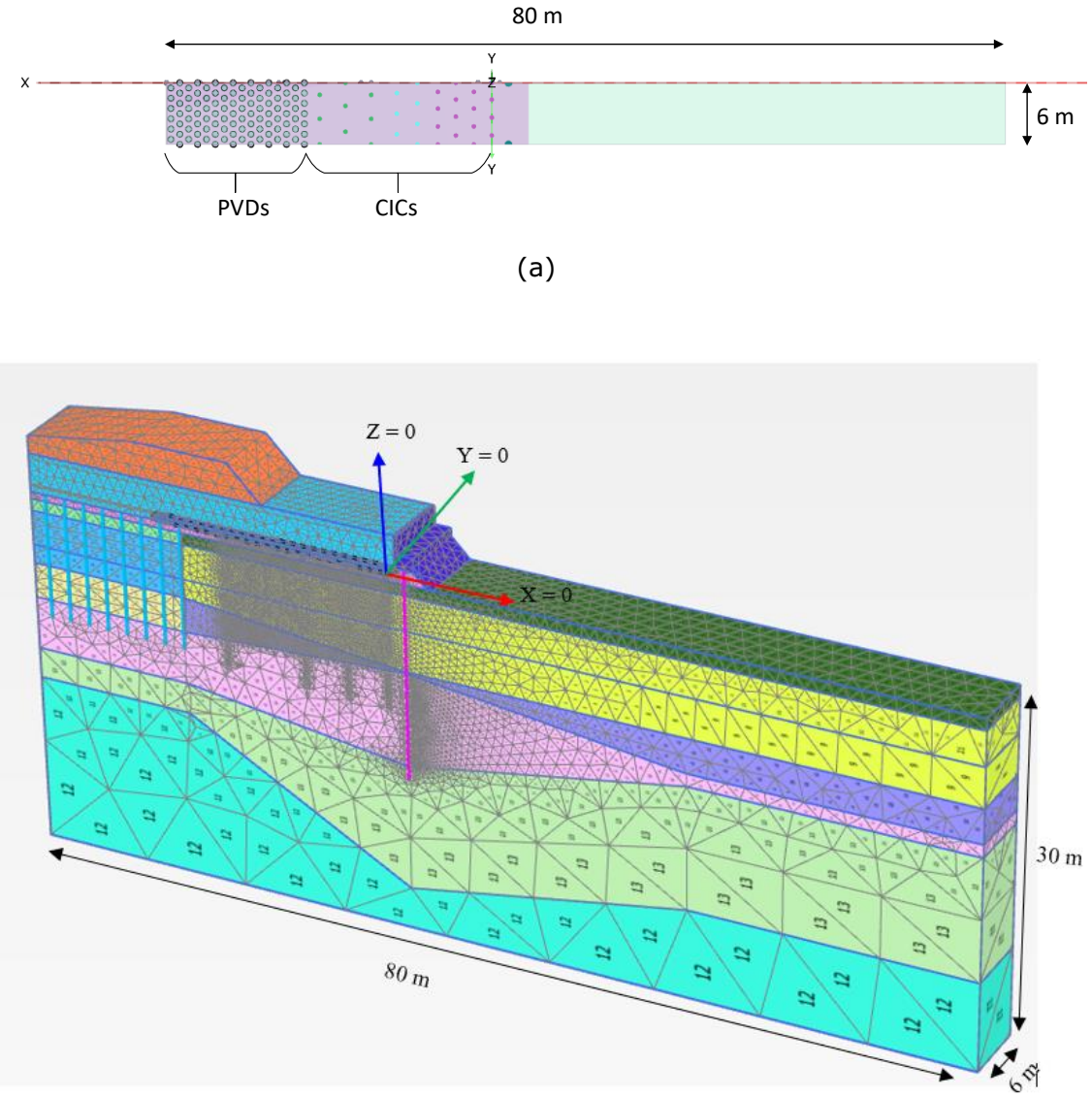

Figure 6.8. Geometry of adopted numerical modelling: (a) plan view and (b) three-dimensional finite-element mesh.

6.5.1. Boundary and Initial Conditions

The 30 m deep soil profile has been modelled with a rough-rigid (zero displacement in three directions) bottom boundary along the plane of z = −30 m. To minimize boundary effects, the lateral boundary of the finite-element mesh was extended 50 m horizontally

(Figure 6.9). The far field lateral boundaries (i.e. the planes of x = −30 m and x = +50 m) were smooth rigid (i.e. zero displacements in x direction while free to displace in z direction). In addition, two vertical planes of symmetry (i.e. y = 0 and y = 6 m) were smooth rigid (zero displacement in the y direction considering symmetricity of the section being considered). With respect to the drainage boundary conditions, the water table was located at 0.8 m below the ground surface (i.e. z = −0.8 m) while the bottom of the finite-element mesh was assumed to be impermeable. In addition, water flow was not permitted across the lateral boundaries at x = −30 m and x = +50 m.

Since in the initial state, columns, piles, and embankments were not present, only the soil deposit was present in the initial phase and considered to calculate the initial stresses. The initial conditions include the initial hydrostatic pore water pressure assuming groundwater table at z = −0.8m. Since the soil layers were not horizontal, the initial stresses in the soil were computed by means of gravity loading followed by equilibrium under K_0 condition. Contours of the initial hydrostatic pore water pressure are displayed in Figure 6.9a; whereas in-situ vertical effective stresses in the soil deposit is shown in Figure 6.9b.

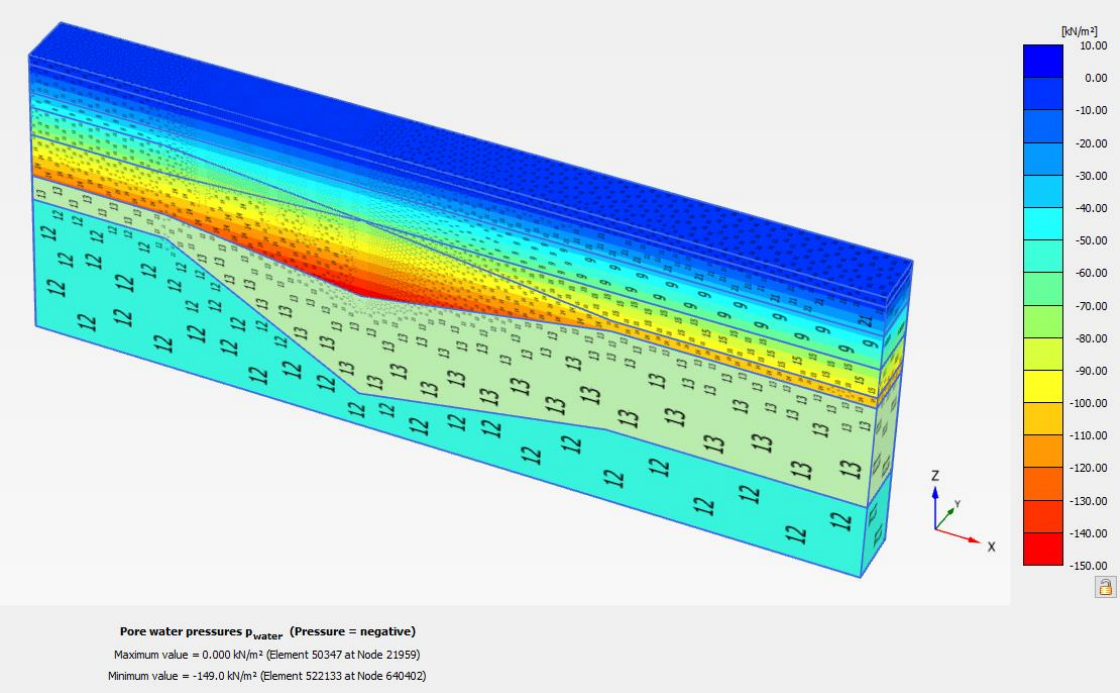

(a)

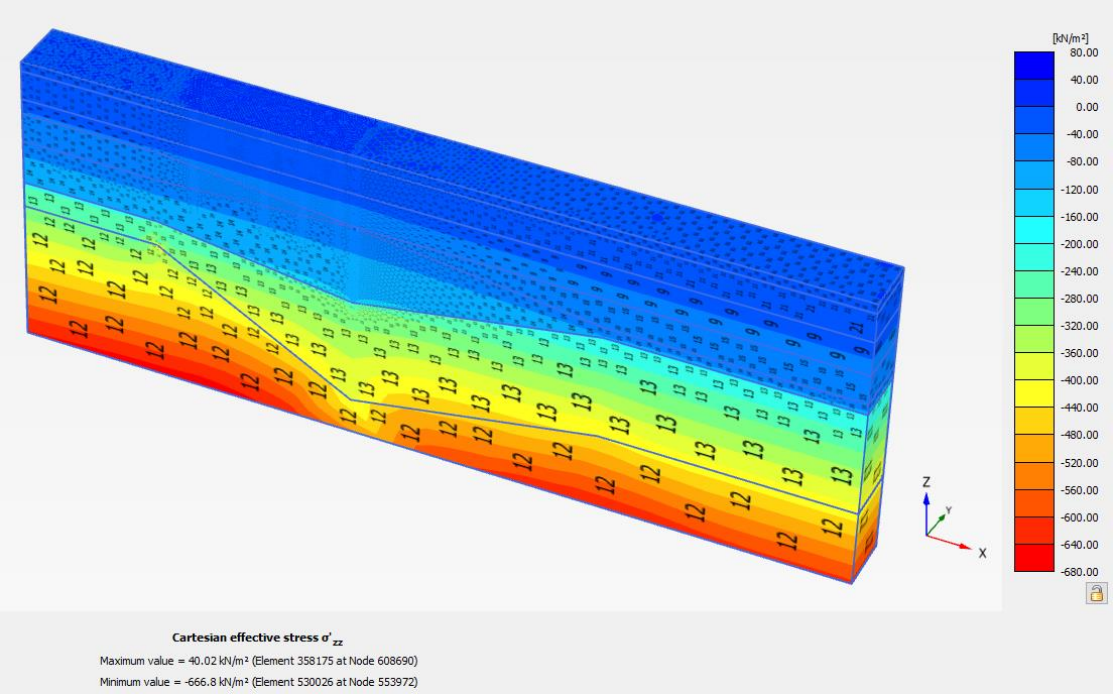

(b)

Figure 6.9. Initial results of: (a) hydrostatic pore water pressure and (b) vertical effective stresses in soil deposit.

6.5.2. Modelling of Concrete Injected Columns

To simulate CIC in a rational way, it is important to have a reasonable estimate of the values of CIC engineering properties such as compressive strength, tensile strength, and modulus of elasticity. All the properties adopted in the finite element analysis are summarised in Table 6.2. Concrete injected columns comprised of vertical inclusions of 40 MPa (at the location where column spacing was 1.75 m and 2.0 m) and 20 MPa (where column spacing was 2.5 m) concrete columns of 450 mm diameter corresponding to Zones C-A and C-B as shown in Figure 6.1, respectively.

Tensile strength is one of the key parameters while modelling the behaviour of CIC. According to Eurocode 2 (2004), the mean axial tensile strength (f_{ctm}) of concrete at 28 days can be related to the 28-day uniaxial compressive strength (f_{ck}) which is shown in Eq. (6.3).

$$f_{ctm} = 0.3 \times f_{ck}^{2/3} \text{ MPa} \tag{6.3}$$

Eurocode 2 (2004) recommends that the design tensile strength of plain concrete ($f_{ctd,pl}$) can be estimated using the following equation.

$$f_{ctd,pl} = \alpha_{ctd,pl} \times f_{ctk,0.05}/(\gamma_c k_f) \text{ MPa} \tag{6.4}$$

where $\alpha_{ctd,pl}$ is the coefficient to account for long-term effects on the tensile strength (0.8); $f_{ctk,0.05}$ is the characteristic tensile strength of concrete ($f_{ctk,0.05} = 0.7 \times f_{ctm}(t)$; t is the age of concrete); γ_c is the concrete partial factor for ultimate limit state in normal use ($\gamma_c = 1.5$); and k_f is a factor to account for calculation of design resistance of cast in place columns without permanent casing ($k_f = 1.1$).

Eurocode 2 (2004) states that the indicative value of the mean secant modulus of elasticity (E_{cm}) of concrete strength class $f_{ck} = 20$ MPa is 30 GPa. However, the estimated E_{cm} should only be regarded as indicative for general applications. According to ASIRI (2012) French national project for the sign of rigid inclusions, the long-term modulus of elasticity (E_c) of concrete inclusions installed in-situ with displacement can be estimated to be of approximately 10 GPa, obtained from the following equation.

$$E_c = 3700 \times f_{ck}^{1/3} \text{ MPa} \tag{6.5}$$

where f_{ck} is the specified 28-days compressive strength of concrete in MPa.

The behaviour of concrete columns differs from the behaviour of soils in the sense that they are generally stiffer and stronger. The dependency of the stiffness of concrete on the stress in the range applicable in this study is insignificant, therefore, stiffness of columns can be considered constant. Whereas, the dependency of the shear strength of the concrete on the stress level is significant (Karam and Tabbara, 2009). Hence, behaviour of concrete columns subjected to shear stresses can be regarded as a frictional material. Therefore, Mohr-Coulomb or isotropic linear elastic failure criteria has been adopted by most of the researchers to simulate shear strength of plain concrete (e.g. Bićanić and Zienkiewicz, 1983). However, as reported by Girgin and Girgin (2015) and Girgin (2009), when the concrete columns are subjected to large axial stresses, a linear stress dependency of shear strength as obtained from Mohr-Coulomb model, would not be realistic and accurate. The Hoek-Brown failure criteria (Hoek et al., 2002; Hoek, 2006) which considers the non-linear approximation of the strength of material as a function of principal stresses was used by several researchers to simulate strength of plain concrete (e.g. Grassl *et al.*, 2002;

Ilki *et al.*, 2004) and therefore was adopted in this study. The generalised Hoek-Brown failure criteria used in this study can be formulated as follows:

$$\frac{\sigma_1}{\sigma_c} = \frac{\sigma_3}{\sigma_c} + \sqrt{m\frac{\sigma_3}{\sigma_c} + s} \tag{6.6}$$

where σ_1 and σ_3 are the major and minor principal stresses at failure, respectively, σ_c is the uniaxial compressive strength of the intact material (e.g. intact rock or uncracked concrete), and A and B are the two Hoek-Brown material constants. The adopted constitutive model in this study incorporates nonlinear Hoek-Brown shear yielding criterion (Hoek and Brown, 1980) combined with a tensile yield criterion adopting a tensile strength of concrete. In addition to the concrete strength σ_c and the dilation angle ψ_c, the Hoek-Brown parameter s =1 were used, assuming that concrete column is intact, and the parameter m = 12 as per the recommendation by Karam and Tabbara (2009). Parameters of the Hoek-Brown model adopted in this analysis are summarised in Table 6.2.

Table 6.2. Material property of concrete columns.

Parameters	Unit	Concrete Grade 20 MPa	Concrete Grade 40 MPa
Unit weight (γ_{unsat})	kN/m^3	24	24
Young's modulus (E_c)	kN/m^2	10 E 6	12.5 E 6
Poisson's ratio (ν)	-	0.2	0.2

6.5.3. Modelling of Geosynthetics and Soft soil

Behaviour of geosynthetics under the applied stresses were considered as linear elastic – perfectly plastic and orthotropic and therefore the maximum tensile strength (T_f) and axial

stiffness in both horizontal directions were assumed the same (i.e. $EA_x = EA_y$). In the three-dimensional finite element modelling, $EA_1 = EA_2 = 500$ kN/m and the tensile strength of 50 kN/m were adopted referring to the geotextile grade ACET ex GT 500/50 used in the field during construction.

The prefabricated vertical drains (PVD) were also installed adjacent to the region improved with concrete injected columns as shown in Figure 6.8a. Following the construction sequence on site, the vertical drains were installed (activated) in the numerical model following the construction of the bridging layer. Due to the installation of the vertical drains via a mandrel, soil around the drains (smear zone) is disturbed resulting in reduced permeability, impacting the excess pore water pressure dissipation rate and therefore the rate of ground settlement. In this study, following the recommendation made by Hansbo (1981), equivalent horizontal permeability of the soil between the installed vertical drains, capturing the smear effect, was reduced to k_{h-PVD} adopting Eq. (6.7).

$$k_{h-PVD} = \frac{\ln(n)-\frac{3}{4}}{\ln\left(\frac{n}{m}\right)+\left(\frac{k_h}{k_s}\right)\ln(m)-\frac{3}{4}} \times k_h \quad (6.7)$$

where n is the ratio of the equivalent radius of the unit cell to that of the PVD ($n = \frac{R}{r_w}$), m is the ratio of equivalent radius of the smear zone to that of the drain ($m = \frac{r_s}{r_w}$) and k_h and k_s are the coefficients of horizontal permeability for the undisturbed and smear zone, respectively. In this study the spacing between the vertical drains was 3 m in triangular pattern (i.e. S = 3 m and R= 1.575 m), while the equivalent radius of the vertical drains was r_w = 33.1 mm (i.e. n = 47.6) and the equivalent radius of the installation mandrel was r_m = 45.4 mm. Considering the local experience with soft soils in New South wales,

$\frac{k_h}{k_s} = 2$ and $\frac{r_s}{r_m} = 3$ were adopted in the numerical modelling to calculate the equivalent horizontal permeability of the soil between vertical drains. For example, referring to Eq. (6.7), $k_{h-PVD} = 1.12E-09\ m/s$ was adopted in the numerical modelling for Unit 2a with PVD.

In this study, the variations of the soil permeability with the void ratio, in accordance with the expression proposed by Taylor (1948) was adopted as follows.

$$\log k = \log k_i - \frac{e_0 - e}{c_k} \tag{6-8}$$

where k_i is the reference permeability at initial void ratio e_0, c_k is the slope of $\log k - e$ graph. According to Tavenas et al. (1983), $c_k = 0.5e_0$ was adopted in this study.

6.5.4. Construction and Modelling Sequence

The embankment construction was modelled in stages as shown in Figure 6.10 following the actual construction sequence. After the initial equilibrium to establish the initial conditions, the CICs were installed and therefore properties of the plain concrete (see Table 6.2) were assigned to the solid element for columns. The subsequent embankment construction was modelled by gradually placing the embankment layers (i.e. activating the gravity loading in the embankment fill for each layer) until the full embankment was constructed. The rate of construction was simulated according to what was constructed on site (as shown in Figure 6.11). A summary of construction stages adopted in this numerical simulation is presented in Table 6.3.

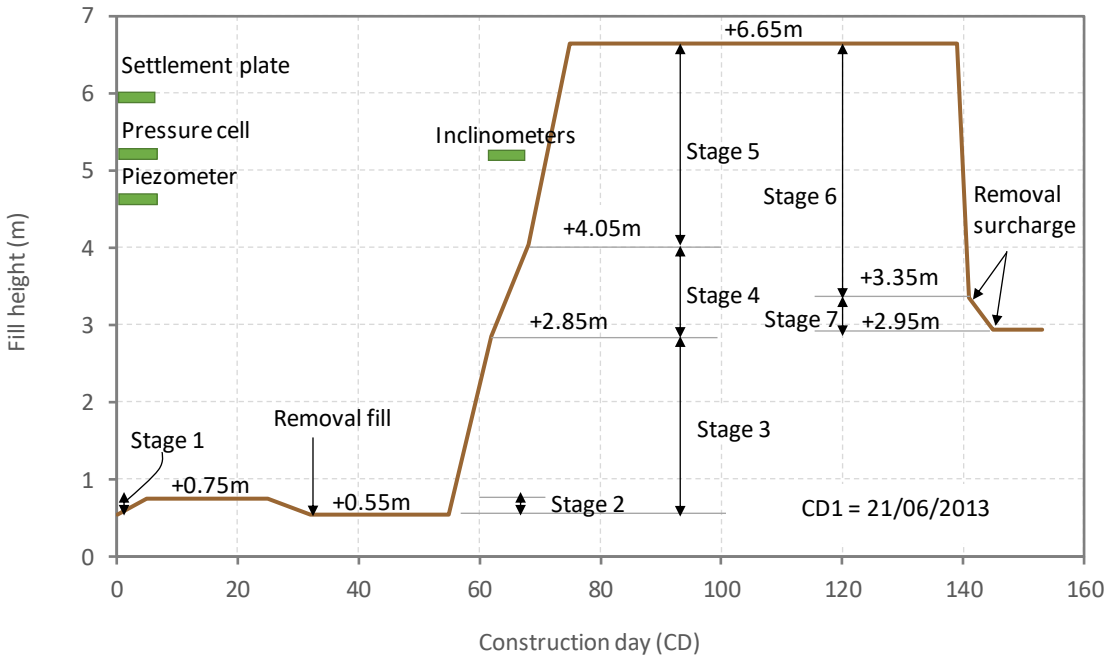

Figure 6.10. Construction sequence and installation of instrumentations in site.

Table 6.3. Numerical modelling stages adopted to analysis the behaviour of the embankment built on CIC improved soft soil.

Stage	Activity	Calculation type	Consolidation interval (days)	Loading type
0	Initial condition	Gravity loading	-	Staged construction
1	Installation of bridging layer	Plastic	-	Staged construction
3	Installation of PVDs	Plastic	-	Staged construction
4	Installation of CICs	Plastic	-	Staged construction
5	Installation of bridge piles	Plastic	-	Staged construction
6	Installation of LTP	Consolidation	1	Staged construction
7	Top up first 0.55 m fill	Consolidation	1	Staged construction

Stage	Activity	Calculation type	Consolidation interval (days)	Loading type
8	Consolidation for 6 days	Consolidation	6	Staged construction
9	Top up to 0.75 m fill	Consolidation	5	Staged construction
10	Consolidation for 20 days	Consolidation	20	Staged construction
11	Fill removal up to 0.55 m	Consolidation	7	Staged construction
12	Consolidation for 23 days	Consolidation	23	Staged construction
13	Fill up to 2.85 m	Consolidation	7	Staged construction
14	Fill up to 4 m	Consolidation	6	Staged construction
15	+1 m surcharge	Consolidation	7	Staged construction
16	+2 m surcharge	Consolidation	7	Staged construction
17	+3 m surcharge	Consolidation	7	Staged construction
18	Consolidation for 64 days	Consolidation	64	Staged construction
19	Remove 1m surcharge	Consolidation	2	Staged construction
20	Remove 2 m surcharge	Consolidation	7	Staged construction
21	Remove 3 m surcharge	Consolidation	7	Staged construction
22	Install abutment and back fill	Consolidation	7	Staged construction

6.6. Results and Discussion

Results obtained from the three-dimensional finite-element analysis are presented and compared with the field measurements for verification purpose and also discussed in this section. The comparisons were carried out in terms of the settlement of ground surface, the lateral displacement and the excess pore water pressure in the soft clay, and the stresses transferred to the columns. The embankment construction began in March 2013 and was completed in 183 days, including two significant consolidation periods of 64 days and 23 days.

6.6.1. Soil Deformation and Evolution of Excess Pore Pressure

6.6.1.1. Ground surface Settlement

Figure 6.12 displays the evolution of the settlements under the base of embankment over time (Refer to Figure 6.11 highlighting the location of Point A for settlement predictions). High downward movements of soils were observed immediately after the embankment fill was placed in case of field measurements as well as numerical predictions. When the embankment height increased from 0.55 m to 6.65 m, numerical analysis predicted increase of soil settlement from 0.12 m to 0.45 m, while corresponding field measurements showed that the settlement increased from 0.02 m to 0.40 m. Since the selected settlement plate was monitored near the interface of the PVD and CIC areas (i.e. SP_M110_1815_N01 in Figure 6.11), the rather quick process of consolidation could be explained by the fact that the excess pore water pressure dissipated hydraulically through PVDs as well as mechanically as a result of load transfer to columns as discussed by Han and Ye (2001). It should be noted that the numerical predictions reproduced satisfactorily the embankment behaviour in qualitative terms, while some disparities were observed.

The disparities were more significant in the early stages of embankment construction, which may be related to uncertainties in the assessment of the soft properties (e.g. OCR).

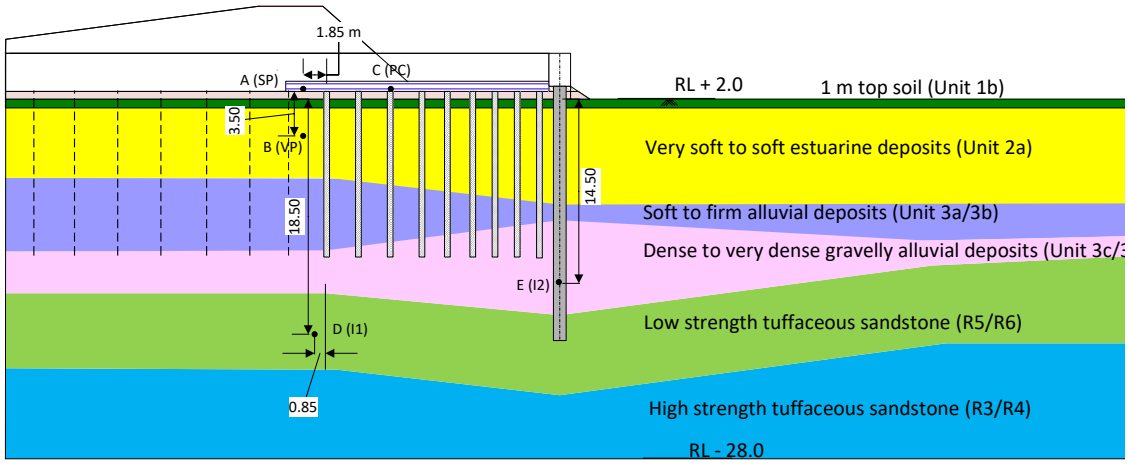

I1: Inclinometers (I_M110_1865_N01)

I2: Inclinometers (I_M110_1885_N01)

VP: Vibrating wire piezometer (VP_M110_1865_N01)

SP: Settlement plate (SP_M110_1865_N01)

PC: Earth pressure cell (PC_M110_1870_N01)

Figure 6.11. Locations of instrumentations for field measurements.

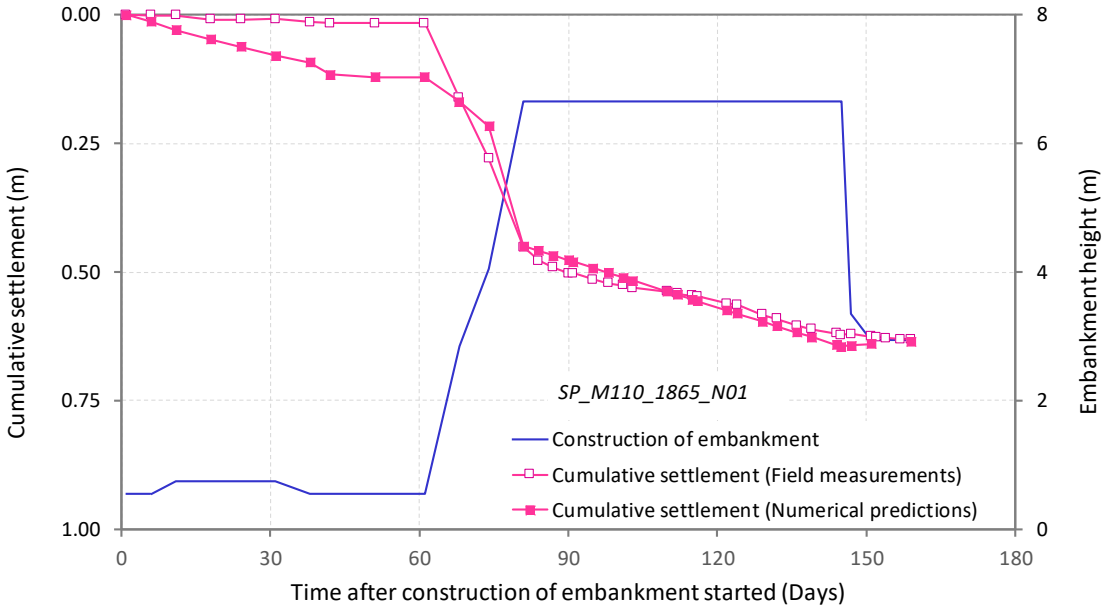

Figure 6.12. Variation of settlement at the base of the embankment.

6.6.1.2. Lateral soil deformation

Inclinometers were used to measure the lateral deformation of the soil as a result of embankment vertical settlement and soil squeezing between columns. Figure 6.13a and Figure 6.13b show the measured and predicted lateral displacement profiles with depth at inclinometers I1 (I_M110_1865_N01) and I2 (I_M110_1885_N01) with time (refer to Figure 6.11 for the position of the inclinometers). It is evident that both predicted and measured lateral soil displacements decreased gradually with depth. It was observed that the maximum measured lateral displacements at the ground surface at the location of I1 (I_M110_1865_N01) were 11 mm and 260 mm, when 2.85 m and 4.05 m of the embankment fill were placed (i.e. corresponding to Construction Days 67 and 78), respectively. On the other hand, numerical analysis predicted the maximum lateral displacement of 32 mm and 210 mm for the same locations, respectively. Although the shape of the lateral displacements profiles is captured by finite element analysis reasonably well, the magnitude of lateral displacements were rather overpredicted in the early stages of construction. This may be attributed to the adopted initial stress state, particularly adopted K_0 profile, and its variation across the site. The lateral displacements along the depth of soft soil closer to the bridge pile (i.e. at I2 (I_M110_1885_N01) in Figure 6.6 and Figure 6.11) and the furthest to the bridge pile (i.e. I1 (I_M110_1865_N01) in Figure 6.11) are shown in Figure 6.13a and 13b, respectively. It can be observed that the lateral displacements increased instantaneously during the construction of the embankment fill and reached a maximum upon completion of the embankment construction. It is also noticed that the lateral displacements significantly reduced at the depth where the soil profile changed from soft to stiff clay.

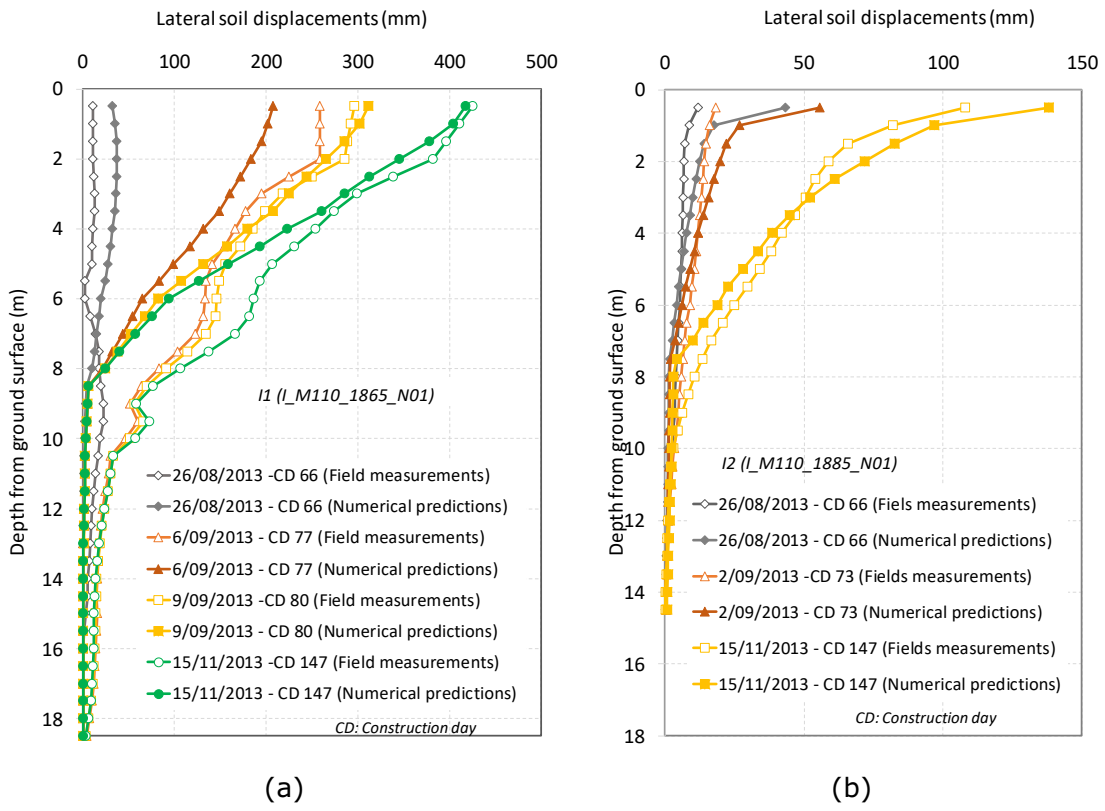

Figure 6.13. Variation of lateral soil displacement with depth at the locations of inclinometer: (a) I1 (I_M110_1865_N01) and (b) I2 (I_M110_1885_N01).

Figure 6.14a and Figure 6.14b show the measured and predicted lateral displacements of the soft soil (measured by I1 and I2) over time. At the end of 78 days (i.e. CD 78), the computed lateral deformation of soil at the location of I1 reduced by 23% (from 392 mm to 299 mm) when the depth of interest incraesed from 0.5 m to 2.0 m. Therefore, it is evident that the soil close to the ground surface would be more disturbed due to both vertical and lateral displacement when compared to the deeper soil deposits. Similarly, 24% reduction in the maximum lateral soil movement was measured in-situ at I1 at CD 78 when depth of the soil increased from 0.5 m to 2.0 m. Whereas, 34% reduction (from 92 mm to 60 mm) in the maximum lateral displacements was observed at the location of

I2 at Construction Day 74 when the depth of point of interest increased from 0.5 m to 2.0 m (see Figure 6.14b).

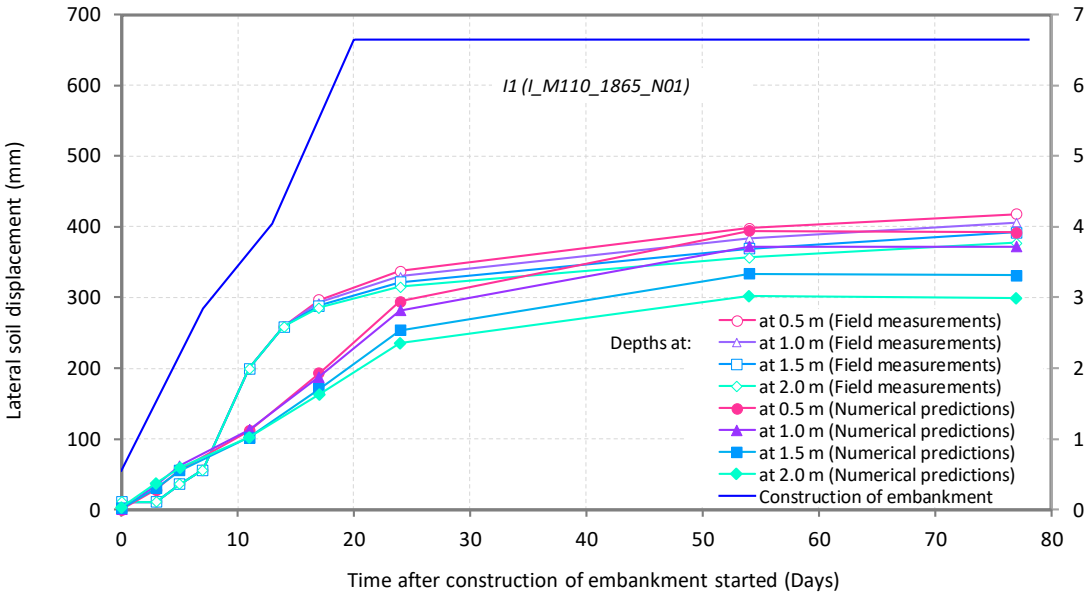

(a)

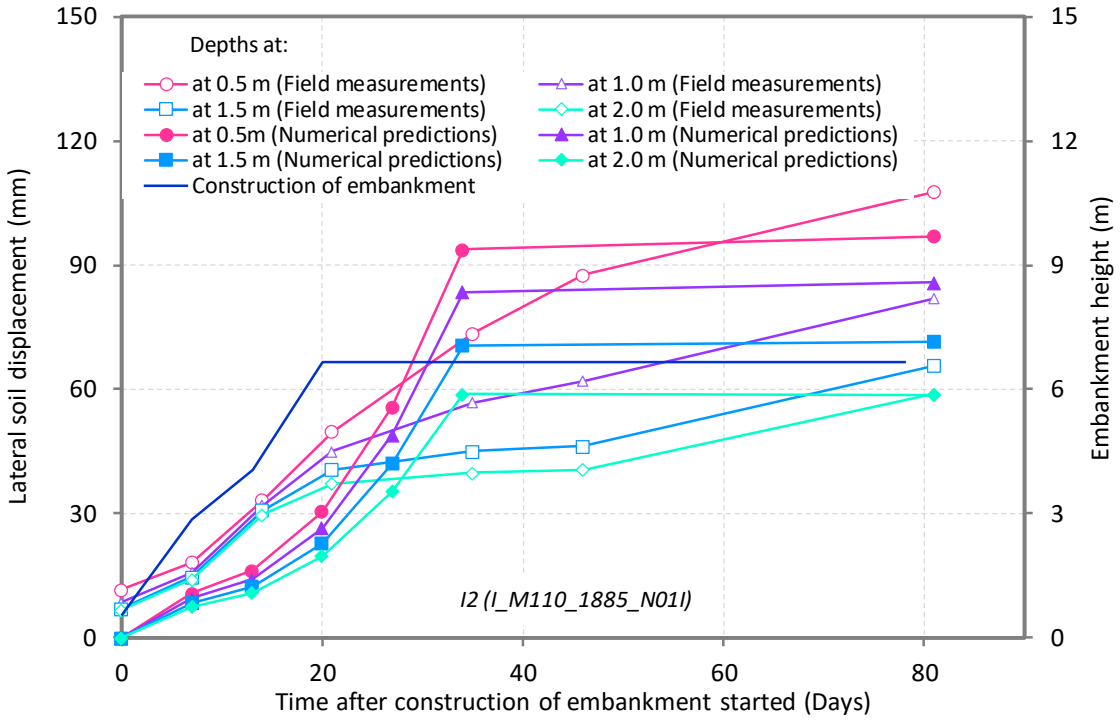

(b)

Figure 6.14. Lateral displacement of soil over time at the location of: (a) inclinometer I1 and (b) inclinometer I2.

6.6.1.3. Excess pore water pressure data

Figure 6.15 illustrates the evolution of excess pore water pressure measured at piezometer VP at Point B (VP_M110_1865_N01). The location of piezometer is shown in Figure 6.6 and Figure 6.11. It is observed that the excess pore water pressures predicted numerically were quite distinct from those field measurements at the early stage of the construction of the embankment similar to many research studies reported in the past (e.g. Liu *et al.*, 2007). It is noticed that numerical analysis predicted lower excess pore pressure than those observed in situ during the early stages of embankment construction. As expected, the evolution of excess pore water pressure was a function of embankment height, the excess pore water pressure increased gradually during the period of embankment construction. As expected, both the measured and computed results illustrate an increase in excess pore pressures during the period of construction due to increase of fill height. Referring to Figure 6.15, the computed excess pore water pressure increased from 17 to 60 kPa when the fill height increases from 0.55 m to 6.65 m (i.e. due to increase of 122 kPa embankment load), whereas, 9 kPa increase in excess pore water pressure was recorded at piezometer location on site. The rather rapid decrease in the excess pore water pressure observed in numerical predictions were due to the removal of the surcharge from 6.65 m to 3.35 m. Indeed, since the soft soil settled with time and hence time dependent arching occurred, further reduction in the excess pore water pressure in addition to the expected hydraulic dissipation from the drainage boundaries would be expected. It should be noted that, the initial stress state, soil constitutive model including shear induced

volume change and anisotropy, and the adopted soil plasticity model and associated flow rule could impact the predictions of soil volume change and therefore induced excess pore water pressure significantly (Fatahi *et al.*, 2013; Leoni *et al.*, 2008).

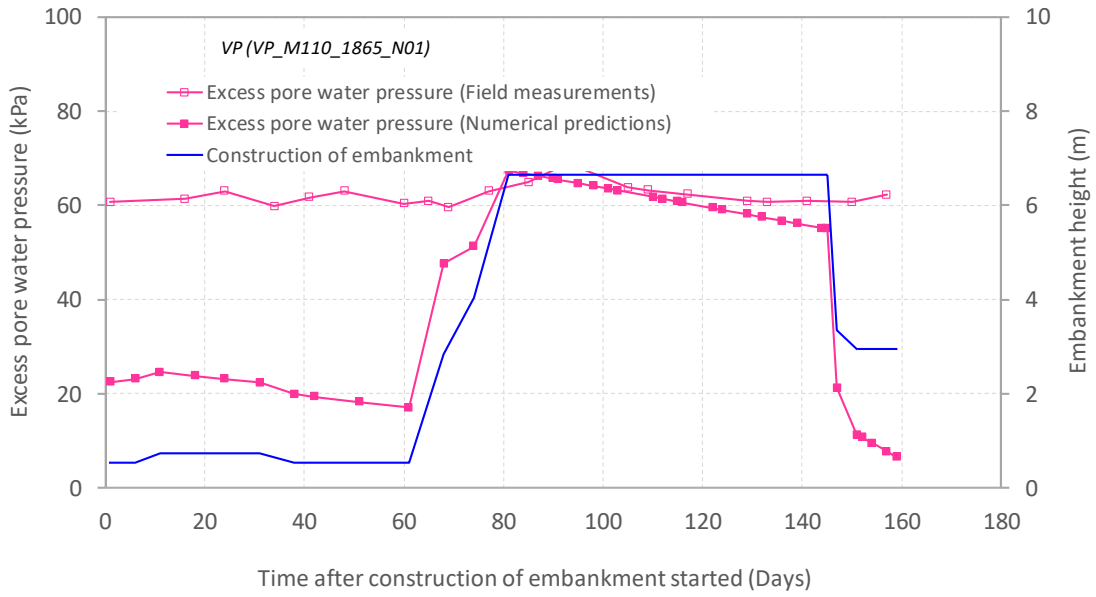

Figure 6.15. Variation of excess pore water pressure with time at the location of piezometer VP at Point B (VP_M110_1865_N01).

6.6.2. Soil-CIC Interaction

6.6.2.1. Vertical Stresses in Column

The distribution of vertical stresses in the columns and soft soil is presented and explained in this section. Figure 6.16 shows the evolution of vertical stresses acting on the CIC 9 (refer to Figure 6.6 for the position), measured by the earth pressure cell PC (PC_M110_1870_N01) on site. Figure 6.16 also displays the computed vertical stresses transferred to CIC 9. The variations of the embankment height are also illustrated in Figure 6.16. As shown in Figure 6.16, a significant increase in the stress transferred to the column in comparisons to the embankment load was evident. Referring to Figure 6.16,

when the fill height increased from 0.55 m to 6.65 m i.e., the embankment load reached about 122 kPa, the measured pressures on CIC 9 at the location of PC (i.e. at pressure cell PC_M110_1870_N01) at ground surface increased from approximately 85 kPa to 372 kPa, which was 2.5 times more than the corresponding embankment load. The corresponding numerically predicted stresses applied to the CIC 9 increased from 10 kPa to 300 kPa (i.e. 2.5 times increased embankment load). It can be noted that the trends of variations in stresses with the embankment height in both the measured and predicted cases were same.

It should be noted that the trends of variations in stresses with the embankment height in both the measured and predicted cases were same. However, there was a difference in the maximum stress acting on column between the measured and computed results. It could be because of the column's engineering properties adopted in the numerical analysis.

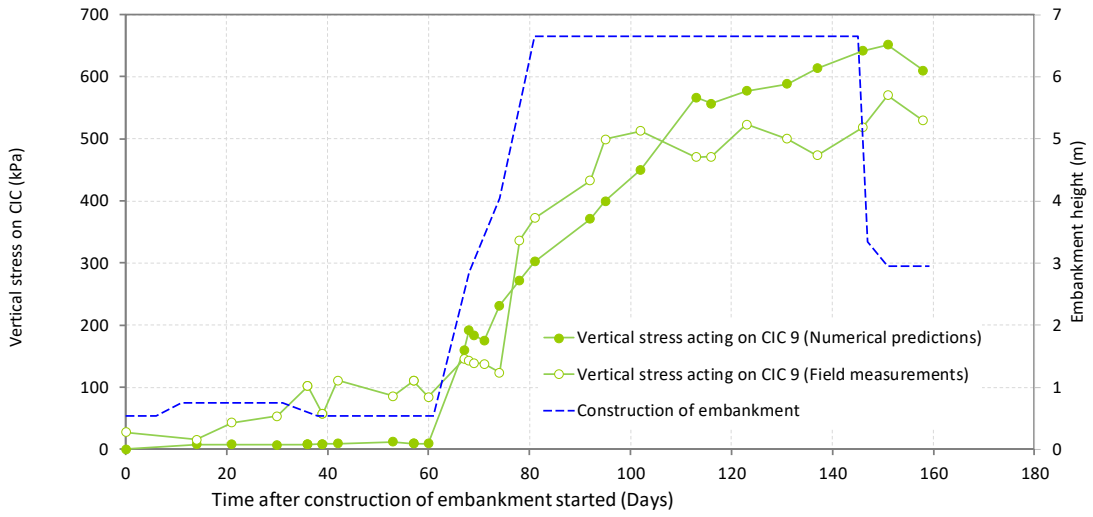

Figure 6.16. Variation of vertical stress acting on top of column with time.

6.6.2.2. Deformation, bending moment and shear force mobilised in CICs

Figure 6.17a shows the predicted lateral displacement profile of various columns including CIC 1, CIC 2, CIC 3, and CIC 4 (refer to Figure 6.6 for identification of columns). It can be seen in Figure 6.17a that, at the end of the construction (i.e. Construction Day 160), the maximum lateral displacement of 425 mm occurred at CIC 3. On the other hand, CIC 4, which was the closest to the bridge pile among the four columns, experienced the least predicted maximum lateral displacement of 280 mm. Hence, CICs 1, 2, and 3, located near the transition between CICs and PVD assisted preloading, experienced higher maximum lateral deflections compared to CIC 4, which was due to less confinement near the PVD area in comparison to rather rigid bridge piles providing significant confinement. Referring to Figure 6.17a, the lateral deflection of the columns reduced with depth as expected.

The displacement curves reported in Figure 6.17a, clearly demonstrated that the columns experienced bending moments and shear forces. The CICs experienced the most significant bending at the tip where the columns were socketed in medium to dense clay. CIC 2 experienced the maximum bending moment (i.e. 108 kN.m) and shear force (i.e. 405 kN) as displayed in Figure 6.17b. Referring to Figure 6.17c, it can be observed that, similar to bending moment diagram, more shear forces were developed in CIC 2 in comparison to other CICs. Figure 6.17d shows the axial forces developed in selected CICs. As evident, the axial forces in the CICs increase with depth in the top part of columns due to negative skin friction induced by soft soil settlement between columns.

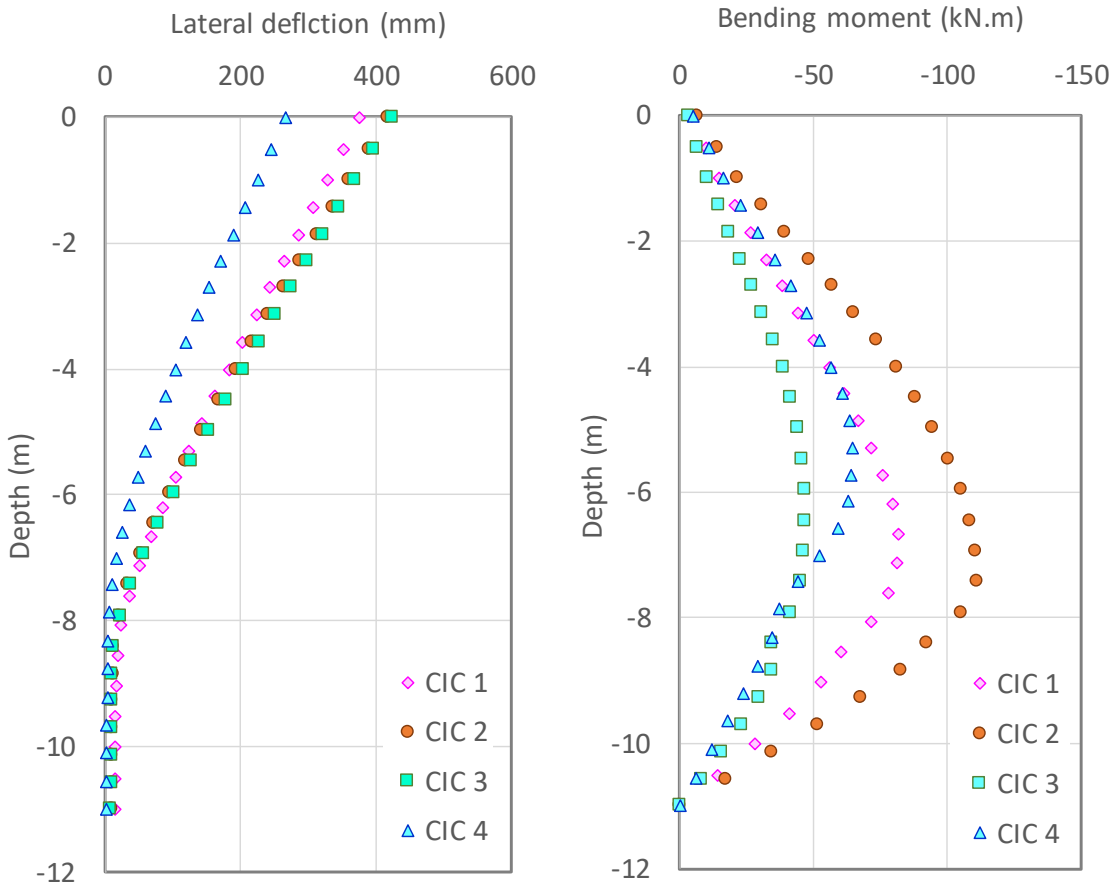
Lateral deflction (mm)
0
200
400
600
0
-2
-4
-6
-8
-10
-12
Depth (m)
CIC 1
CIC 2
CIC 3
CIC 4
(a)
Bending moment (kN.m)
0
-50
-100
-150
0
-2
-4
-6
-8
-10
-12
Depth (m)
CIC 1
CIC 2
CIC 3
CIC 4
(b)

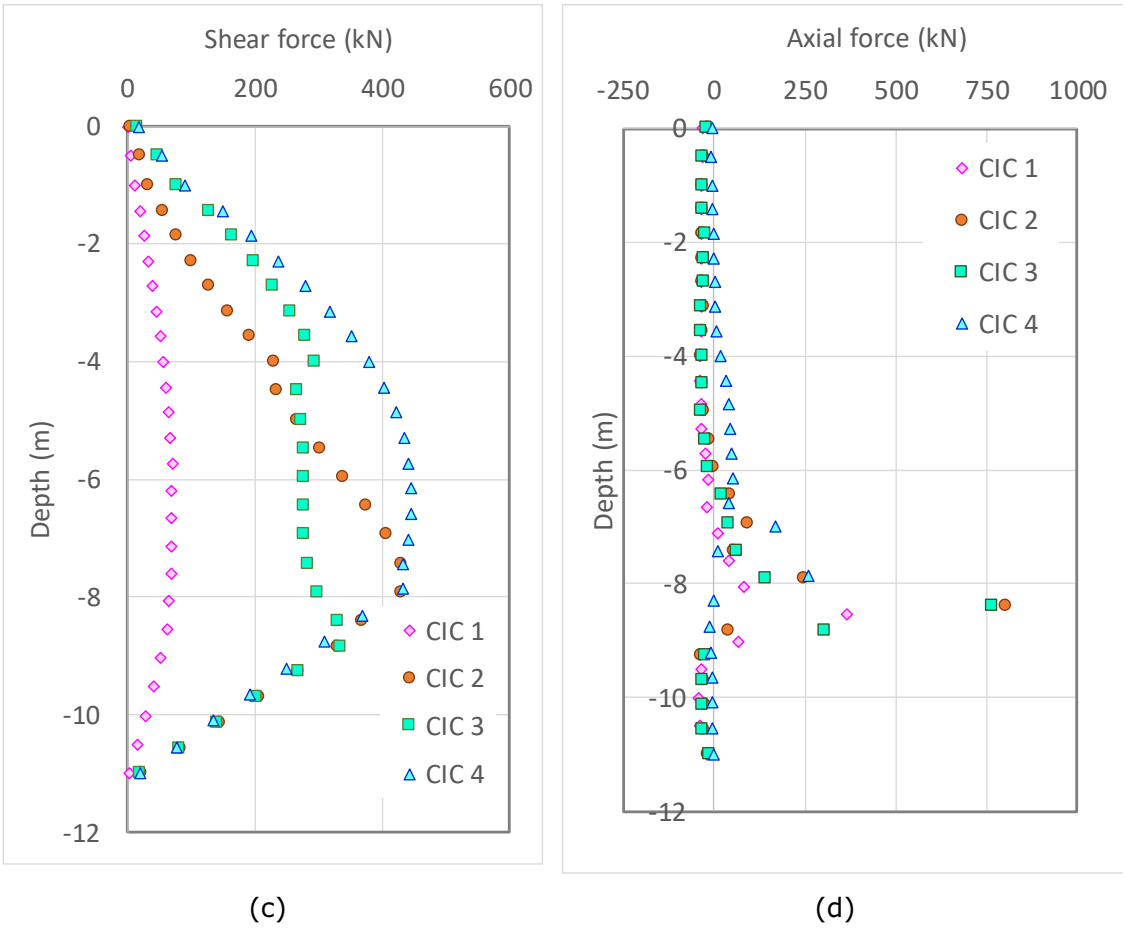

Figure 6.17. Predicted variations of: (a) lateral deflection, (b) bending moment, (c) shear force, and (d) axial force in CICs.

6.6.2.3. Stress distribution on CICs and soft soil

The predicted stresses transferred on to the columns and the soft soil are reported in Figure 6.18. Figure 6.18 shows the distribution of the vertical stresses on the ground surface among three CICs (i.e. CIC 5, CIC 6, and CIC 7) and the soft soil at a transverse Section A – A' about 11 m away from the bridge pile. These stresses are plotted at the construction days CD = 70 and CD = 76 (corresponding to placing 2.85 m and 4.05 m of embankment, respectively). As shown in Figure 6.18, the stresses on the soft soil were significantly less than the stresses on columns, which was a result of soil arching taking place in the embankment fill due to the large differential settlement between columns and

soft soil. When the embankment height increased from 2.85 m to 4.05 m (i.e. the increase of embankment load was about 22 kPa), the predicted maximum pressures acting on the soil surface increased insignificantly. On the other hand, the maximum pressure acting on the column head (e.g. CIC 5) increased by 41 kPa, which is about double the corresponding embankment load.

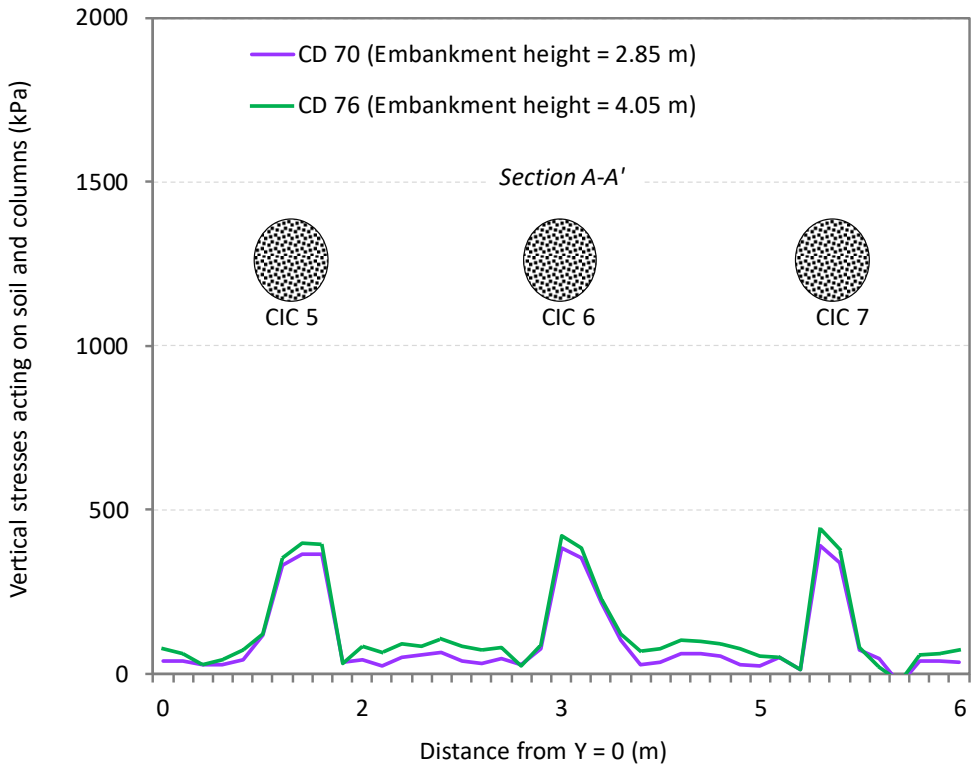

Figure 6.18. Vertical stress on the ground surface at the base of the embankment along Section A-A'.

As shown in Figure 6.19, a similar stress distribution between columns and foundation soil was observed at the longitudinal Section B - B' (see Figure 6.6). Referring to Figure 6.18 and Figure 6.19, it is evident that there was a load transfer from soil to columns as a result of soil arching in the embankment.

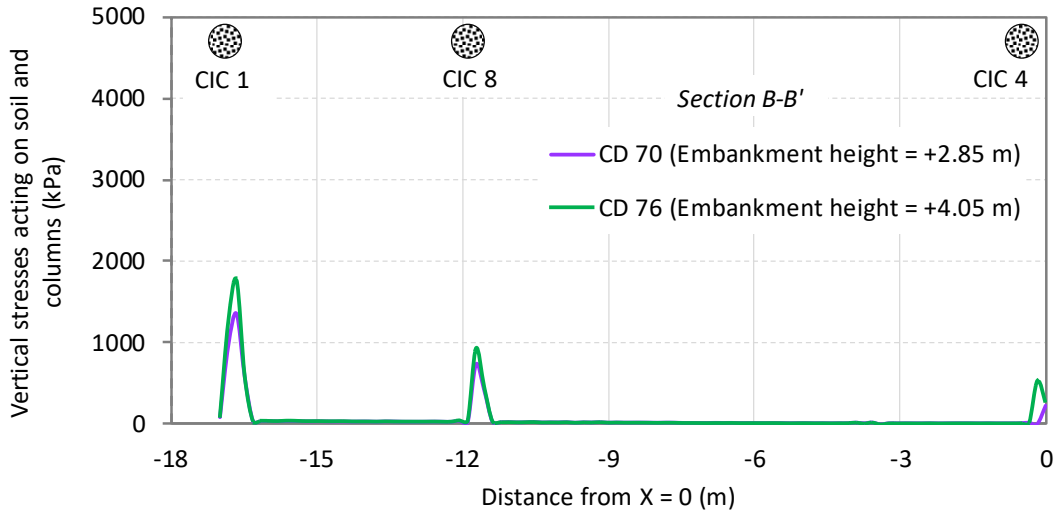

Figure 6.19. Vertical stress on the ground surface at the base of the embankment in long Section B-B′.

6.6.2.4. Comparison of CIC and soft soil settlement

Figure 6.20 demonstrates the computed ground surface settlements corresponding to the column heads and on the soil surface along a Section A-A' (see Figure 6.6) at different embankment construction stages. This is the total settlement at the end of specified construction stage. As evident, the total settlements of columns are insignificant compared to the settlements of the soil. As expected, the maximum settlement occurs at the middle of two adjacent columns. Although a major portion of the embankment load was transferred to the columns through arching mechanism in the embankment, the columns settlement was less than the soft soil due to high stiffness of the columns and the presence of the stiff clay below the CIC tip. At the end of construction of 2.85 m embankment fill (corresponding to CD 70), the computed maximum settlements were 2 mm and 65 mm at the head of CIC 5 and on soil surface at the middle of CIC 5 and CIC 6, respectively. At the end of Construction Day 174 (i.e. after removing 3 m surcharge), the corresponding predicted maximum total settlements of soil surface increased

insignificantly to 125 mm due to remaining consolidation, respectively which means that settlement of soil decreases significantly after removal of surcharge.

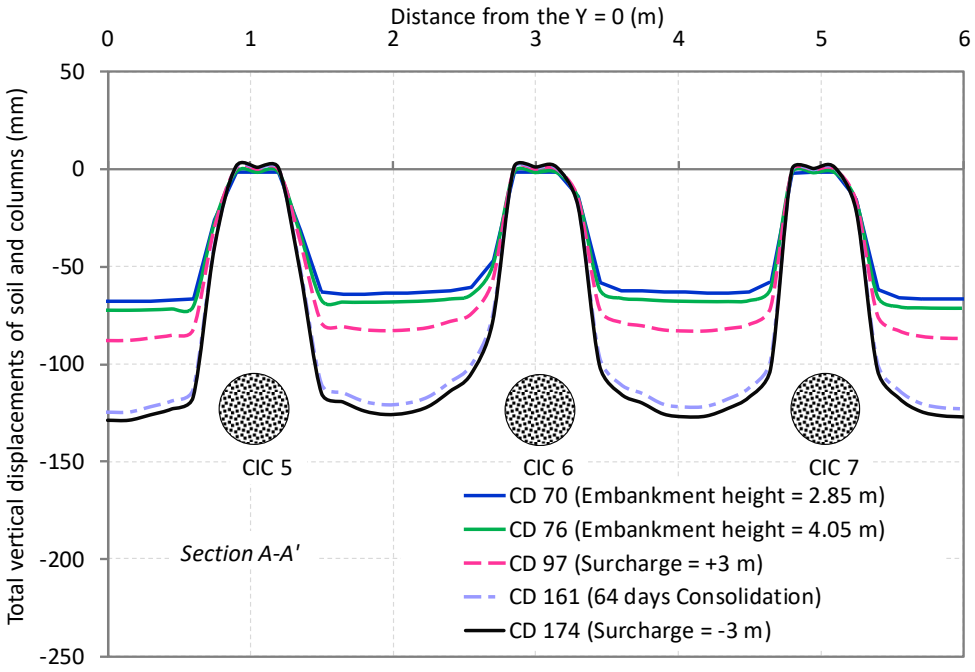

Figure 6.20. Settlement profiles at the end of several construction stages along section A-A'.

6.6.3. Tensile Forces in Top and Bottom Geosynthetics

Due to lateral displacement of the fill material in the embankment and differential settlement between the underneath soft soil and concrete injected columns, geosynthetic experiences tensile forces. Figure 6.21 illustrates tension developed in the geosynthetics at the end of the construction of abutment and backfill at a location section A-A'. It is noted that bottom geosynthetics layer carries greater tension when compare to top geosynthetics. It is observed that the maximum tension developed in bottom geosynthetics is 40% higher than the maximum tension in the top layer. Similar pattern of tension is developed in the geosynthetics while considering a section far away from the pile (refer to Figure 6.21 (b)). Where insignificant tension is generated in along with

section A-A', higher tension observed in farthest section. Since large settlement is observed in the furthest section, higher tension developed in the geosynthetics. In both the locations, maximum tension developed at the edges of the columns due to maximum differential settlement at that location.

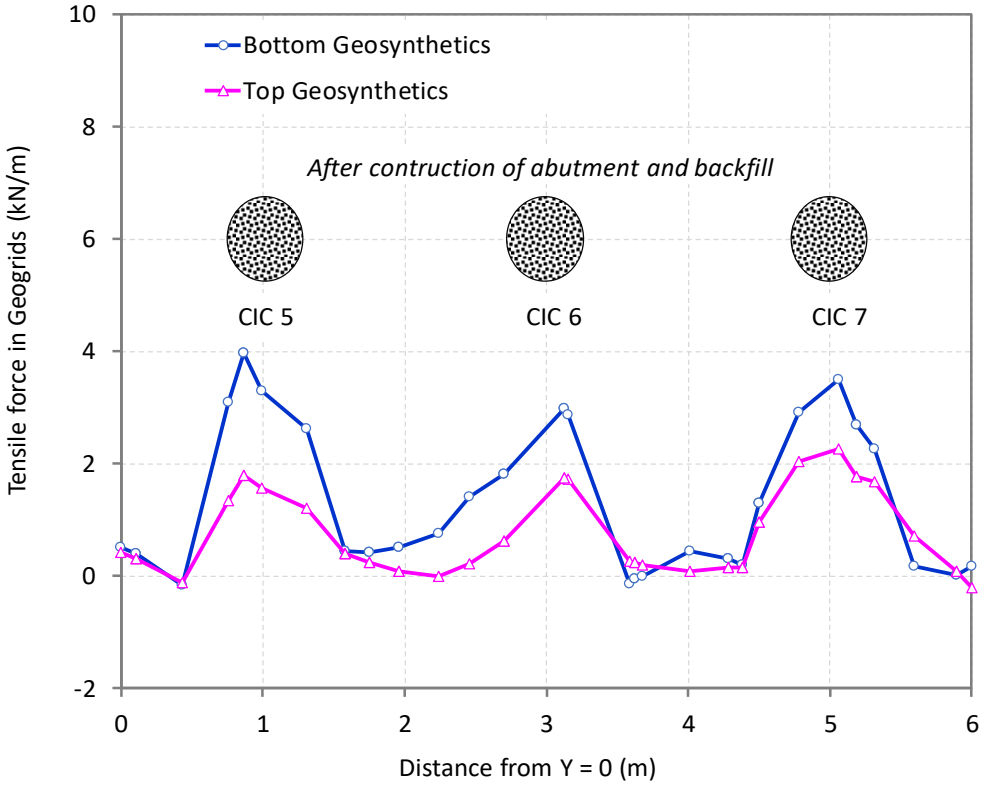

(a)

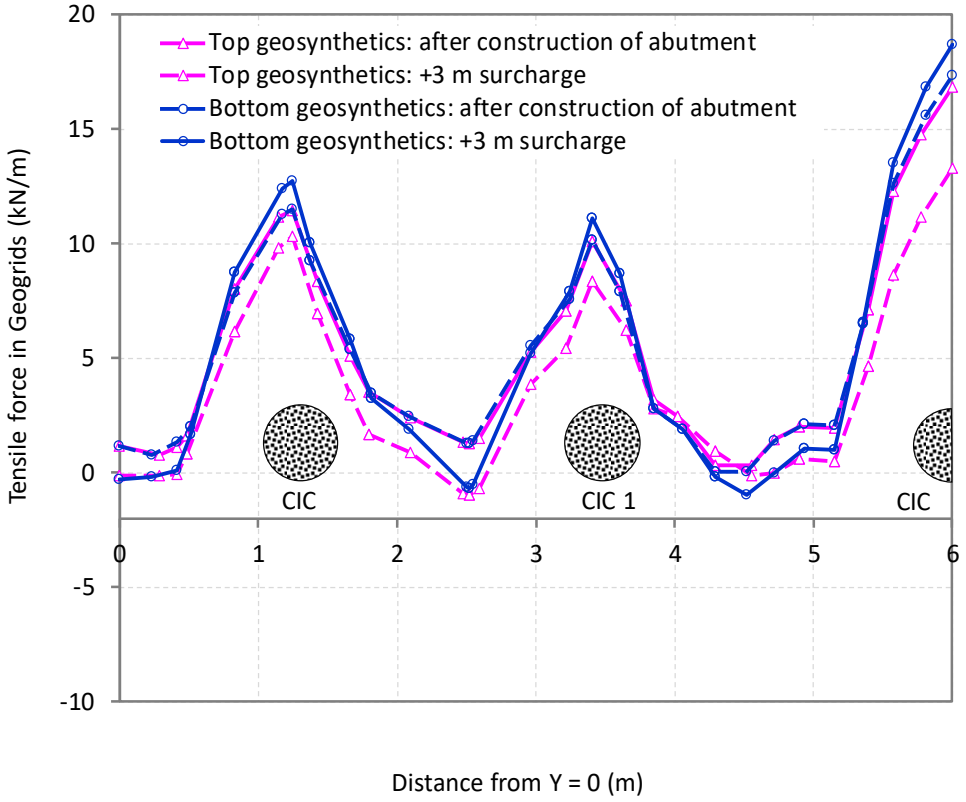

(b)

Figure 6.21. Tensile force produces in the geosynthetics: (a) close to pile along section A-A' and (b) far away from pile.

In can be explained by Figure 6.22. Since large settlement is observed in the furthest section, higher tension developed in the geosynthetics. In both the locations, maximum tension developed at the edges of the columns due to maximum differential settlement at that location.

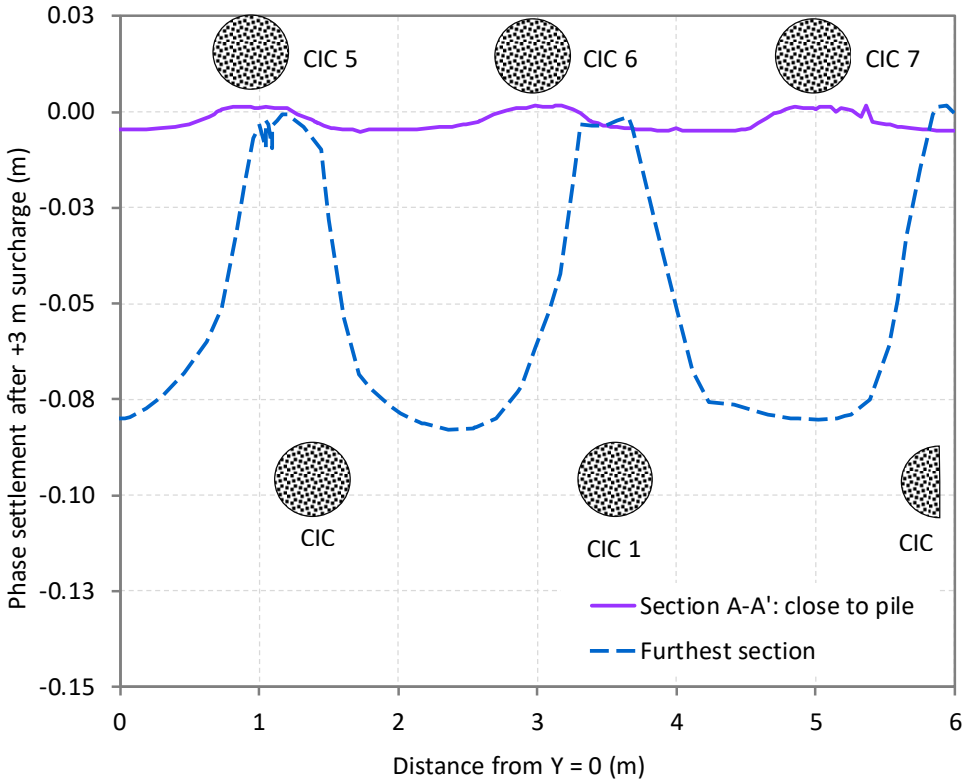

Figure 6.22. Comparison of settlement at various locations after adding 3 m of surcharge.

6.7. Summary

This chapter presents field study and numerical modelling for a case history of geosynthetic reinforced column-supported embankment in south of Sydney. The upgrade of the Princes Highway between Mount Pleasant and Toolijooa Road provided 7.5 kilometres of upgraded highway and include two new interchanges with access to Gerringong and Gerroa. The geology along the proposed alignment within the Gerringong upgrade was classified under the Budgong Sandstone and the Gerringong Volcanic Facies. The alignment was predominantly underlain by weathered rock and residual soils of these formations. Significant sections along the alignment were underlain by alluvial and estuarine deposits, which were typically highly compressible. Therefore, different ground improvement methods were used to reduce post construction settlements and

mitigate the slope instability issues. One of the ground improvement methods for this project was Concrete Injected Columns (CIC) which was used to treat the poor soil located directly behind bridge abutments to control embankment settlement and to improve embankment stability.

Three-dimensional finite element simulation considering soil consolidation was conducted to evaluate behaviour of the embankment on CIC improved soft soil. Modified Cam- Clay and Hoek-Brown constitutive models were adopted to simulate the soft soil and concrete injected columns, respectively. Variation of soil permeability with void ratio was considered in the consolidation analysis. The numerical predictions including settlements and lateral movements of the ground, excess pore water pressure in the soft soil, and stresses transferred to columns were compared with the field measurements for verification purposes. Based on the results of field measurements and three-dimensional finite-element analysis, it was clear that there was a significant load transfer from soil to the columns as a result of soil aching. For example, when the fill height increased from 0.55 m to 6.65 m (i.e.122 kPa increase in embankment load), the measured and predicted settlements of soft soil increased from 20 mm to 400 mm and 120 mm to 350mm, respectively. In addition, the corresponding measured and predicted excess pore water pressures at the depth of 3.5 m below the ground surface in the transition area of concrete injected columns and prefabricated drain increased by 9 kPa and 50 kPa, respectively. It was also noticed that columns close to bridge pile deflected less compared to columns located away from the bridge piles. In addition, it was observed that deflections of columns decrease with depth, while sections of the columns embedded in stiff clay experienced the maximum bending moment and shear forces. Columns located far away from the bridge piles experienced greater deflection, bending moment, shear force as well

as axial forces compared to the columns located closer to the bridge piles. Field measurements and numerical predictions showed that due to arching in the embankment and greater stiffness of the columns compared to soft soil, small portion of stresses were transferred to soft soil while the majority of the embankment load transferred to the columns. Although there were some discrepancies between the field measurements and numerical predictions, the predictions well followed the trends of field measurements. Hence, the proposed three-dimensional numerical approach with adopted modelling features can be used by practicing engineers for analysis and design of embankments on CIC improved soft soil.

CHAPTER 7

7. CONCLUSIONS AND RECOMMENDATIONS

7.1. Summary

A mechanical model for soil or geosynthetics under loading can be described in terms of mechanical elements such as beams (Pasternak beams, Euler-Bernoulli beams or Timoshenko beams), Winkler springs, and Terzaghi's spring-dashpot system, or elastic membranes, and can easily be understood on the basis of fundamental concepts of mechanics. Several efforts have been made by many researchers to develop simple mechanical models of the geosynthetic-reinforced column-supported embankment, attempting to simulate real situations. However, most of the past studies were conducted on soft soils without any rigid or semi rigid inclusions. This research is a further effort in this direction to present a mechanical model that can be applied for the analysis of settlement response of the geosynthetic-reinforced column-supported embankment systems. The main objective of this study was to provide closed form solutions for several cases such as different types of stress distributions on the geosynthetic reinforced granular layer and different mechanical models for the underneath soft soil while adopting Timoshenko beam on composite elastic foundation and to examine the load transfer mechanism in the entire system. In addition, 3-D numerical analyses were conducted to inspect the behaviour of column-supported embankments for a real case study in New South Wales.

An overview and importance of ground improvement techniques, particularly using concrete injected columns (CICs) is provided in Chapter 1. In addition, the scope and objectives of the research are clearly emphasized in this chapter. Chapter 2, on the other hand, delivers a wide-ranging literature review of arching theory in column-supported embankments, and analysis of beam on elastic foundation in soil-structure interaction (SSI) problems. In addition, detailed discussion on the advantages and limitations of existing analytical and numerical models of column reinforced soft soil are presented in Chapter 2.

In Chapter 3, a comprehensive and precise load distribution mechanism of the CIC-soil system are evaluated. In particular, a simplified solution simulating the load transfer platform (LTP) as a reinforced Timoshenko beam was proposed. Properties of LTP (thickness and layers of geosynthetics) was optimised considering the bending moment and the shear capacity of LTP. New parameters were introduced and implemented in analytical formulations taking into account the tensile strength of geosynthetics and non-linearity of soft soil. In the developed model and parameter selection, issues relevant to nonlinearity and cracks in soil were captured. Then the new model was incorporated in simple Excel spread sheet as well as MATLAB to be used by practicing engineers.

A reasonable and easy to implement mechanical model of geosynthetic reinforced granular layer (which is known as load transfer platform) on column-supported embankment on soft soil is proposed in Chapter 4. LTP on the soft soil was idealised by "the membrane reinforced Timoshenko beam" on Kerr foundation. The proposed analytical solution can be used by practicing engineers to predict the primary settlement of the LTP under embankment without a need to use any commercial software.

In Chapter 5, behaviour of geosynthetics under several stress distribution patterns induced by arching in the embankment is investigated. The effects of the column stiffness and consolidation of saturated soft soils were also incorporated in the model simultaneously.

Chapter 6 provides a three-dimensional finite elements models with more effective parameters to predict the stress distribution pattern in the CIC-embankment-soft soil system. The developed finite element model was then used to simulate a real case study in New South Wales and verified by predicting ground behaviour under the applied loads. Load transfer mechanism in geosynthetic reinforced column supported embankment was examined in terms of stresses distributing between columns and soft soil, and settlement of soft soil and columns. The outcomes of this research are valuable to expand the knowledge required for the design considering the nonlinear behaviour of geosynthetic reinforced column supported embankments, while contributing to the development of new design procedures.

7.2. Key Concluding Remarks

Much of the existing literature for mechanical design of the geosynthetic-reinforced granular platform in soil-structure-foundation system is based on the classic thin beam/plate theory (Euler-Bernoulli beam, 1933; Pasternak shear layer, 1954). In Euler-Bernoulli (1933) theory, shear deformations of the beam are neglected, and plane sections remain plane and normal to the longitudinal axis. The modelling of thick granular layers with Euler-Bernoulli beam theory becomes incorrect due to ignoring the transverse shear stresses. Indeed, this assumption may significantly be unrealistic for thicker geosynthetic reinforced granular platform in which shear deformations are significant. As a new foundation model to represent geosynthetic-reinforced soil, a modified Pasternak model

was proposed by Madhav and Poorooshasb (1988), where Pasternak shear layer was combined with Winkler's springs. According to Pasternak (1954) theory, the foundation beam would deform under transverse shear forces only. Therefore, neither Euler-Bernoulli (1933) nor Pasternak (1954) models could consider both bending and shearing of beams. Timoshenko (1970) developed a model that takes into account shear deformation and bending effects, making the proposed beam suitable for describing the behaviour of short and deep beams. In the Timoshenko beam theory, plane sections still remain plane while they do not have to remain normal to the longitudinal axis. Timoshenko beam theory allows a rotation between the cross section and the longitudinal axis. This rotation comes from a shear deformation, which is not included in a Bernoulli beam.

Yin (2000a) derived the ordinary differential equations for a reinforced Timoshenko beam on elastic foundation excluding the stabilizing columns and provided the analytical solution. However, in Yin (2000a) model, LTP was assumed to carry tension, soft soil behaviour was assumed to be linear, and the supporting conditions from the column were ignored. To extend Yin (2000a) work, in this thesis, soil non-linearity was included in the Winkler foundation model by utilising a bi-linear response for the soft soil, while the cracked cross-section of the LTP was considered.

The proposed analytical solutions in Chapter 3 to predict the response of the LTP on column-stabilized soft soil subjected to distributed loadings considers effect of the bending and shear deformations of the LTP and the nonlinear stress-strain behaviour of soft soil. Furthermore, a parametric study was conducted to examine the effect of key model parameters, such as the column spacing, LTP thickness, the tensile stiffness of geosynthetics, and the degree of consolidation on the response of the LTP overlying a

soft soil layer. It has been observed that smaller spacing between the columns and thicker LTP reduce the maximum settlement of the LTP and tension mobilized in the geosynthetics. Although the stiffer geosynthetics reduces the maximum settlement of LTP, it increases the tension in the geosynthetics. Furthermore, the Euler-Bernoulli and the Pasternak theories in addition to the Timoshenko beam theory were used to assess the precision of existing beam theories to analyse the LTP on column-reinforced soft soil. The results from the suggested Timoshenko theory (capturing the combined shear and bending stiffness of the LTP) were compared with results from the Euler-Bernoulli model (capturing deflection due to bending only) and the Pasternak model (capturing deformation due to shear only). It has been observed that the Timoshenko model outperforms the Euler-Bernoulli and the Pasternak models since bending and shear deformations of granular materials and reinforcement are considered. Therefore, it was concluded that simulating the LTP as an Euler-Bernoulli beam or a Pasternak shear layer resulted in an aggressive design in terms of the prediction of the deflection of LTP. It is therefore recommended that practicing engineers use the Timoshenko beam model for design purposes when using mechanical models to simulate LTP. The proposed mathematical model and its analytical solutions for a LTP on a composite soft soil foundation can be adopted to calculate the settlement/deflection of the LTP and tension in the reinforcement for any shape of loading, as well as the linear and nonlinear stress-strain responses of soft soil.

The proposed analytical equations in Chapter 4 are based on the basic differential equations of a Timoshenko beam subjected to a distributed transverse load and a foundation interface pressure, generated from the Kerr foundation model. The proposed mechanical model can be beneficial for practicing engineers in analysing the settlement

response of the multilayer geosynthetic reinforced granular bed overlying column improved soft soil. Furthermore, soft soil idealised by the Winkler and the Pasternak foundations were used to evaluate the accuracy of the adopted Kerr foundation model for detailed study of LTP on column improved soft soil. It was noticed that the Winkler model resulted in higher values of displacements, rotations, bending moments, shear forces, and tensions than the reference solutions adopting the Kerr foundation model. However, the values of the settlements, rotations, bending moments, shear forces, and tensions obtained from Pasternak foundation model were less than the corresponding reference values adopting the Kerr foundation model. Kerr foundation model estimated the response of the soft soil more precisely, which were between two upper and lower bounds corresponding to the Winkler and the Pasternak foundation models, respectively. When double layer geosynthetic reinforced LTP was compared to a single layer geosynthetic reinforced LTP, it was observed that inclusion of the two geosynthetic layers (i.e. 2 × 1000 kN/m) reduced the maximum deflection of the LTP when compared to a single stiffner layer (i.e. 1 × 2000 kN/m). However, in case of the double layer, the strength of geosynthetics was not fully utilised compared to that of the single layer scenario. It was also observed that in the double layer reinforcement, the top geosynthetic layer was more effective at the column location (in the hogging region), whereas the bottom geosynthetic reinforcement was more effective in the middle span (in the sagging region). It was also revealed that geosynthetic layer at the top was subjected to higher mobilised tension than the bottom layer. Furthermore, it can be concluded that the use of one stronger/stiffer geosynthetic layer (e.g. 1 × 2000 kN/m) with the equivalent stiffness of two geosynthetic layers (i.e. 2 × 1000 kN/m), does not necessarily result in the same deformation of LTP and the tension in the geosynthetic reinforcement when compared to two weaker geosynthetic layers (i.e. 2 × 1000 kN/m).

This research has also examined the effects of different stress distribution patterns on LTP on the behaviour of geosynthetic-reinforced concrete injected column (CIC) supported embankment, when simulating LTP as a "reinforced Timoshenko beam". Results demonstrate that the load-settlement response of the LTP-soil-CIC system can significantly be affected by the different arching theories. Uniformly distributed loading on the LTP, following the British Standard predicted the smallest settlement, rotation, shear force and negative moment in the LTP within the soft soil region and the smallest mobilised tension as compared with the triangular and inverse triangular distribution of loading. The outcome of this study certainly poses a question mark on the use of British Standard for design of LTP, in particular for the determination of tension capacity of the geosynthetics and settlement of LTP for the column improved embankment application.

The upgrade of the Princes Highway between Mount Pleasant and Toolijooa Road in New South Wales, Australia provides 7.5 kilometers of upgraded highway and included two new interchanges with access to Gerringong and Gerroa. According to RMS (NSW Road and Maritime Services) report, the geology along the proposed alignment within the Gerringong upgrade was classified under the Budgong Sandstone and the Gerringong Volcanic Facies. The alignment was predominantly underlain by weathered rock and residual soils of these formations. Significant sections along the alignment were underlain by alluvial and estuarine deposits. These were typically highly compressible. One of the adopted ground improvement methods for this project was concrete injected columns (CICs) which were used to treat the poor soil located directly behind bridge abutments to control embankment settlement and to improve embankment stability. Within the applied range of stresses in which CICs behave elastically, the columns carry a large portion of the total applied loads, which can be calculated from the existing theories. However, as

the applied vertical stress is combined with the lateral stresses due to horizontal movement of soil between columns particularly close to slopes, the load transfer mechanism changes and the surrounding soil starts to squeeze and settle further. Currently, there are no existing robust three-dimensional models that can formulate the load transfer mechanism between the in-situ soil and the CICs under the embankments slopes or close to the edges due to complexity of the problem.

A three-dimensional finite elements model in PLAXIS-3D (AE) considering appropriate constitutive models for both soil and CIC to predict the stress distribution pattern in the CIC-embankment-soft soil system has been utilised in this study. The adopted models can be regarded as an integration of several existing models used in the exiting literature for various materials in the composite systems. The three-dimensional model was used to simulate Gerringong Upgrade project and predictions were compared with field measurements for verification purposes. The Hoek-Brown model (HB) was used to simulate the concrete injected columns. Indeed, the isotropic elastic perfectly-plastic behaviour of columns has been considered by using Hoek-Brown model which follows Hoek-Brown failure criteria. This non-linear stress-dependent criteria demonstrates shear failure and tensile failure by continuous function. The proposed model also considered the existence of pre-fabricated vertical drain (PDV) beyond the CICs zone to simulate the real condition of the site. Equivalent permeability of the soil has also been adopted accordingly. Orthotropic behaviour of geogrids has been assumed where $EA_1 = EA_2$ and $GA = {}^1/_2\, EA_1$; when $EA_1$and EA_2 are normal stiffness and stiffness in the out of plane dorection, respectively. In addition, varied OCR values along the depth of the soft soil has also been adopted. The changes of soil permeability during the consolidation were also taken into account.

It was concluded that the developed three-dimensional finite element modelling could be successfully adopted in order to achieve accurate predictions for vertical stresses acting on the columns and soft soil, settlements, and excess pore pressure in CIC supported embankment problems. Although there were some disparities between numerical predictions and field measurements, in general all assessed parameters in the numerical analysis showed a similar trend to the field measurements. Based on the results, it was evident that the load transfer mechanism in column-supported embankment was mainly based on soil arching. It was observed that lateral movement of soft soil reached a maximum value close to the ground surface. This analysis revealed that columns close to the bridge pile deflect less when compared to columns located away from the bridge pile. The maximum shear, axial forces, and bending moment were developed in the column in deepest location of the column where a very stiff clay layer was present. Finally, it could be concluded that practicing engineers can apply a similar approach for analysis of embankment on CIC improved ground to obtain a reliable and optimised design.

7.3. Recommendations for Future Studies

The following recommendations are made for future work to expand this research:

- Validating the developed simplified analytical solution against predictions from rigorous numerical analysis considering soil nonlinearity. This will facilitate to assess the importance of soil nonlinearity in performance assessment of composite ground and reliability of the available analytical solutions.
- Extending the proposed mechanical model by considering the possible pull-out resistance force of geosynthetic from the surrounding granular fill material and creep of geosynthetics. Extended model can be adopted to determine the

interaction between geosynthetic reinforcement and granular soils, which is one of the key factors in the design of geosynthetic-reinforced column-supported embankments.

- Investigating the necessity of load transfer platform (LTP) for the embankment constructed on columns improved soft soil via full scale three-dimensional model, while considering appropriate constitutive models for various soil layers capturing soil arching and nonlinearity. Stress and deformation of CIC can be analyzed in the presence and absence of LTP.
- Assessing the effects of defected CICs on the overall performance of the embankment on improved soft soil in the presence and absence of LTP via 3D numerical solutions. Indeed, the impact of load transfer platform on the degree of redundancy of CIC inclusions can be assessed, helping with quality control requirements on site.

LIST OF REFERENCES

Abusharar, S. W., Zheng, J. J., Chen, B. G. and Yin, J. H., 2009. A simplified method for analysis of a piled embankment reinforced with geosynthetics. *Geotextiles and Geomembranes* **27** (1): 39-52.

ASIRI, 2012. Recommendations for the design, execution and control of foundation soil improvement by rigid inclusions.

Avramidis, I. E. and Morfidis, K., 2006. Bending of beams on three-parameter elastic foundation. *International Journal of Solids and Structures* **43** (2): 357-375.

Azari, B., Fatahi, B. and Khabbaz, H., 2016. Assessment of the elastic-viscoplastic behavior of soft soils improved with vertical drains capturing reduced shear strength of a disturbed zone. *International Journal of Geomechanics* **16** (1): 1-15.

Bergado, D. T., Ruenkrairergsa, T., Taesiri, Y. and Balasubramaniam, A. S., 1999. Deep soil mixing used to reduce embankment settlement. *Ground Improvement* **3** (3): 145-162.

Bhasi, A. and Rajagopal, K., 2015a. Geosynthetic-reinforced piled embankments: comparison of numerical and analytical methods. *International Journal of Geomechanics* **15** (5): 1-12.

Bhasi, A. and Rajagopal, K., 2015b. Numerical study of basal reinforced embankments supported on floating/end bearing piles considering pile–soil interaction. *Geotextiles and Geomembranes* **43** (6): 524-536.

Bićanić, N. and Zienkiewicz, O., 1983. Constitutive model for concrete under dynamic loading. *Earthquake engineering & structural dynamics* **11** (5): 689-710.

Borges, J. L. and Gonçalves, M. S., 2016. Jet-grout column-reinforced soft soils incorporating multilayer geosynthetic-reinforced platforms. *Soils and Foundations* **56** (1): 57-72.

Briançon, L. and Simon, B., 2012. Performance of pile-supported embankment over soft soil: Full-scale experiment. *Journal of Geotechnical and Geoenvironmental Engineering* **134** (4): 551-562.

BS8006-1, 2010. Code of practice for strengthenedreinforced soils and other fills. British Standards Institution.

Carlsson, B., 1987. Reinforced Soil, Principles for Calculation. *Terratema AB, Linköping (in Swedish).*

Chai, J. C., Miura, N. and Shen, S. L., 2002. Performance of embankments with and without reinforcement on soft subsoil. *Canadian Geotechnical Journal* **39** (4): 838-848.

Chandra, S., Madhav, M. R. and Iyengar, N., 1987. A new model for nonlinear subgrades. *Mathematical Modelling* **8**: 513-518.

Chen, R. P., Chen, Y. M., Han, J. and Xu, Z. Z., 2008a. A theoretical solution for pile-supported embankments on soft soils under one-dimensional compression. *Canadian Geotechnical Journal* **45** (5): 611-623.

Chen, Y. M., Cao, W. P. and Chen, R. P., 2008b. An experimental investigation of soil arching within basal reinforced and unreinforced piled embankments. *Geotextiles and Geomembranes* **26** (2): 164-174.

Collin, J., 2004. Column supported embankment design considerations. Proceedings of the 52nd annual geotechnical engineering conference, Minnesota.

Collin, J. G., Watson, C. H. and J., H., 2005. Column-supported embankment solves time constraint for new road construction. Contemporary issues in Foundation Engineering. **GSP 131:** 1-10.

Cowper, G., 1966. The shear coefficient in Timoshenko's beam theory. *Journal of applied mechanics* **33** (2): 335-340.

De Normalisation, C. E., 2004. Eurocode 2: Design of concrete structures—Part 1-1: General rules and rules for buildings. *Brussels, Belgium*.

Deb, K., 2010. A mathematical model to study the soil arching effect in stone column-supported embankment resting on soft foundation soil. *Applied Mathematical Modelling* **34** (12): 3871-3883.

Deb, K., Basudhar, P. K. and Chandra, S., 2007. Generalized model for geosynthetic-reinforced granular fill-soft soil with stone columns. *International Journal of Geomechanics* **7** (4): 266-276.

Deb, K. and Mohapatra, S. R., 2013. Analysis of stone column-supported geosynthetic-reinforced embankments. *Applied Mathematical Modelling* **37** (5): 2943-2960.

EBGEO, 2010. Empfehlungen für den Entwurf und die Berechnung von Erdkörpern mit Bewehrungen aus Geokunststoffen *German Geotechnical Society* **2**.

Farag, G. S. F., 2008. Lateral spreading in basal reinforced embankments supported by pile-like elements. *In: Schiftenreihe Getechnik. Universität Kassel. Heft 20*.

Fatahi, B., Le, T. M., Le, M. Q. and Khabbaz, H., 2013. Soil creep effects on ground lateral deformation and pore water pressure under embankments. *Geomechanics and Geoengineering* **8** (2): 107-124.

Fatahi, B. and Tabatabaiefar, S. H. R., 2014. Fully nonlinear versus equivalent lnear computation method for seismic analysis of midrise buildings on soft soils. *International Journal of Geomechanics* **14** (4): 1-15.

Filonenko-Borodich, M. M., 1940. Some approximate theories of the elastic foundation. *Uchenyie Zapiski Moskovskogo Gosudarstvennogo Universiteta Mekhanica* **46**: 3-18.

Filz, G., Sloan, J., McGuire, M. P., Collin, J. and Smith, M., 2012. Column-supported embankments: settlement and load transfer In: Proceedings of Geo-Congress, Oakland, California.

Filz, G. M. and Smith, M. E., 2007. Net Vertical Loads on Geosynthetic Reinforcement in Column-Supported Embankments. *Soil Improvement GSP 172*: 1-10.

Fowler, J. and Edris Jr, E. V., 1987. Fabric reinforced embankment test section, Plaquemine Parish, Louisiana, USA. *Geotextiles and Geomembranes* **6**: 1-31.

Fulton-Hogan. 2015. Gerringong upgrade project, Mount Pleasant to Toolijooa road Retrieved 20/06/2015, 2015, from http://www.fultonhogan.com.

Gartung, E., Verspohl, J., Alexiew, D. and Bergmair, F., 1996. Geogrid reinforced railway embankment on piles-Monitoring. Proccedings of The First European Geosynthetic Conference, EUROGEO.

Ghosh, B., Fatahi, B., Khabbaz, H. and Yin, J.-H., 2017. Analytical study for double-layer geosynthetic reinforced load transfer platform on column improved soft soil. *Geotextiles and Geomembranes* **45** (5): 508-536.

Girgin, Z. C., 2009. Modified failure criterion to predict ultimate strength of circular columns confined by different materials. *ACI Structural Journal* **106** (6): 800.

Girgin, Z. C. and Girgin, K., 2015. A design-oriented combined model (7 MPa to 190 MPa) for FRP-confined circular short columns. *Polymers* **7** (10): 1905-1917.

Giroud, J., Bonaparte, R., Beech, J. and Gross, B., 1990. Design of soil layer-geosynthetic systems overlying voids. *Geotextiles and Geomembranes* **9** (1): 11-50.

Girout, R., Blanc, M., Thorel, L., Fagundes, D. F. and Almeida, M. S. S., 2016. Arching and deformation in a piled embankment: centrifuge tests compared to analytical calculations. *Journal of Geotechnical and Geoenvironmental Engineering* **142** (12).

Graham, J., Crooks, J. and Bell, A. L., 1983. Time effects on the stress-strain behaviour of natural soft clays. *Géotechnique* **33** (3): 327-340.

Grassl, P., Lundgren, K. and Gylltoft, K., 2002. Concrete in compression: a plasticity theory with a novel hardening law. *International Journal of Solids and Structures* **39** (20): 5205-5223.

Gray, H., 1944. Simultaneous consolidation of contiguous layers of unlike compressible soils. Proceedings of the American Society of Civil Engineers, ASCE.

Gudehus, G., Goldscheider, M. and Winter, H., 1977. Mechanical properties of sand and clay and numerical integration methods: some sources of errors and bounds of accuracy. *Finite elements in geomechanics*: 121-150.

Guido, V. A., 1987. Plate loading tests on geogrid-reinforced earth slab. Geosynthetic'87 Conference.

Han, J., 2001. Simplified method for consolidation rate of stone column reinforced foundations. *Journal of Geotechnical and Geoenvironmental Engineering* **127** (7): 597-603.

Han, J., Bhandari, A. and Wang, F., 2011. DEM analysis of stresses and deformations of geogrid-reinforced embankments over piles. *International Journal of Geomechanics* **12** (4): 340-350.

Han, J., Collin, J. G. and Huang, J., 2004. Recent development of geosynthetic-reinforced column- supported embankments. The 55th Highway Geology Symposium. Kansas City, Missouri**:** 299-321.

Han, J. and Gabr, M. A., 2002. Numerical analysis of geosynthetic-reinforced and pile-supported earth platforms over soft soil. *Journal of Geotechnical and Geoenvironmental Engineering* **128** (1): 44-53.

Han, J., Oztoprak, S., Parsons, R. L. and Huang, J., 2007. Numerical analysis of foundation columns to support widening of embankments. *Computers and Geotechnics* **34** (6): 435-448.

Hansbo, S., 1981. Consolidation of fine-grained soils by prefabricated drains. Proceedings of the 10th international conference on soil mechanics and foundation engineering, Stockholm, AA Balkema Rotterdam, The Netherlands.

Heitz, C., 2006. Bodengewölbe unter ruhender und nichtruhender Belastung bei Berücksichtigung von Bewehrungseinlagen aus Geogittern. *In: Schriftenreihe Geotechnik. Uni Kassel. Heft 19, November 2006 (in German)*.

Hetényi, M., 1946. Beams on elastic foundation: theory with applications in the fields of civil and mechanical engineering, University of Michigan Press.

Hewlett, W. and Randolph, M. A., 1988. Analysis of piled embankments. *Ground Engineering* **21**: 12.

Hird, C. C., Pyrah, I. C. & Russell, D., 1992. Finite element modelling of vertical drains beneath embankments. *Geotechnique* **42** (3): 499-511.

Hoek, E., 2006. Practical rock engineering.

Hoek, E. and Brown, E. T., 1980. Empirical strength criterion for rock masses. *Journal of Geotechnical and Geoenvironmental Engineering* **106** (GT9 - ASCE 15715): 1013-1035.

Hoek, E., Carranza-Torres, C. and Corkum, B., 2002. Hoek-Brown failure criterion-2002 edition. *Proceedings of NARMS-Tac* **1**: 267-273.

Hokmabadi, A. S. and Fatahi, B., 2015. Influence of foundation type on seismic performance of buildings considering soil–structure interaction. *International Journal of Structural Stability and Dynamics*: 1550043.

Horvath, J. S., 1983. Modulus of Subgrade Reaction: New Perspective. *Journal of Geotechnical Engineering* **109** (12): 1591-1596.

Horvath, J. S. and Colasanti, R. J., 2011. Practical subgrade model for improved soil-structure interaction analysis: model development. *International Journal of Geomechanics* **11** (1): 59-64.

Huang, J. and Han, J., 2009. 3D coupled mechanical and hydraulic modeling of a geosynthetic-reinforced deep mixed column-supported embankment. *Geotextiles and Geomembranes* **27** (4): 272-280.

Huang, J. and Han, J., 2010. Two-dimensional parametric study of geosynthetic-reinforced column-supported embankments by coupled hydraulic and mechanical modeling. *Computers and Geotechnics* **37** (5): 638-648.

Huang, J., Han, J. and Oztoprak, S., 2009. Coupled mechanical and hydraulic modeling of geosynthetic-reinforced column-supported embankments. *Journal of Geotechnical and Geoenvironmental Engineering* **135** (8): 1011-1021.

Hutchinson, J. R., 2001. Shear coefficients for Timoshenko beam theory. *Journal of Applied Mechanics* **68** (1): 87.

Ilki, A., Kumbasar, N. and Koc, V., 2004. Low strength concrete members externally confined with FRP sheets. *Structural Engineering and Mechanics* **18** (2): 167-194.

Indraratna, B., Basack, S. and Rujikiatkamjorn, C., 2013a. Numerical solution of stone column–improved soft soil considering arching, clogging, and smear effects. *Journal of Geotechnical and Geoenvironmental Engineering* **139** (3): 377-394.

Indraratna, B., Ngo, N. T. and Rujikiatkamjorn, C., 2013b. Deformation of coal fouled ballast stabilized with geogrid under cyclic load. *Journal of Geotechnical and Geoenvironmental Engineering* **139** (8): 1275-1289.

Indraratna, B., Rujikiatkamjorn, C. and Sathananthan, I., 2005. Radial consolidation of clay using compressibility indices and varying horizontal permeability. *Canadian Geotechinical Journal* **42**: 1330-1341.

Jenck, O., Dias, D. and Kastner, R., 2009. Discrete element modelling of a granular platform supported by piles in soft soil–Validation on a small scale model test and comparison to a numerical analysis in a continuum. *Computers and Geotechnics* **36** (6): 917-927.

Jones, C. J. F. P., Lawson, C. R. and Ayres, D. J., 1990. Geotextile reinforced piled embankments. In: Hoedt, Den (Ed.), Geotextiles, Geomembranes and Related Products, Balkema, Rotterdam.

Jones, R. and Xenophontos, J., 1976. On the Vlasov and Kerr foundation models. *Acta Mechanica* **25**: 45-49.

Karam, G. and Tabbara, M., 2009. Hoek–Brown strength criterion for actively confined concrete. *Journal of Materials in Civil Engineering* **21** (3): 110-118.

Kempfert, H., Stadel, M. and Zaeske, D., 1997. Design of geosynthetic-reinforced bearing layers over piles. *Bautechnik* **74** (12): 818-825.

Kempfert, H., Zaeske, D. and Alexiew, D., 1999. Interactions in reinforced bearing layers over partial supported underground. Geotechnical Engineering for Transportation Infrastructure, Amsterdam, Netherlands, Taylor and Francis US.

Kempfert, H. G., Göbel, C., Alexiew, D. and Heitz, C., 2004. German recommendations for reinforced embankments on pile-similar elements. In: Proceedings of EuroGeo 3, Munich.

Kerr, A. D., 1964. Elastic and viscoelastic foundation models. *Journal of Applied Mechanics* **31** (3): 491-498.

Kerr, A. D., 1965. A study of a new foundation model. *Acta Mechanica* **1**: 135-147.

Khabbazian, M., Kaliakin, V. N. and Meehan, C. L., 2015. Column supported embankments with geosynthetic encased columns: validity of the unit cell concept. *Geotechnical and Geological Engineering* **33** (3): 425-442.

King, D. J., Bouazza, A., Gniel, J. R., Rowe, R. K. and Bui, H. H., 2017. Geosynthetic reinforced column supported embankments and the role of ground improvement installation effects. *Canadian Geotechnical Journal* **55** (6): 792-809.

Kneifati, M. C., 1985. Analysis of plates on a Kerr foundation model. *Journal of Engineering Mechanics* **111** (11): 1325-1342.

Kravtchenko, J. and Sirieys, P., 1966. Rheology and soil mechanics. International Symposium on Rheology and Soil Mechanics, Grenoble, Springer Verlag, Berlin.

Ladd, C., 1991. The Twenty-Second Terzaghi Lecture, American Society of Civil Engineers.

Le Hello, B. and Villard, P., 2009. Embankments reinforced by piles and geosynthetics—numerical and experimental studies dealing with the transfer of load on the soil embankment. *Engineering Geology* **106** (1-2): 78-91.

Le, T. M. and Fatahi, B., 2016. Trust-region reflective optimisation to obtain soil visco-plastic properties. *Engineering Computations* **33** (2).

Le, T. M., Fatahi, B. and Khabbaz, H., 2015. Numerical optimisation to obtain elastic viscoplastic model parameters for soft clay. *International Journal of Plasticity* **65**: 1-21.

Lei, G. H., Fu, C. W. and Ng, C. W. W., 2016. Vertical-drain consolidation using stone columns: An analytical solution with an impeded drainage boundary under multi-ramp loading. *Geotextiles and Geomembranes* **44** (1): 122-131.

Leoni, M., Karstunen, M. and Vermeer, P., 2008. Anisotropic creep model for soft soils. *Géotechnique* **58** (3): 215-226.

Liu, H. L., Ng, C. W. W. and Fei, K., 2007. Performance of a geogrid-reinforced and pile-supported highway embankment over soft clay: case study. *Journal of Geotechnical and Geoenvironmental Engineering* **133** (12): 1483-1493.

Liu, K.-W., Rowe, R. K., Su, Q., Liu, B. and Yang, Z., 2017. Long-term reinforcement strains for column supported embankments with viscous reinforcement by FEM. *Geotextiles and Geomembranes* **45** (4): 307-319.

Liu, K. W. and Rowe, R. K., 2015. Numerical study of the effects of geosynthetic reinforcement viscosity on behaviour of embankments supported by deep-mixing-method columns. *Geotextiles and Geomembranes* **43** (6): 567-578.

Low, B. K., Tang, S. K. and Choa, V., 1994. Arching in piled embankments. *Journal of Geotechical Engineering* **120** (11): 1917-1938

Madhav, M. R. and Poorooshasb, H. B., 1988. A new model for geosynthetic reinforced soil. *Computers and Geotechnics* **6** (4): 277-290.

Maheshwari, P., Basudhar, P. and Chandra, S., 2004. Analysis of beams on reinforced granular beds. *Geosynthetics International* **11** (6): 470-480.

Maheshwari, P. and Khatri, S., 2012. Response of infinite beams on geosynthetic-reinforced granular bed over soft soil with stone columns under moving loads. *International Journal of Geomechanics* **13** (6): 713-728.

Maheshwari, P. and Viladkar, M. N., 2009. A mathematical model for beams on geosynthetic reinforced earth beds under strip loading. *Applied Mathematical Modelling* **33** (4): 1803-1814.

Marston, A. and Anderson, A. O., 1913. The theory of loads on pipes in ditches: and tests of cement and clay drain tile and sewer pipe, Iowa State College of Agriculture and Mechanic Arts.

Mayne, P. W. and Kulhawy, F. H., 1982. Ko - OCR Relationships in Soil. *Journal of the Geotechnical Engineering Division* **108** (6): 851-872.

McCormac, J. C. and Brown, R. H., 2009. Design of reinforced concrete. John Wiley & Sons, USA.

McGuire, M., Sloan, J., Collin, J. and Filz, G., 2012. Critical height of column-supported embankments from Bench-Scale and field-scale tests. In: TC 211 International Symposium on Ground Improvement IS-GI Brussels, ISSMGE.

McKelvey, J. A., 1994. The anatomy of soil arching. *Geotextiles and Geomembranes* **13** (5): 317-329.

McNulty, J. W., 1965. An experimental study of arching in sand, Army engineer waterways experiment station vickburg ms.

Morfidis, K., 2007. Exact matrices for beams on three-parameter elastic foundation. *Computers & Structures* **85** (15-16): 1243-1256.

Muir Wood, D., 1990. Soil Behaviour and Critical State Soil Mechanics, Cambridge University Press.

Naughton, P., 2007. The significance of critical height in the design of piled embankments. *Soil Improvement*: 1-10.

Nguyen, L. and Fatahi, B., 2016. Behaviour of clay treated with cement & fibre while capturing cementation degradation and fibre failure – C3F Model. *International Journal of Plasticity* **81**: 168-195.

Nguyen, L. D., Fatahi, B. and Khabbaz, H., 2014. A constitutive model for cemented clays capturing cementation degradation. *International Journal of Plasticity* **56**: 1-18.

Nogami, T. and Yong, T. Y., 2003. Load-settlement analysis of geosynthetic-reinforced soil with a simplified model. *Soils and Foundations* **43** (3): 33-42.

Nunez, M. A., Briançon, L. and Dias, D., 2013. Analyses of a pile-supported embankment over soft clay: Full-scale experiment, analytical and numerical approaches. *Engineering Geology* **153**: 53-67.

Parry, R. H. G., 1972. Stress-strain behaviour of soils. G T Foulis and Co Ltd. Henley-on-Thames.

Parsa-Pajouh, A., Fatahi, B. and Khabbaz, H., 2016. Experimental and numerical investigations to evaluate two-dimensional modeling of vertical drain–assisted preloading. *International Journal of Geomechanics* **16** (1).

Pasternak, P. L., 1954. On a new method of analysis of an elastic foundation by means of two constants. *Moscow: USSR*.

Qu, C. Z., 2009. Deformation of geocell with different tensile and compressive modulus. *Journal of Geotechnical Engineering* **14**: 1-14.

RMS. 2015. : Roads and Maritime Services: Gerringong upgrade - Princes Highway upgrade. Retrieved 21/08/2018, 2018, from www.rms.nsw.gov.au/gu.

Rogbeck, Y., Gustavsson, S., Södergren, I. and Lindquist, D., 1998. Reinforced piled embankments in Sweden e design aspects. In: Proceedings of the Sixth International Conference on Geosynthetics.

Rowe, R. K. and Li, A. L., 1999. Reinforced embankments over soft foundations under undrained and partially drained conditions. *Geotextiles and Geomembranes* **17** (3): 129-146.

Rowe , R. K. and Li, A. L., 2005. Geosynthetic-reinforced embankments over soft foundations. *Geosynthetics International* **12** (1): 50-85.

Rowe, R. K. and Liu, K. W., 2015. Three-dimensional finite element modelling of a full-scale geosynthetic-reinforced, pile-supported embankment. *Canadian Geotechnical Journal* **52** (12): 2041-2054.

Rowe, R. K. and Soderman, K. L., 1987. Stabilization of very soft soils using high strength geosynthetics: the role of finite element analyses. *Geotextiles and Geomembranes* **6** (1-3): 53-80.

Russell, D. and Pierpoint, N., 1997. An assessment of design methods for piled embankments. *Ground Engineering*: 39-44.

Schmertmann, J. H., 1991. The mechanical aging of soils. *Journal of Geotechnical Engineering* **117** (9): 1288-1330.

Selvadurai, A. P., 1979. Elastic analysis of soil-foundation interaction. Elsevier Scientific, Amsterdam.

Shukla, S. K. and Yin, J. H., 2003. Time-dependent settlement analysis of a geosynthetic-reinforced soil. *Geosynthetics International* **10** (2): 70-76.

Smith, M. E., 2005. Design of bridging layers in geosynthetic-reinforced column-supported embankments, Virginia Tech.

Suksiripattanapong, C., Chinkulkijniwat, A., Horpibulsuk, S., Rujikiatkamjorn, C. and Tanhsutthinon, T., 2012. Numerical analysis of bearing reinforcement earth (BRE) wall. *Geotextiles and Geomembranes* **32** (1): 28-37.

Svanø, G., Ilstad, T., Eiksund, G. and Want, A., 2000. Alternative calculation principle for design of piled embankments with base reinforcement. In: Proceedings of the 4th GIGS Helsinki.

Tan, S. A., Tjahyono, S. and Oo, K. K., 2008. Simplified plane-strain modeling of stone-column reinforced ground. *Journal of Geotechnical and Geoenvironmental Engineering* **134** (2): 185-194.

Tandel, Y. K., Solanki, C. H. and Desai, A. K., 2013. 3D FE Analysis of an Embankment Construction on GRSC and Proposal of a Design Method. *ISRN Civil Engineering* **2013**.

Tavenas, F., Jean, P., Leblond, P. and Leroueil, S., 1983. The permeability of natural soft clays. Part II: Permeability characteristics. *Canadian Geotechnical Journal* **20** (4): 645-660.

Taylor, D., 1948. Fundamentals of soil mechanics, Chapman And Hall, Limited.; New York.

Terzaghi, K., 1936. The shearing resistance of saturated soils and the angle between the planes of shear. First international conference on soil Mechanics, 1936.

Terzaghi, K., 1943. Theoretical soil mechanics. John Wiley and Sons, New York.

Timoshenko, S. P., 1921. On the correction for shear of the differential equation for transverse vibrations of prismatic bars. *Philosophical Magazine and Journal of Science* **41** (245): 744-746.

Timoshenko, S. P. and Gere, J. M., 1961. Theory of elastic stability. McGrawHill-Kogakusha Ltd, Tokyo.

van Eekelen, S. J. M., Bezuijen, A., Lodder, H. J. and Van Tol, A. F., 2012a. Model experiments on piled embankments. Part I. *Geotextiles and Geomembranes* **32** (2012): 69-81.

van Eekelen, S. J. M., Bezuijen, A., Lodder, H. J. and Van Tol, A. F., 2012b. Model experiments on piled embankments. Part II. *Geotextiles and Geomembranes* **32** (2012): 82-94.

van Eekelen, S. J. M., Bezuijen, A. and Oung, O., 2003. Arching in piled embankments; experiments and design calculations. In: Proceedings of Foundations: Innovations, Observations, Design and Practice.

van Eekelen, S. J. M., Bezuijen, A. and van Tol, A. F., 2011. Analysis and modification of the British Standard BS8006 for the design of piled embankments. *Geotextiles and Geomembranes* **29** (3): 345-359.

van Eekelen, S. J. M., Bezuijen, A. and van Tol, A. F., 2013. An analytical model for arching in piled embankments. *Geotextiles and Geomembranes* **39** (2013): 78-102.

van Eekelen, S. J. M., Bezuijen, A. and van Tol, A. F., 2015. Validation of analytical models for the design of basal reinforced piled embankments. *Geotextiles and Geomembranes* **43** (1): 56-81.

Wang, C., 1995. Timoshenko beam-bending solutions in terms of Euler-Bernoulli solutions. *Journal of Engineering Mechanics* **121** (6): 763-765.

Winkler, E., 1867. Die Lehre von der Elasticitaet und Festigkeit: mit besonderer Rücksicht auf ihre Anwendung in der Technik für polytechnische Schulen. Dominicus.

Yapage, N. N. S. and Liyanapathirana, D. S., 2014. A parametric study of geosynthetic-reinforced column-supported embankments. *Geosynthetics International* **21** (3): 213-232.

Yin, J. H., 1997a. Modelling geosynthetic-reinforced granular fills over soft soil. *Geosynthetics International* **4** (2): 165-185.

Yin, J. H., 1997b. A nonlinear model of geosynthetic-reinforced granular fill over soft soil. *Geosynthetics International* **4** (5): 523-537.

Yin, J. H., 1999. Properties and behaviour of Hong Kong marine deposits with different clay contents *Canadian Geotechnical Journal* **36** (6): 1085-1095.

Yin, J. H., 2000a. Closed form solution of reinforced Timoshenko beam on elastic foundation. *Journal of Engineering Mechanics* **126** (8): 868-874.

Yin, J. H., 2000b. Comparative modeling study of reonforced beam on elastic foundation. *Journal of Geotechnical and Geoenvironmental Engineering* **126** (3): 265-271.

Yoo, C., 2015. Settlement behavior of embankment on geosynthetic-encased stone column installed soft ground – A numerical investigation. *Geotextiles and Geomembranes* **43** (6): 484-492.

Yu, Y. and Bathurst, R. J., 2017. Modelling of geosynthetic-reinforced column-supported embankments using 2D full-width model and modified unit cell approach. *Geotextiles and Geomembranes* **45** (2): 103-120.

Zaeske, D., 2001. Zur Wirkungsweise von unbewehrten und bewehrten mineralischen Tragschichten über pfahlartigen Gründungselementen. *Schriftenreihe Geotechnik, Uni Kassel. Heft 10 (in German)*.

Zaeske, D., 2002. Berechnung und Wirkungsweise von unbewehrten und bewehrten mineralischen Tragschichten ueber punkt-und linienfoermigen Traggliedern/Calculation and behaviour of unreinforced and reinforced bearing layers over point-or lineshaped bearing elements. *Bauingenieur* **77** (2).

Zhang, L., Zhao, M., Hu, Y., Zhao, H. and Chen, B., 2012a. Semi-analytical solutions for geosynthetic-reinforced and pile-supported embankment. *Computers and Geotechnics* **44**: 167-175.

Zhang, L., Zhao, M., Shi, C. and Zhao, H., 2012b. Nonlinear analysis of a geocell mattress on an elastic–plastic foundation. *Computers and Geotechnics* **42**: 204-211.

Zhang, L., Zhao, M., Zou, X. and Zhao, H., 2010. Analysis of geocell-reinforced mattress with consideration of horizontal–vertical coupling. *Computers and Geotechnics* **37** (6): 748-756.

Zhao, L. S., Zhou, W. H., Fatahi, B., Li, X. B. and Yuen, K. V., 2016. A dual beam model for geosynthetic-reinforced granular fill on an elastic foundation. *Applied Mathematical Modelling* **40** (21-22): 9254-9268.

Zheng, J. J., Chen, B., Lu, Y. E., Abusharar, S. W. and Yin, J. H., 2009. The performance of an embankment on soft ground reinforced with geosynthetics and pile walls. *Geosynthetics International* **16** (1): 1-10.

Zhuang, Y., 2009. Numerical modelling of arching in piled embankments including the effects of reinforcement and subsoil. PhD, University of Nottingham.

Appendix A: Algebraic Equations Obtained from the Boundary and the Continuity Conditions

According to the boundary condition $\theta_1(x,t)|_{x=0} = 0$, the following equation is obtained:

$$a_1(A_1 - B_1) + a_2(B_1 + A_1) - a_3(A_1 + B_1) + a_4(B_1 - A_1) = Z_1 \quad \textbf{(A 1)}$$

Boundary condition $V_1(x,t)|_{x=0} = -K_c w_1(x,t)|_{x=0}$ results:

$$a_1\left(G_1 - H_1 + \frac{K_c}{D_h}\right) - a_2\left(G_1 + H_1 - \frac{K_c}{D_h}\right) + a_3\left(H_1 + G_1 + \frac{K_c}{D_h}\right) - a_4\left(G_1 - H_1 - \frac{K_c}{D_h}\right) = Z_2 \quad \textbf{(A 2)}$$

From the boundary condition $\theta_3(x,t)|_{x=s'} = 0$ following equation is obtained:

$$c_1 c^{\vartheta_3 s'}(A_3 \cos\delta_3 s' - B_3 \sin\delta_3 s') + c_2 e^{\vartheta_3 s'}(B_3 \cos\delta_3 s' + A_3 \sin\delta_3 s') - c_3 e^{-\vartheta_3 s'}(A_3 \cos\delta_3 s' + B_3 \sin\delta_3 s') + c_4 e^{-\vartheta_3 s'}(B_3 \cos\delta_3 s' - A_3 \sin\delta_3 s') = Z_3 \quad \textbf{(A 3)}$$

The equation below is obtained from the boundary condition $V_3(x,t)|_{x=s'} = +K_c w_3(x,t)|_{x=s'}$:

$$c_1 e^{\vartheta_3 s'}\left(G_3 \sin\delta_3 s' - H_3 \cos\delta_3 s' + \frac{K_c \cos\delta_3 s'}{D_h}\right) - c_2 e^{\vartheta_3 s'}\left(G_3 \cos\delta_3 s' + H_3 \sin\delta_3 s' - \frac{K_c \sin\delta_3 s'}{D_h}\right) + c_3 e^{-\vartheta_3 s'}\left(H_3 \cos\delta_3 s' + G_3 \sin\delta_3 s' + \frac{K_c \cos\delta_3 s'}{D_h}\right) - c_4 e^{-\vartheta_3 s'}\left(G_3 \cos\delta_3 s' - H_3 \sin\delta_3 s' - \frac{K_c \sin\delta_3 s'}{D_h}\right) = Z_4 \quad \text{(A 4)}$$

From the boundary condition $w_1(x,t)|_{x=r_1} = w_2(x,t)\big|_{x=r_1}$ the following equation is obtained:

$$a_1 e^{\vartheta_1 r_1}\cos\delta_1 r_1 + a_2 e^{\vartheta_1 r_1}\sin\delta_1 r_1 + a_3 e^{-\vartheta_1 r_1}\cos\delta_1 r_1 + a_4 e^{-\vartheta_1 r_1}\sin\delta_1 r_1 - b_1 e^{\vartheta_2 r_1}\cos\delta_2 r_1 - b_2 e^{\vartheta_2 r_1}\sin\delta_2 r_1 - b_3 e^{-\vartheta_2 r_1}\cos\delta_2 r_1 - b_4 e^{-\vartheta_2 r_1}\sin\delta_2 r_1 = Z_5 \quad \text{(A 5)}$$

According to the boundary condition $M_1(x,t)|_{x=r_1} = 0$ the following equation is obtained:

$$a_1 e^{\vartheta_1 r_1}(F_1\cos\delta_1 r_1 + E_1\sin\delta_1 r_1) + a_2 e^{\vartheta_1 r_1}(F_1\sin\delta_1 r_1 - E_1\cos\delta_1 r_1) + a_3 e^{-\vartheta_1 r_1}(F_1\cos\delta_1 r_1 - E_1\sin\delta_1 r_1) + a_4 e^{-\vartheta_1 r_1}(E_1\cos\delta_1 r_1 + F_1\sin\delta_1 r_1) = Z_6 \quad \text{(A 6)}$$

The following equation is after $M_2(x,t)|_{x=r_1} = 0$:

$$b_1 e^{\vartheta_2 r_1}(F_2\cos\delta_2 r_1 + E_2\sin\delta_2 r_1) + b_2 e^{\vartheta_2 r_1}(F_2\sin\delta_2 r_1 - E_2\cos\delta_2 r_1) + b_3 e^{-\vartheta_2 r_1}(F_2\cos\delta_2 r_1 - E_2\sin\delta_2 r_1) + b_4 e^{-\vartheta_2 r_1}(E_2\cos\delta_2 r_1 + F_2\sin\delta_2 r_1) = Z_7 \quad \text{(A 7)}$$

The following equation is obtained from $w_2(x,t)|_{x=r_2} = \hat{w}$:

$$b_1 e^{\vartheta_2 r_2} \cos \delta_2 r_2 + b_2 e^{\vartheta_2 r_2} \sin \delta_2 r_2 + b_3 e^{-\vartheta_2 r_2} \cos \delta_2 r_2 + b_4 e^{-\vartheta_2 r_2} \sin \delta_2 r_2 = Z_8 \quad \text{(A 8)}$$

The next equation is obtained using $w_3(x,t)|_{x=r_2} = \hat{w}$:

$$c_1 e^{\vartheta_3 r_2} \cos \delta_3 r_2 + c_2 e^{\vartheta_3 r_2} \sin \delta_3 r_2 + c_3 e^{-\vartheta_3 r_2} \cos \delta_3 r_2 + c_4 e^{-\vartheta_3 r_2} \sin \delta_3 r_2 = Z_9 \quad \text{(A 9)}$$

The equation below is obtained from $M_2(x,t)|_{x=r_2} = M_3(x,t)|_{x=r_2}$:

$$\begin{aligned} &b_1 e^{\vartheta_2 r_2}(F_2 \cos \delta_2 r_2 + E_2 \sin \delta_2 r_2) + b_2 e^{\vartheta_2 r_2}(F_2 \sin \delta_2 r_2 - E_2 \cos \delta_2 r_2) + b_3 e^{-\vartheta_2 r_2}(F_2 \cos \delta_2 r_2 - E_2 \sin \delta_2 r_2) + \\ &b_4 e^{-\vartheta_2 r_2}(E_2 \cos \delta_2 r_2 + F_2 \sin \delta_2 r_2) - c_1 e^{\vartheta_3 r_2}(F_3 \cos \delta_3 r_2 + E_3 \sin \delta_3 r_2) - c_2 e^{\vartheta_3 r_2}(F_3 \sin \delta_3 r_2 - E_3 \cos \delta_3 r_2) - \\ &c_3 e^{-\vartheta_3 r_2}(F_3 \cos \delta_3 r_2 - E_3 \sin \delta_3 r_2) - c_4 e^{-\vartheta_3 r_2}(E_3 \cos \delta_3 r_2 + F_3 \sin \delta_3 r_2) = Z_{10} \end{aligned} \quad \text{(A 10)}$$

The following equation is obtained from $w_3(x,t)|_{x=r_3} = \hat{w}$:

$$c_1 e^{\vartheta_3 r_3} \cos \delta_3 r_3 + c_2 e^{\vartheta_3 r_3} \sin \delta_3 r_3 + c_3 e^{-\vartheta_3 r_3} \cos \delta_3 r_3 + c_4 e^{-\vartheta_3 r_3} \sin \delta_3 r_3 = Z_{11} \quad \text{(A 11)}$$

The equation below is obtained using $w_2(x,t)|_{x=r_3} = \hat{w}$:

$$b_1 e^{\vartheta_2 r_2} \cos \delta_2 r_3 + b_2 e^{\vartheta_2 r_2} \sin \delta_2 r_3 + b_3 e^{-\vartheta_2 r_2} \cos \delta_2 r_3 + b_4 e^{-\vartheta_2 r_2} \sin \delta_2 r_3 = Z_{12} \quad \text{(A 12)}$$

The following equation is obtained from $M_2(x,t)|_{x=r_3} = M_3(x,t)|_{x=r_3}$:

$$b_1 e^{\vartheta_2 r_3}(F_2 \cos \delta_2 r_3 + E_2 \sin \delta_2 r_3) + b_2 e^{\vartheta_2 r_2}(F_2 \sin \delta_2 r_3 - E_2 \cos \delta_2 r_3) + b_3 e^{-\vartheta_2 r_2}(F_2 \cos \delta_2 r_3 - E_2 \sin \delta_2 r_3) + b_4 e^{-\vartheta_2 r_3}(E_2 \cos \delta_2 r_3 + F_2 \sin \delta_2 r_3) - c_1 e^{\vartheta_3 r_3}(F_3 \cos \delta_3 r_3 + E_3 \sin \delta_3 r_3) - c_2 e^{\vartheta_3 r_3}(F_3 \sin \delta_3 r_3 - E_3 \cos \delta_3 r_3) - c_3 e^{-\vartheta_3 r_3}(F_3 \cos \delta_3 r_3 - E_3 \sin \delta_3 r_3) - c_4 e^{-\vartheta_3 r_3}(E_3 \cos \delta_3 r_3 + F_3 \sin \delta_3 r_3) = Z_{13} \quad \text{(A 13)}$$

The next equation is established from $w_1(x,t)|_{x=r_4} = w_2(x,t)|_{x=r_4}$:

$$a_1 e^{\vartheta_1 r_4} \cos \delta_1 r_4 + a_2 e^{\vartheta_1 r_4} \sin \delta_1 r_4 + a_3 e^{-\vartheta_1 r_4} \cos \delta_1 r_4 + a_4 e^{-\vartheta_1 r_4} \sin \delta_1 r_4 - b_1 e^{\vartheta_2 r_4} \cos \delta_2 r_4 - b_2 e^{\vartheta_2 r_4} \sin \delta_2 r_4 - b_3 e^{-\vartheta_2 r_4} \cos \delta_2 r_4 - b_4 e^{-\vartheta_2 r_4} \sin \delta_2 r_4 = Z_{14} \quad \text{(A 14)}$$

The equation below is acquired $M_1(x,t)|_{x=r_4} = 0$:

$$b_1 e^{\vartheta_2 r_4}(F_2 \cos \delta_2 r_4 + E_2 \sin \delta_2 r_4) + b_2 e^{\vartheta_2 r_4}(F_2 \sin \delta_2 r_4 - E_2 \cos \delta_2 r_4) + b_3 e^{-\vartheta_2 r_4}(F_2 \cos \delta_2 r_4 - E_2 \sin \delta_2 r_4) + b_4 e^{-\vartheta_2 r_4}(E_2 \cos \delta_2 r_4 + F_2 \sin \delta_2 r_4) = Z_{15} \quad \text{(A 15)}$$

The following equation is attained from $M_2(x,t)|_{x=r_4} = 0$:

$$a_1 e^{\vartheta_1 r_4}(F_1 \cos\delta_1 r_4 + E_1 \sin\delta_1 r_4) + a_2 e^{\vartheta_1 r_4}(F_1 \sin\delta_1 r_4 - E_1 \cos\delta_1 r_4) + a_3 e^{-\vartheta_1 r_4}(F_1 \cos\delta_1 r_4 - E_1 \sin\delta_1 r_4) + a_4 e^{-\vartheta_1 r_4}(E_1 \cos\delta_1 r_4 + F_1 \sin\delta_1 r_4) = Z_{16} \quad \text{(A 16)}$$

where

$$Z_1 = \sum_{m=1}^{m=\infty}\left\{\left[\frac{D_h}{C_h}\left(\frac{2m\pi}{s'}\right)^2 - \left(1 - \frac{k_{0s}D_h}{UC_h{}^2}\right)\right] q_{m1} - \frac{D_h}{C_h{}^2} Q_m\right\}\left(\frac{2m\pi}{s'}\right) \quad \text{(A 17)}$$

$$Z_2 = -K_c\left(\frac{UP_0}{k_{0s}} + \sum_{m=1}^{m=\infty} p_{m1}\right) - D_h\left\{\left[\left(\frac{2m\pi}{s'}\right)^2 + \frac{k_{0s}D_h}{UC_h}\right] q_{m1} - \frac{Q_m}{C_h}\right\}\left(\frac{2m\pi}{s'}\right) \quad \text{(A 18)}$$

$$Z_3 = \sum_{m=1}^{m=\infty}\left\{\left[\frac{D_s}{C_s}\left(\frac{2m\pi}{s'}\right)^2 - \left(1 - \frac{k_{1s}D_s}{UC_s{}^2}\right)\right] q_{m3} - \frac{D_s}{C_s{}^2} Q_m\right\}\left(\frac{2m\pi}{s'}\right)\cos(2m\pi) -$$

$$\sum_{n=1}^{n=\infty}\left\{\left[\frac{D_s}{C_s}\left(\frac{2m\pi}{s'}\right)^2 - \left(1 - \frac{k_{1s}D_s}{UC_h{}^2}\right)\right] p_{m3} - \frac{D_s}{C_h{}^2} P_m\right\}\left(\frac{2m\pi}{s'}\right)\sin(2m\pi) \quad \text{(A 19)}$$

$$Z_4 = K_c\left\{\frac{\hat{w}(k_{1s}-k_{0s})}{k_{1s}} + \frac{UP_0}{k_{1s}} + \sum_{m=1}^{m=\infty}[p_{m3}\cos(2m\pi)]\right\} - D_s\sum_{m=1}^{m=\infty}\left\{\left[\left(\frac{2m\pi}{s'}\right)^2 + \frac{k_{1s}D_s}{UC_s}\right] q_{m3} - \frac{Q_m}{C_s}\right\}\left(\frac{2m\pi}{s'}\right)\cos(2m\pi) \quad \text{(A 20)}$$

$$Z_5 = \sum_{m=1}^{m=\infty}\left[(p_{m2} - p_{m1})\cos\left(\frac{2m\pi r_1}{s'}\right) + (q_{m2} - q_{m1})\sin\left(\frac{2m\pi r_1}{s'}\right)\right] \quad \text{(A 21)}$$

$$Z_6 = \sum_{m=1}^{m=\infty}\left\{\left[\frac{D_h}{C_h}\left(\frac{2m\pi}{s'}\right)^2 - \left(1-\frac{k_{0s}D_h}{UC_h{}^2}\right)\right]q_{m1} - \frac{D_h}{C_h{}^2}Q_m\right\}\left(\frac{2m\pi}{s'}\right)^2 \sin\left(\frac{2m\pi r_1}{s'}\right) - \sum_{m=1}^{m=\infty}\left\{\left[\frac{D_h}{C_h}\left(\frac{2m\pi}{s'}\right)^2 - \left(1-\frac{k_{0s}D_h}{UC_h{}^2}\right)\right]p_{m1} - \frac{D_h}{C_h{}^2}P_m\right\}\left(\frac{2m\pi}{s'}\right)^2 \cos\left(\frac{2m\pi r_1}{s'}\right) \quad \text{(A 22)}$$

$$Z_7 = \sum_{m=1}^{m=\infty}\left\{\left[\frac{D_s}{C_s}\left(\frac{2m\pi}{s'}\right)^2 - \left(1-\frac{k_{0s}D_s}{UC_s{}^2}\right)\right]q_{m2} - \frac{D_s}{C_s{}^2}Q_m\right\}\left(\frac{2m\pi}{s'}\right)^2 \sin\left(\frac{2m\pi r_1}{s'}\right) - \sum_{m=1}^{m=\infty}\left\{\left[\frac{D_s}{C_s}\left(\frac{2m\pi}{s'}\right)^2 - \left(1-\frac{k_{0s}D_s}{UC_s{}^2}\right)\right]p_{m2} - \frac{D_s}{C_s{}^2}P_m\right\}\left(\frac{2m\pi}{s'}\right)^2 \cos\left(\frac{2m\pi r_1}{s'}\right) \quad \text{(A 23)}$$

$$Z_8 = \hat{w} - \frac{UP_0}{k_{0s}} + \sum_{m=1}^{m=\infty}\left[p_{m2}\cos\left(\frac{2m\pi r_2}{s'}\right) + q_{m2}\sin\left(\frac{2m\pi r_2}{s'}\right)\right] \quad \text{(A 24)}$$

$$Z_9 = \hat{w} - \frac{\hat{w}(k_{1s}-k_{0s})}{k_{1s}} - \frac{UP_0}{k_{1s}} - \sum_{m=1}^{m=\infty}\left[p_{m3}\cos\left(\frac{2m\pi r_2}{s'}\right) + q_{m3}\sin\left(\frac{2m\pi r_2}{s'}\right)\right] \quad \text{(A 25)}$$

$$Z_{10} = \sum_{m=1}^{m=\infty}\left\{\left[\frac{D_s}{C_s}\left(\frac{2m\pi}{s'}\right)^2 - \left(1-\frac{k_{1s}D_s}{UC_s{}^2}\right)\right]p_{m3} - \frac{D_s}{C_s{}^2}P_m\right\}\left(\frac{2m\pi}{s'}\right)^2 \cos\left(\frac{2m\pi r_2}{s'}\right) - \sum_{m=1}^{m=\infty}\left\{\left[\frac{D_s}{C_s}\left(\frac{2m\pi}{s'}\right)^2 - \left(1-\frac{k_{0s}D_s}{UC_s{}^2}\right)\right]p_{m2} - \frac{D_s}{C_s{}^2}P_m\right\}\left(\frac{2m\pi}{s'}\right)^2 \cos\left(\frac{2m\pi r_2}{s'}\right) - \sum_{m=1}^{m=\infty}\left\{\left[\frac{D_s}{C_s}\left(\frac{2m\pi}{s'}\right)^2 - \left(1-\frac{k_{1s}D_s}{UC_s{}^2}\right)\right]q_{m3} - \frac{D_s}{C_s{}^2}Q_m\right\}\left(\frac{2m\pi}{s'}\right)^2 \sin\left(\frac{2m\pi r_2}{s'}\right) + \sum_{m=1}^{m=\infty}\left\{\left[\frac{D_s}{C_s}\left(\frac{2m\pi}{s'}\right)^2 - \left(1-\frac{k_{0s}D_s}{UC_s{}^2}\right)\right]q_{m2} - \frac{D_s}{C_s{}^2}Q_m\right\}\left(\frac{2m\pi}{s'}\right)^2 \sin\left(\frac{2m\pi r_2}{s'}\right) \quad \text{(A 26)}$$

$$Z_{11} = \hat{w} - \frac{UP_0}{k_{0s}} + \sum_{m=1}^{m=\infty}\left[p_{m2}\cos\left(\frac{2m\pi r_3}{s'}\right) + q_{m2}\sin\left(\frac{2m\pi r_3}{s'}\right)\right] \quad \text{(A 27)}$$

$$Z_{12} = \hat{w} - \frac{\hat{w}(k_{1s}-k_{0s})}{k_{1s}} - \frac{UP_0}{k_{1s}} - \sum_{m=1}^{m=\infty}\left[p_{m3}\cos\left(\frac{2m\pi r_3}{s'}\right) + q_{m3}\sin\left(\frac{2m\pi r_3}{s'}\right)\right] \quad \text{(A 28)}$$

$$Z_{13} = \sum_{m=1}^{m=\infty}\left\{\left[\frac{D_s}{C_s}\left(\frac{2m\pi}{s'}\right)^2 - \left(1-\frac{k_{1s}D_s}{UC_s{}^2}\right)\right]p_{m3} - \frac{D_s}{C_s{}^2}P_m\right\}\left(\frac{2m\pi}{s'}\right)^2\cos\left(\frac{2m\pi r_3}{s'}\right) - \sum_{m=1}^{m=\infty}\left\{\left[\frac{D_s}{C_s}\left(\frac{2m\pi}{s'}\right)^2 - \left(1-\frac{k_{0s}D_s}{UC_s{}^2}\right)\right]p_{m2} - \frac{D_s}{C_s{}^2}P_m\right\}\left(\frac{2m\pi}{s'}\right)^2\cos\left(\frac{2m\pi r_3}{s'}\right) - \sum_{m=1}^{m=\infty}\left\{\left[\frac{D_s}{C_s}\left(\frac{2m\pi}{s'}\right)^2 - \left(1-\frac{k_{1s}D_s}{UC_s{}^2}\right)\right]q_{m3} - \frac{D_s}{C_s{}^2}Q_m\right\}\left(\frac{2m\pi}{s'}\right)^2\sin\left(\frac{2m\pi r_3}{s'}\right) + \sum_{m=1}^{m=\infty}\left\{\left[\frac{D_s}{C_s}\left(\frac{2m\pi}{s'}\right)^2 - \left(1-\frac{k_{0s}D_s}{UC_s{}^2}\right)\right]q_{m2} - \frac{D_s}{C_s{}^2}Q_m\right\}\left(\frac{2m\pi}{s'}\right)^2\sin\left(\frac{2m\pi r_3}{s'}\right) \quad \text{(A 29)}$$

$$Z_{14} = \sum_{m=1}^{m=\infty}\left[(p_{m2}-p_{m1})\cos\left(\frac{2m\pi r_4}{s'}\right) + (q_{m2}-q_{m1})\sin\left(\frac{2m\pi r_4}{s'}\right)\right] \quad \text{(A 30)}$$

$$Z_{15} = \sum_{m=1}^{m=\infty}\left\{\left[\frac{D_h}{C_h}\left(\frac{2m\pi}{s'}\right)^2 - \left(1-\frac{k_{0s}D_h}{UC_h{}^2}\right)\right]q_{m1} - \frac{D_h}{C_h{}^2}Q_m\right\}\left(\frac{2m\pi}{s'}\right)^2\sin\left(\frac{2m\pi r_4}{s'}\right) - \sum_{m=1}^{m=\infty}\left\{\left[\frac{D_h}{C_h}\left(\frac{2m\pi}{s'}\right)^2 - \left(1-\frac{k_{0s}D_h}{UC_h{}^2}\right)\right]p_{m1} - \frac{D_h}{C_h{}^2}P_m\right\}\left(\frac{2m\pi}{s'}\right)^2\cos\left(\frac{2m\pi r_4}{s'}\right) \quad \text{(A 31)}$$

and

$$Z_{16} = \sum_{m=1}^{m=\infty}\left\{\left[\frac{D_s}{C_s}\left(\frac{2m\pi}{s'}\right)^2 - \left(1-\frac{k_{0s}D_s}{UC_s{}^2}\right)\right]q_{m2} - \frac{D_s}{C_s{}^2}Q_m\right\}\left(\frac{2m\pi}{s'}\right)^2\sin\left(\frac{2m\pi r_4}{s'}\right) - \sum_{m=1}^{m=\infty}\left\{\left[\frac{D_s}{C_s}\left(\frac{2m\pi}{s'}\right)^2 - \left(1-\frac{k_{0s}D_s}{UC_s{}^2}\right)\right]p_{m2} - \frac{D_s}{C_s{}^2}P_m\right\}\left(\frac{2m\pi}{s'}\right)^2\cos\left(\frac{2m\pi r_4}{s'}\right) \quad \text{(A 32)}$$

Appendix B: Summary of Thirteen Algebraic Equations Obtained from the Adopted Boundary and Continuity Conditions

According to the boundary condition $V_s^{LTP} = 0$, the following equation is obtained:

$$c_1K_1 - c_2K_1 + c_3L_1 - c_4M_1 - c_5L_1 - c_6M_1 = R_1 \quad \text{(B 1)}$$

Boundary condition $w_s^{LTP'} = 0$ results:

$$c_1\delta_s - c_2\delta_s + c_3\varepsilon_s - c_4\sigma_s - c_5\varepsilon_s - c_6\sigma_s = R_2 \quad \text{(B 2)}$$

From the boundary condition $V_h^{LTP} = -(K_c)_{eq} w_h^{LTP}$ following equation is obtained:

$$-d_1e^{-\left(\frac{\delta_h s}{2}\right)}A_{22} + d_2e^{\left(\frac{\delta_h s}{2}\right)}B_{22} - d_3e^{-\left(\frac{\varepsilon_h s}{2}\right)}\left[C_{22}\sin\left(\frac{\sigma_h s}{2}\right) + E_{22}\cos\left(\frac{\sigma_h s}{2}\right)\right] - d_4e^{-\left(\frac{\varepsilon_h s}{2}\right)}\left[E_{22}\sin\left(\frac{\sigma_h s}{2}\right) - C_{22}\cos\left(\frac{\sigma_h s}{2}\right)\right] - d_5e^{\left(\frac{\varepsilon_h s}{2}\right)}\left[C_{22}\sin\left(\frac{\sigma_h s}{2}\right) - D_{22}\cos\left(\frac{\sigma_h s}{2}\right)\right] + d_6e^{\left(\frac{\varepsilon_h s}{2}\right)}\left[D_{22}\sin\left(\frac{\sigma_h s}{2}\right) + C_{22}\cos\left(\frac{\sigma_h s}{2}\right)\right] = R_3 \quad \text{(B 3)}$$

Assuming

$$A_{22} = K_2C - (K_c)_{eq};\ B_{22} = K_2C + (K_c)_{eq};\ C_{22} = CM_2;\ D_{22} = CL_2 + (K_c)_{eq};\ \text{and}\ E_{22} = CL_2 - (K_c)_{eq} \quad \text{(B 4)}$$

The equation below is obtained from the boundary condition $\theta_h^{LTP} = 0$:

$$-d_1 e^{-\left(\frac{\delta_h s}{2}\right)} A_2 + d_2 e^{\left(\frac{\delta_h s}{2}\right)} A_2 - d_3 e^{-\left(\frac{\varepsilon_h s}{2}\right)} \left[B_2 \sin\left(\frac{\sigma_h s}{2}\right) - C_2 \cos\left(\frac{\sigma_h s}{2}\right)\right] + d_4 e^{-\left(\frac{\varepsilon_h s}{2}\right)} \left[C_2 \sin\left(\frac{\sigma_h s}{2}\right) + B_2 \cos\left(\frac{\sigma_h s}{2}\right)\right] -$$

$$d_5 e^{\left(\frac{\varepsilon_h s}{2}\right)} \left[B_2 \sin\left(\frac{\sigma_h s}{2}\right) + C_2 \cos\left(\frac{\sigma_h s}{2}\right)\right] - d_6 e^{\left(\frac{\varepsilon_h s}{2}\right)} \left[C_2 \sin\left(\frac{\sigma_h s}{2}\right) - B_2 \cos\left(\frac{\sigma_h s}{2}\right)\right] = R_4 \quad \text{(B 5)}$$

From the boundary condition $w_s^{LTP} = w_h^{LTP}$ the following equation is obtained:

$$-c_1 e^{-\delta_s r} - c_2 e^{\delta_s r} - c_3 e^{-\varepsilon_s r} \cos\sigma_s r - c_4 e^{-\varepsilon_s r} \sin\sigma_s r - c_5 e^{\varepsilon_s r} \cos\sigma_s r - c_6 e^{\varepsilon_s r} \sin\sigma_s r + d_1 e^{-\delta_h r} + d_2 e^{\delta_h r} +$$

$$d_3 e^{-\varepsilon_h r} \cos\sigma_h r + d_4 e^{-\varepsilon_h r} \sin\sigma_h r + d_5 e^{\varepsilon_h r} \cos\sigma_h r + d_6 e^{\varepsilon_h r} \sin\sigma_h r = R_5 \quad \text{(B 6)}$$

According to the boundary condition $\theta_s^{LTP} = \theta_h^{LTP}$ the following equation is obtained:

$$c_1 e^{-\delta_s r} A_1 - c_2 e^{\delta_s r} A_1 + c_3 e^{-\varepsilon_s r}(B_1 \sin\sigma_s r - C_1 \cos\sigma_s r) - c_4 e^{-\varepsilon_s r}(C_1 \sin\sigma_s r + B_1 \cos\sigma_s r) + c_5 e^{\varepsilon_s r}(B_1 \sin\sigma_s r +$$

$$C_1 \cos\sigma_s r) + c_6 e^{\varepsilon_s r}(C_1 \sin\sigma_s r - B_1 \cos\sigma_s r) - d_1 e^{-\delta_h r} A_2 + d_2 e^{\delta_h r} A_2 - d_3 e^{-\varepsilon_h r}(B_2 \sin\sigma_h r - C_2 \cos\sigma_h r) +$$

$$d_4 e^{-\varepsilon_h r}(C_2 \sin\sigma_h r + B_2 \cos\sigma_h r) - d_5 e^{\varepsilon_h r}(B_2 \sin\sigma_h r + C_2 \cos\sigma_h r) - d_6 e^{\varepsilon_h r}(C_2 \sin\sigma_h r - B_2 \cos\sigma_h r) = R_6 \quad \text{(B 7)}$$

The following equation is after $M_h^{LTP} = 0$:

$$d_1 e^{-\delta_h r}\delta_h A_2 + d_2 e^{\delta_h r}\delta_h A_2 + d_3 e^{-\varepsilon_h r}(J_2 \sin\sigma_h r - I_2 \cos\sigma_h r) - d_4 e^{-\varepsilon_h r}(I_2 \sin\sigma_h r + J_2 \cos\sigma_h r) -$$

$$d_5 e^{\varepsilon_h r}(J_2 \sin\sigma_h r + I_2 \cos\sigma_h r) - d_6 e^{\varepsilon_h r}(I_2 \sin\sigma_h r - J_2 \cos\sigma_h r) = R_7 \quad \text{(B 8)}$$

The following equation is obtained from $V_s^{LTP} = V_h^{LTP}$:

$$-c_1 e^{-\delta_s r}K_1 C + c_2 e^{\delta_s r}K_1 C - c_3 e^{-\varepsilon_s r}C(M_1 \sin\sigma_s r + L_1 \cos\sigma_s r) - c_4 e^{-\varepsilon_s r}C(L_1 \sin\sigma_s r - M_1 \cos\sigma_s r) -$$

$$c_5 e^{\varepsilon_s r}C(M_1 \sin\sigma_s r - L_1 \cos\sigma_s r) + c_6 e^{\varepsilon_s r}C(L_1 \sin\sigma_s r + M_1 \cos\sigma_s r) + d_1 e^{-\delta_h r}K_2 C - d_2 e^{\delta_h r}K_2 C +$$

$$d_3 e^{-\varepsilon_h r}C(M_2 \sin\sigma_h r + L_2 \cos\sigma_h r) + d_4 e^{-\varepsilon_h r}C(L_2 \sin\sigma_h r - M_2 \cos\sigma_h r) + d_5 e^{\varepsilon_h r}C(M_2 \sin\sigma_h r - L_2 \cos\sigma_h r) -$$

$$d_6 e^{\varepsilon_h r}C(L_2 \sin\sigma_h r + M_2 \cos\sigma_h r) = R_8 \quad \text{(B 9)}$$

The next equation is obtained using $M_s^{LTP} = 0$:

$$c_1 e^{-\delta_s r}\delta_s A_1 + c_2 e^{\delta_s r}\delta_s A_1 + c_3 e^{-\varepsilon_s r}(J_1 \sin\sigma_s r - I_1 \cos\sigma_s r) - c_4 e^{-\varepsilon_s r}(I_1 \sin\sigma_s r + J_1 \cos\sigma_s r) - c_5 e^{\varepsilon_s r}(J_1 \sin\sigma_s r +$$

$$I_1 \cos\sigma_s r) - c_6 e^{\varepsilon_s r}(I_1 \sin\sigma_s r - J_1 \cos\sigma_s r) = R_9 \quad \text{(B 10)}$$

The equation below is obtained from $V_h^{ls} = (K_c)_{eq}\left(\frac{G}{C}\right) w_h^{ls}$:

$$d_1 e^{-\left(\frac{\delta_h s}{2}\right)} L_{22} - d_2 e^{\left(\frac{\delta_h s}{2}\right)} L_{22} + d_3 e^{-\left(\frac{\varepsilon_h s}{2}\right)} \left[M_{22} \cos\left(\frac{\sigma_h s}{2}\right) - N_{22} \sin\left(\frac{\sigma_h s}{2}\right)\right] + d_4 e^{-\left(\frac{\varepsilon_h s}{2}\right)} \left[N_{22} \cos\left(\frac{\sigma_h s}{2}\right) + M_{22} \sin\left(\frac{\sigma_h s}{2}\right)\right] -$$

$$d_5 e^{\left(\frac{\varepsilon_h s}{2}\right)} \left[M_{22} \cos\left(\frac{\sigma_h s}{2}\right) + M_{22} \sin\left(\frac{\sigma_h s}{2}\right)\right] + d_6 e^{\left(\frac{\varepsilon_h s}{2}\right)} \left[N_{22} \cos\left(\frac{\sigma_h s}{2}\right) - M_{22} \sin\left(\frac{\sigma_h s}{2}\right)\right] = R_{10} \quad \text{(B 11)}$$

Assuming

$$L_{22} = -\delta_h \left\{\delta_h{}^4 U_2 - \frac{\delta_h{}^2 U_2 k_u}{C} + Y_2\right\}; M_{22} = -(\varepsilon_h{}^5 - 10\varepsilon_h{}^3 \sigma_h{}^2 + 5\varepsilon_h \sigma_h{}^4) U_2 + (\varepsilon_h{}^3 - 3\varepsilon_h \sigma_h{}^2) \frac{U_2 k_u}{C} - Y_2 \varepsilon_h; \text{ and}$$

$$N_{22} = (5\varepsilon_h{}^4 \sigma_h - 10\varepsilon_h{}^2 \sigma_h{}^3 + \sigma_h{}^5) U_2 - (3\varepsilon_h{}^2 \sigma_h - \sigma_h{}^3) \frac{U_2 k_u}{C} + Y_2 \sigma_h \quad \text{(B 12)}$$

The following equation is obtained from $w_s^{ls\prime} = 0$:

$$c_1 L_{11} - c_2 L_{11} + c_3 M_{11} + c_4 N_{11} - c_5 M_{11} + c_6 N_{11} = R_{11} \quad \text{(B 13)}$$

Assuming

$$L_{11} = -\delta_s \left(\delta_s{}^4 U_1 - \frac{U_1 k_u \delta_s{}^2}{C} + Y_1\right); \; M_{11} = -(\varepsilon_s{}^5 - 10\varepsilon_s{}^3 \sigma_s{}^2 + 5\varepsilon_s \sigma_s{}^4) U_1 + (\varepsilon_s{}^3 - 3\varepsilon_s \sigma_s{}^2) \frac{U_1 k_u}{C} - Y_1 \varepsilon_s \text{ ; and}$$

$$N_{11} = (5\varepsilon_s{}^4 \sigma_s - 10\varepsilon_s{}^2 \sigma_s{}^3 + \sigma_s{}^5) U_1 - (3\varepsilon_s{}^2 \sigma_s - \sigma_s{}^3) \frac{U_1 k_u}{C} + \sigma_s Y_1 \quad \text{(B 14)}$$

The equation below is obtained using $w_s^{ls} = w_h^{ls}$:

$$c_1 e^{-\delta_s r} F_{11} + c_2 e^{\delta_s r} F_{11} + c_3 e^{-\varepsilon_s r}(G_{11} \sin \sigma_s r + H_{11} \cos \sigma_s r) + c_4 e^{-\varepsilon_s r}(H_{11} \sin \sigma_s r - G_{11} \cos \sigma_s r) -$$

$$c_5 e^{\varepsilon_1 r}(G_{11} \sin \sigma_s r - H_{11} \cos \sigma_s r) + c_6 e^{\varepsilon_s r}(H_{11} \sin \sigma_s r + G_{11} \cos \sigma_s r) - d_1 e^{-\delta_h r} F_{22} - d_2 e^{\delta_h r} F_{22} -$$

$$d_3 e^{-\varepsilon_h r}(G_{22} \sin \sigma_h r + H_{22} \cos \sigma_h r) - d_4 e^{-\varepsilon_h r}(H_{22} \sin \sigma_h r - G_{22} \cos \sigma_h r) + d_5 e^{\varepsilon_h r}(G_{22} \sin \sigma_h r - H_{22} \cos \sigma_h r) -$$

$$d_6 e^{\varepsilon_h r}(H_{22} \sin \sigma_h r + G_{22} \cos \sigma_h r) = R_{12} \qquad \text{(B 15)}$$

Assuming

$$G_{11} = U_1(4{\varepsilon_s}^3 \sigma_s - 4\varepsilon_s {\sigma_s}^3) - \frac{U_1 k_u}{C}(2\varepsilon_s \sigma_s);\ H_{11} = U_1({\varepsilon_s}^4 - 6{\varepsilon_s}^2 {\sigma_s}^2 + {\sigma_s}^4) - \frac{U_1 k_u}{C}({\varepsilon_s}^2 - {\sigma_s}^2) + Y_1;\ F_{11} = {\delta_s}^4 U_1 -$$

$${\delta_s}^2 \frac{Q_1 k_u}{C} + Y_1;\ G_{22} = U_2(4{\varepsilon_h}^3 \sigma_h - 4\varepsilon_h {\sigma_h}^3) - \frac{U_2 k_u}{C}(2\varepsilon_h \sigma_h)\ ;\ H_{22} = U_2({\varepsilon_h}^4 - 6{\varepsilon_h}^2 {\sigma_h}^2 + {\sigma_h}^4) - \frac{U_2 k_u}{C}({\varepsilon_h}^2 - {\sigma_h}^2) + \qquad \text{(B 16)}$$

$$Y_2\ ;\ F_{22} = {\delta_h}^4 U_2 - {\delta_h}^2 \frac{U_2 k_u}{} + Y_2$$

The following equation is obtained from $w_s^{ls'} = w_h^{ls'}$:

$$c_1 e^{-\delta_s r} L_{11} - c_2 e^{\delta_s r} L_{11} + c_3 e^{-\varepsilon_s r}(M_{11} \cos \sigma_s r - N_{11} \sin \sigma_s r) + c_4 e^{-\varepsilon_s r}(N_{11} \cos \sigma_s r + M_{11} \sin \sigma_s r) -$$

$$c_5 e^{\varepsilon_s r}(M_{11} \cos \sigma_s r + N_{11} \sin \sigma_s r) + e^{\varepsilon_s r} c_6(N_{11} \cos \sigma_s r - M_{11} \sin \sigma_s r) - d_1 e^{-\delta_h r} L_{22} + d_2 e^{\delta_h r} L_{22} -$$

$$d_3 e^{-\varepsilon_h r}(M_{22} \cos \sigma_h r - N_{22} \sin \sigma_h r) - d_4 e^{-\varepsilon_h r}(N_{22} \cos \sigma_h r + M_{22} \sin \sigma_h r) + d_5 e^{\varepsilon_h r}(M_{22} \cos \sigma_h r + N_{22} \sin \sigma_h r) -$$

$$d_6 e^{\varepsilon_h r}(N_{22} \cos \sigma_h r - M_{22} \sin \sigma_h r) = R_{13} \qquad \text{(B 17)}$$

where

$$R_1 = 0 \tag{B 18}$$

$$R_2 = 0 \tag{B 19}$$

$$R_3 = -P_0(K_c)_{eq}\frac{(k_u+k_l)}{k_u k_l} - C\sum_{n=1}^{n=\infty}\left\{\left[D_2 + E_2\left(\frac{2n\pi}{s}\right)^4 - F_2\left(\frac{2n\pi}{s}\right)^2 - 1\right]p_{nh}\right\}\left(\frac{2n\pi}{s}\right)\sin n\pi - \sum_{n=1}^{n=\infty}(K_c)_{eq}p_{nh}\cos n\pi \tag{B 20}$$

$$R_4 = \sum_{n=1}^{n=\infty}\left\{\left[D_2 + E_2\left(\frac{2n\pi}{s}\right)^4 - F_2\left(\frac{2n\pi}{s}\right)^2\right]p_{nh} + \left[\left(\frac{GF_2{D_s}^2}{C^2}\right)\left(\frac{2n\pi}{s}\right)^2 + \left[\left(\frac{GF_2D_s}{C}\right) + \frac{D_s}{C^2}\right]\right]P_n\right\}\left(\frac{2n\pi}{s}\right)\sin n\pi \tag{B 21}$$

$$R_5 = \sum_{n=1}^{n=\infty}\left[(p_{nh} - p_{ns})\cos\left(\frac{2n\pi r}{s}\right)\right] \tag{B 22}$$

$$R_6 = \sum_{n=1}^{n=\infty}\left\{\left[D_1 + E_1\left(\frac{2n\pi}{s}\right)^4 - F_1\left(\frac{2n\pi}{s}\right)^2\right]p_{ns} + \left[\left(\frac{GF_1{D_s}^2}{C^2}\right)\left(\frac{2n\pi}{s}\right)^2 + \left[\left(\frac{GF_1D_s}{C}\right) + \frac{D_s}{C^2}\right]\right]P_n\right\}\left(\frac{2n\pi}{s}\right)\sin\left(\frac{2n\pi r}{s}\right) -$$

$$\sum_{n=1}^{n=\infty}\left\{\left[D_2 + E_2\left(\frac{2n\pi}{s}\right)^4 - F_2\left(\frac{2n\pi}{s}\right)^2\right]p_{nh} + \left[\left(\frac{GF_2{D_h}^2}{C^2}\right)\left(\frac{2n\pi}{s}\right)^2 + \left[\left(\frac{GF_2D_h}{C}\right) + \frac{D_h}{C^2}\right]\right]P_n\right\}\left(\frac{2n\pi}{s}\right)\sin\left(\frac{2n\pi r}{s}\right) \tag{B 23}$$

$$R_7 = \sum_{n=1}^{n=\infty}\left\{\left[D_1 + E_1\left(\frac{2n\pi}{s}\right)^4 - F_1\left(\frac{2n\pi}{s}\right)^2\right]p_{ns} + \left[\left(\frac{GF_1{D_s}^2}{C^2}\right)\left(\frac{2n\pi}{s}\right)^2 + \left[\left(\frac{GF_1D_s}{C}\right) + \frac{D_s}{C^2}\right]\right]P_n\right\}\left(\frac{2n\pi}{s}\right)^2\cos\left(\frac{2n\pi r}{s}\right) \tag{B 24}$$

$$R_8 = -C\sum_{n=1}^{n=\infty}\left\{\left[D_1 + E_1\left(\frac{2n\pi}{s}\right)^4 - F_1\left(\frac{2n\pi}{s}\right)^2 - 1\right]p_{ns} + \left[\left(\frac{GF_1{D_s}^2}{C^2}\right)\left(\frac{2n\pi}{s}\right)^2 + \left[\left(\frac{GF_1D_s}{C}\right) + \frac{D_s}{C^2}\right]\right]P_n\right\}\left(\frac{2n\pi}{s}\right)\sin\left(\frac{2n\pi r}{s}\right) +$$

$$C\sum_{n=1}^{n=\infty}\left\{\left[D_1 + E_1\left(\frac{2n\pi}{s}\right)^4 - F_1\left(\frac{2n\pi}{s}\right)^2 - 1\right]p_{nh} + \left[\left(\frac{GF_1{D_h}^2}{C^2}\right)\left(\frac{2n\pi}{s}\right)^2 + \left[\left(\frac{GF_1D_h}{C}\right) + \frac{D_h}{C^2}\right]\right]P_n\right\}\left(\frac{2n\pi}{s}\right)\sin\left(\frac{2n\pi r}{s}\right) \tag{B 25}$$

$$R_9 = \sum_{n=1}^{n=\infty}\left\{\left[D_2 + E_2\left(\frac{2n\pi}{s}\right)^4 - F_2\left(\frac{2n\pi}{s}\right)^2\right]p_{nh} + \left[\left(\frac{GF_2{D_h}^2}{C^2}\right)\left(\frac{2n\pi}{s}\right)^2 + \left[\left(\frac{GF_2D_h}{C}\right) + \frac{D_h}{C^2}\right]\right]P_n\right\}\left(\frac{2n\pi}{s}\right)^2\cos\left(\frac{2n\pi r}{s}\right) \tag{B 26}$$

$$R_{10} = \frac{(K_c)_{eq} P_n}{C}\left[Z_2\left(\frac{k_u+k_l}{k_u k_l}\right) - \left(\frac{(K_c)_{eq}}{C}\right)\left(\frac{U_2}{D_h}\right)\right] P_0 - \sum_{n=1}^{n=\infty}\left\{\left[\left(\frac{U_2}{D_h}\right) + \left(\frac{U_2}{C}\right)\left(\frac{2n\pi}{s}\right)^2\right] + \left[V_2\left(\frac{2n\pi}{s}\right)^4 + X_2\left(\frac{2n\pi}{s}\right)^2 + Z_2\right] p_{nh}\right\} \cos n\pi - \sum_{n=1}^{n=\infty}\left\{\left[\left(\frac{U_2}{D_h}\right) - \left(\frac{U_2}{C}\right)\left(\frac{2n\pi}{s}\right)^2\right]\left(\frac{2n\pi}{s}\right) P_n - \left[U_2\left(\frac{2n\pi}{s}\right)^4 + W_2\left(\frac{2n\pi}{s}\right)^2 + Y_2\right]\left(\frac{2n\pi}{s}\right) p_{nh}\right\} \sin n\pi \quad \text{(B 27)}$$

$$R_{11} = \sum_{n=1}^{n=\infty} \frac{U_1}{C}\left(\frac{2n\pi}{s}\right)^3 P_n \quad \text{(B 28)}$$

$$R_{12} = \left[\frac{(k_1+k_2)(Y_2-Y_1)}{k_1} + \left(\frac{U_1}{D_s} - \frac{U_2}{D_h}\right)\right] P_0 + \sum_{n=1}^{n=\infty}\left[\left(\frac{U_1}{D_s} - \frac{U_2}{D_h}\right) - \left(\frac{U_1}{C} - \frac{U_2}{C}\right)\left(\frac{2n\pi}{s}\right)^2\right] P_n \cos\left(\frac{2n\pi r}{s}\right) - \sum_{n=1}^{n=\infty}\left[\left(1 + \frac{U_1 {k_u}^2}{CG}\right) - \left(\frac{U_1 k_u}{C}\right)\left(\frac{2n\pi}{s}\right)^2 + U_1\left(\frac{2n\pi}{s}\right)^4\right] p_{ns} \cos\left(\frac{2n\pi r}{s}\right) + \sum_{n=1}^{n=\infty}\left[\left(1 + \frac{U_2 {k_u}^2}{CG}\right) + \left(\frac{U_2 k_u}{C}\right)\left(\frac{2n\pi}{s}\right)^2 + U_2\left(\frac{2n\pi}{s}\right)^4\right] p_{nh} \cos\left(\frac{2n\pi r}{s}\right) \quad \text{(B 29)}$$

and

$$R_{13} = \sum_{n=1}^{n=\infty}\left[\left(\frac{U_2}{C} - \frac{U_1}{C}\right)\left(\frac{2n\pi}{s}\right)^2 - \left(\frac{U_1}{D_s} + \frac{U_2}{D_h}\right)\right]\left(\frac{2n\pi}{s}\right) P_n \sin\left(\frac{2n\pi r}{s}\right) + \sum_{n=1}^{n=\infty}\left[U_1\left(\frac{2n\pi}{s}\right)^4 + W_1\left(\frac{2n\pi}{s}\right)^2 + Y_1\right]\left(\frac{2n\pi}{s}\right) p_{ns} \sin\left(\frac{2n\pi r}{s}\right) - \sum_{n=1}^{n=\infty}\left[U_2\left(\frac{2n\pi}{s}\right)^4 + W_2\left(\frac{2n\pi}{s}\right)^2 + Y_2\right]\left(\frac{2n\pi}{s}\right) p_{nh} \sin\left(\frac{2n\pi r}{s}\right) \quad \text{(B 30)}$$

Assuming

$$W_1 = \frac{U_1 k_u}{C}\,;\; Y_1 = \frac{U_1 k_u k_l}{CG} + 1;\; W_2 = \frac{U_2 k_u}{C};\;\; Y_2 = \frac{U_2 k_u k_l}{CG} + 1;\; X_2 = \frac{(K_c)_{eq} U_2 k_u}{C^2}\,;\text{ and } Z_2 = \left(\frac{(K_c)_{eq}}{C}\right)\left(\frac{U_2 k_u k_l}{CG} + 1\right) \quad \text{(B 31)}$$

Appendix C: MATLAB 2016a Code to Solve Non-Linear Equations

```
function x = Solve_Kerr_R2

global Kc S d h1 h2 niu1 niu2 Es1 Es2 Sr1 Sr2 yr1 yr2 Pr k s ksc Gs h H Eg niug niur1 niur2 gamma
close all
clear variables
clc

%================= x0 = Initial values of unknowns=================
x0 = [281013921511;0.447281013921511;0.0776456973682230;-0.161108674439219;0.0776456973682230;0.161108674439219;-0.512056112678815;-
0.472075765866754;0.246308799350512;-0.230563080479509;0.0906650421213553;0.114977961896917;0.575591626819095];

A = [0,0,0,0,0,0,0,0,0,0,0,0,1;0,0,0,0,0,0,0,0,0,0,0,0,-1];  %  Matrix for linear inequality constraints
 b = [0.75;0];  %Vector for linear inequality constraints if Spacing=2.5m
% A=[];
% b=[];
lb = []; %Vector of lower bounds
ub = []; %Vector of upper bounds

%================= Input parameters=================
%-------------------------Properties of soft soil-------------------------
H = 10; % thickness of soft soil in m
h1 = 1; % thickness of top layer in m
h2 = H-h1; % thickness of bottom layer in m
Es1 = 1000; % Elastic modulus of soil in top layer in kPa
Es2 = 1000; % Elastic modulus of soil in bottom layer in kPa
niu1 = 0.3; % Poisson's of top layer
niu2 = 0.3; % Poisson's of bottom layer
gamma = 0.181; % need to change according to h1

%-------------------------Properties of granular materials-------------------------
h = 0.75; % thickness of LTP in m
Eg = 35000; % Young Modulus of granular materials in kPa
niug = 0.3; % Poisson's of granular layer
```

```
%-------------------------Properties of GR-------------------------
Sr1 = 1000; % Tensile stiffness of GR  top layer
Sr2 = 1000; % Tensile stiffness of GR bottom layer
niur1 = 0.3; % Poisson's of GR  top layer
niur2 = 0.3; % Poisson's of GR  bottom layer

%-------------------------Properties of CMC-------------------------
d = 0.5; % diameter of column in m
S = 2.0; % centre to centre spacing in m
Ec = 10000000; % Elastic modulus of column in kPa
a_r = (pi*d^2/4)/(S*S); % area replacement ratio
Hc = H; %Length of column
Ec_eq = (Ec*a_r)+(Es1*(1-a_r));
Kc = (Ec_eq/Hc)*(S*d/S);

%-------------------------Calculated parameters-------------------------
s = S-d; % spacing in m
h2 = H-h1; % thickness of bottom layer in m
yr1 = h/6; % location of top layer of GR from CL in m
yr2 = h/6; % location of bottom layer of GR from CL in m
  k1 = Es1*(1-niu1)/(h1*(1-niu1-(2*niu1^2))); % modulus of subgrade
  k2 = Es2*gamma*(1-niu2)*(sinh(gamma*h2)*cosh(gamma*h2)+(gamma*h2))/(2*(1-niu2-(2*niu2^2))*sinh(gamma*h2)*sinh(gamma*h2)); % modulus of
subgrsde reaction of upper soil layer in kPa/m
 Gs = Es2*(sinh(gamma*h2)*cosh(gamma*h2)-(gamma*h2))/(4*gamma*(1+niu2)*sinh(gamma*h2)*sinh(gamma*h2)); % shear modulus of soft soil for winkler
ksc = (10*(1+niug))/(12+11*niug); % Cross-section correction factor of Timoshenko beam
hbs = sqrt((Sr2/Eg)^2+((Sr2/Eg)*(2*yr2+h)))-(Sr2/Eg); % location of NA in sagging moment moment zone in m
ybs = (h/2) - hbs; % distance between NA and CL of LTP within the sagging in m
Igs = hbs^3/3; % second moment of inertia of granular materials within sagging in m^4
 Dbs = (Eg*Igs+(Sr2*(ybs+yr2)^2))*1; % equivalent bending stiffness of LTP in sagging
Cbs = ksc*(((Eg*h)/(2*(1+niug)))+(Sr1/(2*(1+niur1)))+(Sr2/(2*(1+niur2)))); % equivalent shear stiffness in sagging
 if Sr1 == 0; % Tensile stiffness of GR  top layer
      hbh = sqrt((Sr2/Eg)*((Sr2/Eg)-(2*yr2-h)))-(Sr2/Eg);
      Igh = hbh^3/3; % second moment of inertia of granular materials within hogging in m^4
      ybh = (h/2) - hbh; % distance between NA and CL of LTP within the hogging in m
      Dbh = (Eg*Igh+(Sr2*(ybh-yr2)^2))*1; % equivalent bending stiffness of LTP in sagging
      Cbh = ksc*(((Eg*h)/(2*(1+niug)))+(Sr1/(2*(1+niur1)))+(Sr2/(2*(1+niur2)))); % equivalent shear stiffness in hogging
```

```
 else
     hbh = sqrt((Sr1/Eg)^2+((Sr1/Eg)*(2*yr1+h)))-(Sr1/Eg); % location of NA in hogging moment zone in m
     ybh = (h/2) - hbh; % distance between NA and CL of LTP within the hogging in m
     Igh = hbh^3/3; % second moment of inertia of granular materials within hogging in m^4
     Dbh = (Eg*Igh+(Sr1*(ybh+yr1)^2))*1; % equivalent bending stiffness of LTP in sagging
     Cbh = ksc*(((Eg*h)/(2*(1+niug)))+(Sr1/(2*(1+niur1)))+(Sr2/(2*(1+niur2)))); % equivalent shear stiffness in hogging
 end

%================ loadings =================
Pr = 200 ; % (maximum pressure from embankment)
k = 300; %(no. of loop)
i = 0; %(initialization of loop)
f = @(c) c.^0;
P0 = (Pr/s)*integral(f,0,s);

%================Calculated parameters=================
X1 = - (1/Gs)*(k1+k2+(k1*Gs/Cbs));
X2 = - (1/Gs)*(k1+k2+(k1*Gs/Cbh));

Y1 = (k1/Dbs)+(k1*k2/(Gs*Cbs));
Y2 = (k1/Dbh)+(k1*k2/(Gs*Cbh));

Z1 = -k1*k2/(Gs*Dbs);
Z2 = -k1*k2/(Gs*Dbh);

alpha1 = (1/3)*(Y1-(X1^2/3));
alpha2 = (1/3)*(Y2-(X2^2/3));

beta1 = (1/2)*((2*X1^3/27)-(X1*Y1/3)+Z1);
beta2 = (1/2)*((2*X2^3/27)-(X2*Y2/3)+Z2);

DELTA1 = alpha1^3+beta1^2;
DELTA2 = alpha2^3+beta2^2;

m1 = -(1/2)*((2*X1/3) + nthroot(-beta1+sqrt(DELTA1), 3) + nthroot(-beta1-sqrt(DELTA1), 3));
m2 =  -(1/2)*((2*X2/3) + nthroot(-beta2+sqrt(DELTA2), 3) + nthroot(-beta2-sqrt(DELTA2), 3));
```

```
n1 = (sqrt(3)/2)*(nthroot((-beta1+sqrt(DELTA1)), 3)-nthroot((-beta1-sqrt(DELTA1)), 3));
n2 = (sqrt(3)/2)*(nthroot((-beta2+sqrt(DELTA2)), 3)-nthroot((-beta2-sqrt(DELTA2)), 3));

delta1 = sqrt(-(X1/3) + nthroot(-beta1+sqrt(DELTA1), 3) + nthroot(-beta1-sqrt(DELTA1), 3));
delta2 = sqrt(-(X2/3) + nthroot(-beta2+sqrt(DELTA2), 3) + nthroot(-beta2-sqrt(DELTA2), 3));

epsilon1 = sqrt((1/2)*(sqrt(m1^2+n1^2)+m1)); %correct
epsilon2 = sqrt((1/2)*(sqrt(m2^2+n2^2)+m2));

sigma1 = sqrt((1/2)*(sqrt(m1^2+n1^2)-m1)); %correct
sigma2 = sqrt((1/2)*(sqrt(m2^2+n2^2)-m2));

A1 = 1/((k1*Dbs)+(k2*Dbs)-(Gs*Cbs));  %checked
A2 = 1/((k1*Dbh)+(k2*Dbh)-(Gs*Cbh));

B1 = - (Gs*A1*Dbs^2/Cbs); %checked
B2 = - (Gs*A2*Dbh^2/Cbh);

C1 = (Dbs/Cbs)+(Gs*k1*A1*Dbs^2/Cbs^2); %checked
C2 = (Dbh/Cbh)+(Gs*k1*A2*Dbh^2/Cbh^2);

D1 = 1-(k1*k2*A1*Dbs^2/Cbs^2);  %checked
D2 = 1-(k1*k2*A2*Dbh^2/Cbh^2);

H1 = epsilon1^3-(3*epsilon1*sigma1^2); %checked
H2 = epsilon2^3-(3*epsilon2*sigma2^2);

I1 = sigma1^3-(3*sigma1*epsilon1^2); %checked
I2 = sigma2^3-(3*sigma2*epsilon2^2);

O1 = (sigma1*H1)-(epsilon1*I1); %checked
O2 = (sigma2*H2)-(epsilon2*I2);

P1 = (sigma1*I1)+(epsilon1*H1); %checked
P2 = (sigma2*I2)+(epsilon2*H2);

Q1 = epsilon1^2-sigma1^2; %checked
```

```
Q2 = epsilon2^2-sigma2^2;

R1 = 2*epsilon1*sigma1; %checked
R2 = 2*epsilon2*sigma2;

S1 = (sigma1*O1)-(epsilon1*P1); %checked
S2 = (sigma2*O2)-(epsilon2*P2);

T1 = (sigma1*P1)+(epsilon1*O1); %checked
T2 = (sigma2*P2)+(epsilon2*O2);

E1 = delta1*((delta1^4*B1)+(delta1^2*C1)+D1); %checked
E2 = delta2*((delta2^4*B2)+(delta2^2*C2)+D2);

F1 = (T1*B1)-(I1*C1)+(sigma1*D1); %checked
F2 = (T2*B2)-(I2*C2)+(sigma2*D2);

G1 = (S1*B1)-(H1*C1)-(epsilon1*D1);  %checked
G2 = (S2*B2)-(H2*C2)-(epsilon2*D2);

J1 = (epsilon1*F1)-(sigma1*G1); %checked
J2 = (epsilon2*F2)-(sigma2*G2);

K1 = (F1*sigma1)+(epsilon1*G1); %checked
K2 = (F2*sigma2)+(epsilon2*G2);

L1 = delta1-E1; %checked
L2 = delta2-E2;

M1 = (sigma1-F1); %checked
M2 = (sigma2-F2);

N1 = (epsilon1+G1);  %checked
N2 = ( epsilon2+G2);

A22 = (L2*Cbh)-Kc; B22 = (L2*Cbh)+Kc; C22 = (M2*Cbh); D22 = Cbh*N2+Kc; E22 = Cbh*N2-Kc; %checked
```

```
Q11 = (epsilon1*Q1) - (sigma1*R1); %checked
Q22 = (epsilon2*Q2) - (sigma2*R2);

R11 = (epsilon1*R1) + (sigma1*Q1); %checked
R22 = (epsilon2*R2) + (sigma2*Q2);

Q111 = (epsilon1*Q11) - (sigma1*R11); %checked
Q222 = (epsilon2*Q22) - (sigma2*R22);

R111 = (epsilon1*R11) + (sigma1*Q11); %checked
R222 = (epsilon2*R22) + (sigma2*Q22);

Q1111 = (epsilon1*Q111) - (sigma1*R111); %checked
Q2222 = (epsilon2*Q222) - (sigma2*R222);

R1111 = (epsilon1*R111) + (sigma1*Q111); %checked
R2222 = (epsilon2*R222) + (sigma2*Q222);

U1 = Dbs*Cbs*Gs/(k1*((Cbs*Gs)-(Dbs*(k1+k2))));
U2 = Dbh*Cbh*Gs/(k1*((Cbh*Gs)-(Dbh*(k1+k2))));

W1= Dbs*Gs/((Cbs*Gs)-(Dbs*(k1+k2)));
W2= Dbh*Gs/((Cbh*Gs)-(Dbh*(k1+k2)));

Y1= ((Cbs*Gs)-(Dbs*k1))/((Cbs*Gs)-(Dbs*(k1+k2)));
Y2= ((Cbh*Gs)-(Dbh*k1))/((Cbh*Gs)-(Dbh*(k1+k2)));

L11 = (-delta1^5*U1)+(delta1^3*W1)-(delta1*Y1);%checked
L22 = (-delta2^5*U2)+(delta2^3*W2)-(delta2*Y2);%checked
L22a = -delta2-((-delta2^5*U2)+(delta2^3*W2)-(delta2*Y2));

M11 = -(Q1111*U1)+(W1*Q11)-(epsilon1*Y1);
M22 = -(Q2222*U2)+(W2*Q22)-(epsilon2*Y2);
M22a = -epsilon2-(-(Q2222*U2)+(W2*Q22)-(epsilon2*Y2));

N11 = +(R1111*U1)-(W1*R11)+(sigma1*Y1);
N22 = +(R2222*U2)-(W2*R22)+(sigma2*Y2);
```

```
N22a = sigma2-(+(R2222*U2)-(W2*R22)+(sigma2*Y2));

F11 = (delta1^4*U1)-(delta1^2*W1)+(Y1);%checked
F22 = (delta2^4*U2)-(delta2^2*W2)+(Y2);%checked

G11 = (U1*R111)-(W1*R1); %checked
G22 = (U2*R222)-(W2*R2); %checked

H11 = (U1*Q111)-(W1*Q1)+Y1; %checked
H22 = (U2*Q222)-(W2*Q2)+Y2; %checked

% =================For BC1: at x = 0, Vs = 0 (at symmetry line)=================
    V1(1) = - L1;%*(Cbs/Dbs)
    V1(2) = + L1;
    V1(3) = - N1;
    V1(4) = + M1;
    V1(5) = + N1;
    V1(6 ) = + M1;
    V1(7) = 0; V1(8) = 0; V1(9) = 0; V1(10) = 0; V1(11) = 0; V1(12) = 0;
    V1(13) = 0;
    ZZ1 = 0;

% =================For BC2: at x = 0, w's = 0 (at symmetry line )=================
    V2(1) = - delta1;
    V2(2) = + delta1;
    V2(3) = - epsilon1;
    V2(4) = + sigma1;
    V2(5) = + epsilon1;
    V2(6 ) = + sigma1;
    V2(7) = 0;    V2(8) = 0;    V2(9) = 0;    V2(10) = 0;    V2(11) = 0;    V2(12) = 0;
    V2(13) = 0;
    ZZ2 = 0;

 % =================For BC3: at x = s/2, Vh = -Kcwh (at support )=================
    V3(1) = 0;    V3(2) = 0;    V3(3) = 0;    V3(4) = 0;    V3(5) = 0;    V3(6 ) = 0;
    V3(7) = - exp(-delta2*s/2)*A22;
    V3(8) = + exp(+delta2*s/2)*B22;
```

```
    V3(9) = - exp(-epsilon2*s/2)*((C22*sin(sigma2*s/2))+(E22*cos(sigma2*s/2)));
    V3(10) = - exp(-epsilon2*s/2)*((E22*sin(sigma2*s/2))-(C22*cos(sigma2*s/2)));
    V3(11) = - exp(+epsilon2*s/2)*((C22*sin(sigma2*s/2))-(D22*cos(sigma2*s/2)));
    V3(12) = + exp(+epsilon2*s/2)*((D22*sin(sigma2*s/2))+(C22*cos(sigma2*s/2)));
    V3(13) = 0;
    ZZ3 = (-Kc*P0*(k1+k2)/(k1*k2))+000;

% =================For BC4: at x = s/2, Rh = 0 (at support )================
    V4(1) = 0;    V4(2) = 0;    V4(3) = 0;    V4(4) = 0;    V4(5) = 0;    V4(6 ) = 0;
    V4(7) = - exp(-delta2*s/2)*E2;
    V4(8) = + exp(+delta2*s/2)*E2;
    V4(9) = - exp(-epsilon2*s/2)*((F2*sin(sigma2*s/2))-(G2*cos(sigma2*s/2)));
    V4(10) = + exp(-epsilon2*s/2)*((G2*sin(sigma2*s/2))+(F2*cos(sigma2*s/2)));
    V4(11) = - exp(+epsilon2*s/2)*((F2*sin(sigma2*s/2))+(G2*cos(sigma2*s/2)));
    V4(12) = - exp(+epsilon2*s/2)*((G2*sin(sigma2*s/2))-(F2*cos(sigma2*s/2)));
    V4(13) = 0;
    ZZ4 = 0;

 % =================For BC5: at x = 0, d(w2s) = 0================
    V5(1) = + L11;
    V5(2) = - L11;
    V5(3) = + M11;
    V5(4) = + N11;
    V5(5) = - M11;
    V5(6 ) = + N11;
    V5(7) = 0;    V5(8) = 0;    V5(9) = 0;    V5(10) = 0;    V5(11) = 0;    V5(12) = 0;
    V5(13) = 0;
    ZZ5 = 0;

% =================For BC6a: at x = s/2, shear strain in LTP=shear strain in shear layer================
    V6(1) = 0;    V6(2) = 0;    V6(3) = 0;    V6(4) = 0;    V6(5) = 0;    V6(6 ) =   0;
    V6(7) = + exp(-delta2*s/2)*L22a;
    V6(8) = - exp(+delta2*s/2)*L22a;
    V6(9) = + exp(-epsilon2*s/2)*((M22a*cos(sigma2*s/2))-(N22a*sin(sigma2*s/2)));
    V6(10) = + exp(-epsilon2*s/2)*((N22a*cos(sigma2*s/2))+(M22a*sin(sigma2*s/2)));
    V6(11) = - exp(+epsilon2*s/2)*((M22a*cos(sigma2*s/2))+(N22a*sin(sigma2*s/2)));
    V6(12) = + exp(+epsilon2*s/2)*((N22a*cos(sigma2*s/2))-(M22a*sin(sigma2*s/2)));
```

```
    V6(13) = 0;
    ZZ6 = 0;

Aeq = [V1(1),V1(2),V1(3),V1(4),V1(5), V1(6), V1(7), V1(8), V1(9), V1(10), V1(11), V1(12), V1(13); ...
            V2(1),V2(2),V2(3),V2(4),V2(5), V2(6), V2(7), V2(8), V2(9), V2(10), V2(11), V2(12), V2(13);...
            V3(1),V3(2),V3(3),V3(4),V3(5), V3(6), V3(7), V3(8), V3(9), V3(10), V3(11), V3(12), V3(13);...
            V4(1),V4(2),V4(3),V4(4),V4(5), V4(6), V4(7), V4(8), V4(9), V4(10), V4(11), V4(12), V4(13);...
            V5(1),V5(2),V5(3),V5(4),V5(5), V5(6), V5(7), V5(8), V5(9), V5(10), V5(11), V5(12), V5(13);...
            V6(1),V6(2),V6(3),V6(4),V6(5), V6(6), V6(7), V6(8), V6(9), V6(10), V6(11), V6(12), V6(13)];

beq = [ZZ1; ZZ2; ZZ3; ZZ4; ZZ5; ZZ6];

options = optimoptions('fmincon','display','iter','Algorithm','interior-point','TolFun', 1e-10,'TolX',1e-20,'MaxIter',5000, 'MaxFunEvals',
20000);
[x,fval, exitflag] = fmincon(@(x) myfun(x),x0, A, b, Aeq, beq, lb, ub, @(x) mycon(x),options)

function f = myfun(x)

%=================For BC7: at x = r1, wbh = wbs=================
    V7(1) = + exp(-delta1*x(13));
    V7(2) = + exp(+delta1*x(13));
    V7(3) = + exp(-epsilon1*x(13))*cos(sigma1*x(13));
    V7(4) =  + exp(-epsilon1*x(13))*sin(sigma1*x(13));
    V7(5) =  + exp(+epsilon1*x(13))*cos(sigma1*x(13));
    V7(6 ) = + exp(+epsilon1*x(13))*sin(sigma1*x(13));
    V7(7) = - exp(-delta2*x(13));
    V7(8) = - exp(+delta2*x(13));
    V7(9) = - exp(-epsilon2*x(13))*cos(sigma2*x(13));
    V7(10) = - exp(-epsilon2*x(13))*sin(sigma2*x(13));
    V7(11) = - exp(+epsilon2*x(13))*cos(sigma2*x(13));
    V7(12) = - exp(+epsilon2*x(13))*sin(sigma2*x(13));
    V7(13) = 0;
    ZZ7 = 0;

% =================For BC8: at x = r1, Mbh = 0=================
    V8(1) = 0;    V8(2) = 0;    V8(3) = 0;    V8(4) = 0;    V8(5) = 0;    V8(6 ) = 0;
    V8(7) = - exp(-delta2*x(13))*delta2*E2;
```

```
    V8(8) = - exp(+delta2*x(13))*delta2*E2;
    V8(9) = - exp(-epsilon2*x(13))*((J2*sin(sigma2*x(13)))-(K2*cos(sigma2*x(13))));
    V8(10) = + exp(-epsilon2*x(13))*((K2*sin(sigma2*x(13)))+(J2*cos(sigma2*x(13))));
    V8(11) = + exp(+epsilon2*x(13))*((J2*sin(sigma2*x(13)))+(K2*cos(sigma2*x(13))));
    V8(12) = + exp(+epsilon2*x(13))*((K2*sin(sigma2*x(13)))-(J2*cos(sigma2*x(13))));
    V8(13) = 0;
    ZZ8 = 0;

    % =================For BC9: at x = r1, Mbs = 0=================
    V9(1) = + exp(-delta1*x(13))*delta1*E1;
    V9(2) = + exp(+delta1*x(13))*delta1*E1;
    V9(3) = + exp(-epsilon1*x(13))*((J1*sin(sigma1*x(13)))-(K1*cos(sigma1*x(13))));
    V9(4) = - exp(-epsilon1*x(13))*((K1*sin(sigma1*x(13)))+(J1*cos(sigma1*x(13))));
    V9(5) = - exp(+epsilon1*x(13))*((J1*sin(sigma1*x(13)))+(K1*cos(sigma1*x(13))));
    V9(6 ) = - exp(+epsilon1*x(13))*((K1*sin(sigma1*x(13)))-(J1*cos(sigma1*x(13))));
    V9(7) = 0;    V9(8) = 0;    V9(9) =0;    V9(10) = 0;    V9(11) = 0;    V9(12) = 0;
    V9(13) = 0;
    ZZ9 = 0;

% =================For BC10: at x = r1, Vbh = Vbs=================
    V10(1) = - exp(-delta1*x(13))*L1*Cbs;
    V10(2) = + exp(+delta1*x(13))*L1*Cbs;
    V10(3) = - exp(-epsilon1*x(13))*Cbs*((M1*sin(sigma1*x(13)))+(N1*cos(sigma1*x(13))));
    V10(4) = - exp(-epsilon1*x(13))*Cbs*((N1*sin(sigma1*x(13)))-(M1*cos(sigma1*x(13))));
    V10(5) = - exp(+epsilon1*x(13))*Cbs*((M1*sin(sigma1*x(13)))-(N1*cos(sigma1*x(13))));
    V10(6 ) =  + exp(+epsilon1*x(13))*Cbs*((N1*sin(sigma1*x(13)))+(M1*cos(sigma1*x(13))));
    V10(7) =  + exp(-delta2*x(13))*L2*Cbh;
    V10(8) = - exp(+delta2*x(13))*L2*Cbh;
    V10(9) = + exp(-epsilon2*x(13))*Cbh*((M2*sin(sigma2*x(13)))+(N2*cos(sigma2*x(13))));
    V10(10) = + exp(-epsilon2*x(13))*Cbh*((N2*sin(sigma2*x(13)))-(M2*cos(sigma2*x(13))));
    V10(11) = + exp(+epsilon2*x(13))*Cbh*((M2*sin(sigma2*x(13)))-(N2*cos(sigma2*x(13))));
    V10(12) = - exp(+epsilon2*x(13))*Cbh*((N2*sin(sigma2*x(13)))+(M2*cos(sigma2*x(13))));
    V10(13) = 0;
    ZZ10 = 0;

    % =================For BC11: at x = r1, Rbh = Rbs=================
    V11(1) = - exp(-delta1*x(13))*E1;
```

```
    V11(2) = + exp(+delta1*x(13))*E1;
    V11(3) = - exp(-epsilon1*x(13))*((F1*sin(sigma1*x(13)))-(G1*cos(sigma1*x(13))));
    V11(4) = + exp(-epsilon1*x(13))*((G1*sin(sigma1*x(13)))+(F1*cos(sigma1*x(13))));
    V11(5) = - exp(+epsilon1*x(13))*((F1*sin(sigma1*x(13)))+(G1*cos(sigma1*x(13))));
    V11(6 ) = - exp(+epsilon1*x(13))*((G1*sin(sigma1*x(13)))-(F1*cos(sigma1*x(13))));
    V11(7) = + exp(-delta2*x(13))*E2;
    V11(8) =  - exp(+delta2*x(13))*E2;
    V11(9) = + exp(-epsilon2*x(13))*((F2*sin(sigma2*x(13)))-(G2*cos(sigma2*x(13))));
    V11(10) =  - exp(-epsilon2*x(13))*((G2*sin(sigma2*x(13)))+(F2*cos(sigma2*x(13))));
    V11(11) =  + exp(+epsilon2*x(13))*((F2*sin(sigma2*x(13)))+(G2*cos(sigma2*x(13))));
    V11(12) =  + exp(+epsilon2*x(13))*((G2*sin(sigma2*x(13)))-(F2*cos(sigma2*x(13))));
    V11(13) = 0;
    ZZ11 = 0;

% =================For BC12: at x = r1, w2s = w2h=================
    V12(1) = + exp(-delta1*x(13))*F11;
    V12(2) = + exp(+delta1*x(13))*F11;
    V12(3) = + exp(-epsilon1*x(13))*((G11*sin(sigma1*x(13)))+(H11*cos(sigma1*x(13))));
    V12(4) = + exp(-epsilon1*x(13))*((H11*sin(sigma1*x(13)))-(G11*cos(sigma1*x(13))));
    V12(5) = - exp(+epsilon1*x(13))*((G11*sin(sigma1*x(13)))-(H11*cos(sigma1*x(13))));
    V12(6 ) =  + exp(+epsilon1*x(13))*((H11*sin(sigma1*x(13)))+(G11*cos(sigma1*x(13))));
    V12(7) = - exp(-delta2*x(13))*F22;
    V12(8) = - exp(+delta2*x(13))*F22;
    V12(9) = - exp(-epsilon2*x(13))*((G22*sin(sigma2*x(13)))+(H22*cos(sigma2*x(13))));
    V12(10) = - exp(-epsilon2*x(13))*((H22*sin(sigma2*x(13)))-(G22*cos(sigma2*x(13))));
    V12(11) = + exp(+epsilon2*x(13))*((G22*sin(sigma2*x(13)))-(H22*cos(sigma2*x(13))));
    V12(12) = - exp(+epsilon2*x(13))*((H22*sin(sigma2*x(13)))+(G22*cos(sigma2*x(13))));
    V12(13) = 0;
 ZZ12=(((Cbs*Gs)/(k1*((Cbs*Gs)-(Dbs*(k1+k2)))))-((Cbh*Gs)/(k1*((Cbh*Gs)-(Dbh*(k1+k2))))))*P0-...
     (((1)/(k1*((Cbs*Gs)-(Dbs*(k1+k2)))))-((1)/(k1*((Cbh*Gs)-(Dbh*(k1+k2))))))*(k1+k2)*P0;


% =================For BC13: at x = r1, d(w2s) = d(w2h)=================
    V13(1) = + exp(-delta1*x(13))*L11;
    V13(2) = - exp(+delta1*x(13))*L11;
    V13(3) = + exp(-epsilon1*x(13))*((M11*cos(sigma1*x(13)))-(N11*sin(sigma1*x(13))));
    V13(4) =  + exp(-epsilon1*x(13))*((N11*cos(sigma1*x(13)))+(M11*sin(sigma1*x(13))));
```

```
    V13(5) = - exp(+epsilon1*x(13))*((M11*cos(sigma1*x(13)))+(N11*sin(sigma1*x(13))));
    V13(6 ) =  + exp(+epsilon1*x(13))*((N11*cos(sigma1*x(13)))-(M11*sin(sigma1*x(13))));
    V13(7) = - exp(-delta2*x(13))*L22;
    V13(8) = + exp(+delta2*x(13))*L22;
    V13(9) = - exp(-epsilon2*x(13))*((M22*cos(sigma2*x(13)))-(N22*sin(sigma2*x(13))));
    V13(10) = - exp(-epsilon2*x(13))*((N22*cos(sigma2*x(13)))+(M22*sin(sigma2*x(13))));
    V13(11) = + exp(+epsilon2*x(13))*((M22*cos(sigma2*x(13)))+(N22*sin(sigma2*x(13))));
    V13(12) = - exp(+epsilon2*x(13))*((N22*cos(sigma2*x(13)))-(M22*sin(sigma2*x(13))));
    V13(13) = 0;
    ZZ13 =  0;
%=================Summary of equations=================
f1=  x(1)*V1(1)   + x(2)*V1(2)  + x(3)*V1(3)    + x(4)*V1(4)+x(5)*V1(5)    +x(6)*V1(6)+x(7)*V1(7)    +x(8)*V1(8)+x(9)*V1(9)+x(10)*V1(10)
+x(11)*V1(11)+x(12)*V1(12)+x(13)*V1(13) - ZZ1;
f2=  x(1)*V2(1)   + x(2)*V2(2)  + x(3)*V2(3)    + x(4)*V2(4)+x(5)*V2(5)    +x(6)*V2(6)+x(7)*V2(7)    +x(8)*V2(8)+x(9)*V2(9)+x(10)*V2(10)
+x(11)*V2(11)+x(12)*V2(12)+x(13)*V2(13) - ZZ2;
f3=  x(1)*V3(1)   + x(2)*V3(2)  + x(3)*V3(3)    + x(4)*V3(4)+x(5)*V3(5)    +x(6)*V3(6)+x(7)*V3(7)    +x(8)*V3(8)+x(9)*V3(9)+x(10)*V3(10)
+x(11)*V3(11)+x(12)*V3(12)+x(13)*V3(13) - ZZ3;
f4=  x(1)*V4(1)   + x(2)*V4(2)  + x(3)*V4(3)    + x(4)*V4(4)+x(5)*V4(5)    +x(6)*V4(6)+x(7)*V4(7)    +x(8)*V4(8)+x(9)*V4(9)+x(10)*V4(10)
+x(11)*V4(11)+x(12)*V4(12)+x(13)*V4(13) - ZZ4;
f5 =  x(1)*V5(1)   + x(2)*V5(2)  + x(3)*V5(3)   + x(4)*V5(4)+x(5)*V5(5)    +x(6)*V5(6)+x(7)*V5(7)    +x(8)*V5(8)+x(9)*V5(9)+x(10)*V5(10)
+x(11)*V5(11)+x(12)*V5(12)+x(13)*V5(13) - ZZ5;
f6 =  x(1)*V6(1)   + x(2)*V6(2)  + x(3)*V6(3)   + x(4)*V6(4)+x(5)*V6(5)    +x(6)*V6(6)+x(7)*V6(7)    +x(8)*V6(8)+x(9)*V6(9)+x(10)*V6(10)
+x(11)*V6(11)+x(12)*V6(12)+x(13)*V6(13) - ZZ6;
f7=  x(1)*V7(1)   + x(2)*V7(2)  + x(3)*V7(3)    + x(4)*V7(4)+x(5)*V7(5)    +x(6)*V7(6)+x(7)*V7(7)    +x(8)*V7(8)+x(9)*V7(9)+x(10)*V7(10)
+x(11)*V7(11)+x(12)*V7(12)+x(13)*V7(13) - ZZ7;
f8=  x(1)*V8(1)   + x(2)*V8(2)  + x(3)*V8(3)    + x(4)*V8(4)+x(5)*V8(5)    +x(6)*V8(6)+x(7)*V8(7)    +x(8)*V8(8)+x(9)*V8(9)+x(10)*V8(10)
+x(11)*V8(11)+x(12)*V8(12)+x(13)*V8(13) - ZZ8;
f9=  x(1)*V9(1)   + x(2)*V9(2)  + x(3)*V9(3)    + x(4)*V9(4)+x(5)*V9(5)    +x(6)*V9(6)+x(7)*V9(7)    +x(8)*V9(8)+x(9)*V9(9)+x(10)*V9(10)
+x(11)*V9(11)+x(12)*V9(12)+x(13)*V9(13) - ZZ9;
f10=x(1)*V10(1) + x(2)*V10(2)+ x(3)*V10(3) +
x(4)*V10(4)+x(5)*V10(5)+x(6)*V10(6)+x(7)*V10(7)+x(8)*V10(8)+x(9)*V10(9)+x(10)*V10(10)+x(11)*V10(11)+x(12)*V10(12)+x(13)*V10(13) - ZZ10;
f11=x(1)*V11(1) + x(2)*V11(2)+ x(3)*V11(3) +
x(4)*V11(4)+x(5)*V11(5)+x(6)*V11(6)+x(7)*V11(7)+x(8)*V11(8)+x(9)*V11(9)+x(10)*V11(10)+x(11)*V11(11)+x(12)*V11(12)+x(13)*V11(13)- ZZ11;
f12=x(1)*V12(1) + x(2)*V12(2)+ x(3)*V12(3) +
x(4)*V12(4)+x(5)*V12(5)+x(6)*V12(6)+x(7)*V12(7)+x(8)*V12(8)+x(9)*V12(9)+x(10)*V12(10)+x(11)*V12(11)+x(12)*V12(12)+x(13)*V12(13)- ZZ12;
f13=x(1)*V13(1) + x(2)*V13(2)+ x(3)*V13(3) +
x(4)*V13(4)+x(5)*V13(5)+x(6)*V13(6)+x(7)*V13(7)+x(8)*V13(8)+x(9)*V13(9)+x(10)*V13(10)+x(11)*V13(11)+x(12)*V13(12)+x(13)*V13(13)- ZZ13;
```

```
f =abs(f1)+ abs(f2)+ abs(f3)+abs(f4)+abs(f5)+abs(f6)+abs(f7)+abs(f8)+abs(f9)+abs(f10)+abs(f11)+abs(f12)+abs(f13);

end

function [c,ceq] = mycon(x)

%=================For BC7: at x = r1, wbh = wbs=================
    V7(1) = + exp(-delta1*x(13));
    V7(2) = + exp(+delta1*x(13));
    V7(3) = + exp(-epsilon1*x(13))*cos(sigma1*x(13));
    V7(4) =  + exp(-epsilon1*x(13))*sin(sigma1*x(13));
    V7(5) =  + exp(+epsilon1*x(13))*cos(sigma1*x(13));
    V7(6 ) = + exp(+epsilon1*x(13))*sin(sigma1*x(13));
    V7(7) = - exp(-delta2*x(13));
    V7(8) = - exp(+delta2*x(13));
    V7(9) = - exp(-epsilon2*x(13))*cos(sigma2*x(13));
    V7(10) = - exp(-epsilon2*x(13))*sin(sigma2*x(13));
    V7(11) = - exp(+epsilon2*x(13))*cos(sigma2*x(13));
    V7(12) = - exp(+epsilon2*x(13))*sin(sigma2*x(13));
    V7(13) = 0;
    ZZ7 = 0;

% =================For BC8: at x = r1, Mbh = 0=================
    V8(1) = 0;    V8(2) = 0;    V8(3) = 0;    V8(4) = 0;    V8(5) = 0;    V8(6 ) = 0;
    V8(7) = - exp(-delta2*x(13))*delta2*E2;
    V8(8) = - exp(+delta2*x(13))*delta2*E2;
    V8(9) = - exp(-epsilon2*x(13))*((J2*sin(sigma2*x(13)))-(K2*cos(sigma2*x(13))));
    V8(10) = + exp(-epsilon2*x(13))*((K2*sin(sigma2*x(13)))+(J2*cos(sigma2*x(13))));
    V8(11) = + exp(+epsilon2*x(13))*((J2*sin(sigma2*x(13)))+(K2*cos(sigma2*x(13))));
    V8(12) = + exp(+epsilon2*x(13))*((K2*sin(sigma2*x(13)))-(J2*cos(sigma2*x(13))));
    V8(13) = 0;
    ZZ8 = 0;

    % =================For BC9: at x = r1, Mbs = 0=================
    V9(1) = + exp(-delta1*x(13))*delta1*E1;
    V9(2) = + exp(+delta1*x(13))*delta1*E1;
```

```
    V9(3) = + exp(-epsilon1*x(13))*((J1*sin(sigma1*x(13)))-(K1*cos(sigma1*x(13))));
    V9(4) = - exp(-epsilon1*x(13))*((K1*sin(sigma1*x(13)))+(J1*cos(sigma1*x(13))));
    V9(5) = - exp(+epsilon1*x(13))*((J1*sin(sigma1*x(13)))+(K1*cos(sigma1*x(13))));
    V9(6 ) = - exp(+epsilon1*x(13))*((K1*sin(sigma1*x(13)))-(J1*cos(sigma1*x(13))));
    V9(7) = 0;    V9(8) = 0;    V9(9) =0;    V10(10) = 0;    V9(11) = 0;    V9(12) = 0;
    V9(13) = 0;
    ZZ9 = 0;

% =================For BC10: at x = r1, Vbh = Vbs=================
    V10(1) = - exp(-delta1*x(13))*L1*Cbs;
    V10(2) = + exp(+delta1*x(13))*L1*Cbs;
    V10(3) = - exp(-epsilon1*x(13))*Cbs*((M1*sin(sigma1*x(13)))+(N1*cos(sigma1*x(13))));
    V10(4) = - exp(-epsilon1*x(13))*Cbs*((N1*sin(sigma1*x(13)))-(M1*cos(sigma1*x(13))));
    V10(5) = - exp(+epsilon1*x(13))*Cbs*((M1*sin(sigma1*x(13)))-(N1*cos(sigma1*x(13))));
    V10(6 ) =  + exp(+epsilon1*x(13))*Cbs*((N1*sin(sigma1*x(13)))+(M1*cos(sigma1*x(13))));
    V10(7) =  + exp(-delta2*x(13))*L2*Cbh;
    V10(8) = - exp(+delta2*x(13))*L2*Cbh;
    V10(9) = + exp(-epsilon2*x(13))*Cbh*((M2*sin(sigma2*x(13)))+(N2*cos(sigma2*x(13))));
    V10(10) = + exp(-epsilon2*x(13))*Cbh*((N2*sin(sigma2*x(13)))-(M2*cos(sigma2*x(13))));
    V10(11) = + exp(+epsilon2*x(13))*Cbh*((M2*sin(sigma2*x(13)))-(N2*cos(sigma2*x(13))));
    V10(12) = - exp(+epsilon2*x(13))*Cbh*((N2*sin(sigma2*x(13)))+(M2*cos(sigma2*x(13))));
    V10(13) = 0;
    ZZ10 = 0;

    % =================For BC11: at x = r1, Rbh = Rbs=================
    V11(1) = - exp(-delta1*x(13))*E1;
    V11(2) = + exp(+delta1*x(13))*E1;
    V11(3) = - exp(-epsilon1*x(13))*((F1*sin(sigma1*x(13)))-(G1*cos(sigma1*x(13))));
    V11(4) = + exp(-epsilon1*x(13))*((G1*sin(sigma1*x(13)))+(F1*cos(sigma1*x(13))));
    V11(5) = - exp(+epsilon1*x(13))*((F1*sin(sigma1*x(13)))+(G1*cos(sigma1*x(13))));
    V11(6 ) = - exp(+epsilon1*x(13))*((G1*sin(sigma1*x(13)))-(F1*cos(sigma1*x(13))));
    V11(7) = + exp(-delta2*x(13))*E2;
    V11(8) =  - exp(+delta2*x(13))*E2;
    V11(9) = + exp(-epsilon2*x(13))*((F2*sin(sigma2*x(13)))-(G2*cos(sigma2*x(13))));
    V11(10) =  - exp(-epsilon2*x(13))*((G2*sin(sigma2*x(13)))+(F2*cos(sigma2*x(13))));
    V11(11) =  + exp(+epsilon2*x(13))*((F2*sin(sigma2*x(13)))+(G2*cos(sigma2*x(13))));
    V11(12) =  + exp(+epsilon2*x(13))*((G2*sin(sigma2*x(13)))-(F2*cos(sigma2*x(13))));
```

```
    V11(13) = 0;
    ZZ11 = 0;

% =================For BC12: at x = r1, w2s = w2h=================
     V12(1) = + exp(-delta1*x(13))*F11;
    V12(2) = + exp(+delta1*x(13))*F11;
    V12(3) = + exp(-epsilon1*x(13))*((G11*sin(sigma1*x(13)))+(H11*cos(sigma1*x(13))));
    V12(4) = + exp(-epsilon1*x(13))*((H11*sin(sigma1*x(13)))-(G11*cos(sigma1*x(13))));
    V12(5) = - exp(+epsilon1*x(13))*((G11*sin(sigma1*x(13)))-(H11*cos(sigma1*x(13))));
    V12(6 ) =  + exp(+epsilon1*x(13))*((H11*sin(sigma1*x(13)))+(G11*cos(sigma1*x(13))));
    V12(7) = - exp(-delta2*x(13))*F22;
    V12(8) = - exp(+delta2*x(13))*F22;
    V12(9) = - exp(-epsilon2*x(13))*((G22*sin(sigma2*x(13)))+(H22*cos(sigma2*x(13))));
    V12(10) = - exp(-epsilon2*x(13))*((H22*sin(sigma2*x(13)))-(G22*cos(sigma2*x(13))));
    V12(11) = + exp(+epsilon2*x(13))*((G22*sin(sigma2*x(13)))-(H22*cos(sigma2*x(13))));
    V12(12) = - exp(+epsilon2*x(13))*((H22*sin(sigma2*x(13)))+(G22*cos(sigma2*x(13))));
    V12(13) = 0;
    ZZ12=(((Cbs*Gs)/(k1*((Cbs*Gs)-(Dbs*(k1+k2)))))-((Cbh*Gs)/(k1*((Cbh*Gs)-(Dbh*(k1+k2))))))*P0-...
     (((1)/(k1*((Cbs*Gs)-(Dbs*(k1+k2)))))-((1)/(k1*((Cbh*Gs)-(Dbh*(k1+k2))))))*(k1+k2)*P0;

% =================For BC13: at x = r1, d(w2s) = d(w2h)=================
    V13(1) = + exp(-delta1*x(13))*L11;
    V13(2) = - exp(+delta1*x(13))*L11;
    V13(3) = + exp(-epsilon1*x(13))*((M11*cos(sigma1*x(13)))-(N11*sin(sigma1*x(13))));
    V13(4) =  + exp(-epsilon1*x(13))*((N11*cos(sigma1*x(13)))+(M11*sin(sigma1*x(13))));
    V13(5) = - exp(+epsilon1*x(13))*((M11*cos(sigma1*x(13)))+(N11*sin(sigma1*x(13))));
    V13(6 ) =  + exp(+epsilon1*x(13))*((N11*cos(sigma1*x(13)))-(M11*sin(sigma1*x(13))));
    V13(7) = - exp(-delta2*x(13))*L22;
    V13(8) = + exp(+delta2*x(13))*L22;
    V13(9) = - exp(-epsilon2*x(13))*((M22*cos(sigma2*x(13)))-(N22*sin(sigma2*x(13))));
    V13(10) = - exp(-epsilon2*x(13))*((N22*cos(sigma2*x(13)))+(M22*sin(sigma2*x(13))));
    V13(11) = + exp(+epsilon2*x(13))*((M22*cos(sigma2*x(13)))+(N22*sin(sigma2*x(13))));
    V13(12) = - exp(+epsilon2*x(13))*((N22*cos(sigma2*x(13)))-(M22*sin(sigma2*x(13))));
    V13(13) = 0;
    ZZ13 =  0;

%================ c= nonlinear inequalities; ceq= nonlinear equalities =================
```

```
c = [];
ceq (1) = x(1)*V7(1)    + x(2)*V7(2)   + x(3)*V7(3)    + x(4)*V7(4) + x(5)*V7(5)     + x(6)*V7(6)   + x(7)*V7(7)   + x(8)*V7(8)   + x(9)*V7(9)
+ x(10)*V7(10) + x(11)*V7(11) + x(12)*V7(12) + x(13)*V7(13)  - zz7;
ceq (2) = x(1)*V8(1)    + x(2)*V8(2)   + x(3)*V8(3)    + x(4)*V8(4) + x(5)*V8(5)     + x(6)*V8(6)   + x(7)*V8(7)   + x(8)*V8(8)   + x(9)*V8(9)
+ x(10)*V8(10) + x(11)*V8(11) + x(12)*V8(12) + x(13)*V8(13)  - zz8;
ceq (3) = x(1)*V9(1)    + x(2)*V9(2)   + x(3)*V9(3)    + x(4)*V9(4) + x(5)*V9(5)     + x(6)*V9(6)   + x(7)*V9(7)   + x(8)*V9(8)   + x(9)*V9(9)
+ x(10)*V9(10) + x(11)*V9(11) + x(12)*V9(12) + x(13)*V9(13)  - zz9;
ceq (4) = x(1)*V10(1)  + x(2)*V10(2) + x(3)*V10(3) + x(4)*V10(4) + x(5)*V10(5) + x(6)*V10(6) + x(7)*V10(7) + x(8)*V10(8) + x(9)*V10(9) +
x(10)*V10(10) + x(11)*V10(11) + x(12)*V10(12) + x(13)*V10(13) - zz10;
ceq (5) =  x(1)*V11(1) + x(2)*V11(2) + x(3)*V11(3) + x(4)*V11(4) + x(5)*V11(5) + x(6)*V11(6) + x(7)*V11(7) + x(8)*V11(8) + x(9)*V11(9) +
x(10)*V11(10) + x(11)*V11(11) + x(12)*V11(12) + x(13)*V11(13) - zz11;
ceq (6) = x(1)*V12(1) + x(2)*V12(2) + x(3)*V12(3)  + x(4)*V12(4) + x(5)*V12(5) + x(6)*V12(6) + x(7)*V12(7) + x(8)*V12(8) + x(9)*V12(9) +
x(10)*V12(10) + x(11)*V12(11) + x(12)*V12(12) + x(13)*V12(13) - zz12;
ceq (7) = x(1)*V13(1) + x(2)*V13(2) + x(3)*V13(3)  + x(4)*V13(4) + x(5)*V13(5) + x(6)*V13(6) + x(7)*V13(7) + x(8)*V13(8) + x(9)*V13(9) +
x(10)*V13(10) + x(11)*V13(11) + x(12)*V13(12) + x(13)*V13(13) - zz13;

end
end
```

Iter	F-count	f(x)	Feasibility	First-order optimality	Norm of step
0	14	4.053208e+12	3.128e+12	2.317e+04	
1	28	3.061373e+12	2.233e+12	4.804e+10	3.076e+10
2	42	7.698970e+04	6.778e+04	1.641e+07	2.602e+11
3	56	8.868129e+01	8.841e+01	1.005e+05	7.123e+03
4	70	6.558123e+01	6.425e+01	1.334e+05	8.516e-01
5	84	1.401866e+01	1.365e+01	1.279e+05	2.741e-01
6	98	5.163332e+00	5.057e+00	1.207e+05	2.333e-01
7	112	4.204036e-01	4.176e-01	1.195e+05	4.174e-02
8	126	1.287186e-03	1.275e-03	1.217e+05	2.826e-03
9	140	3.784795e-08	3.748e-08	1.217e+05	1.146e-05
10	154	7.283508e-12	7.276e-12	1.217e+05	8.434e-11
11	168	7.730361e-15	7.105e-15	2.812e+01	2.537e-16
12	185	5.659535e-16	3.018e-16	2.812e+01	6.577e-17

```
Local minimum possible. Constraints satisfied.

fmincon stopped because the size of the current step is less than
```

```
the selected value of the step size tolerance and constraints are
satisfied to within the default value of the constraint tolerance.



x =

   -0.6127
   -0.6127
   -0.0564
   -0.0404
   -0.0564
    0.0404
   -0.6127
   -0.6127
   -0.0564
   -0.0404
   -0.0564
    0.0404
    0.4345


fval =

   5.6595e-16


exitflag =

     2


ans =

   -0.6127
   -0.6127
```

```
-0.0564
-0.0404
-0.0564
 0.0404
-0.6127
-0.6127
-0.0564
-0.0404
-0.0564
 0.0404
 0.4345
```

Published with MATLAB® R2016a